

Universität der Bundeswehr München
Fakultät für Luft- und Raumfahrttechnik
Institut für Thermodynamik

Experimental Investigation of Reacting Near-Wall Jets

M.Sc. Rahand Dalshad

Vollständiger Abdruck der von der
Fakultät für Luft- und Raumfahrttechnik
der Universität der Bundeswehr München
zur Erlangung des akademischen Grades eines

Doktor-Ingenieurs (Dr.-Ing.)

genehmigten Dissertation

1. Berichterstatter: Univ.-Prof. Dr. rer. nat. Michael Pfitzner
2. Berichterstatter: Prof. Dr. habil. Andreas Dreizler

Die Dissertation wurde am 24.01.2022 bei der Universität der Bundeswehr München eingereicht und durch die Fakultät für Luft- und Raumfahrttechnik am 29.06.2022 angenommen.

Tag der Prüfung: 05.07.2022

بۇ دايە نالىدە، يېفا و ميران
إن شاء الله، خوا دەتان پارىزى

Acknowledgements

The following study was created during my work as research associate at the institute for thermodynamics of the Bundeswehr University Munich.

I would first like to thank my supervisor, Professor Michael Pfitzner. His trust in my abilities and motivation enabled the position in the first place. Despite occasional setbacks and times of frustration, he always provided help and solutions. I appreciate his invaluable expertise and the insightful discussions. His feedback and ideas pushed me to think a step further and bring the work to a next level.

I want to express my thank to Professor Andreas Dreizler for his role as co-supervisor. I appreciate his time and efforts.

I am grateful and lucky to have had such an experienced and patient technical adviser like Professor Tobias Sander. He introduced me to optical measurement techniques, accompanied the experiments and the data post-processing. Without his support and contribution, most of the results would not have been obtained.

In the last few years, I met a number of colleagues I could count on and appreciate their time: Paola Breda, Lukas Fischer, Arne Lampmann, Michael Straußwald, Markus Hosbach, Nikolas Perakis (TUM). A special thank to my friend Paola for the discussions, numerical support and proofreading of the thesis, and to my friend Lukas. He performed simulations of the setup, helped to perform the numerical investigation in this work and spent much of his time with proofreading.

I would like to take the opportunity to thank my students for their work, especially Brian Better from France for his numerical work in remote, as the pandemic situation refused personal attendance.

Finally, my thank goes to all my family members, each one has a special place. In particular, I am grateful for having such a great mother (kurkish: *Daya*) in my life. *Daya*, you gave me faith, motivation, guided me in every stage of my life and give me shelter in difficult times. Another family member I want to explicitly mention, is my wife. You supported me and had much patience, during good and difficult times and despite long working hours and insufficient time, I could provide for you. Thank you.

Abstract

The near-wall jet in crossflow (JICF) is a configuration applied for different purposes. In gas turbine combustion chambers, the injection of dilution air and the injection of fuel into a crossflow for mixing and subsequent reacting are examples of reacting JICF. In the field of film cooling, air injections help to isolate a component's surface from aggressive flows and cool it. Active cooling is necessary and even inevitable to protect the combustor as well as turbine vanes and blades from the high thermal loads, which exceed the material capability limits. Obviously, non-reacting and slow mixing processes and interaction with the mainstream are intended in this case. However, the injected air for film cooling may mix and ignite near the surface due to the presence of reactive elements and residual fuel within the turbulent main flow in combination with high temperature conditions. The desired cooling of the component changes to heat release to the surface. This phenomenon was already demonstrated in literature.

Thus, the accurate thermal design of components and the JICF investigation are essential processes. To study the appearance and structure of reacting JICF together with the heat release to the wall, a test bench was designed and operated for the injection of cold gaseous fuels into a hot oxygen-rich mainstream of 1600 K. The focus was on hydrogen, methane and propane, as the interest in these fuels has increased lately. Optical measurement techniques were applied to give insight into the reaction zone. Additionally, installed thermocouples within the surface provided temperature data, which were used in a post-processing step to determine the wall heat fluxes by means of the inverse heat conduction method. Hydrogen showed highest reactivity and led to the highest heat flux augmentation even at low fuel mass flow rates. The stable flames were directly anchored to the injection locations. From two-line laser-induced thermometry, reaction temperatures around 1800 K were determined, which were higher than that of the hydrocarbons. The reaction zone of methane on the other hand was least stable and highly turbulent. A significant ignition delay was found for methane. In addition, lowest heat fluxes were detected. In general, the ignition location of the hydrocarbons shifted upstream with increasing momentum ratio, but moved away from the surface, such that the heat release to the surface declined. Compared to angled injection, the normal injection reduced the ignition delay, as enhanced mixing occurred. Even though lower fuel mass flows were injected in the angled configuration, the heat fluxes were comparable to those of normal injection. The structure of the reaction zone was validated by numerical results. RANS simulations with the Eddy Dissipation Concept combustion model were performed. The shape of the simulated reaction was in good agreement with the experimental findings and also an ignition delay length could be predicted by the simulation. However, the combustion model overestimated the reaction temperature.

Kurzfassung

Die wandnahe *jet in crossflow* (JICF) Konfiguration findet für diverse Zwecke eine Anwendung. Beispiele für reaktive JICF sind u.a. die Einblasung von Luft zur Verdünnung einer Reaktionszone und die Injektion von Brennstoff in einen Querstrom zur Vermischung und anschließender Verbrennung in Gasturbinenbrennkammern. Auf dem Gebiet der Filmkühlung dagegen wird die Injektion von Luft zum Schutz einer Komponentenoberfläche und zur dessen Kühlung eingesetzt. Die aktive Kühlung ist notwendig und unverzichtbar, um die Brennkammer als auch die Turbinenleit- und laufschaufeln vor hohen thermischen Lasten zu schützen, die die Materialgrenzen übersteigen. Hier werden nicht-reagierende JICF mit möglichst geringer Interaktion und Vermischung mit der Querströmung angestrebt. Allerdings können durchaus chemische Reaktionen auftreten, wenn sich die Kühlluft mit dem heißen Hauptstrom vermischt, der eventuell reaktive Produkte und unverbrannten Brennstoff enthält. Aus der beabsichtigten Kühlung kann eine Wärmebelastung der Oberfläche entstehen. Dieses Phänomen wurde bereits in der Literatur beschrieben.

Die sorgfältige thermische Auslegung eines Bauteils und die JICF Untersuchung sind daher wichtige Prozesse. Um das Auftreten und die Struktur der reagierenden JICF neben der Wärmefreisetzung an einer angrenzenden Fläche zu untersuchen, wurde ein Prüfstand zur Injektion von gasförmigen Brenngasen in einen heißen, sauerstoffreichen Hauptstrom mit 1600 K konstruiert. Das Hauptaugenmerk lag hierbei auf Wasserstoff, Methan und Propan, da das Interesse an diesen Brennstoffen größer geworden ist. Um einen Einblick in die Reaktionszone zu bekommen wurden optische Messtechniken angewandt. Zusätzlich wurden Thermoelemente in das Bauteil integriert. Die Temperaturmessdaten wurden in einem späteren Datenverarbeitungsschritt zur inverse Berechnung der Wärmeströme genutzt. Wasserstoff zeigte höchste Reaktivität und erzeugte die höchsten Wandwärmelasten, sogar bei geringem Massenstrom. Die stabilen Flammen ankerten direkt an den Injektionsdüsen. Mittels der laserinduzierten Zwei-Linien-Thermometrie wurden Reaktionstemperaturen von ca. 1800 K bestimmt und diese lagen höher als die der Kohlenwasserstoffe. Dagegen zeigte die Reaktionszone von Methan die geringste Stabilität und wies eine beträchtliche Zündverzugslänge auf. Die geringsten Wandwärmeströme wurden bei Methan festgestellt. Im Allgemeinen wanderte die Zündposition stromauf Richtung der Injektionsposition mit steigendem Impulsverhältnis, aber entfernte sich gleichzeitig von der Wand, sodass der Wärmestrom abfiel. Im Vergleich zu angestellter Injektion, reduzierte die senkrechte Injektion die Zündverzugslänge aufgrund der verstärkten Vermischung. Obwohl geringere Brennstoffmengen in der angestellten Konfiguration injiziert wurden, waren die resultierenden Wandwärmeströme vergleichbar zu denen im senkrechten Fall. Mittels RANS Simulationen konnte die Struktur der Reaktionszone auch untersucht werden. Die Simulation konnte auch einen Zündverzug wiedergeben. Allerdings überschätzte das Eddy Dissipation Verbrennungsmodell die Temperaturen.

Contents

Table of contents	iv
List of figures	vii
List of tables	xi
Nomenclature	xii
1 Introduction	1
1.1 Motivation	1
1.2 Structure of the work	3
2 Theoretical Background	4
2.1 Wall heat transfer	4
2.2 Flow parameters	8
2.3 Vortex structure of JICF	9
2.4 Influence of the injection geometry	10
2.5 Crossflow condition and mixing process	11
2.6 Jet trajectory	15
2.7 Reactive flows	17
3 Laser-Induced Fluorescence	28
3.1 Diatomic molecules	29
3.2 Multiatomic tracer molecules	38
4 LIF Validation Procedure	43
4.1 Hardware	43
4.2 OH LIF validation	48
4.3 Cold tracer LIF	64
5 Test Bench	67
5.1 Hot gas generator	68
5.2 Test section	70
5.3 Peripheral components	73
6 Inverse Heat Conduction Method	76
6.1 Principle	76
6.2 Governing equations	77

6.3	Implementation routine	80
6.4	Algorithm validation	81
7	CFD Setup	89
7.1	Numerical domain and settings	90
8	Experimental and Numerical Results	92
8.1	Non-reactive PLIF experiments	92
8.2	Reactive experiments	106
8.3	Heat flux results	133
8.4	CFD results	146
9	Conclusions	154
Appendices		157
A	Additional Theoretical Background	158
B	Spectroscopy of Diatomic Molecules	161
C	Test Bench Details	172
D	CFD Simulation	173
E	Inverse Heat Transfer	177
F	Complementary Results	179
G	Additional Subjects	185
Bibliography		188

List of Figures

1.1	Schematic illustration of a combustor and different cooling devices	1
1.2	Development of the turbine inlet temperature	2
1.3	Sections of a combustor coated with temperature sensitive paint	3
2.1	Schematic illustration of film cooling	6
2.2	Schematic illustration of a transient jet in crossflow	9
2.3	Energy cascade for the turbulence kinetic energy	12
2.4	OH PLIF of CH ₄ JICF from literature	23
2.5	Formaldehyde and OH PLIF of H ₂ -C ₂ H ₄ JICF	24
2.6	Counterflow H ₂ /O ₂ diffusion flame	25
2.7	OH chemiluminescence and integral heat release rate	26
2.8	OH PLIF of H ₂ /N ₂ JICF from literature	27
3.1	Two-level model of laser-induced fluorescence	29
3.2	OH spectral emission	33
3.3	Morse potentials with corresponding LIF processes.	33
3.4	OH absorption look-up table and spectral laser profiles	38
3.5	OH spatial intensity profiles from calibration burner	38
3.6	Jablonski diagram	40
3.7	Fluoroketone absorption and emission spectra	41
4.1	Spectral laser pulse energy	44
4.2	SNR of PI MAX2 camera.	45
4.3	Gain characteristics of the Hamamatsu intensifier	46
4.4	Band-pass filter properties for OH LIF	47
4.5	Band-pass filter for fluoroketone LIF	48
4.6	Sectional view of a McKenna burner	49
4.7	Simulated 1D chemical kinetics temperature and number density profiles	50
4.8	Flat flame calibration setup	51
4.9	Simulated intensity for different rotational branches	53
4.10	Calculated Boltzmann distributions	53
4.11	Calibration curves for intensity ratio to temperature conversion	55
4.12	Time resolved OH LIF signal	55
4.13	Fluorescence signal of excited flat flame OH over the pulse energy.	56
4.14	Flowchart of LIF post-processing routine	58
4.15	Theoretical LIF error analysis	59
4.16	2D LIF temperature distributions of calibration cases	60

4.17	2D intensity attenuation and temperature errors	61
4.18	Fluoroketone fluorescence in a dye cell	64
4.19	Fluoroketone saturation and time resolved results	65
4.20	Fluoroketone spatial intensity distribution and absorption coefficient	66
5.1	3D illustration of the test bench	67
5.2	Schematic illustration of the main experiment setup	68
5.3	Hot gas generator drawing	69
5.4	Test section drawing	70
5.5	Test section wall drawing	71
5.6	Drawing of normal injection slot	72
5.7	Drawing of angled injection slot	72
5.8	Thermal simulation results of the test plate	73
5.9	Schematic illustration of the gas supply of the test bench	74
5.10	Simulated flow field of the exhaust gas system	74
6.1	Numerical domain of the wall for IHC calculation	81
6.2	Calculation process of inverse heat conduction.	82
6.3	Transient direct and inverse calculated heat flux profiles for IHC validation	83
6.4	Centerline direct and inverse calculated temperature and heat flux profiles for IHC validation	84
6.5	Lateral direct and inverse calculated temperature and heat flux profiles for IHC validation	85
6.6	IHT error resulting from constant temperature deviations.	85
6.7	Position variation results	86
6.8	Calculation process of inverse position correction.	88
7.1	Domain for CFD simulations	91
8.1	Hot-wire measurement locations in the test section cross section	93
8.2	2D velocity and TI distribution measured by hot-wire technique	95
8.3	Energy spectra from hot-wire data	95
8.4	Tracer LIF image post-processing steps	98
8.5	Tracer LIF intensity results of normal injection	99
8.6	Concentration trajectories of normal jets for different momentum ratios	100
8.7	Concentration trajectories of normal jets for different mainstream Reynolds numbers	100
8.8	Analytical fitting of concentration trajectories	101
8.9	Concentration decay along the tracer LIF trajectory of normal jets	102
8.10	PMF of normal tracer LIF results	102
8.11	Tracer LIF intensity results of angled injection	103
8.12	Concentration trajectories of normal jets for different momentum ratios and mainstream Reynolds numbers	104
8.13	Concentration decay along the tracer LIF trajectory of angled jets	105
8.14	Visual view of reacting JICF in the current test section	106
8.15	Hot gas generator condition and measured exhaust gas temperature	107
8.16	Hot gas generator supply gas and injected cold fuel temperatures	108
8.17	2D cross sectional temperature of the exhaust gas	109

8.18 Chemical kinetic setup of the test bench	110
8.19 Calculated fuel/air IDT in a PSR and CH ₄ /air reaction properties in a PFR	112
8.20 Calculated Damköhler numbers for applied hydrocarbon/air combustion	113
8.21 Calculated strain rate profiles from a counterflow diffusion flames	114
8.22 Image distortion correction	115
8.23 Spatial laser intensity correction of PLIF images	116
8.24 Instantaneous and averaged OH* chemiluminescence images of normal H ₂ injection	117
8.25 Averaged OH* chemiluminescence and standard deviation images of normal H ₂ injections	117
8.26 Instantaneous and averaged OH* chemiluminescence images of normal CH ₄ injection	118
8.27 Averaged OH* chemiluminescence and standard deviation images of normal CH ₄ injections	119
8.28 Instantaneous and averaged OH* chemiluminescence images of normal C ₃ H ₈ injection	120
8.29 Averaged OH* chemiluminescence and standard deviation images of normal C ₃ H ₈ injections	121
8.30 Integrated OH* chemiluminescence intensities for normal fuel injection	121
8.31 Ignition delay length, integral heat release rate and flame length from normally injected fuels	122
8.32 OH* chemiluminescence from the front side of reacting fuel jets injected normally	123
8.33 Instantaneous and averaged OH PLIF images of normal H ₂ injections	124
8.34 Averaged OH PLIF and two-line temperatures of normal H ₂ injections	125
8.35 Instantaneous and averaged OH PLIF images of normal CH ₄ injections	125
8.36 Averaged OH PLIF and two-line temperatures of normal CH ₄ injections	126
8.37 Instantaneous and averaged OH PLIF images of normal C ₃ H ₈ injections	126
8.38 Averaged OH PLIF and two-line temperatures of normal C ₃ H ₈ injections	127
8.39 OH PLIF of inverse diffusion flames from literature	128
8.40 Averaged OH* chemiluminescence images of angled fuel injections	129
8.41 Integrated OH* chemiluminescence intensities for angled fuel injection	130
8.42 Ignition delay length, integral heat release rate and flame length from angled fuel injections	130
8.43 OH* chemiluminescence from the front side of reacting fuel jets injected in angled configuration	131
8.44 Instantaneous and averaged OH PLIF intensities of angled fuel injection	131
8.45 Averaged OH PLIF and two-line temperatures of angled fuel injections	132
8.46 Measured and Savitzky-Golay filtered transient temperatures.	134
8.47 IHC transient temperature and heat flux distribution	135
8.48 Transient IHC results for normal H ₂ injection	136
8.49 2D temperature distribution for normal H ₂ injection	137
8.50 2D surface heat flux for normal H ₂ injection	137
8.51 IHC temperature and heat flux distributions from literature	138
8.52 Centerline IHC results for normal H ₂ injection	139
8.53 Transient IHC results for normal C ₃ H ₈ injection	139
8.54 2D surface heat flux for normal C ₃ H ₈ injection	140

8.55 Centerline IHC results for normal C ₃ H ₈ injection	141
8.56 Transient IHC results for normal CH ₄ injection	141
8.57 Centerline IHC results for normal CH ₄ injection	142
8.58 Transient IHC results for angled H ₂ injection	143
8.59 Centerline IHC results for angled H ₂ injection	144
8.60 Transient IHC results for angled C ₃ H ₈ injection	144
8.61 Centerline IHC results for angled C ₃ H ₈ injection	144
8.62 Transient IHC results for angled CH ₄ injection	145
8.63 Centerline IHC results for angled CH ₄ injection	145
8.64 Inert LES simulation results of the HGG and test section inlet region	147
8.65 Cross sectional LES results near the injection location	147
8.66 Location of the extracted planes from the RANS CFD simulation	148
8.67 Cross sectional CFD results of normal H ₂ injection	149
8.68 Centerplane CFD results of fuel injections	150
8.69 Magnified view of H ₂ injection with added streamlines	151
8.70 Magnified views of C ₃ H ₈ and CH ₄ injection with added streamlines	151
8.71 Line-of-sight averaged CFD results of normal injections	152
A.1 Schematic illustration of the CVP generation	158
B.1 Illustration of Hund's cases	165
B.2 OH rotational transition structure	168
B.3 Hönl-London factors for OH.	169
B.4 Simulated spectral profiles	171
C.1 Actual test bench and test section photographed from different angles.	172
C.2 TC mounting mechanism drawing.	172
D.1 CFD mesh sensitivity analysis.	176
E.1 2D temperature and heat flux distribution of direct and IHC validation	177
E.2 IHC heat flux profile construction scheme	178
F.1 PMF of angled tracer LIF results	181
F.2 Centerplane CFD results for crossflow temperature 1570 K	181
F.3 Line-of-sight averaged CFD results for crossflow temperature 1570 K	182
F.4 Cross sectional CFD results of angled H ₂ injection	183
F.5 Centerplane CFD results of angled injection	184
F.6 Magnified view of angled injections with added streamlines	184
F.7 Line-of-sight averaged CFD results of angled injections	184
G.1 Comparison of Nusselt correlations	186
G.2 Standard deviation depending on number of averaged data.	187
G.3 Spatial light sheet distribution of different transitions.	187

List of Tables

3.1	Fluoroketone vs. acetone properties	42
4.1	Flat flame conditions for LIF calibration	49
4.2	Selected rotational lines for two-line PLIF thermometry investigation.	54
4.3	LIF calibration results and validation. Part 1	62
4.4	LIF calibration results and validation. Part 2	63
8.1	Crossflow boundary conditions of tracer experiments.	94
8.2	Injection conditions of the PLIF tracer experiments.	96
8.3	Crossflow conditions and properties of the reactive experiments.	111
8.4	Boundary conditions of the reactive experiments.	111
8.5	CFD boundary conditions of normal injection cases.	148
E.1	Positions of wall implemented TC. Part 1	177
E.2	Locations of wall implemented TC. Part 2	177
F.1	Tracer PLIF. Boundary conditions of normal injection.	179
F.2	Tracer PLIF. Boundary conditions of angled injection. Part 1.	179
F.3	Tracer PLIF. Boundary conditions of angled injection. Part 2.	180
F.4	Boundary conditions of the reactive normal experiments.	180
F.5	Boundary conditions of the reactive angled experiments.	180
F.6	CFD boundary conditions of angled injection cases.	182

Nomenclature

Roman characters

\dot{q}	Specific heat flux	$\text{W} \cdot \text{m}^{-2}$
A	Einstein coefficient for spontaneous emission	s^{-1}
B	Einstein coefficient for absorption	$\text{m}^2 \cdot \text{J}^{-1} \cdot \text{s}^{-1}$
C	Constant	-
c	Molar concentration	$\text{mol} \cdot \text{m}^{-3}$
c	Speed of light	$\text{m} \cdot \text{s}^{-1}$
D	Diameter	m
d	Diameter	m
Da	Damköhler number	-
DR	Density ratio	-
E	Ground state energy	J
h	Heat transfer coefficient	$\text{W} \cdot \text{m}^{-2} \cdot \text{K}^{-1}$
h	Planck constant	$\text{J} \cdot \text{s}$
h	Specific enthalpy	$\text{kg} \cdot \text{m}^2 \cdot \text{s}^{-2}$
HAB	Height above burner	mm
I	Momentum ratio	-
I_F	Fluorescence signal power	W
I_{fl}	Fluorescence intensity	photon/s
J	Rotational quantum number	-
k	Boltzmann constant	$\text{J} \cdot \text{K}^{-1}$
k	Thermal conductivity	$\text{W} \cdot \text{m}^{-1} \cdot \text{K}^{-1}$
k	Turbulence kinetic energy	$\text{m}^2 \cdot \text{s}^{-2}$
k	Turbulent kinetic energy	$\text{mm}^2 \cdot \text{s}^{-2}$
L	Length	m
M	Blowing ratio	-
N	Number density	m^{-3}
nl	Normal liter	m^3
Nu	Nusselt number	-
p	Pressure	$\text{kg} \cdot \text{m}^{-1} \cdot \text{s}^{-2}$
Pr	Prandtl number	-
Q	Quenching rate	s^{-1}
Re	Reynolds number	-
Sc	Schmidt number	-
T	Temperature	K
t	Time	s

<i>TI</i>	Turbulence intensity	%
<i>u</i>	Velocity	$\text{m} \cdot \text{s}^{-1}$
<i>v</i>	Vibrational quantum number	-
<i>VR</i>	Velocity ratio	-
<i>X</i>	Mole fraction	-
<i>Y</i>	Mass fraction	-

Greek characters

α	Absorption coefficient	m^{-1}
$\Delta\nu$	Full width at half maximum	nm
δ	Boundary layer thickness	m
η	Dynamic viscosity	$\text{kg} \cdot \text{m}^{-1} \cdot \text{s}^{-1}$
κ	Wavenumber	cm^{-1}
λ	Air-fuel ratio	-
λ	Wavelength	nm
μ	IHC dumping parameter	-
μ	Reduced mass	kg
ν	Frequency	cm^{-1}
ν	Kinematic viscosity	$\text{m}^2 \cdot \text{s}^{-1}$
Ω	Collection angle	nm
ϕ	Fuel-air ratio	-
ϕ	Stern-Volmer factor	-
ρ	Density	$\text{kg} \cdot \text{m}^{-3}$
σ	Absorption cross section	cm^2
σ	Standard deviation	-
σ	Stefan-Boltzmann constant	$\text{W} \cdot \text{m}^{-2} \cdot \text{K}^{-4}$
τ	Timescale	s
ε	Turbulence dissipation rate	$\text{m}^2 \cdot \text{s}^{-2}$

Subscripts

0	Initial
0	Normalized
∞	Environment
λ	Batchelor
ν	Spectral
<i>abs</i>	Absorption
<i>ad</i>	Adiabatic
<i>avr</i>	Average
<i>c</i>	Cold flow
<i>e</i>	Effective
<i>F</i>	Fluorescence signal power
<i>fd</i>	Fully developed
<i>fl</i>	Fluorescence intensity
<i>h</i>	Hot flow
<i>h</i>	Hydraulic

<i>k</i>	Kolmogorov
<i>lam</i>	Laminar
<i>react</i>	Reactive
<i>s</i>	Surface
<i>t</i>	Turbulent
<i>w</i>	Wall

Abbreviations

(P)LIF	(Planar) Laser-induced fluorescence
CAD	Computer-aided design
CFD	Computational fluid dynamics
CMOS	Complementary Metal-Oxide Semiconductor
CTA	Constant temperature anemometry
CVP	Counter-rotating vortex pair
EDC	Eddy Dissipation Concept
FEM	Finite element method
FWHM	Full Width at Half Maximum
HGG	Hot gas generator
HS	High-speed
IC	Internal conversion
ICCD	Intensified charge-coupled device
IDL	Ignition delay length
IDT	Ignition delay time
IHC	Inverse heat conduction
ISC	Intersystem crossing
JICF	Jet in crossflow
LES	Large eddy simulation
LP	Line pair
MFC	Mass flow controller
NHFR	Net heat flux reduction
PDF	Probability density function
PFR	Plug flow reactor
PIV	Particle image velocimetry
PMF	Probability mass function
PSR	Perfectly stirred reactor
RANS	Reynolds-averaged Navier-Stokes
RET	Rotational energy transfer
SD	San Diego reaction mechanism
SNR	Signal-to-noise ratio
Std	Standard deviation
TC	Thermocouple
TS	Test section
UV	Ultraviolet
VET	Vibrational energy transfer
VR	Vibrational relaxation

Chapter 1

Introduction

1.1 Motivation

The jet in crossflow (JICF) is a simple configuration, that has relevance to many industrial applications. Especially in the field of aerospace engineering, it is used for various inert and reactive purposes. Rocket vehicles and missiles employ jet injections for thrust vector controlling, whereas in gas turbine combustors the focus is on the dispersion of gaseous or liquid fuels injected into the crossflow by swirlers or atomizers, respectively [102, 122]. JICF is also of interest in ram- and scramjets engines to introduce fuel into the crossflow without the necessity of additional periphery [139, 186]. Another application is dilution air in *Rich Burn - Quick Quench - Lean Burn* (RQL) combustors [100]. In this concept, the combustor is divided into a primary and a secondary zone as shown on the left part of Fig. 1.1. In the first zone, a fuel-rich composition is established to obtain low temperatures and production of sufficient amounts of radicals. Then, a high amount of dilution air is supplied through combustion liners to mix quickly with the reactive flow and oxidize the remaining reactants in the secondary zone. The air injection basically occurs through normal JICF configuration, as seen on the mentioned figure. This two-step combustion process helps to avoid stoichiometric conditions and consequently high combustion temperatures, which is the driving factor for the formation of thermal nitric oxides (NO and NO₂ referred to as NO_x). Temperatures around 1600 - 1800 K lead to the production of these harmful species. Additionally, the RQL concept provides stable combustion due to the initial generation of radicals. Another important application presented in Fig. 1.1 is film cooling. Different cool-

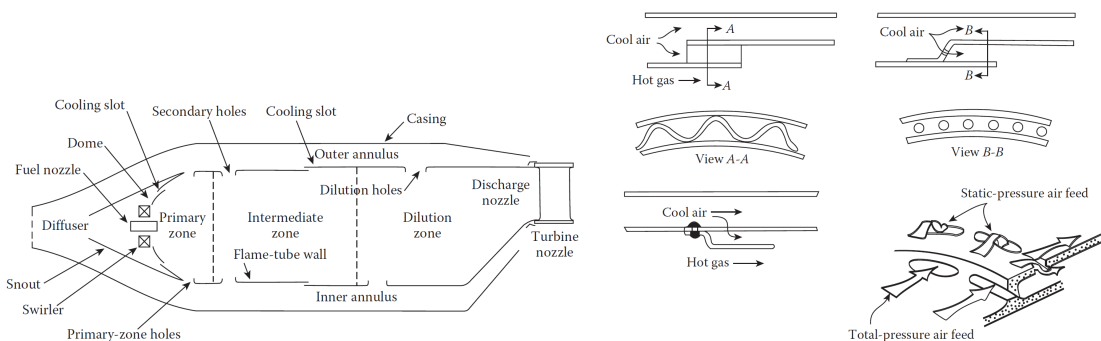


Figure 1.1: Left: schematic illustration of a combustor. Right: different cooling devices. Images from [122].

ing geometries are additionally selected. Other configurations, like angled discrete holes and hole patterns may be found in the turbine blades and vanes, but are not shown here explicitly. In gas turbines, cooling is a crucial and non-negligible process, in which the film cooling constitutes one of the most effective techniques. The demand for higher thrust-specific fuel efficiency and improvement of performance of gas turbines has led to an gradual increase of the turbine inlet temperature (TIT). As Fig. 1.2 shows, the TIT has decoupled in the 1960s from the trend followed by the material capability limits and since then a significant temperature gap is reached. Thus, the uncooled components will not withstand the thermal loads. To avoid material failure and safety risks, active cooling, such as film cooling, is applied. Relatively cold compressor air is injected along the component's surface and reduces its

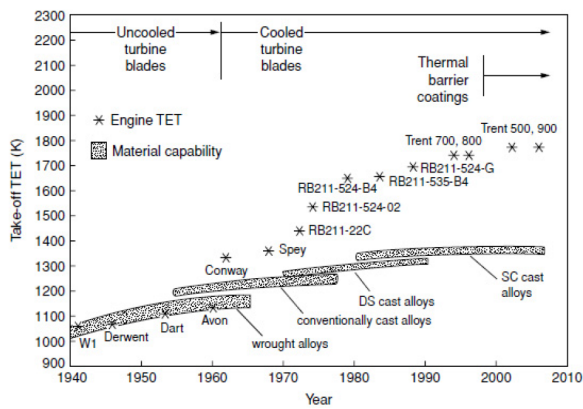


Figure 1.2: Development of the turbine inlet temperature. Image from [199].

temperature as well as the temperature gradients in the wall normal direction. Further, the secondary flow establishes an air film which forms a protective layer and isolates the surface from reactive products. Generally, maximum attachment of the coolant to the surface and reduced mixing of the jet with the crossflow are striven for. Ideally, the film cooling application results in an inert flow configuration. For example, cooling of the secondary zone of the combustor, where lean combustion occurs, or cooling the subsequent vanes and blades, which are situated in oxygen-rich exhaust gas, are expected to be non-reactive. However, insufficient mixing of air and fuel may lead to local fuel-rich compositions. These reactive, turbulent streaks may penetrate the cooling film layer and form an ignitable mixture. Due to temperatures above the auto-ignition limit of the fuel, which enables the overcome of the activation barrier, and available reactive species, chemical reactions may occur. The intended cooling turns then into thermal loads to the wall. The effect of reactions between hot main flow reactants and cold injected air is indicated on the sections of a combustor in Fig. 1.3. The temperature sensitive paint indicates thermal loads occurred at the locations where air was injected. Thus, detailed knowledge of this phenomenon is required in order to perform the thermal design of a gas turbine appropriately. The occurrence of reactive cooling films and secondary reactions were also subject of investigation in the framework of Ultra Compact Combustor (UCC) introduced by Zelina et al. [200, 201]. In the quest to reduce weight of the gas turbine, shorter combustion chambers come into the focus, such as in the UCC. Subsequently, the mixing length and time and combustion volume are reduced, posing a risk of generation of incomplete combustion products, which then enter the turbine stage. The appearance of chemical reactions from cooling air jets in a fuel-rich environment was demonstrated experimentally and numerically by the Air Force Research Laboratory

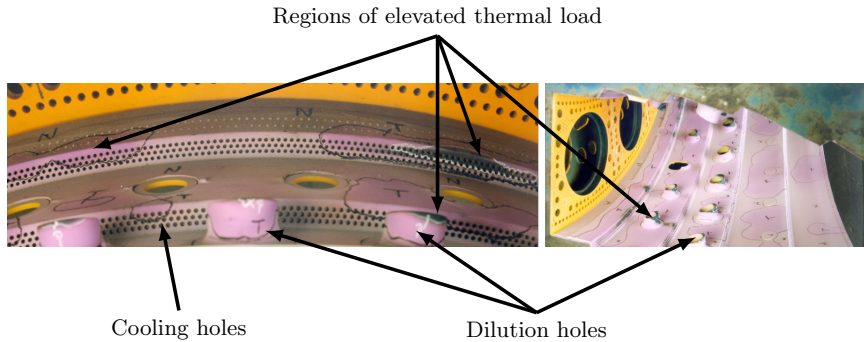


Figure 1.3: Sections of a combustor coated with temperature sensitive paint. Darker colors indicate high thermal stress. Images from [157], labeled for this study.

(AFRL), as discussed in the next chapter.

The objective of this work is the fundamental research of reacting near-wall jets using available measurement techniques. In contrast to the AFRL configuration, fuel JICF in oxygen-rich hot exhaust gas at atmospheric pressure is subject of the investigation. For this purpose, a newly designed test bench is established and characterized. Due to growing interest in hydrogen (H_2) and methane (CH_4), these fuels in gaseous form are used alongside propane (C_3H_8). The focus is on optical analysis of the reaction zone and heat transfer to the surface. The results may serve as validation data for numerical tools describing such conditions.

1.2 Structure of the work

In order to understand the physical phenomena related to JICF, chapter 2 summarizes the theoretical background with focus on relevant measurement techniques. The next two chapters, chapter 3 and 4, are dedicated to the applied optical diagnostic techniques. The theory to the extent relevant to this work is discussed beside a presentation of the hardware and the validation of the methods. In chapter 5, the actual test bench is fully described, followed by two chapters presenting the numerical tools and settings to determine the heat transfer and to simulate the reactive JICF. The experimental and numerical results are presented in chapter 8. Finally, a summary of the findings is given in chapter 9.

Chapter 2

Theoretical Background

In inert as well as in reactive JICF applications, two simple configurations are the normal and the inclined (30° to the crossflow) jets. Those directed perpendicular to the crossflow are also referred to as transverse jets. Despite the geometrical simplicity, the complex three-dimensional (3D) flow field generated by a jet exhausting into crossflow is a great challenge for researchers and has been subject of investigation for several decades. A number of experimental, analytical and numerical studies and thorough investigations have been carried out on the JICF problem, standardized as a single round injection through a flat surface into a crossflow to analyze different aspects. Based on experimental data of an ideal jet configuration, extensive efforts are made to describe and predict the path or trajectory of the deflected jet and its interaction with the crossflow in terms of vortex generation, entrainment, mixing, penetration depth, lift-off and reattachment. Other studies related to film cooling deal with the heat transfer to the wall and cooling effectiveness. While early studies on this field addressed the non-reactive film cooling, it is the near-wall reaction and the reacting near-wall jets which drew attention lately, especially due to sophisticated measurement techniques and numerical simulations. Within the near-wall region chemical reaction occurs and heat is released to the surface.

This chapter summarizes the theoretical background and state-of-the-art of non-reactive and reactive JICF investigations. Measurement techniques and literature which are relevant to this work are discussed.

2.1 Wall heat transfer

The heat of combustion from the chemical reaction within the combustor affects the thermal condition of different components. Thermal energy is transferred to the combustion chamber walls and in aero-engines additionally to blades and vanes by conduction, convection and radiation. Convection is generally of interest for film cooling analysis and thermal design, where bleed air is injected through discrete holes. Film cooling reduces the heat flux to the wall, but it does not prevent the heat transfer entirely. Wall heat losses and temperature differences between the coolant and the wall still yield in heat fluxes. Microscopically, thermal energy is transferred between a solid surface and a fluid by diffusion and collision of molecules. It is described by the Fourier's law as the product of thermal conductivity k of the fluid and the temperature gradient at the surface s [25, 188], here defined in one-

dimensional form as:

$$\dot{q}_n = -k \frac{dT}{dn} \Big|_s \quad (2.1)$$

where \dot{q} is the area-specific heat flux and n is the normal direction to the surface. However, as the temperature gradient is difficult to determine, an engineering approach, the so-called Newton's cooling law [76], is used to model the heat transfer as the product of a heat transfer coefficient h and an *appropriate* temperature difference ΔT :

$$\dot{q}_n = \dot{q}_0 = h_0 \Delta T = h_0 (T_{ref} - T_w) \quad (2.2)$$

where the subscripts 0 and w denotes non-cooled conditions and wall properties, respectively, and T is the temperature. Difficulties arise in selecting the *appropriate* reference (*ref*) temperature for film cooling, as in this situation two temperatures, namely the main flow temperature and the coolant temperature, exist. The latter alters after the injection due to interaction and mixing with the crossflow and is difficult to determine. Using the mainstream temperature as reference results in the dependency of the heat transfer coefficient on the coolant temperature [25]. For film cooling applications, Goldstein [76] proposed the adiabatic temperature as a suitable reference temperature for the driving potential of the heat transfer, as this would be the temperature of the fluid above the wall in case of an adiabatic boundary condition and thus the limiting temperature the wall can acquire. It becomes:

$$\dot{q}_f = h_f (T_{ad} - T_w) \quad (2.3)$$

where the subscript f labels properties at film cooled conditions. T_{ad} is usually expressed by the non-dimensional film cooling effectiveness and describes how the cooling film temperature develops after injection and consequently how the cooling film effectiveness diminishes due to interaction with the mainstream. A schematic illustration of an angled, non-reactive cooling film is shown in Fig. 2.1 on the left side. The undisturbed mainstream is displaced and the boundary layer is thickened by the jet. At the same time, the jet is deflected and pushed to the wall. Within the cooling layer, the temperature gradient is flattened, such that the heat transfer to the wall is reduced considering Eq. (2.1) or the reference temperature is reduced considering Newton's law in Eq. (2.3). As indicated, the temperature profile is altered downstream of the injection due to interaction with the mainstream.

The demand for efficiency and thrust prompted modern gas turbines to run at high operating temperatures and fuel-air equivalence ratios near stoichiometry. These conditions favor the existence and survival of reactive species such as hydroxyl (OH) and carbonmonoxide (CO) at thermodynamic equilibrium within the exhaust gas in the combustor. As the temperature drops on the way to the turbine stage and additionally cooling air is injected to protect the blades by a film, the reactive species may enter the cooling film and react with the oxygen. These chemical reactions, referred to as secondary reactions, may also occur due to imperfect mixing within the combustor and the existence of hot, reactive fuel streaks entering the turbine stage or due to fuel-rich operation. Instead of the intended cooling, the component is stressed by increased heat loads from exothermic recombination processes. The discussed heat flux calculation methods so far deal with incompressible, non-reacting films, ideally with constant temperature-independent properties. However, chemical reactions within the film layer alter the thermal condition of the near-wall flow due to heat release. This leads to changes in the flow field and the fluid properties. Fig. 2.1 shows on the right side a principle scheme of a reactive film layer. The definition of an adiabatic

reference temperature as for non-reactive film cooling does not hold and will be invalid. The potential of chemical reaction occurring in the near-wall region was investigated in the

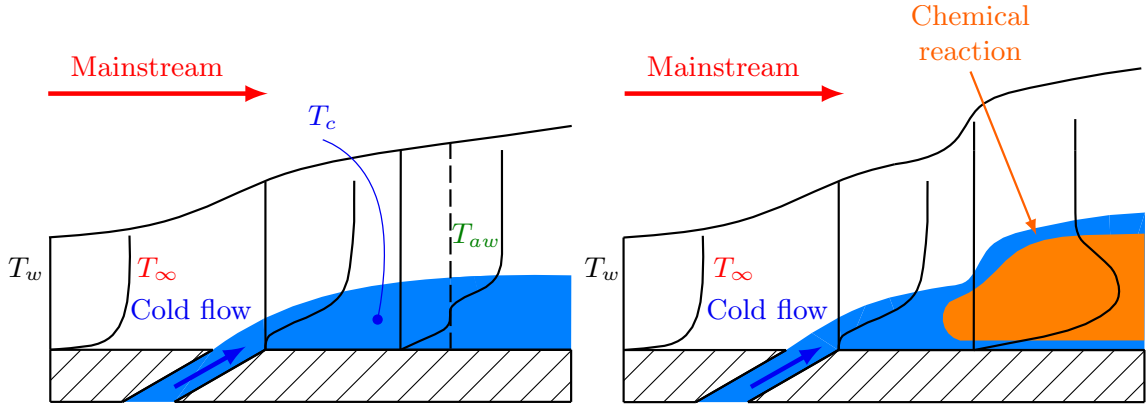


Figure 2.1: Schematic illustration of film cooling. Left: non-reactive film cooling. Right: reactive film-cooling. Chemical reaction takes place downstream the injection location.

literature [110, 128, 140]. Kirk et al. [110] conducted experiments on a film-cooled flat plate in a fuel-rich mainstream consisting of an ethylene argon mixture. A scaling method for the heat flux increase depending on the adiabatic flame temperature T_{ad} was proposed for reactive film cooling:

$$\Delta\dot{q}_s = \frac{\dot{q}_{react} - \dot{q}_{inert}}{\dot{q}(T_{ad}) - \dot{q}_{inert}} \quad (2.4)$$

where the subscript *inert* terms non-reactive cases, *react* denotes the reactive ones. Local heat flux was measured by one-dimensional (1D) thin-film heat flux sensors and validated using analytic correlations. This type of sensor consists of a number of small thermocouples (TC) connected in series and the heat flux is obtained from a calibration constant and from the measured thermoelectric voltage based on the Seebeck effect. The simple working principle, small dimension and fast response feature are the benefits of this sensor type. However, the result of this measurement technique is 1D and the implementation of the gauge on surfaces exposed to combustion is challenging. Heat flux data for non-reactive and reactive conditions were obtain directly for Eq. (2.4) from the transient nature of the experiment, reducing the risk of inaccuracy and inconsistencies from conducting multiple experiments. The maximum achievable heat flux, $\dot{q}(T_{ad})$, was evaluated at the adiabatic flame temperature assuming constant heat flux coefficient h . Meaning, $\dot{q}_s \rightarrow 0$ for $\dot{q}_{react} \rightarrow \dot{q}_0 = \dot{q}_{inert}$ and $\dot{q}_s \rightarrow 1$ for $\dot{q}_{react} \rightarrow \dot{q}(T_{ad})$. An elevation of the scaled heat flux $\Delta\dot{q}_s$ by up to 80% were detected for reacting cooling jets compared to inert cooling jets.

Secondary reactions were analyzed analytically, experimentally and numerically in a series of studies conducted by AFRL [24, 26, 43, 54, 105, 114, 160, 167, 168]. The investigations aimed to assess the secondary reactions occurring in UCC introduced previously by Zelina et al. [200, 201]. Within the framework of increasing efficiency of aero-engines, the UCC technology addresses the downsizing of the combustion chamber by reducing its axial length in order to save weight. At the same time, to counter the reduced residence time of the flow and provide enough time for the chemical reaction to take place, the gases are put in swirling motion in circumferential direction. This design might reduce the axial length by up to 66% [200] and could be of interest as inter-turbine burners [54]. However,

the risk of secondary reactions needed to be investigated as incomplete combustion could occur and hot products consisting of residual fuel or fuel streaks could enter the cooling film layer of turbine vanes and blades and trigger chemical reactions. On a newly designed test bench at the AFRL facilities hot, turbulent exhaust gas from the fuel-rich combustion of propane and air was led to an optically accessible duct with a flat plate configuration. Within the flat plate cold air was injected into the crossflow. The authors tested various geometries. Secondary reaction in form of an inverse diffusion flame was observed near the wall downstream the injection location. TC implemented at two locations within the wall were detecting the increase in temperature. Knowing the material thermal conductivity and assuming 1D heat conduction, the heat flux was determined based on Fourier's law in Eq. (2.1), and based on Eq. (2.2) and by setting $T_{ref} = T_\infty$ an effective heat transfer coefficient h_{eff} was calculated. Depending on the blowing ratio, the injection of air and resulting chemical reaction showed an increase in h_{eff} of up to 8 % for perpendicular jets and 14 % for 30° inclined jets compared to the inert case with nitrogen (N_2) injection. In order to compare the heat flux for different injection geometries, main flow compositions and blowing ratios, a non-dimensional parameter was proposed as by Delallo et al. [43]:

$$\Delta \dot{q}_s = \frac{\dot{q}_{react} - \dot{q}_{inert}}{\dot{q}_{inert}} \quad (2.5)$$

where the inert heat flux was obtained from the injection of N_2 as a reference condition. A drawback of this method is the difficulty to maintain the same thermal condition for non-reactive and reactive injection during the experiment. However, this parameter was used in the current work. Note that this approach is basically the reactive counterpart of the so-called *net heat flux reduction* (NHFR) in inert film cooling studies, which compares the heat flux \dot{q}_f at film cooled condition to \dot{q}_0 of the non-cooled case [18]:

$$NHFR = 1 - \frac{\dot{q}_f}{\dot{q}_0} = 1 - \frac{h_f(T_{aw} - T_w)}{h_0(T_\infty - T_w)} \quad (2.6)$$

with T_∞ as the main flow temperature and driving potential without secondary injection.

The method of heat flux determination from studies of AFRL is 1D and physically limited by the number of TC or heat flux gauges. A promising approach for 3D heat and temperature distribution reconstruction from 1D TC temperature measurement was presented and applied to lab-scale combustors by Perakis et al. [155] based on the theoretical principles proposed by Ozisik [152]. In the so-called inverse heat conduction (IHC) method, the heat flux of the unknown boundary is iteratively optimized such that the theoretical temperature converges to the measured temperature at the specific location. More precisely, a residual function is defined and is subject to minimization. The numerical procedure consists of direct and inverse calculations. The optimization is based on a sensitivity or Jacobian matrix, which basically specifies the temperature dependency on the heat flux and which is calculated in advance. This type of problem is *ill-posed* in the sense that small variations in the input data (to optimize boundary) result in large changes in the answer (result at the measurement location). Thus, a convergence criteria in the range of the measurement accuracy is typically set and the number of optimization points corresponds to the number of discrete measurement points. In order to solve transient problems, discrete time steps are optimized. A time-consuming factor of the approach is attributed to the calculation of the Jacobian matrix. However, the authors in [155] demonstrated that it is sufficient for transient simulations to calculate the matrix once as long as the locations of the

integrated TC are unchanged. An extensive evaluation in [155] showed systematic heat flux errors of up to 15 % originating from TC measurement and a maximum error of 7 % from the inverse method. The optimization routine was implemented in Python, while the direct heat conduction simulation was performed using a commercial tool. Shortcomings of this method are related to the number of discrete measurement and the resulting resolution. As the discrete heat fluxes are converted into two-dimensional (2D) profiles using interpolation and extrapolation schemes, large local fluctuations may occur depending on the degree of the interpolation polynomial, as found in [155]. A detailed implementation procedure is discussed in chapter 6, as the method was used for this study.

2.2 Flow parameters

Different parameters play a role when studying, designing and comparing JICF applications, for example small scale investigation in lab vs. real application in gas turbines. Especially relevant to film cooling, three parameters have been identified to describe the characteristics of JICF related to injection orifice geometry (shape, angle, pattern, etc.) and related to fluid mechanical properties of the jet-crossflow interaction [25, 76, 181]: density ratio (DR), velocity ratio (VR), mass flux ratio or blowing ratio(M) and momentum flux ratio (I).

$$DR = \frac{\rho_c}{\rho_\infty} \quad VR = \frac{u_c}{u_\infty} \quad M = DR \cdot VR \quad I = DR \cdot VR^2 \quad (2.7)$$

where ρ is the density, u is the velocity and the subscripts c and ∞ refer to the cold injected fluid and the crossflow, respectively. In some literature an effective velocity ratio VR_e is chosen out of convenience as the square root of the momentum ratio I [88, 108] $VR_e = \sqrt{I}$. As obvious, the parameters are inherently related to each other by the density ratio.

The choice of the suitable parameter is determined by the physical phenomenon of interest, as discussed by Goldstein [76]. The velocity ratio is particularly important for the scaling of jet centerlines, and for shear layer processes such as vortex and turbulence generation and acceleration or deceleration of the jet flow by the crossflow. Hence, it is practical for 2D cooling films. The momentum ratio is significant for the dynamics of the jet-crossflow interaction and describes the 3D behavior of the injectant due to its pressure ratio definition. Penetration depth into the crossflow, mixing, separation tendency of the jet from the surface and the ability of the crossflow to bend the jet flow and deflect it to the wall are scaled by the momentum ratio. Considering film cooling applications with low momentum ratios and attached coolants, the blowing ratio is generally of interest for characterizing the cooling performance. For example, it was found, that the film cooling effectiveness η downstream of the injection is related to M by $\eta \sim 1/M^C$, where C depends on the injection geometry [76]. The significance of M for heat transfer is due to the proportionality of the convective transport capacity of the injectant to $c_p \rho_c u_c$ [25] and the dependency of the Nusselt number and the heat transfer coefficient on M . Depending on the injection geometry, blowing ratios between 0.5 - 2 or 3 are applied for turbine cooling [91, 162], but mostly around 1 to keep the cooling jet attached to the surface [154]. At lower blowing ratios, the jet tends to get dismantled and dissolves directly after the injection. Andreopoulos et al. [11] showed that the flow structure of a jet with $VR = 0.5$ has no indication of a jet left (*no memory of the jet*) shortly downstream of the injection location. Higher blowing ratios or momentum ratios are applied for dilution purposes in gas turbines or vertical take-off technologies, to name a few examples. According to Bogard et al. [25] momentum

ratios around 50 are used for dilutions, but with hole diameters far larger than cooling hole diameters.

2.3 Vortex structure of JICF

During the development of vertical and/or short take-off and landing (V/STOL) aircraft it was observed in wind-tunnel experiments, that the jet-mainstream interaction affected the aerodynamics of the airplane's body parts [136]. Specifically, the vortex generation downstream of a jet was identified as the main cause. The discharge of a jet into a crossflow results in the formation of four large-scale vortical systems as illustrated in Fig. 2.2 mainly in the near field region due to 3D interaction between the crossflow and the jet. Those were first entirely visualized by smoke streaklines and identified by Fric et al. [65] and analyzed further by Kelso et al. [108]. Following vortices were observed: horseshoe vortices, counter-rotating vortex pair (CVP), jet shear-layer vortices and wake vortices. A summary is given in the appendix A.1. The wake vortices and the shear-layer vortices are unsteady, while the horseshoe vortices and the CVP are features of the mean flow and despite having unsteady components they are represented in time-averaged fields. The CVP dominates the cross-section of the jet and is the preliminary factor for mixing. From experimental measurements, Fearn et al. [57] predicted the CVP vortex generation close to the point of injection and reported the presence of these vortices 45 jet diameters downstream, while Pratt et al. [163] detected them even up to 1000 jet diameters downstream.

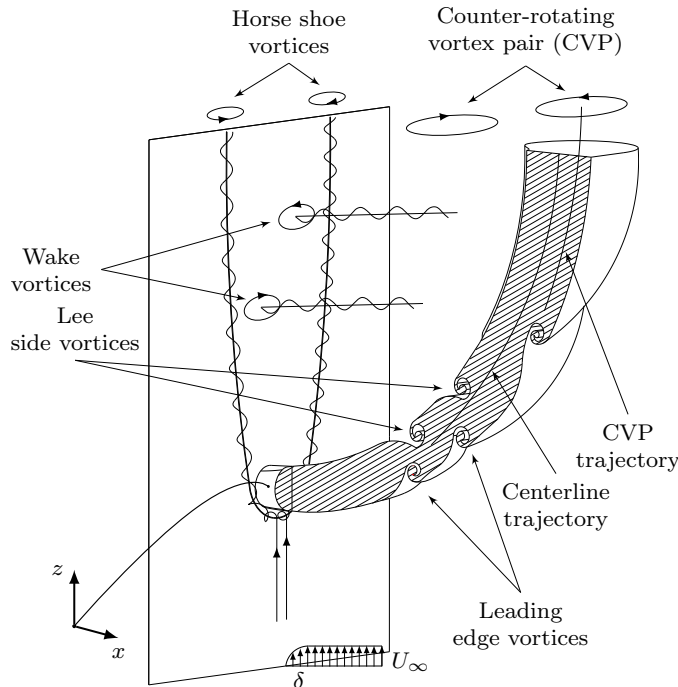


Figure 2.2: Schematic illustration of a transient jet in crossflow generating four types of vortices. Drawing adapted from [30].

2.4 Influence of the injection geometry

The flow structure of the jet and the interaction with the mainstream are essentially determined by the injection orifice geometry and the configuration of multiple orifices. These properties can be divided into shape of the injection geometry, the inclination and orientation to the crossflow, the pattern and distance of multiple orifices, and eventually the ratio of hole diameter to its length, just to name some. The choice of the geometry is determined by the application: maximum lasting and attaching film layer for cooling application or enhanced mixing and interaction with the mainstream.

For the current work, the most common variation, namely the inclination, is of interest. An inclined jet tends to preserve its structure further downstream compared to normal jets. Due to enhanced mixing of the jet with the mainstream and detachment, a transverse jet generally leads to lower film cooling effectiveness compared to its angled counterpart. However, this is not always valid, as observed by Foster et al. [64]. The authors analyzed cylindrical holes with a diameter of 2.27 mm and injection angles of 35°, 55° and 90°. They found, that small injection angles yielded higher cooling effectiveness at low blowing ratio ($M = 0.5$), but at a higher blowing ratio ($M = 1.4$) the normal jets gave better results despite higher trajectory. The effect was explained by the fact, that at higher blowing ratios the angled jet lifted off the surface and main flow entered the space beneath the jet and reduced the cooling effectiveness. Likewise, the jet at 90° detached from the surface, but due to its intense interaction with the mainstream and rapid lateral spread the jet reattached sooner downstream the injection location than inclined jets. Further, a more homogeneous lateral effectiveness was determined for normal jets. Similar results were presented by Baldauf et al. [17] for 30°, 60° and 90° injections using 2D infrared (IR) thermographic measurements of the surface temperature. For reactive experiments the focus is not only on film cooling performance but also on the promotion and acceleration of the chemical reactions and the location of those. Evans et al. [54] from AFRL compared normal, 30° and laidback fanshaped geometries to each other and determined lowest effective heat transfer coefficient for the latter geometry at non-reactive conditions using N₂ as coolant and hot, fuel rich mainstream flow. However, changing to air injection and inducing chemical reactions, the fanshaped geometry performed worst, especially at low blowing ratios significant heat augmentation was observed. The benefit of laidback fanshaped geometries changed to disadvantage as the chemical reaction was generated close to the wall compared to chemical reactions induced by the normal or angled cylindrical holes. Optical investigation of normal holes, fanshaped holes and a slot by means of OH laser-induced fluorescence (LIF) spectroscopy showed a flame anchored to the injection holes for the transverse air jets, while the fanshaped and the slot geometries produced a flame further downstream the injection location [114, 167]. These results indicate that the mixing of transverse jets favors chemical reactions and at the same time the heat flux augmentation depends highly on the distance of the chemical reaction to the surface, which is for fanshaped geometries in close proximity to the wall. Hence, normal injection is more suitable for rapid mixing and promotion of chemical reaction of injected fuel.

Another geometrical parameter for designing injection orifices is the length of the pipe or rather the length to diameter ratio L/D . Generally, a pipe flow requires some distance until it is fully developed in the sense that its hydrodynamic boundary layer and its thermal boundary layer reach a spatially independent state. When the fluid enters the pipe, the boundary layer thickness increases and finally reaches the centerline. This length is called

hydrodynamic entrance length. For laminar flow ($Re_D \leq 2300$) this length is [195]:

$$\left(\frac{L_{fd}}{D} \right)_{lam} \approx 0.05 Re_D \quad (2.8)$$

where the subscript fd stands for fully developed. The turbulent entry length is independent of the Reynolds number (Re) and in the range [22]:

$$10 \leq \left(\frac{L_{fd}}{D} \right)_t \leq 60 \quad (2.9)$$

For practical applications, $L/D > 10$ may be sufficient. The laminar thermal entry length is given as [22]:

$$\left(\frac{L_{fd}}{D} \right)_{lam} \approx 0.05 Re_D Pr \quad (2.10)$$

where Pr is the Prandtl number. For the turbulent case, the length is independent of the Prandtl number and it is assumed to be:

$$\left(\frac{L_{fd}}{D} \right)_t = 10 \quad (2.11)$$

Comparing Eq. (2.8) to Eq. (2.10), it is obvious, that the hydrodynamic boundary layer develops before the thermal boundary layer for $Pr > 1$. The impact of L/D on the film cooling performance was investigated by Lutum et al. [131] for cylindrical angled (35°) jets. The author found little to no effect for $L/D > 5$, while for lower values ($L/D = 1.75$) the film cooling effectiveness reduced by around 45 % for $M = 1.56$. The effect was justified by the undeveloped pipe flow leading to different flow structure at the exit, and the effective larger injection angle for the undeveloped case increased the detachment tendency of the jet. Once the pipe flow was developed, there was no effect on the effectiveness. Similar findings were made by Gritsch et al. [77] for fan-shaped holes with large L/D . Numerical studies of normal cylindrical JICF by Muppidi et al. [143] showed that the jet profile and the crossflow boundary layer determine the penetration into the mainstream. For example, jets with high centerline velocities penetrated deeper into the crossflow compared to jets with same VR but lower centerline velocities due to different velocity profiles, such as a parabolic profile vs. turbulent or *top-hat* profile. Additionally, the penetration depth is also affected by the thickness of the mainstream boundary layer as a thinner boundary layer exhibits higher momentum at the injection location and has the ability to deflect the jet flow earlier, while the penetration increases in thicker boundary layers. These results were confirmed by New et al. [146], who studied parabolic and top-hat jet profiles using LIF and particle-image velocimetry (PIV).

2.5 Crossflow condition and mixing process

A crucial process in reactive flows is the mixing of the reactants to form an ignitable composition. This on the other hand is strongly affected by turbulence. The source of turbulence in gas turbines is generally the combustor. Laser Doppler Velocimetry (LDV) measurements of real swirl combustors showed turbulence intensities (TI) of around 5 - 20 % [74, 75]. The definition of TI follows later. More recent literature confirm values around 20 % and integral scales in the range of the diameter of the dilution holes [25]. Considering the desire

for rapid mixing of fuel and main flow in the combustion chamber, higher values may be striven for. In the framework of JICF, one has to differentiate between the turbulence level of the mainstream, the one of the jet flow and the induced turbulence by those two after the interaction. The main flow in this study is of turbulent nature and the jet flows are mostly laminar. The difference between laminar and turbulent flows is the chaotic, random fluctuations of the latter in velocity and pressure, which induce fluctuations in other scalars like density, temperature, etc. A non-dimensional parameter to classify the two regimes is the Reynolds number:

$$Re = \frac{\rho u_c L_c}{\eta} = \frac{\rho u_c^2}{\frac{\eta u_c}{L_c}} = \frac{\text{inertia forces}}{\text{viscous forces}} \quad (2.12)$$

where ρ and η are the fluid density and dynamic viscosity, respectively, u is the flow velocity and L is a characteristic length on large scale. The subscript c denotes characteristic properties. These properties correspond to global scales. For pipe flows a characteristic dimension is the diameter, while for a flat plate it is the plate length or local distance from the leading edge. The critical Reynolds number beyond which the laminar-turbulent transition is expected for pipe flows is $Re_{crit} > 2300$ and for flat plates it is around $10^5 - 3 \cdot 10^6$ [106]. These reference values may vary depending on geometrical and surface conditions, such as positioning a trip wire or an obstacle to enforce the transition.

The definition of the Re-number depending on geometrical configuration is inadequate for turbulence modeling. A generally valid definition is required which can be referred to flow characteristics. The concept of turbulence quantification is described by the so-called energy cascade [161], where the turbulence process is divided into generation, convection and dissipation of kinetic energy. The spectrum E of the kinetic energy as a function of the wavenumber κ is illustrated in Fig. 2.3. The length scale is expressed as the reciprocal

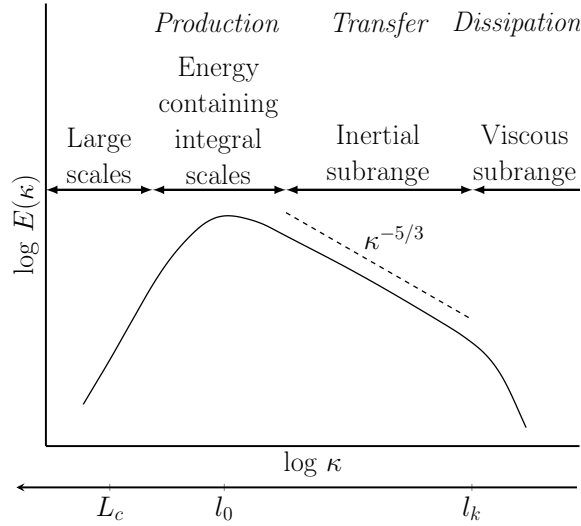


Figure 2.3: Energy cascade for the turbulence kinetic energy $E(\kappa)$ as a function of the wavenumber κ . Illustration adapted from [121, 161].

of the length scale or wavelength, $\kappa = 2\pi/l$ [161]. At large scale, vortices emerge due to disturbances in the flow motion or due to velocity gradients in the shear layer of two flows. These vortices are also referred to as *eddies* in literature. The energy spectrum basically describes the distribution of the kinetic energy k among the eddies of different wavenumbers

(length scale) or among eddies with different frequency modes f (a time scale). The kinetic energy k is essentially described by the integral of the energy spectrum in Fig. 2.3. Within the integral (macro) scales turbulent kinetic energy is generated. The macro scale vortices l_0 with small wavenumbers are of unstable nature and a breakup process takes place due to interaction with the crossflow. The kinetic energy is transferred to smaller scale eddies by inviscid mechanisms. This process continues until the smallest scales are reached and the energy is dissipated to heat by molecular viscosity. The initialization of the process requires sufficiently high Reynolds numbers. However, considering the physical meaning of Eq. (2.12), a $Re > 1$ might be sufficient. During the process, the Re-number $Re(l)$, which depends on a present length scale l , decreases continuously. At the micro scale range, the corresponding smallest length scale associated to the eddies is referred to as the Kolmogorov length scale l_k or dissipation length scale. Fig. 2.3 shows that the peak of the energy spectrum is located at the integral length scale. Thereafter, the energy decays proportionally to $\kappa^{-5/3}$ within the inertial subrange (-5/3-law).

Apart from the characteristic length scales, a characteristic velocity is necessary. In the field of turbulence investigation, the instantaneous velocity field $\mathbf{u}(t)$ is decomposed into a time-averaged velocity field $\bar{\mathbf{u}}(t)$ and a superimposed random velocity fluctuation field $\mathbf{u}'(t)$:

$$\mathbf{u}(t) = \bar{\mathbf{u}}(t) + \mathbf{u}'(t) \quad (2.13)$$

where t is the time. Now, a turbulent Re-number Re_t can be defined as:

$$Re_t = \frac{\rho u'_0 l_0}{\eta} \quad (2.14)$$

The turbulence kinetic energy associated to the eddies is then determined from the root-mean-square (RMS) velocity fluctuations (standard deviation of velocity), which can be obtained from experimental data. Another important parameter for the characterization of a turbulent flow is its turbulence intensity TI . It specifies the magnitude of velocity fluctuations:

$$TI = \frac{\sqrt{\frac{1}{3} (u'_x^2 + u'_y^2 + u'_z^2)}}{\sqrt{u_x^2 + u_y^2 + u_z^2}} = \frac{\sqrt{\frac{2}{3} k}}{\mathbf{u}} \quad \text{isotropic: } u'_x^2 = u'_y^2 = u'_z^2 \quad (2.15)$$

Even though, turbulent flows appear random and chaotic, the velocity fluctuation at the location x can be correlated to that at $x + r$, as well as the fluctuations at the time t can be related to $t + \tau$ using the autocorrelation analysis. The variable r denotes the spatial distance, while τ is an arbitrarily selected time interval. Further, the integral length scale l_0 and the integral time scale t_0 can be calculated from the spatial autocorrelation in downstream direction or the temporal autocorrelation at one location. The first method is difficult to realize experimentally as simultaneous velocity measurements of two points are required. However, the spatial correlation can be approximated by the temporal correlation according to the Taylor's hypothesis (assuming local isotropy and frozen turbulence) [161]. Using temporal data of a single point, the length scale and the time scale can be determined [62, 78, 116, 169]:

$$l_0 = \bar{u} \int_0^\infty R(\tau) d\tau \quad t_0 = \int_0^\infty R(\tau) d\tau \quad (2.16)$$

where the time correlation coefficient $R(\tau)$ is:

$$R(\tau) = \frac{\overline{u'(t)u'(t+\tau)}}{u'(t)^2} \quad (2.17)$$

Additionally, the energy spectrum $E(\kappa)$ can be derived by means of Fourier-transformation of $R(\tau)$. Using dimensional analyses, the Kolmogorov quantities can be derived from the macroscale quantities, namely the length scale l_k and the time scale t_k [121]:

$$l_k \approx \left(\frac{\nu^3}{\varepsilon} \right)^{1/4} \approx l_0 Re_t^{-3/4} \quad t_k \approx \left(\frac{\nu}{\varepsilon} \right)^{1/2} \approx t_0 Re_t^{-1/2} \quad \varepsilon \approx \frac{k^{3/2}}{l_0} \approx \frac{u_0'^3}{l_0} \quad (2.18)$$

where ε is the rate of energy dissipation at Kolmogorov scale and ν is the kinematic viscosity. The subscript k denotes Kolmogorov state properties.

JICF are often associated with enhanced mixing. Generally, bringing two quiescent fluids in contact leads to mixing on small-scale, molecular level due to scalar gradients and diffusion. However, injecting a fluid into a crossflow forms a shear layer. At high Reynolds numbers the turbulence has the ability to transport and mix the fluids on a large level, also referred to as turbulent mixing. During the turbulence generation, vortices form at the contact surface of the two fluids due to the flow motion and increase the interface area. This surface expands even more rapidly as the turbulence enters the decay process approaching l_k from the initial length scale l_0 (taken as a *visual thickness* [142]) and the eddies become smaller. Broadwell et al. [28] investigated the mixing at the shear layer of turbulent flows and proposed a turbulent mixing model based on the distinction of the process in a break-down time of the large-scale vortices leading to entrainment of fluid into the shear layer and a diffusion time for homogeneous mixing. The turbulence break-down time or large-scale mixing time for $Re_{l_0} \gg 1$ is given as:

$$t_0 = C_0 \frac{l_0}{\Delta u} \left[1 - \frac{C_1}{Re_{l_0}^{1/2}} \right] \approx C_0 \frac{l_0}{\Delta u} \quad (2.19)$$

where C_0 and C_1 are constant and taken as 1 in [142], Δu is the velocity difference across the shear layer and $Re_{l_0} = \frac{l_0 \Delta u \rho}{\eta}$. The approximation on the right side is valid for high Reynolds numbers. The small-scale diffusion time across the Kolmogorov scale is [142]:

$$t_k \approx \frac{l_k^2}{D} \approx t_0 Sc Re_{l_0}^{-1/2} \quad (2.20)$$

where $Sc = \eta/(\rho D)$ is the Schmidt number with D as the mass-diffusion coefficient. The ratio of the two time scales $t_R = t_k/t_0$ determines the limitation of the mixing process. For $t_R \gg 1$ the molecular diffusion is the limiting factor, while for $t_R \ll 1$ the large-scale motion limits the mixing. Similar to the smallest scales l_k in turbulent flows, a smallest scale for mixing exists where the finest scalar fluctuations occur. The so-called Batchelor length scale l_λ is related to the Kolmogorov length scale and can be approximated for JICF as [174, 182]:

$$l_\lambda = \frac{l_k}{Sc^{1/2}} \quad \text{JICF: } l_\lambda = \beta \delta Re_\delta^{-3/4} Sc^{-1/2} \quad (2.21)$$

where β is a constant and Re_δ depends on the local jet velocity and the local jet width δ . Values of 1 and 25 for β are found in literature [182]. The Batchelor scale poses a criteria

for the required resolution of optical detectors for mixing measurements. For gaseous flows l_λ is in the range of l_k as $Sc \approx 1$, while for liquids Sc is several order of magnitudes higher than in gases and the resolution requirements are stricter. For turbulent shear layers, the Re-number may be defined based on $0.5\Delta d$ with Δd as the shear layer thickness and $0.5\Delta u$ where Δu is the local velocity difference of the adjacent fluids [125].

The enhanced mixing nature of JICF compared to free, regular jets was found to be associated to the CVP [144]. Smith et al. [182] visualized a normal jet in crossflow by seeding the jet flow with acetone vapor and applied the planar LIF (PLIF) technique. They visualized the jet in the downstream direction as well as the cross section in lateral direction to resolve the CVP and followed its development. From the average of 400 images they determined the (relative to maximum) concentration along the centerline of the jet and, based on the cross sectional results, they identified three regions of the jet: vortex interaction region, a near-field region and a far-field region. In the first region the CVP were formed and developed. In this region, the centerline concentration showed the highest decay. Thus, the author concluded that the mixing is dominated by the formation and development of the CVP rather than by its fully developed presence. Numerical studies of normal JICF by Muppudi et al. [144] revealed higher fluid entrainment and mixing on the lee-side than on the leading side, confirming the effect of CVP formation on mixing. To determine the composition field of a turbulent flow, the probability density function (PDF) of the mixture fraction is evaluated. The mixed fluid exhibit a distinctive peak at the most-probable scalar concentration compared to the initial unmixed state. The shape of the PDF curve becomes more pronounced with decreased fluctuations and higher homogeneous mixture condition. The effect of mixing on chemical reaction was also observed in the experiments conducted by AFRL, e.g. by Richardson et al. [167]. Air (containing oxygen) was injected into a fuel-rich hot gas and triggered chemical reaction. Increasing the blowing ratio and consequently the Re-number shifted the location of the chemical reaction further upstream closer to the location of injection. The authors justified that effect through the enhanced turbulence generation and mixing caused by the increased blowing ratio.

2.6 Jet trajectory

The characterization of a JICF is mostly based on its shape and appearance. Properties of interest are for example the velocity trajectory, maximum concentration trajectory or boundaries of the wake based on specific criteria. The determination of velocity trajectories from experimental results requires velocity data for example from PIV. Scalar concentration trajectories can be obtained from PLIF images and other imaging techniques. The aim of such investigations is to find similarities of the jet global structure for different conditions applying dimensional analysis. For example, self-similar flows with average properties would collapse when scaled by an appropriate spatial variable such as self-similar boundary layers. Most literature addresses scaling methods for non-reacting and incompressible flows. Scaling parameters are often orifice diameter, VR , M and I .

Considering the available measurement techniques at that time and facing difficulties to investigate the vortices, Margason [136] visualized the wake of jets with different injection angles using a mixture of water and compressed air. The study aimed to find the trajectory of the wake based on photographic images. The following empirical equation was proposed

to describe the path of 90° jets:

$$\frac{x}{D} = A \left(\frac{z}{D} \right)^B (VR_e)^C \quad (2.22)$$

where x and z are the vertical and tangential direction of the free stream, D is the diameter of the orifice and the constants A , B and C were determined from fitting the equation above to centerlines of experimentally obtained images of the mentioned jets. Generally, the coefficient A includes the rate of crossflow entrainment and exponent B is a shape constant. An extension of the empirical equation for 30° injections was developed based on the slope of jet, which is mathematically of cotangent nature, leading to:

$$\frac{z}{D} = \frac{1}{4\sin^2(\delta)(VR_e)^2} \left(\frac{x}{D} \right)^3 + \frac{x}{D} \cot(\delta) \quad (2.23)$$

with δ as the deflection angle of the jet to the crossflow direction. Based on the findings, the author concluded that the jet trajectory depends on the deflection angle and the effective velocity ratio. However, despite the universal definition of Eq. (2.23), it failed to predict trajectories of jets with deflection angle of 150° and the fitting of the curves to the wake path seemed more qualitatively. Kamotani et al. [101] used smoke photography for visualization of the jets and hot-wire technique for quantitative measurement at different downstream position and found satisfactory results for the trajectory collapse using the Eq. (2.22) with momentum ratio I instead of the effective velocity ratio. The authors reported increased turbulence intensity and well-developed vortices with rising momentum ratios. Using similarity analysis on the far-field region after the injection and considering the injection orifice as the source of momentum, Broadwell et al. [29] supported the scaling by the product $(VR_e)D$ leading to a general form as:

$$\frac{x}{(VR_e)D} = A \left(\frac{z}{(VR_e)D} \right)^B \quad (2.24)$$

with $A = 2.05$, $B = 0.28$ for $VR_e = 5 - 35$. Conducting PLIF with acetone as tracer molecule for visualization of jets at $VR_e = 5 - 25$, Smith et al. [182] proposed values of $A = 1.5$ and $B = 0.27$ for the best collapsing. The authors also analyzed the decay rate of the concentration along the centerline of the jet and found that the concentration reduces with the centerline coordinate $s^{-1.3}$ in the near-field and with $s^{-2/3}$ in the far-field. The increased decay rate in the near-field was attributed to the formation of CVP. Hasselbrink et al. [88] on the other hand distinguished between a near-field and a far-field or wake-like region using similarity theory and suggested $B = 1/2$ and $B = 1/3$, respectively. In fact, reviewing different literature, a wide range of values can be found as: $A = 1.2 - 2.6$ and $B = 0.27 - 0.34$ [102, 143]. The spread may result from different definitions of the jet path (maximum velocity or maximum scalar concentration), different ranges of VR_e and different calculation approaches of the jet velocity (maximum jet velocity, average velocity or momentum average) [88].

The presented scaling methods are strictly valid for incompressible and (mostly) non-reacting flows. *Mostly*, because Broadwell et al. [29] applied the scaling from Eq. (2.24) to reacting but incompressible flows, where a red solution of sodium hydroxide and phenolphthalein was injected into a transparent main flow of sulphuric acid. When mixing occurred, the injected solution became transparent and disappeared. Steinberg et al. [186] investigated H_2 normal injection into a hot crossflow with a mass flux ratio of $M \approx 1$ by means of PIV

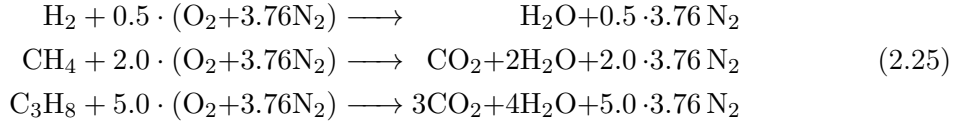
and OH PLIF. The authors successfully applied a scaling of the type of Eq. (2.24) using the mass flux ratio instead of the velocity ratio with $1.2 < A < 1.3$ and $0.42 < B < 0.43$ obtained from fitting. Note, H₂ fuel jets discharged into a hot oxygen-rich crossflow ignite directly after the injection and thus scalar distribution of intensity is available starting from the injection location. Using other fuels, such as CH₄ and C₃H₈ in this work, significant ignition delay may exist and complicate the determination of a centerline.

2.7 Reactive flows

The fundamentals of chemical reactions are discussed in the following section, before proceeding with reactive JICF investigations.

2.7.1 Characterization of chemical reactions

The focus of the current work is on gaseous H₂, CH₄ and C₃H₈ combustion. The global stoichiometric reaction equations of 1 mole fuel in air (21 mol % oxygen (O₂), 79 mol % N₂) as oxidizer are [198]:



where carbon dioxide (CO₂) and water vapor (H₂O) are the products. Based on the mole numbers, the mole fractions of fuel $x_{fuel,stoich}$ in a stoichiometric composition are 29.6 mol %, 9.50 mol % and 4.03 mol % for the considered fuels, respectively. At stoichiometric condition, fuel and oxidizer are completely consumed. Combustion processes taking place under fuel excess are referred to as fuel-rich combustion, while an oxidizer excess is called lean combustion. The system is characterized by the fuel-air equivalence ratio ϕ , defined as the ratio of effective condition to the stoichiometric condition:

$$\phi = \frac{m_{fuel}/m_{oxidizer}}{(m_{fuel}/m_{oxidizer})_{stoich}} = \frac{x_{fuel}/x_{oxidizer}}{(x_{fuel}/x_{oxidizer})_{stoich}} \quad (2.26)$$

The reciprocal of ϕ is the air-fuel equivalence ratio $\lambda = 1/\phi$.

To describe the chemical kinetics, Eq. (2.25) is converted into a general equilibrium form:



where the uppercase letters denote species, while the lowercase ones are the stoichiometric coefficients. The reaction rate with respect to the reactants describes the change in concentration per unit time as:

$$\text{consumption/production rate} = \frac{-1}{a} \frac{d[A]}{dt} = \frac{-1}{b} \frac{d[B]}{dt} = \frac{1}{c} \frac{d[C]}{dt} = \frac{1}{d} \frac{d[D]}{dt} \quad (2.28)$$

where the square brackets around the species denote the concentration and k is the rate coefficient of the forward and reverse reaction path, respectively. The reaction rates of the

reactants and the products can be related to their individual concentrations described by the rate law:

$$\text{forward rate} = -k_{for}[A]^a[B]^b \quad \text{reverse rate} = k_{rev}[C]^c[D]^d \quad (2.29)$$

and the rate expression is then:

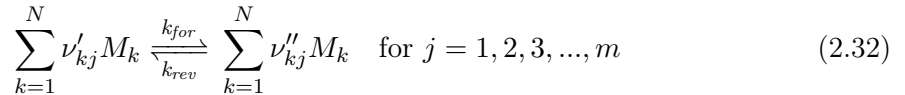
$$\text{net rate} = k_{for}[A]^a[B]^b - k_{rev}[C]^c[D]^d \quad (2.30)$$

For a system that is in chemical equilibrium (without complete consumption of the reactants), the forward and backward reaction rates are equal (no net reaction). This allows the calculation of the reaction specific equilibrium constant $K = k_{for}/k_{rev}$. The forward reaction rate coefficient is described by the Arrhenius law as:

$$k_{for} = AT^b e^{-\frac{E_a}{RT}} \quad (2.31)$$

The coefficient depends on the temperature T and the reaction specific activation energy E_a , pre-exponential factor A and the exponent b . E_a represents a potential barrier which needs to be exceeded to initiate a reaction and A corresponds to the lifetime of an activated molecule in case of uni-molecular reactions (dissociation/rearrangement), while it corresponds to collisions per time for bi- and tri-molecular reactions [198].

The discussion of the chemical reactions in Eq. (2.25) or in general form in Eq. (2.27) were based on one-step mechanisms, which means that only the overall reaction consisting of reactants and products was considered. However, in reality a complex series of individual reactions take place gradually, which are called elementary reactions. Thus, Eq. (2.27) can be written in a general form [196]:



where the superscripts ' and " label reactants and products, respectively. Using the terminology of combustion simulation, the reaction rate \dot{q}_{kj} for the species k and the specific reaction j with the corresponding reaction rate source term $\dot{\omega}_k$ are [196]:

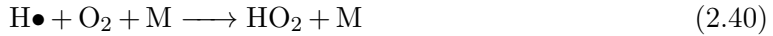
$$\dot{q}_{kj} = (\nu''_k - \nu'_k) \left[k_{for} \prod_{k=1}^N c_{M_k}^{\nu'_{kj}} - k_{rev} \prod_{k=1}^N c_{M_k}^{\nu''_{kj}} \right] \quad (2.33)$$

$$\dot{\omega}_k = M_k \sum_{j=1}^m \dot{q}_{kj} \quad (2.34)$$

with c as the molar concentration. The quantity $\dot{\omega}_k$ appears as a source term in the species conservation equation.

The combustion process consisting of different elementary reactions is characterized by radical chain reactions. These are categorized into following types, described by means of

H_2/O_2 combustion exemplary [100]:



The dot indicates radical species. During the chain initiation process 2.35, reactive species are generated. They react with other stable species to form additional reactive species by chain propagation processes 2.36. 2.37 and 2.38 are chain branching processes, where two radicals are formed from a single radical. Finally, the stable species are formed from the radical by chain termination processes 2.39 and 2.40. Those may occur during collision with a cold surface, which removes thermal energy and initiates recombination. The chain reactions for hydrocarbon combustion is similar.

In this context, the autoignition is an important term. Autoignition describes the process of self-ignition of a flammable mixture, characterized by the explosive formation of radicals during the chemical reactions 2.37 and 2.38. The period from the mixture existence to the state of defined radical density (OH , CH^* , CO , etc.), heat release rate, temperature or reaction progress is referred to as ignition delay time. It depends on the fuel type, fuel-oxidizer composition, temperature and pressure. Empirical correlations for ignition delay times are generally expressed according to the Arrhenius law, similar to Eq. (2.31). The factor A is then a function of the fuel and oxygen concentration and pressure. Some correlations are reported in [100]. According to the empirical correlation, the ignition delay time increases with increasing equivalence ratio ϕ .

2.7.2 Diffusion flames

Combustion processes may proceed through premixed or non-premixed conditions. In premixed combustion, fuel and oxidizer are mixed prior to the reaction, while in non-premixed combustion the fuel and oxidizer are separately introduced into the reaction zone and mixed during the combustion, such as in the current study the introduction of fuel jets into a cross-flow. This type of flame is referred to as diffusion flame. Here, the reactants diffuse to the reaction zone through molecular and turbulent diffusion processes from the corresponding sides. During the combustion, those react to products by chemical kinetics, whereas energy and reaction products diffuse away into either side. The flame front is fixed near the region of $\phi = 1$ and the highest temperature is found in this region. An important feature of non-premixed operation for technical application is its safe handling as the flame cannot propagate due to the lack of fuel or oxidizer on the oxidizer or fuel size, respectively. On the downside, the high reaction temperatures (above 1200 °C) result in increased production of thermal NO_x due to the oxidation of the atmospheric N_2 [100]. NO_x is harmful to the health and to the environment. Further, fuel-rich combustion of hydrocarbons leads to soot formation. Soot consists of conglomerated polycyclic aromatic hydrocarbons to particle sizes and shapes [198].

Beside the mixing state, the flow condition is also of interest, which can be categorized into laminar and turbulent. A typical laminar diffusion flame is generated by a candle, while

turbulent diffusion flames are found in internal combustion engines, rocket motors and gas turbine combustors.

2.7.3 Optical measurement techniques for reactive flows

As pointed out in section 2.7.1, a number of intermediate species are formed and consumed during the chemical reaction, which are described by the elementary reactions. Some of the intermediate species are suitable as indicators for optical measurement techniques since contact-less, non-intrusive methods allow the investigation of the reaction zone without interference. A straightforward approach is the observation of the energy radiation from different molecules within the flame. While H₂/air flames without impurity emit rarely energy in the visible wavelength due to lack of carbon molecules, a premixed hydrocarbon/air flame with complete combustion shows a blue, green color in the core originating from CH* radiation. Changing the second case to a non-premixed flame, a shift to orange, red color is observed, mainly due to soot formation. Often the OH is of interest in H₂/air and hydrocarbon/air combustion as its formation and presence indicates chemical reaction. In addition, the radical's spectroscopic properties are well documented. The energy emission here is in the ultra-violet (UV) range of the electromagnetic spectrum with its peak at 306.4 nm [67]. Chemical excitation is the main mechanism in flames below 2500 K [59]. During the H₂/air reaction, unstable chemically excited OH radicals are formed by the following elementary reaction [67, 120, 150]:



$$(2.42)$$

where M is an arbitrary collision partner. The dominant reaction identified for OH* formation in hydrocarbon/air flames is:



The reactions are generally determined in flame and shock tube experiments. The de-excitation of the upper state to the ground state mainly occurs through non-radiating quenching (Eq. (2.44)) and only a minor fraction is released by spontaneous emission of a photon (Eq. (2.45)):



The part $(hc)/\lambda$ represents the photon energy E , where h is the Planck's constant, c is the speed of light and λ is the photon wavelength. Using a UV sensitive detector with an intensifier and mounted band-pass filter, the radiation during the spontaneous transition of OH* to the ground level can be collected and visualized. Hydrocarbon reactions produce also other excited species suitable for flame imaging, such as CH*, CN* or CO₂*. The latter has a broadband emission over a wide range of the spectrum, considered as background emission [119]. The emission from chemical excitation is called chemiluminescence and the excited species is highlighted by an asterisk (*). A detailed literature review and analysis on chemiluminescence is found in [59, 67, 120, 149, 150], mainly applied to ordinary flames

with known composition (premixed) and pressure for fundamental investigation. A drawback of chemiluminescence imaging is its line-of-sight feature. This means that the intensity along the direction of sight is integrated. Thus, small-scale flame structures are difficult to determine. Spatial resolution in this direction is basically unavailable straightaway. Except, by means of the Abel transform the shape of simple axially symmetric flames can be reconstructed [10, 59].

As the chemiluminescence intensity depends on the temperature and on the concentration of the excited OH* (disregarding quenching), the signal level may be too low for detection in some cases. Hence, the detector exposure time is usually increased to microseconds (or to milliseconds, as reported in [183]) to integrate in time the emission which then yields in lower time resolution beside spatial integration. The natural lifetime of excited OH is around 700 ns [119], at atmospheric pressure even far lower due to quenching with other species. To increase the population of OH in the excited level and detect its concentration, OH in the ground level can be elevated to an excited level by an UV laser and the subsequent emission after the relaxation is collected. This method, laser-induced fluorescence (LIF), allows the detection of OH concentrations below 1% within a narrow width of the laser beam and within a time range of nanoseconds. The technique is species sensitive and selective. Further, knowing the spectroscopic parameters of OH, the emission from two or more specifically excited rotational lines of OH allows the determination of the rotational temperature by means of the Boltzmann distribution of the energy among the rotational energy levels. Assuming thermal equilibrium of the OH radicals justified by fast rotational and vibrational relaxation processes (reasonable for fuel/air flames), the rotational temperature corresponds to the vibrational temperature. Compared to chemiluminescence detection, LIF requires a complex measurement setup and post-processing routine for quantitative analysis. Note that OH* is present in the reaction zone and is used as an indicator for heat release and reaction position, while OH in ground level is also present in high temperature regions. First detailed analysis and experimental results of OH concentration measurement and two- and multi-line LIF thermometry were presented in [31, 32] for a wide range of premixed CH₄/air stoichiometries. The authors used a tuneable dye laser pumped by a flash lamp and frequency doubling unit. Temperature point measurements with an accuracy of 5% were reported for calibration flames. Different types of lasers were tested for excitation in [176]. Lowest systematic errors were reported for dye laser excitation compared to XeCl and KrF lasers. The accuracy of rotational LIF results depends highly on the rotational line selection and, in case of two-line thermometry (or two-color thermometry), on the combined two lines. The excitation of high populated levels yields in high signal-to-noise ratio (SNR), but low temperature sensitivity, while low populated levels yield in poor SNR and high temperature sensitivity. Based on a large number of rotational line investigation in [175], the authors proposed to combine two lines with an energy gap in the range of the expected temperatures as a trade-off between sensitivity and measurement uncertainty.

2.7.4 Near-wall reactive jets in crossflow

As outlined at the beginning of this chapter, reactive JICF occur in various applications and thus the configuration is subject of many investigations. Theoretical and numerical investigations on reactive JICF were performed in [110, 128]. Using a shock tube, a hot fuel-rich mainstream of ethylene/argon mixture was generated and cooler air was injected through 35° holes representing a film cooling configuration. Four non-dimensional parameters were

identified to characterize the potential for secondary reactions, the heat release and the heat flux to the surface: mass flux ratio M , the Damköhler number Da , the heat release potential H^* and the scaled heat flux q_s (Eq. 2.4). The latter two parameters describe the enthalpy increase of the crossflow due to the fuel and the ratio of heat augmentation to the maximum possible augmentation. The Damköhler number relates convective time scales to chemical time scales and determines the location of reactions. The two reported citations chose the flow time τ_{flow} as the period the mainstream needed to pass a distance of $10D$ for convenience, where D is the injection orifice diameter. The chemical time scale τ_{chem} corresponds to the time of 95 % completion of the reaction, chosen as ten times the ignition delay time of the fuel. The Damköhler number is then:

$$Da = \frac{\tau_{flow}}{\tau_{chem}} = \frac{10D/u}{\tau_{chem}} \quad (2.46)$$

where u is the mainstream velocity. When $Da > 1$, the flow time scale is the limiting factor, while in case of $Da < 1$, the chemical reaction is the limiting factor. Maximum heat augmentation was detected for the highest tested Da numbers due to the fact that the reaction zone shifted upstream in the direction of the injection holes. Optical data of inverse diffusion flames were presented by the AFRL, as described in section 2.1. Cold air was injected into a hot fuel-rich continuous flow (containing CO and H₂) from different geometries and with different blowing ratios. As the mainstream contained hydrogen, the authors identified the chain breaching reaction (2.38) responsible for the ignition [24]. The composition of the mainstream was determined from chemical kinetics calculation. Using OH LIF (rotational line $Q_{11}(5)$), the reaction zone was detected and the flame tip seemed independent of the blowing ratio for the tested slot geometry, as the ignition delay time was only depending on the temperature, pressure and chemistry. The principles of LIF are discussed in chapter 3. The flame tip of the wall-anchored reaction zone exhibited fluctuations, denoted as instabilities. Based on the standard deviation of the intensities those instabilities were 35 %. However, it is questionable why the increased mixing with increasing blowing ratio did not shift the flame tip upstream. 2D reactive computational fluid dynamics (CFD) simulation of the test case revealed that the flame anchoring position was determined by the preferential diffusion of reactive species. Especially H₂ in the fuel-rich mainstream with its high diffusivity contributes to the formation of reactive stoichiometric mixtures at lower temperatures compared to other species. First two-line OH PLIF thermometry results ($Q_{11}(14)/Q_{11}(5)$) by AFRL were presented in [114] using two excitation and emission collection systems (10 Hz), while for an extensive investigation in [167] the authors changed to a single measurement system because of simplicity and to prevent inaccuracies. See Fig. 8.39 in chapter 8 for some of the author's intensity results. The injection configuration was found to be the driving factor determining the shape and temperature distribution of the secondary reaction zone. Normal jets penetrated further into the crossflow and formed a confined reaction zone in the streamwise direction with peak temperatures along the entire reaction field. At high blowing ratios, the flame anchored to the injection orifice. Angled air injection on the other hand produced a wall anchored flame, confined in the spanwise direction and with temperatures increasing in the streamwise direction. The difference may be attributed to the flow characteristics of the particular injection angles and the related flow interaction and vortex formation. Including CO PLIF, the authors in [167] identified three characteristic regions: the injection region, where the mainstream is displaced, the mixing and reaction zone, where CO is consumed and OH is produced, and the mix-out

region, where OH decreases and CO levels increase from the main flow. Interestingly, the reaction zone shifted upstream with increasing blowing rates justified by increased mixing, contrary to findings in [24]. Chemical kinetics simulations were also conducted to estimate the chemical time scales and assure that the reaction occurred within the test section. For the Damköhler number calculation, the chemical time scale was taken as the time until 95 % of the peak temperature was reached. In contrast to [110], a diffusion based flow time scale from the reciprocal of a similar scalar dissipation rate was chosen due to the fact that diffusion is the dominant factor in inverse diffusion flames. Further, the authors argued that convective-based times scales yielded in Da-numbers below one and did not represent the findings experimentally observed. From the description of the chemical kinetics case, it is unclear, how the composition of the reactive mixture consisting of hot crossflow products and cold air was determined. It seemed that the authors introduced the experimentally mass flows to a 0D reactor and assumed perfect mixing, while a diffusion flame on the other hand is characterized by chemical reactions on the stoichiometric interface. Introducing a theoretical air flow to reach stoichiometry seems appropriate, as done in [54, 55], due to the lack of spatial resolution of 0D reactors. Thus, the reported Da-numbers in [167] increased with increasing blowing ratio, even though the reactor does not account for mixing time scales while the experimental upstream shift was attributed to mixing effects.

Reactive JICF configurations forming diffusion-based flames are often used for fuel injection, dispersion/mixing and combustion in gas turbines, and more recently in ramjets and scramjets [139]. There are different properties of interest in experimental investigations of this type of jets, such as reaction zone shape, wall distance, ignition delay length/time or autoignition and flame stability. Hasselbrink et al. [87] investigated a reacting jet of CH₄ discharged normally from a tube with a diameter of less than 5 mm into a cold air crossflow by means of simultaneous PIV and OH PLIF at the centerplane. The low temperature sensitive rovibrational line $Q_{11}(6)$ was excited and broadband emission was collected around 310 nm. High velocity ratios of 10 and 21 were tested. Even though crossflow velocities up to 10 m/s were possible, the authors reduced the velocity to 3 m/s to establish a stable diffusion flame within the test channel. The instantaneous PIV data showed the presence of a stagnation point at the lee-side of the jet, indicating the out-of-plane air stream flowing around the jet. On the basis of the OH images, the reaction zone appeared to be highly turbulent and unstable despite the moderate conditions, see Fig. 2.4 for some exemplary PLIF instantaneous shots of the named study. Larger flame thickness on the lee-side in-

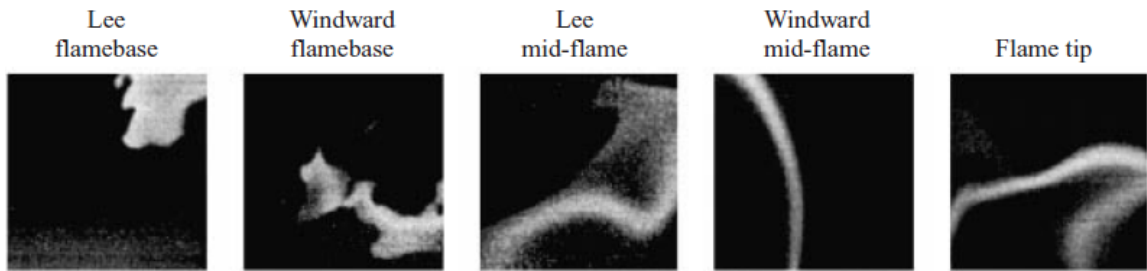


Figure 2.4: OH PLIF of CH₄ JICF at $VR = 21$. Images extracted from [87].

dicated partially premixed conditions. On the windward side, the flame front was often discontinuous or broken and wrinkled. The condition was more pronounced for the case with higher velocity ratio. Also, the reactive jet was found to penetrate further into the

crossflow compared to non-reactive jet due to heat release. The reason for the lift-off of the jet was most probably due to the high strain rates at the nozzle, as a result the flame extinguished. Extinction is the convective-diffusion heat removal rate from the reaction zone leading to lower temperatures. Simultaneously, the heat generation is reduced due to high velocities (shorter residence time) of the reactants and reduced reaction rates [198]. The strain rate, defined as the maximum of the velocity gradient, is also an important quantity for autoignition to account for flow effects on the chemistry (turbulence-chemistry interaction) beside the properties named in section 2.7.1. An analogous model is the counterflow diffusion flame (or opposed jet flow) and the concept of flamelets, where the turbulent flame front is considered as an ensemble of laminar flamelets. The critical strain rate for autoignition at constant temperature (above the autoignition temperature) is determined by decreasing the counterflow velocities until chemical reaction appears [137]. According to Mastorakos [137], autoignition of fuel jets in hot crossflows occurs in regions of *most reactive mixture fraction*, which for turbulent non-premixed cases is different from the stoichiometric mixture fraction and is located in the lean side of CH₄ and H₂ flames.

Micka et al. [139] investigated transverse jets of ethylene (C₂H₄)-H₂ (50 %/50 %) and H₂ in high velocity hot crossflows using CH* and OH* chemiluminescence and CH, formaldehyde (CH₂O) and OH LIF. CH₂O is formed in the decomposition process in the fuel-rich region before OH is generated. The authors focused on moderate velocity ratios around 2 with main flow velocities of 480 m/s and crossflow temperatures around 1364 K which is above the autoignition point of the fuels. Due to the high velocity and relatively low velocity ratio, a turbulent wake-like flame occurred (near-field flow is referred to as jet-like, while the far-field is wake-like [88]), see Fig. 2.5. Autoignition, determined from the formalde-

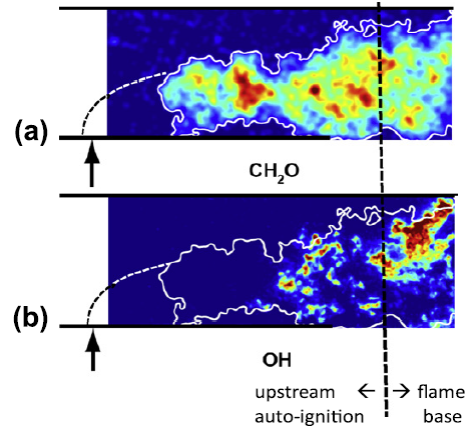


Figure 2.5: Formaldehyde and OH PLIF of H₂-C₂H₄ JICF. Black arrow indicates the injection location. Images extracted from [139].

hyde signal, appeared on the lee-side of the jet and prior to the location of heat release, determined from chemiluminescence signals. This is also expected based on Fig. 2.5. The structure of the flame was categorized into a premixed, lifted flame base with significant heat release and a turbulent, non-premixed flame of shredded and thickened flame. Thus, the reaction zone was found to be *autoignition-assisted*. Interestingly, the authors observed a linearity between the flame length and fuel flow rates, even though non-premixed flames were reported to be independent. This anomaly was attributed to the wake-like structure of the flame and the high mixing behavior of the mainstream. The flame length was specified

as the location where 90 % of the heat release rate had occurred. The local heat release rate $q(z)$ with the coordinates according to the illustration in Fig. 2.2 was related to the OH* chemiluminescence by:

$$\frac{q(z)}{Q} = \frac{I(z)_{OH^*}}{A_{OH^*}} \quad (2.47)$$

where Q is the heat release in J/s and obtained from the fuel flow rate and its heating value, $I(z)$ is the local intensity integrated in the x -direction and A is the integral of $I(z)$ in z -direction. This definition is only an approximate of the spatially resolved heat release rate, especially for non-premixed combustion due to the non-linear dependency of the chemiluminescence intensity on strain rate, turbulent fluctuations and curvature [16, 120]. Further, it was found, that the ignition delay length decreased with increasing crossflow temperature. However, it is unclear how the authors determined the ignition location experimentally. In contrast to Micka et al. [139], Fiala [59] stated that for non-premixed combustion the OH* radiation is not necessarily an indicator for the spatially resolved heat release rate, as radiation and heat release appear at different locations. Radiation depends on temperature and OH concentration, while heat release leads to temperature increase and can occur in regions of low OH. This is explained in Fig. 2.6 by means of a counterflow diffusion flame taken from Fiala et al. [60]. On the left graph of the mentioned figure, it is observed that

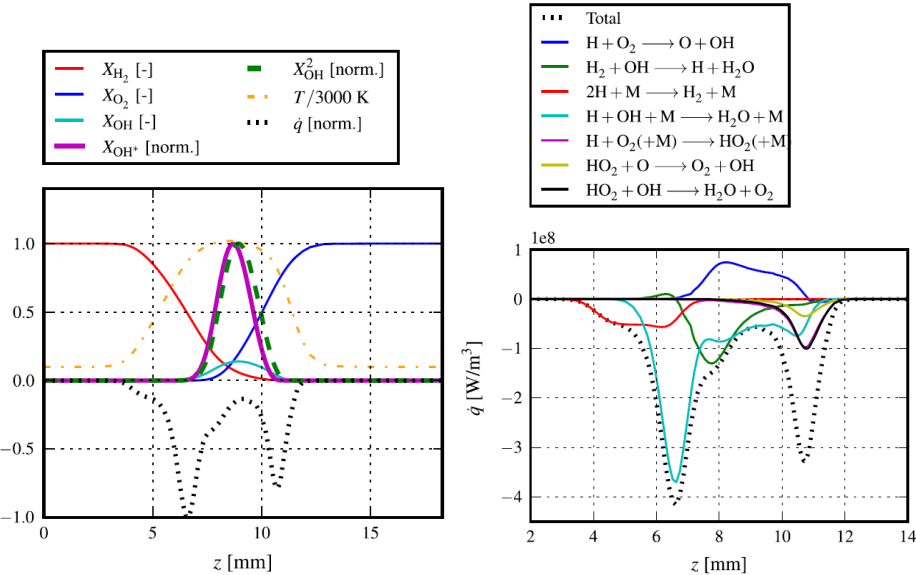


Figure 2.6: Counterflow H₂/O₂ diffusion flame. Left: global reactant concentration and properties. Right: selected elementary reactions. Fuel enters from left. Oxidizer enters from right. Images extracted from Fiala et al. [60].

normalized heat release rate \dot{q} has two peaks, which are on different locations than the peak OH* concentration. In fact, only the relatively broad temperature profile corresponds to the location of heat release. The reason for the decline of heat release around $z = 9$ mm is found on the right graph of Fig. 2.6. In the region of maximum temperature, heat is removed by the endothermic reaction H + O₂ forming O + OH. For turbulent flames, additionally straining affects the emission such that the heat release rate does not correlate with the radiation. Further, in optically *thick* media self-absorption occurs, which reduces the observed radiation but not the heat release. Due to these reasons, line-of-sight integration

of chemiluminescence may fail to predict the location of heat release. More recently, He et al. [89] investigated laminar CH_4/O_2 co-flow diffusion flames numerically and experimentally by means of OH^* chemiluminescence. The authors found, that for global equivalence ratios $\phi \geq 1$ the integral intensity, basically $A_{\text{OH}*}$ in Eq. (2.47), and the integral heat release rate show the same trend, such that the integral intensity serves as an indicator for integral heat release and was independent on the fuel mass flow rate. For $\phi = 1$, it was demonstrated, that the integral OH^* concentration as well as the integral heat release rate were linearly proportional to the fuel mass flow rate. The intensity and heat release rate curves are provided in Fig. 2.7. According to their results, the linearity is only given for global $\phi \geq 1$. Thus, the integral intensity may be used as indicator for the integral heat release. As soon as $\phi < 1$, the intensity decoupled from the heat release. The latter remained constant, because the entire fuel was consumed, whereas the radiation further increased. Additionally, the intensity depended on the fuel flow rate and was not scalable. For accurate and

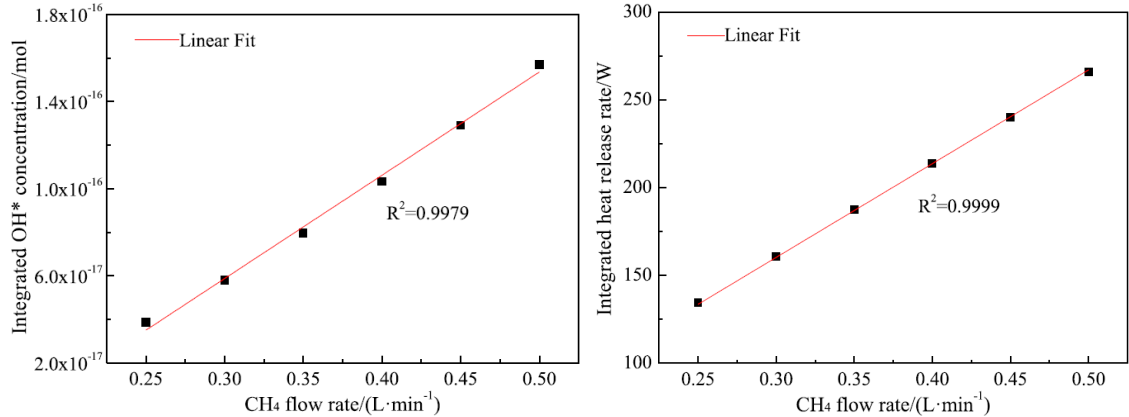


Figure 2.7: Left: integral heat release rate vs. fuel mass flow rate. Right: integral OH^* intensity vs. fuel mass flow rate. Results for global $\phi = 1$. Images extracted from [89].

spatially resolved quantitative heat release rates, Lauer et al. [120] presented a detailed approach consisting of chemiluminescence imaging data (OH^* , CH^* , CO_2^*), simultaneous PIV measurement for the flow field and incorporated chemical kinetics results to account for strain effects. However, the method was applied to premixed rotationally symmetrical fuel/air flames and its applicability to highly turbulent non-premixed flames is questionable, beside the complex measurement setup and post-processing steps.

Fleck et al. [63] conducted H_2/N_2 fuel jet injection experiments in hot, vitiated cross-flows with momentum ratios of 2.4 and 4.7 and pressure conditions of 5, 10 and 15 bar. The focus was on autoignition investigation using high-speed, broadband luminosity imaging at 30 kHz. The autoignition delay times were determined from the location of single ignition kernels and the average main flow velocity. Additionally, chemical kinetics simulations using perfectly stirred reactors (PSR) and plug flow reactors (PFR) were performed for comparison. Shorter ignition delay times were obtained experimentally than from the homogeneous kinetics simulations. The difference was attributed to turbulent mixing and crossflow characteristics. Further, it was found, that temperature had a major effect on the ignition. The determination of ignition delay location from experimental data differs in literature. While in shock tube experiments, an instant rapid signal peak from a photomultiplier is observed [42, 156], reactive JICF may not indicate a clear spike or a clear ignition kernel is not visible.

Hence, optical 2D data, such as chemiluminescence intensity images, are integrated in the corresponding direction to obtain an intensity profile. The ignition delay distance can then be defined as the location of the maximum gradient, the inflection point or the intensity maximum [112]. There are also individual arbitrary thresholds like 10 % of the maximum intensity value [66].

Steinberg et al. [186] conducted experiments with transverse jets of H_2/N_2 (70/30 vol. %) in preheated air crossflows. The main flow temperature was 750 K, thus above the autoignition temperature of H_2 . Velocity ratios of 1.4 - 2.9 with a crossflow velocity of 55 m/s were chosen. OH LIF ($Q_{11}(8)$) and stereoscopic PIV measurement techniques were conducted at a frame rate of 4.9 Hz. The moderate crossflow velocities allowed the formation of a jet-like flame near the injection location. A lifted and a lee-stabilized flame were identified, as see in Fig. 2.8 from [186]. It was found, that at higher velocity ratios a low speed recirculation

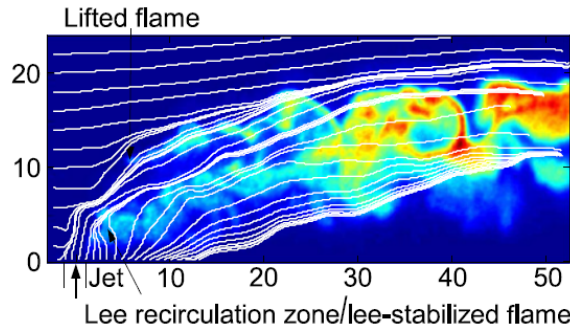


Figure 2.8: OH PLIF of H_2/N_2 JICF with $VR = 2.9$. Velocity streamlines in white. Images extracted from [186].

region beneath the jet developed and provided a stable anchor location for the lee-side jet. In comparison, the lifted jet anchored in the mainstream and it was exposed to high strain rates and main flow properties. Thus, large fluctuations were observed for the lifted flame. Also, non-reactive scaling laws could be applied to the jet trajectory.

Based on the discussed literature, OH PLIF and OH* chemiluminescence are appropriate methods for reacting JICF and were applied in this work.

Chapter 3

Laser-Induced Fluorescence

The knowledge of atomic and molecular discrete energetic levels and their relation to temperature and number density offers a wide range of diagnostic techniques. Especially in the field of combustion, inelastic scattering methods became standard tools to provide insight into the species concentration and temperature fields of reactive flows. Inelastic scattering means that kinetic energy during the interaction of radiation with matter, such as of an incident photon with a target molecule, is not conserved. Thus, the wavelength of the emitted photon differs from the absorbed one. A widely applied spectroscopic method is the laser-induced fluorescence (LIF). By means of a light source, i.e. a laser, a specific molecule type is selectively promoted to an excited energetic level by absorption of energy. The light source helps to increase the population of the excited state, which is otherwise poorly populated. Within a short time, meaning the lifetime of the excited state, the molecules release the energy by spontaneous emission. Based on the detected fluorescence intensity and from the knowledge of the population distribution over the energy levels, species concentration and temperature can be determined. Particularly, the non-resonant fluorescence is of interest, where the emission wavelength is shifted from the excitation wavelength of the incident electromagnetic radiation. Thereby, Mie scattering and thus laser interference may be reduced, as discussed later. The capability of LIF detecting minor species concentrations in the range of 0.01 %, makes it superior over other techniques like Raman spectroscopy [50]. Due to high fluorescence intensity and emission in every direction, high sensitivity and good signal quality can be achieved for 0D, 1D and 2D spatial resolutions depending on the excitation beam form. Further, using a short pulsed laser and due to the time delay between the excitation and emission, time-resolved measurements are also possible to analyze the temporal evolution of the depopulation process.

The applicability of LIF is not limited to atoms or molecules occurring during combustion and reactive processes. The resonance of atoms, flame radicals, di- and multi-atomic molecules at different conditions (at room temperature or electric arc temperature) with energy gaps corresponding to the energy of incident photons can be detected [50, 85]. Within this work, the hydroxyl molecule mostly referred to by its chemical composition OH is chosen for the investigation of combustion processes and fluoroketone is selected as a tracer molecule for inert flow visualizations and studies.

3.1 Diatomic molecules

The basic principles of OH LIF and OH LIF thermometry are discussed briefly in the following subsections based on relevant literature [15, 21, 46, 50, 176]. For a deeper understanding of molecular spectroscopy, the reader is referred to these publications or to the summary provided in the appendix B.

3.1.1 Linear fluorescence regime

A well-known representation of the LIF processes is by means of the two-level model, as illustrated in Fig. 3.1. A molecule is promoted from the ground state energy E_1 to the excited state energy E_2 . Thereafter, the energy is released by different competing processes in order to return to state of equilibrium. The constants describing the processes between the quantified energy levels E_1 and E_2 are called rate constants. The absorption b_{12} and stimulated emission b_{21} can be related to Einstein coefficients B by:

$$b = \frac{BI_\nu}{c} \quad (3.1)$$

where I_ν is the laser spectral irradiance and c is the speed of light. The remaining rate constants are spontaneous emission A_{21} defined by the Einstein coefficient for emission, collisional quenching Q_{21} , photoionization W_{2i} and predissociation P . The temporal change

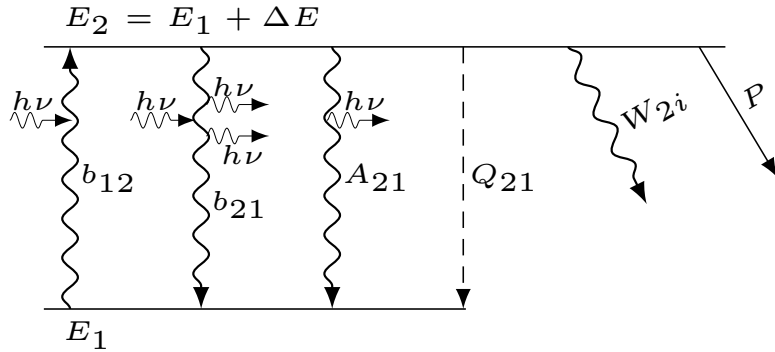


Figure 3.1: Two-level principle according to Eckbreth [50].

of the population densities N_i of the two (rotational) states are related to the rate constants by the differential equations [50]:

$$\frac{dN_1}{dt} = -N_1 b_{12} + N_2 (b_{21} + A_{21} + Q_{21}) \quad (3.2)$$

$$\frac{dN_2}{dt} = N_1 b_{12} - N_2 (b_{21} + A_{21} + Q_{21} + P + W_{2i}) \quad (3.3)$$

In the current case, OH molecules from ground state rotational levels are elevated to rotational levels within the excited electronic state where dissociation and ionization (moderate laser energy) are negligible. Thus, the structure can be considered as a closed system and according to the conservation law, the sum of the derivatives and its integral are:

$$\frac{dN_1}{dt} + \frac{dN_2}{dt} = 0 \quad , \text{ and: } N_1 + N_2 = N_1^0 \quad (3.4)$$

where N_1^0 is the initial number density in the ground state before excitation with the assumption of negligible initial population in the excited level. The fluorescence originates from the excited state. Hence it is of interest to formulate a relation between the initial population and the excited population. Substituting N_1 from Eq. (3.3) using Eq. (3.4) and integrating the result, one obtains:

$$N_2(t) = \frac{b_{12}N_1^0}{r} (1 - e^{-rt}) \quad (3.5)$$

where the variable r was introduced for easier handling and is $r = b_{12} + b_{21} + A_{21} + Q_{21}$. This equation describes the linear build-up process of the excited population for $rt \leq 1$ and a steady state condition for $rt > 1$. Thereby is t the pumping period to the upper level by the excitation source. As the quenching rate of OH at atmospheric pressure has an order of magnitude of 10^8 s^{-1} , while the pulse length of the laser used in this work is around 10^{-7} s , the steady state condition is an appropriate assumption. The detected fluorescence signal power is proportional to $N_2 A_{21}$ and the signal can be divided into the emission periods $t < \tau_{LP}$ and $t > \tau_{LP}$, where τ_{LP} is the laser pulse length [50, 111]:

$$F = h\nu A_{21} N_2(t) = h\nu A_{21} \frac{b_{12}N_1^0}{r} (1 - e^{-rt}) \quad \text{for } t < \tau_{LP} \quad (3.6)$$

$$F = h\nu A_{21} N_2(\tau_{LP}) e^{-(A_{21}+Q_{21})(t-\tau_{LP})} \quad \text{for } t > \tau_{LP} \quad (3.7)$$

Eq. (3.7) shows that the fluorescence decays exponentially after the excitation duration. Integrating Eq. (3.6) and Eq. (3.7) and combining the result yields in the integral fluorescence term:

$$F = h\nu N_1^0 \tau_{LP} \frac{B_{12}}{B_{12} + B_{21}} \frac{A_{21}}{1 + \frac{I_{\nu,sat}}{I_\nu}} \quad (3.8)$$

where the photon energy is defined by $h\nu$ with the frequency ν . Note, b_{12} was substituted using the relation Eq. (3.1). This equation shows, that the fluorescence intensity increases with the number density in the upper level and with the spontaneous emission coefficient. The used saturation irradiance $I_{\nu,sat}$ depends on local properties by:

$$I_{\nu,sat} = \frac{A_{21} + Q_{21}}{B_{12} + B_{21}} c \quad (3.9)$$

Depending on the application, further simplification can be made for saturated conditions and for linear conditions. Saturated LIF requires a strong excitation source, while in the linear LIF $I_\nu \ll I_{\nu,sat}$ and the fluorescence is linearly proportional to the laser intensity. In the current work, the linear regime is of interest and Eq. (3.8) reduces to:

$$F = \frac{h\nu}{c} N_1^0 \frac{E_L}{A} B_{12} \frac{A_{21}}{A_{21} + Q_{21}} = \frac{h\nu}{c} N_1^0 \frac{E_L}{A} B_{12} \phi_F \quad (3.10)$$

where the spectral laser intensity I_ν was substituted by the laser energy E_L per focal area A and pulse duration τ_{LP} ($E_L/(A\tau_{LP})$). Now, according to Eq. (3.10) the fluorescence depends on the initial number density of the excited rotational level, which then can be determined by the Boltzmann distribution in Eq. (B.24). The expression $\phi_F = A_{21}/(A_{21} + Q_{21})$ is the fluorescence quantum yield also referred to as Stern-Volmer factor in some literature. It is basically the fraction of excited OH, which emits energy by radiation. Due to the fact

that most of the energy is dissipated by non-radiating quenching processes, $A_{21} \ll Q_{21}$, the linear LIF faces a lower detectable concentration limit of N_1^0 .

The relation in Eq. (3.1) assumes perfectly overlapping molecule absorption line shape and instrumental, namely laser, line shape, and line broadening effects were neglected. However, the general expression accounting for line shape and overlapping is [50]:

$$b = \frac{B}{c} I_\nu^0 \int_{-\infty}^{\infty} g_L(\nu) g_\alpha(\nu) d\nu = \frac{B}{c} I_\nu^0 g \quad (3.11)$$

where I_ν^0 is the normalized spectral irradiance, $g_L(\nu)$ is the laser spectral line shape and g_α is the molecular absorption line shape. The line shapes are normalized such that $\int_{-\infty}^{\infty} g(\nu) d\nu = 1$. A discussion about types of line shapes and line broadening is found in the appendix B.5. Considering the right side of Eq. (3.11), g basically represents a correction factor for Eq. (3.10).

So far, the derived fluorescence expression in Eq. (3.10) described the emission originating from the excited rotational levels. The observed fluorescence signal power by a detector pixel is then given by:

$$I_F = C \frac{h\nu}{c} \frac{\Omega}{4\pi} l A N(v'', J'') B_{12} E_{LG} \phi = C \frac{h\nu}{c} \frac{\Omega}{4\pi} l A N_{OH} f_B(T) B_{12} E_{LG} \phi \quad (3.12)$$

where the Boltzmann distribution from Eq. (B.24) was included. The constant C accounts for transmission efficiency of the optical components, the efficiency of the detector, absorption effects, background noise, etc. The term $\Omega/(4\pi)$ is the observed solid angle between the emission source and the collection optics, l is the thickness of the laser beam and A its focal area. Thus, the product lA basically defines the volume V of excitation and emission. N_{OH} is the number density of OH as previously introduced.

Note, when taking B_{12} in $\text{m}^2/(\text{J}\cdot\text{s})$, I_F represents the collected photon power (unit W). In some literature however, the expression is provided for counts per second or photons per second. In order to avoid inconsistencies, Eq. (3.12) can be expressed by:

$$I_F = I_{fl} h\nu \quad (3.13)$$

where I_{fl} is referred to as the fluorescence signal (intensity) in the units photons/s.

3.1.2 Line broadening

According to the Heisenberg's Uncertainty Principle, energy cannot be defined infinitely accurately and it is subject to deviations. A spread of the energy, and thus of the frequency, across a range of wavelengths occurs in emission and absorption spectra. This is known as the natural linewidth. Hence, molecular spectra, as well as instrumental spectrum, are represented by a non-zero spectral width, referred to as line shape. Different aspects contribute to this shape. Eq. (3.10) considers the fluorescence at the central wavelength, whereas deviations and thus spectral distribution have to be accounted for and multiplied by the line shape.

The absorption line shape of a molecule consists of three components: Natural line broadening, collision broadening, Doppler broadening [50]. The first two are mathematically represented by a Lorentzian profile, while the latter one is described by a Gaussian profile. The convolution of these two types of profiles is a Voigt profile. Similarly, the laser spectrum

is subject of line broadening, described by the Gaussian and Lorentzian profiles. For a summary of line shapes see appendix B.5.

The overlap integral in Eq. (3.11) contains the instrumental line shape. Generally, it is found in the manual of the laser. According to the data of the currently used device, the pump laser has a full width at half maximum (FWHM) of 0.1 cm^{-1} , while the line shape is not specified. However, the instrumental line shape is affected by the resonator of a dye laser and a Lorentzian proportion is added [51]. Hence, it can be of Gaussian, Lorentzian or Voigt type. To obtain the laser line shape, a deconvolution of experimental spectral measurement data can be applied. Though, this method is mathematically demanding. Alternatively, an iterative method of the least square type was used to fit a Voigt profile to the measured data and obtain the parameters. A Voigt function is invariant with respect to convolution. Which means, that the convolution of a Voigt absorption line with a Voigt instrumental line leads to another Voigt curve. Assuming decoupled Gaussian and Lorentzian effects, it was assumed that the FWHM are:

$$\Delta\nu_G = \sqrt{\Delta\nu_D^2 + \Delta\nu_{LG}^2} \quad (3.14)$$

$$\Delta\nu_L = \Delta\nu_C + \Delta\nu_{LL} \quad (3.15)$$

where the subscripts G is Gaussian, D the molecular Doppler (Gaussian), LG the instrumental Gaussian, L Lorentzian, C the molecular collision (Lorentzian) and LL the instrumental Lorentzian FWHM. The first and second graphs in Fig. 3.2 show the effect of altering the line shapes. The increase of the Gaussian FWHM results in an uniform broadening, while the Lorentzian part affects mostly the flanks.

To obtain the instrumental line shape parameters, an excitation scan on a constant, atmospheric pressure flame was performed by tuning the excitation laser with a step size of 0.0005 nm over a range of wavelengths. At each wavelength, 50 fluorescence images were taken for time-averaging purposes in order to crease the data quality. At the center of the flame a 5×5 superpixel was evaluated. The experimental data is plotted in Fig. 3.2, showing that the intensity peaks of the different rotational lines are approximately independent of the line shape, which means that the ratio of two overlap integrals is $g_2/g_1 \approx 1$. Then, based on the experimental intensity peaks, a temperature of 1919 K followed. According to Eq. (B.34) and Eq. (B.32), $\Delta\nu_D = 0.269 \text{ cm}^{-1}$ and $\Delta\nu_c = 0.034 \text{ cm}^{-1}$ were determined for the molecular spectrum. Then, a Voigt profile was fitted to the measured data using the least-square minimization and the Gaussian and Lorentzian parameters were determined for the laser profile considering Eq. (3.14) and Eq. (3.15). The experimental and the simulated spectra are provided in Fig. 3.2 on the right. The error between experimental and fitting curve was around 3 %. An instrumental Gaussian FWHM of 0.26 cm^{-1} and a Lorentzian FWHM of 0.09 cm^{-1} were calculated. Due to the small Lorentzian contribution, instrumental and molecular, only Gaussian line shapes were considered. This instrumental broadening was assumed to remain constant for every measurement.

3.1.3 OH LIF and effect of collisional processes

The spectrum of OH allows for different transition possibilities. In the temperature range of $1200 - 2300 \text{ K}$ (relevant to this work), the vibrational population fraction in the $v'' = 0$ level is around 98 % - 89 % [129]. Thus, this level is the most important one for excitation. From a technical point of view, the excitation ($v' = 1 \leftarrow v'' = 0$) within ($X^2\Pi \leftarrow A^2\Sigma$) and

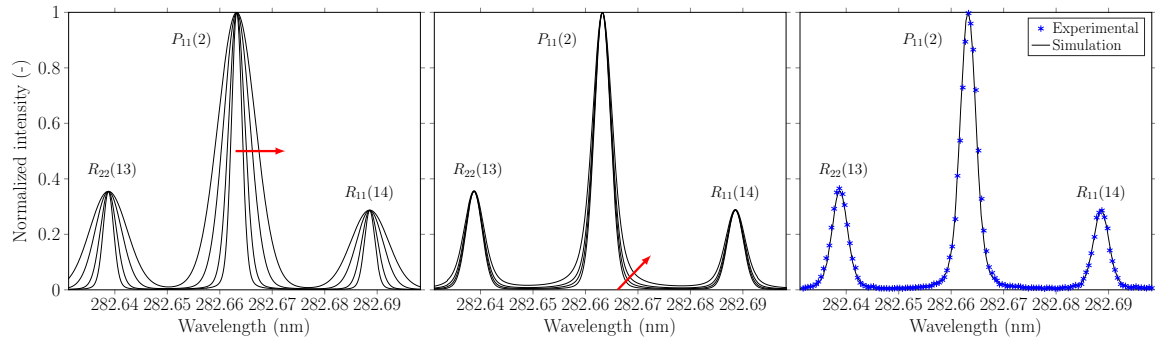


Figure 3.2: Left: increasing the Gaussian width. Center: increasing the Lorentzian width. Right: overlap of experimental and simulated spectra at 1919 K and atmospheric pressure.

emission collection of the transitions ($v'' = 0 \leftarrow v' = 0$) and ($v'' = 1 \leftarrow v' = 1$) are practical, as the excitation takes place around 283 nm ($\approx 35000 \text{ cm}^{-1}$) and the broadband emission around 300 nm - 320 nm ($\approx 32000 \text{ cm}^{-1}$) and the two processes can be spectrally separated. In the following, the shorter notation convention (v',v'')(1,0) is used. The reason for the shift from $v' = 1$ to $v' = 0$ is due to relaxation. Theoretically, exciting an isolated OH molecule to a specific ro-vibrational branch of the excited state should result in emission from the pumped level. However, in reactive environments, such as flames, different species of various concentrations are present and act as collision partners resulting in relaxation processes within the excited electronic state. These deactivation processes compete with the spontaneous emission and are depending highly on the pressure and temperature. Rotational energy transfer (RET) is the population redistribution within the same vibrational manifold and vibrational energy transfer is the redistribution within the same electronic state. Fig. 3.3 illustrates the process of excitation, the subsequent relaxation and emission to the ground state according to the selection rules found in appendix B. This means, after the excitation,

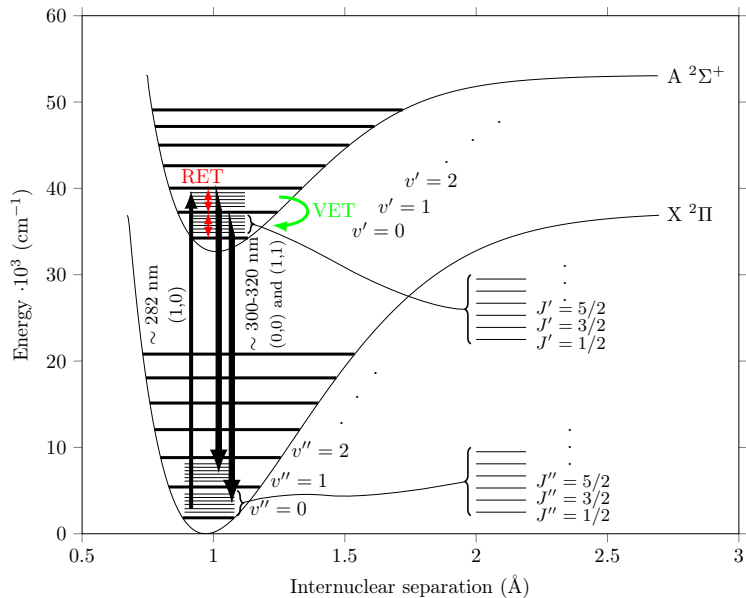


Figure 3.3: Morse potentials with corresponding LIF processes.

relaxation processes take place and the emission originates from various ro-vibrational levels. The two-level scheme is insufficient to describe the relaxation processes analytically. Multi-level, complex models have been introduced in literature therefore [50, 178, 183, 197]. The applicability of such models require the knowledge of the composition, the collisional cross-section and the rate constant of each molecule involved in the process. The composition is in most cases unavailable and rate constants are inadequately investigated for most molecules. As the RET is a fast process and its time scale is some order of magnitude smaller than VET and quenching [197], it requires short-pulsed lasers and short-gated detectors to resolve the process temporally [147, 183]. The small time scales of RET compared to VET is attributed to the small energy gaps between rotational lines ($\approx 40 - 400 \text{ cm}^{-1}$ in most cases) compared to the gaps between vibrational levels ($\approx 3000 \text{ cm}^{-1}$).

Compared to the relaxation processes, where emission with an altered spectrum can still be detected after the redistribution, quenching is a non-radiative electronic transition and thus loss of signal. The fluorescence effective lifetime τ is generally expressed as:

$$\tau = \frac{1}{A_{21} + Q_{21}} = \frac{1}{\frac{1}{\tau_0} + Q_{21}} \quad (3.16)$$

where τ_0 is the natural lifetime. An analytic model for the calculation of the quenching rate is [50]:

$$Q_{21} = \sum_i N_i \sigma_{Q_i} \left(\frac{8kT}{\pi\mu_i} \right)^{0.5} \quad (3.17)$$

where N_i is the number density of the colliding partner i , σ_{Q_i} is the temperature dependent cross section for quenching and μ_i is the reduced mass of the two colliding partners. Values and analytic expressions of σ_{Q_i} for various collision partner of OH are reported in [189]. Experimentally, the quenching can be determined using time-resolved measurement of the fluorescence signal, as seen in Fig. 4.12, and fitting an exponential intensity decay $I \propto I_0 e^{-t/\tau}$ to the intensity after the excitation period to obtain τ . However, to determine the quenching rate, the temperature and composition are required. Further, as clearly seen in Fig. 4.12, the natural lifetime of OH, which should be around 700 ns [129], is reduced to effective lifetimes around 20 ns. Hence, for an accurate experimental determination of the lifetime in first place, a laser with shorter pulse length is required for atmospheric conditions or the time-resolved experiments need to be conducted at lower pressures.

The calculation of collisional effects requires different information a priori, which is in most reactive experiments unavailable. Further, the consideration of RET, VET and electronic quenching is vital for quantitative measurement of OH concentration, as otherwise the LIF signal is not proportional to the number density due to altered emission spectrum, and it is necessary for temporal and spectral fluorescence measurements. In this work, OH LIF is used for reaction zone detection and flame structure visualization at atmospheric pressure. The laser had a pulse length above the RET time scale and the emission was collected at broadband. For the temperature determination, the intensity ratio of two successively excited rotational lines was used where fast RET is assumed, such that the upper vibrational states are considered in rotational thermal equilibrium and the quantum yield was assumed to be independent of the rotational number. According to [71], the presence of N_2 as collisional partner of OH, as in the current work, leads to fast VET and the assumption of constant quantum yield is further justified. Due to lack of the reaction zone composition and similar to literature [47, 167], quenching remains unconsidered in the

applied two-line technique assuming that the ratio of the two quantum efficiencies $\phi_2/\phi_1 \approx 1$, despite the quenching dependency on the rotational quantum number [175].

3.1.4 Laser-induced fluorescence thermometry

As mentioned before, the sensitivity advantage of LIF is preliminary used to detect minor species. Under some circumstances the technique allows the quantitative concentration and temperature measurement. In this work, the focus was on 2D spatial detection and thus a broadband emission collection was conducted, rather than 0D spectrally resolved methods which require spectrometers. Generally, quantitative measurement approaches are based on the quantification of the detected signal, see Eq. (3.12). Essentially, the signal depends on a number of constants, which can be calculated, determined a priori or simplified, and on the number density and the Boltzmann distribution. The latter is expressed through the involved energy and the rotational temperature, as discussed in appendix B.3.2. Spectroscopic constants were obtain from literature. In [90, 178] the authors presented a single line technique to determine the absolute concentration of OH in flames. To avoid the temperature dependency of the signal, rotational lines ($Q_1(9.5)/Q_2(7.5)$) (v',v'') (1,0) and $Q_1(6.5)$ (v',v'') (0,0), respectively) insensitive to temperature variations within the expected range were excited. However, as premixed flames were investigated, the knowledge of the composition allowed a kinetic equilibrium combustion simulation to determine an initial number density of OH for absorption correction purposes and the quantum yield was shown to be almost constant for the considered conditions. The applicability of this approach was limited to specific cases. For temperature measurement, the single line method might be unsuitable due to the unknown dependency of the number density on temperature. A widely applied method to determine the rotational temperature is the two-line method [31, 47, 72, 115, 117, 167, 175]. Sometimes also referred to as line-peak or two-color method. Here, two rotational lines are excited and the ratio of the separately collected intensities is set in relation to the temperature. Assuming same geometrical conditions for both lines and constant number density N_{OH} , one obtains from the quantified fluorescence equation:

$$I_{ratio} = \frac{(I_F/E_L)_2}{(I_F/E_L)_1} = \frac{(C)_2}{(C)_1} \frac{(B_{12g}\phi)_2}{(B_{12g}\phi)_1} \frac{(f_B(T))_2}{(f_B(T))_1} = C' \frac{(B_{12g}\phi)_2}{(B_{12g}\phi)_1} e^{-\frac{E_2-E_1}{kT}} \quad (3.18)$$

where the subscripts 1 and 2 correspond to the first and second excited lines, respectively. Note, the mathematical expression for the Boltzmann function was substituted and summarized on the right side. The constant C' is referred to as calibration constant and determined using a second measurement technique, as done in [47], or as in this case, assuming spectrally independent constant C , $C' \approx 1$ [167]. As discussed before, the quantum yield was considered as independent of the rotational number due to fast RET and VET, leading to $\phi_2/\phi_1 \approx 1$. The remaining constants and variables were calculated and the final equation resulted in a calibration curve, which converted intensity ratios pixel-by-pixel into temperature. For instantaneous temperature determination, the two excitations and image recordings need to be performed simultaneously using two laser and detection systems triggered shortly after each other. However, due to SNR limitations the data quality is generally poor. To overcome this issue, each line is excited multiple times and the obtained images were time-averaged. Further, using two systems requires accurate adjustment and synchronization, beside increasing the costs. Thus, in most cases one system is applied and the two lines are excited successively. This procedure improved the data quality at the cost of the time

resolution and under the assumption of steady state condition (constant number density and temperature). Therefore, the determined temperature field is of average nature and only accurate for steady-state flows.

More accurate, but time-consuming temperature determination methods for steady state applications, such as laminar flat flame or plasma [197], are line-scanning and multi-line or Boltzmann plot approaches. For the first method, the laser scans a wavelength range successively, while the emission is collected thereby. The line-scanning is a two-line technique, except instead of calculating the line-peak ratio and relating it to temperature according to Eq. (3.18), the spectral intensities around two peaks are integrated spectrally and the ratio is related to a temperature based on a calibration curve calculated in advance. Such a procedure can be conducted for example on the experimental data of Fig. 3.2. The integrals of two of the peaks, basically the areas enclosed by the curve, are calculated and related to temperature. For the Boltzmann method, multiple rotational transitions of the same vibrational level are selected successively and the recorded intensities are plotted according to:

$$\ln \left(\frac{I_F}{(2J'' + 1)B_{12}} \right) = -\frac{F_{rot}}{kT_{rot}} + const. \quad (3.19)$$

where constant detection efficiency for all transition is assumed and the emission originates from the same location. The vibrational energy term, as well as the Stern-Volmer factor are constant. Further, rotational and vibrational equilibrium is assumed, $T = T_{rot} = T_{vib}$. This equation yields in a straight line with a negative slope and the temperature as variable. It is recommended to use rotational lines with different quantum numbers and energies (or population densities) to generate temperature sensitive calibration curves.

The reaction zone of the main experiment was highly turbulent. Even though, a diffusion flame was generated for several minutes, the flame fluctuations rule out scanning and multi-line thermometry methods. Further, the employed excitation laser was operated at 10 Hz and there is usually an additional tuning time to vary the wavelength. A scanning process requires a significant amount of time during the experiment. Thus, the focus here was on two-line/line-peak thermometry.

3.1.5 Absorption correction

As the laser beam passes through a flame absorption of the laser intensity occurs. This leads to a decay of intensity in the beam direction and to less available energy to excite the following molecules. At the same time, scaling the fluorescence signal according to Eq. (3.12) by a constant laser energy yields in erroneous results. Further, the spectral shape of the beam is affected in the process due to the overlapping of beam and absorption line shapes. Two similar methods are described in literature to determine the local absorption and apply a correction to fluorescence data. The author refers to [115] for the theoretical method and to [46, 47, 71, 94, 178] to a detailed description of the experimental method.

The attenuation of the local intensity can be described by the Lambert-Beer law as:

$$-\frac{dI(x)}{dx} = \alpha(x)I(x) = C_1 f_B(T(x)) N_{OH}(x) B_{12} I(x) g(x) \quad (3.20)$$

where x is the beam direction coordinate, α is the local absorption coefficient and C_1 a proportionality coefficient. For convenience, the normalized laser intensity I is used instead of I_ν . The overlap integral g is introduced in Eq. (3.11). Another important finding is the

altering effect of the molecular absorption line shape on the local laser line shape, which can be expressed in terms of the Lambert-Beer law as:

$$g_L(\nu, x) = g_L(\nu, 0)e^{-\int_0^x \alpha(\nu, x') dx'} \quad (3.21)$$

Combining Eq. (3.12) and Eq. (3.20) results in:

$$\frac{dI(x)}{dx} = -C_1 \frac{I_F(x)}{C\phi} = \frac{dI(x)_{eff}}{dx} \quad (3.22)$$

where I_{eff} is the fraction of intensity, which leads to the excitation of a molecule and can be expressed and normalized as:

$$I(x)_{eff} = I(x)g(x) \quad , \text{and:} \quad \frac{I(x)_{eff}}{I(0)_{eff}} = \frac{I(x)}{I(0)} \frac{g(x)}{g(0)} \quad (3.23)$$

$I_{eff}/I(0)_{eff}$ is the fraction of available local intensity and is considered as the local correction factor. It is calculated in two steps. First Eq. (3.22) is integrated assuming constant quantum efficiency:

$$\frac{I(x)}{I(0)} = -\frac{C_1}{C\phi} \int_0^x I_F(x) dx + 1 = C_2 \int_0^x I_F(x) dx + 1 \quad (3.24)$$

The new constant C_2 can be determined from the integration of Eq. (3.24) from $x = 0$ m (before entering the flame) to $x = L$ in the beam direction:

$$C_2 = \frac{\frac{I(0) - I(L)}{I(0)}}{\int_0^L I_F(x) dx} \quad (3.25)$$

The intensities $I(0)$ and $I(L)$ represent the initial, unaffected intensity and the altered intensity after passing through the flame of length L , respectively. Both quantities are usually accessed by recording the laser intensities before and after the flame, for example on a dye cell. In the second step, $g(x)/g(0)$ is related to the determined $I(x)/I(0)$ using Eq. (3.21) and the overlap integral in Eq. (3.11) by:

$$\frac{I(x)}{I(0)} = \int_0^\infty g_L(\nu, 0) e^{-\int_0^x \alpha(\nu, x') dx'} d\nu \quad (3.26)$$

considering a temperature independent molecular absorption line shape $g_\alpha(\nu)$. The process leads to a look-up table for the normalized overlap $g(x)/g(0)$ depending on $I(x)/I(0)$. A detailed iterative scheme is reported in [71]. Fig. 3.4 shows exemplarily calculated look-up tables for different laser FWHM and the spectral line shapes during the travel through an absorbing medium by the $P_{11}(2.5)$ line at $T = 2000$ K. The laser intensity decreases more significantly as the FWHM increases. This is due to the fact that a larger laser and molecular absorption line shape overlap occurs. The spectral laser line shape is affected at the central wavelength in the absorption process and the shape is broadened. The absorption correction theory presented so far is applied to spatial intensity distribution from a flat flame burner on Fig. 3.5. A signal decay is experienced from right to left in the beam direction due to absorption. Scaling the curve by the correction function in blue, the intensity decay is countered and reversed. As pointed out in the beginning, there is also a theoretical method

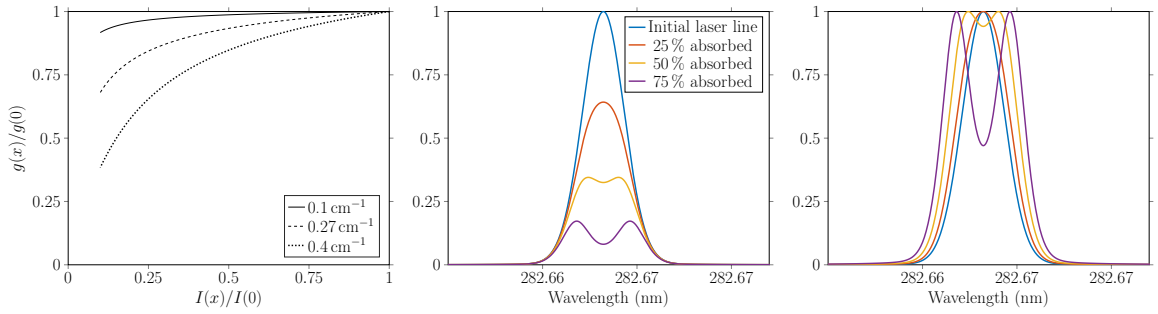


Figure 3.4: Left: look-up curves for overlap vs. intensity decay for different laser FWHM. Middle: laser spectral line shapes at different absorbed states normalized by initial line. Right: laser spectral line shapes at different absorption states normalized by individual maximum. Data for $P_{11}(2.5)$, $T = 2000 \text{ K}$ and laser FWHM = 0.4 cm^{-1} .

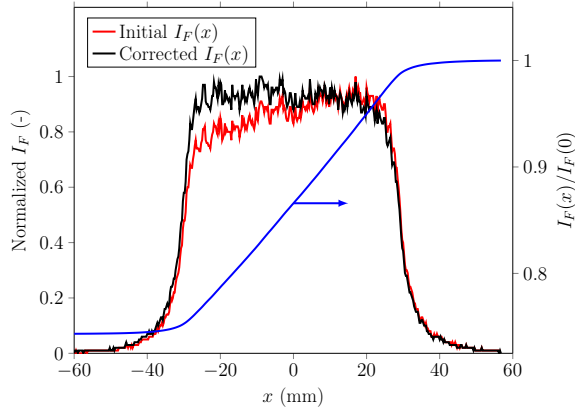


Figure 3.5: Absorbed spatial intensity and corrected spatial intensity distribution. Correction function in blue. Laser entered from right.

for absorption correction, which presumes a spatially constant flame. Integrating Eq. (3.20) yields in:

$$I(x) = I(0)e^{-\int_0^x \alpha(x')dx'} \quad (3.27)$$

where α is accounted for by the properties on the right side of Eq. (3.20). From experimental data, such as in Fig. 3.5, the slope of the curve at the center around $x = 0 \text{ mm}$ is determined. In the next step, α is iteratively altered until the gradient of I_F at $x = 0 \text{ mm}$ reaches a predefined minimum. The authors in [115] defined the constants for α , determined the number density N_{OH} from chemical equilibrium calculation and basically solved for the constant C_1 in Eq. (3.20), iteratively. The final result is equally a correction function, as presented in Fig. 3.5.

3.2 Multiaatomic tracer molecules

The utilization of OH as tracer molecule is limited to chemical reaction regions, for example in the field of combustion diagnostics, as the molecule is an intermediate species generated and consumed during the process. To gain information about phenomena occurring prior to the reaction using the LIF method, other tracer molecules are required. The selection

of an appropriate tracer is subject to different requirements. In the current work, the cold flow analysis by means of LIF was conducted at room temperature, atmospheric pressure and separately from the combustion analysis. Thus, atomic tracers which require high temperatures for atomization are not considered and other critical and vital specifications become unnecessary, such as high temperature stability, solubility of the tracer in the fuel and similarity of the tracer to the applied fuel. For a detailed review of tracers, the reader is referred to Schulz et al. [173]. Some most frequently used and adequately investigated tracers for LIF excitation are organic molecules. A brief description of the quantum mechanic processes is given in the following subsection, before proceeding to the selection and tracer molecular and spectroscopic properties.

3.2.1 Photophysical process

Di-/Tri-atomic and multi-atomic organic LIF share the same basic principles, which were discussed in the previous sections, see for example Fig. 3.1 and Fig. 3.3. The energetic state of molecules is divided into the electronic, vibrational and rotational fine structures. By means of an excitation source, the energetic state of the molecules is elevated to an excited state. Thereby, vibrational and rotational states also get altered. To return to the ground state at thermal equilibrium, spontaneous emission takes place, which is broadband collected, beside other processes. However, the structure of the molecule determines the quantum mechanic processes taking place after the excitation. Depending on the number and orientation of the unpaired electrons, the electronic state is characterized by the spin multiplicity $2S + 1$, where S is the sum of the unpaired individual electron spins $s_i = +1/2$, see section B.1.3. Consequently, the electronic state multiplicity is 1, 2, 3, ... and called singlet, doublet, triplet, ..., respectively. The OH radical has a single unpaired electron, which results in a multiplicity of 2, and according to the selection rules in section B.3.1, the multiplicity remains constant during the electronic transition ($\Delta S = 0$). On the other hand, organic molecules used as flow indicators contain only paired electrons in the ground state and the corresponding multiplicity is 1 or singlet. After the excitation of organic molecules, radiative and non-radiative deactivation processes compete with the fluorescence, which are generally visualized by a Jablonski diagram, e.g. in Fig. 3.6. The mentioned figure contains the essential information. Non-illustrated points are rotational bands, quenching, triplet-triplet absorption and dissociation. Within an excited electronic state, non-radiative vibrational relaxation takes place (in OH spectroscopy VET) through collision of the molecule with the carrier gas. While in liquids the relaxation is fast, in gases a complete relaxation may not occur. Between states of same multiplicity, non-radiative internal conversion (IC) is another transition process. Due to small energy gaps, the IC occurs fast. The non-radiative transition between states of different spin multiplicities is called intersystem crossing (ISC), during which the total energy remains constant, such that the molecule obtains its vibrational energy. On the other hand, there are the radiative fluorescence and phosphorescence processes. Fluorescence is an spontaneous emission process between states of same multiplicity with a duration in the range of 1 - 100 ns, while phosphorescence may reach lifetimes in the range of milliseconds [173]. Due to the non-radiative deactivation and energy transfer processes, the fluorescence is red shifted compared to the excitation wavelength similarly to OH LIF.

According to [68, 173, 193], the detected fluorescence signal in the linear regime is

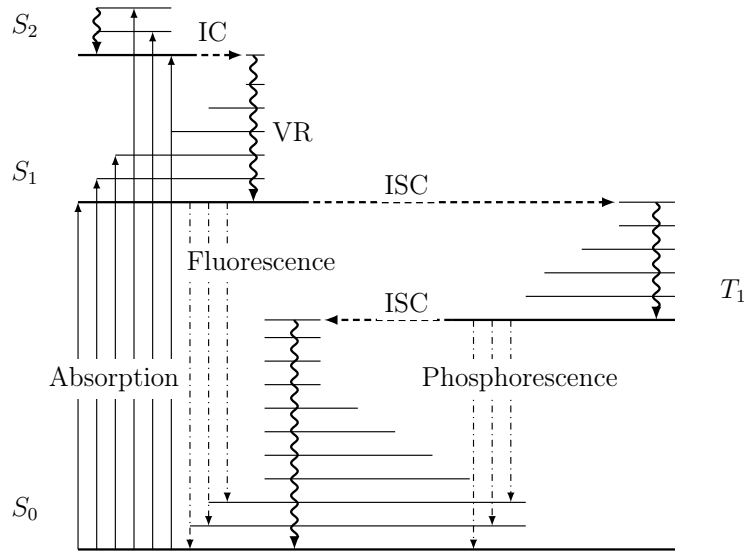


Figure 3.6: Jablonski diagram describing the molecular singlet (S) and triplet (T) systems. IC: internal conversion, ISC: intersystem crossing, VR: vibrational relaxation. Each electronic level (S, T) consists of a number of vibrational branches. Adapted from [82].

quantified by:

$$I_{fl} = C \frac{E_L}{h\nu} \frac{\Omega}{4\pi} l A n_{abs}(T) \sigma_{abs} g \phi_F = C \frac{E_L}{h\nu} \frac{\Omega}{4\pi} V \left(\frac{Xp}{kT} \right) \sigma_{abs} \phi_F \quad (3.28)$$

where X and p are the mole fraction of the absorbing species (abs) and pressure, substituting the number density n ($n = Xp/(kT)$, where p is the total pressure). The variable T is the temperature. Despite the fact, that Eq. (3.28) appears to differ from the OH fluorescence signal power Eq. (3.12), they can be transformed into one another. First of all, Eq. (3.28) describes the fluorescence signal (photons counts), while Eq. (3.12) represents the signal power, see the conversion Eq. (3.13). Further, the molecular absorption cross-section σ_{abs} (generally in cm^2) is proportional to the Einstein coefficient for absorption $\sigma_{abs} \propto \frac{h\nu}{c} g B_{12}$ thus substituted in the current fluorescence expression. σ_{abs} is a spectrally sensitive property. The remaining constants and variables correspond to the definitions in section 3.1.1.

3.2.2 Tracer selection

After the discussion of the LIF processes, the question of the appropriate organic tracer remains open. A detailed review of common tracers are reported by Schulz et al. [173]. General characteristics of tracers for non-reactive, turbulent flow field and mixing studies are commercial availability, price, toxicity (e.g. toluene, hexafluoroacetone), harmfulness for environment, flammability (acetone, acetaldehyde), corrosiveness to components, ... Specific requirements on the other hand are seeding properties, well-defined spectroscopic characterization data and availability of material properties. A widely applied tracer for investigations at room temperature and atmospheric pressure is acetone [69, 88, 193]. Its absorption is in the UV range, while the peak emission occurs in the visible spectrum. This allows the

utilization of non-UV lenses, non-intensified and non-gated (with mounted band-pass filters) detectors, leading to high quality and high SNR [182]. Further, according to Smith et al. [182], the fluorescence signal shows a linear behavior to the laser energy and the acetone concentration, and it is not subject to self-quenching and O₂ quenching. Additionally, acetone has a high vapor pressure, which leads to high mole concentration in the carrier gas and high seeding density. Another organic ketone found and characterized in literature for seeding and tracer purposes is 2-trifluoromethyl-1,1,1,2,4,4,5,5,5-nonafluoro-3-pentanone, or just fluoroketone [79, 80, 170]. It has similar absorption and emission wavelengths sensitivities to acetone and has a high vapor pressure at atmospheric pressure, except it is non-flammable, inert, of low toxicity, environmentally accepted and has a high fluorescence strength attributed to its quantum efficiency.

Gerold [68] presented a review of different tracers and compared acetone and fluoroketone to each other for an excitation wavelength of 355 nm. Basically, as the fluorescence signal $I_{fl} \propto X\sigma_{abs}\phi_F$, the author introduced this term as a selection parameter K :

$$K = X\sigma_{abs}\phi_F \quad (3.29)$$

To perform the analysis and compare acetone to fluoroketone for the excitation wavelength of 283 nm, as applied in this work, the parameters of Eq. (3.29) were required. The mole fraction is obtained from the vapor pressure on the basis of Raoult's law [14]:

$$p_v = p_v^*X \quad (3.30)$$

where p_v is the vapor pressure at the present temperature and p_v^* is the equilibrium vapor pressure of the pure substance. Since the tracer was a single component, p_v^* is equal the present pressure (atmospheric). The vapor pressure was calculated by the Antoine equation. Corresponding parameters for acetone and fluoroketone were found in [1] and [79], respectively. Absorption cross-sections were obtained from Fig. 3.7. Both molecules have a value of $\sigma_{abs} = 4.429 \cdot 10^{-20} \text{ cm}^2$ at a wavelength of 283 nm. Note, the broadband (continuous) absorption and emission characteristics of organic molecules are especially advantageous for excitation and fluorescence detection. Minor laser decalibration does not have severe consequences, as it would have for OH LIF, see for example Fig. 3.2. Finally, the quantum

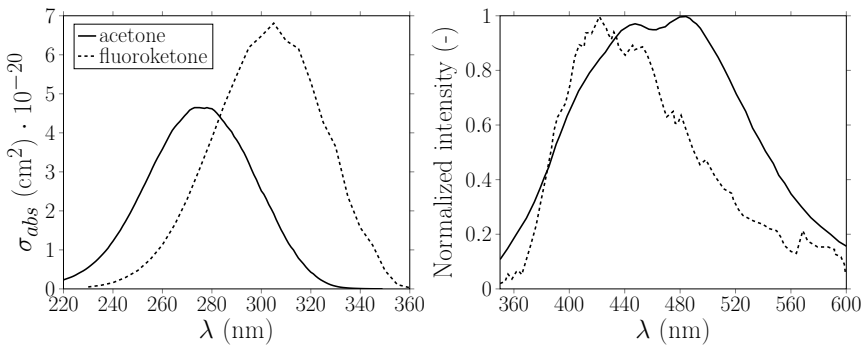


Figure 3.7: Spectral properties at $T = 298 \text{ K}$, $p = 1 \text{ bar}$. Left: absorption cross sections. Right: normalized fluorescence intensity. Acetone absorption from [70], fluoroketone absorption from [190], emission from [80].

efficiency of acetone fluorescence was specified as $\phi_F = 0.2 \%$ for $\lambda = 225 - 320 \text{ nm}$ in [126],

while it was quantified as $\phi_F = 0.58\%$ for $\lambda = 282\text{ nm}$, $T = 298\text{ K}$ and atmospheric pressure in [70], presumably in percentage as not explicitly stated by the latter authors and since values above 1 were also provided in this literature. According to [79], the *fluorescence efficiency* of fluoroketone excited at 266 nm is three times higher than that of acetone. Also Gerold's [68] analysis was based on this statement. Consequently, the quantum yield of fluoroketone was set to $\phi_F = 0.6 - 1.74\%$. Considering the lower quantum yield value, Tab. 3.1 presents the comparison of the tracers. K_r is the ratio of the acetone parameter K to the fluoroketone parameter K . Thus, the value of fluoroketone was set to 100 %.

Table 3.1: Calculated values for parameter K at 294 K and atmospheric pressure.

Molecule	X (%)	σ_{abs} ($\text{cm}^2 \cdot 10^{-20}$)	ϕ_F (%)	K_r (%)
Acetone	30	4.429	0.2	24.6
Fluoroketone	40.6	4.429	0.6	100

As the straightforward analysis shows and despite the conservative consideration of the quantum efficiency, acetone had a smaller mole fraction in the carrier gas under the specified conditions and a significantly lower quantum yield than fluoroketone. Thus, the fluorescence signal of excited acetone molecules was expected to be only 24.6 % of the signal strength of fluoroketone. The tracer fluoroketone should improve the image quality, such as SNR, and was taken for cold flow analysis in this work. Further, fluoroketone was more favorable over acetone due to the mentioned safety reasons.

Chapter 4

LIF Validation Procedure

4.1 Hardware

A summary of the employed optical instruments is given in this section. The devices and optical components in mounted condition are illustrated in Fig. 5.1.

4.1.1 Laser system

A commonly used combination of pump and dye laser was used in this study. The pump laser was a Nd:YAG (neodymium-doped yttrium aluminum garnet) of Lotis TII type LS2137/2 and was operated at 532 nm. This second harmonic generation (SHG, 1064 nm to 532 nm) was enabled by an integrated non-linear crystal. The maximum pulse repetition rate of the laser was 10 Hz with a pulse duration around 12 - 18 ns according to the manual.

The pulse of the first laser pumped a dye laser of Lambda Physik (type ScanMate). This laser model has an oscillator and an amplifier unit. The oscillator consisted of a grating for wavelength selection and decoupling, and an independent dye cell system for excitation. Then, the consequent emission was led to the amplifier unit containing a second independent dye cell and was amplified. The output (fundamental wavelength) required a frequency doubling, which was done by a non-linear barium borate (BBO) SHG crystal. A subsequent beam compensator corrected the beam shift afterwards. After the frequency doubling, there is generally still an amount of fundamental beam, which was separated from the UV beam using a combination of four prisms. Finally, laser light at wavelengths between 280 - 288 nm could be obtained.

A solution of ethanol and Rhodamine 6G was chosen for any dye cell. The composition varied depending on the dye cell application (oscillator or amplifier). The spectral energy and thus the efficiency of the dye laser is shown in Fig. 4.1 on the left graph. The energy distribution results from the dye efficiency and hardware efficiency of the dye laser, such as of the SHG, compensator and prisms. As the laser pulse energy was subject of fluctuations, a fraction of the energy was usually reflected by a fused silica plate to an energy sensor. The graph on the right side of Fig. 4.1 shows the spectral distribution of the fraction of energy removed from the laser beam. The reflection seems slightly depending on the wavelength and on the efficiency of the dye laser. However, some measurements were conducted within 282.636 - 286.456 nm, while most were in the range of 282.636 - 282.663 nm. Here, the maximum fluctuation was around 0.4 % and negligible.

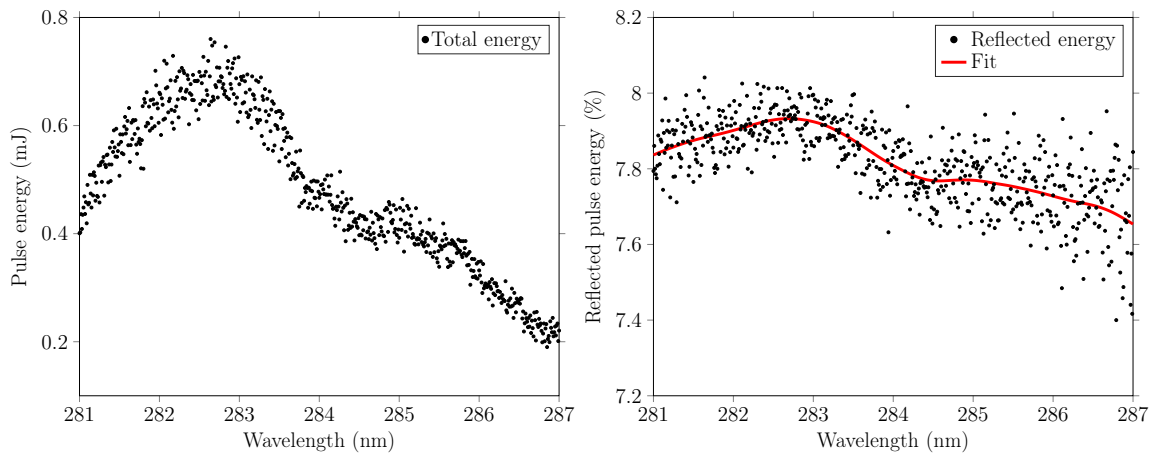


Figure 4.1: Left: spectral laser energy. Right: reflected fraction of laser energy for pulse energy measurement.

4.1.2 Detectors

Detectors for different purposes and measurements are summarized below.

PI camera

The energy emission from excited OH in reactive experiments, either flat flame burner or main experiment, was collected by the ICCD (intensified charge-coupled device) camera PI MAX2 Gen III Unigen. These experiments required a UV sensitive detector for the wavelength range of 300 - 320 nm, which this camera fulfilled with the specified sensitivity in the range of 190 - 900 nm. The camera sensor had a pixel size of $12.8 \times 12.8 \mu\text{m}$ and a frame rate of around 4 Hz was feasible at the maximum image resolution of 1024 x 1024 pixels. The acquisition frame rate was limited by the read-out time of the sensor and this in turn depended on the number of vertical pixels. However, for reactive experiments a higher frame rate was of benefit, as a large number of images were recorded. Hence, the field of view (FOV) was reduced to the minimum necessary region of interest (ROI) and a 2 x 2 hardware pixel binning to a superpixel was applied. The latter step reduced the image resolution, but also raised the SNR. The SNR is the ratio of signal magnitude relative to the uncertainty, also referred to as noise, of it. Noise is a statistical fluctuation in the photoelectric signal after the photon incident and during its conversion. The SNR determines the quality of an image and consists of photon noise, read noise and dark noise. The first type of noise is the dominant part for high signal magnitudes and exhibits a Poisson distribution. Fig. 4.2 shows the SNR in dB for the mentioned camera. For the measurement, the camera recorded a series of images of a homogeneous surface illuminated by a uniform light source with successively increasing intensity. The SNR was then determined from the signal to the standard deviation of a region of 25 x 25 pixels [36, 71, 84]:

$$SNR = \frac{\bar{I}}{\sigma_I} = \frac{\bar{I}}{\sqrt{\frac{\sum_i (I_i - \bar{I})^2}{N}}} \quad (4.1)$$

where i is the i -th number of N pixels, I is the pixel intensity and σ the standard deviation. \bar{I} is the spatial average intensity. The data shows an improvement of almost 50 % using a

2×2 pixel binning.

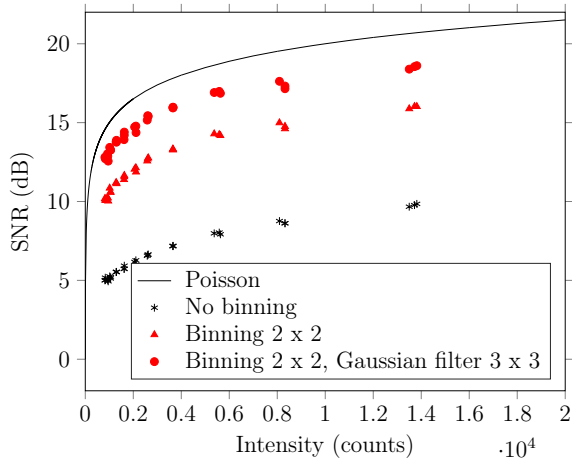


Figure 4.2: SNR of PI MAX2 camera.

Andor iStar

For recording light sheet profiles and the emission of excited tracers for cold flow analyses, the ICCD camera Andor iStar A-DH334T-18F-E3 Gen 2 was utilized. The device had the same sensitivities and frame rate specifications as the PI MAX2 camera. Hence, same ROI and binning were set for light sheet recordings. The pixel size was slightly different with $13 \times 13 \mu\text{m}$. To reduce the dark noise, the device offered an internal cooling operation mode, which was set to -30°C . For tracer measurements, a higher resolution was required leading to a non-binning operation mode.

Phantom V710 camera and Hamamatsu intensifier

The OH chemiluminescence was recorded by the high-speed (HS) camera Phantom V710 from Vision Research. An image frame rate of 7500 Hz at a full resolution of 1280×800 pixels and a minimum exposure time of $290 \mu\text{s}$ were selected. The pixel size was $20 \times 20 \mu\text{m}$. The CMOS (Complementary Metal-Oxide Semiconductor) sensor of the camera lacks an intensifier and had a wavelength sensitivity in the range of 350 - 1100 nm. These features make the camera unsuitable for capturing the OH emission directly. Hence, an UV sensitive intensifier from Hamamatsu (C10880-03F) was mounted in front of the camera. The device was equipped with a UV sensitive photocathode for wavelengths of 185 - 900 nm with maximum sensitivity at 430 nm. The maximum exposure time at the frame rate of 7500 Hz was $120 \mu\text{s}$, which determined the overall exposure time of the system, making the exposure time of the Phantom camera of secondary importance. According to the specifications, the resolution was 38 lp/mm yielding in a pixel size of around $13 \mu\text{m}$. Hence, the maximum resolution of the system (camera + intensifier) was determined by the camera properties.

Depending on the OH* recordings, different gain factors were set. Maximum values were aimed at to gain maximum intensity of low emission events, but at the same time to avoid pixel saturation from high emission cases. Saturated pixels provide less information about the actual emission and long-term saturation causes hardware damages. Fig. 4.3 shows the

luminous gain depending on the gain factor (*dial scale*) for the current device with a single stage microchannel plate (MCP). The min. and max. limits correspond to the hardware specific values 600 and 999 (gain value range).

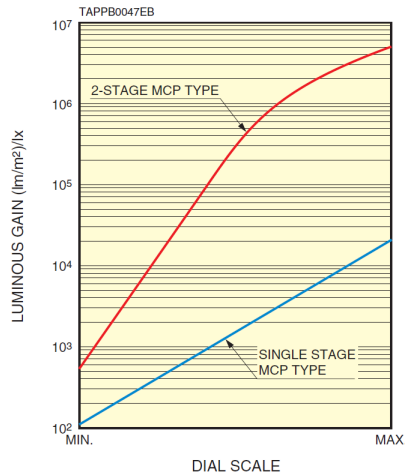


Figure 4.3: Gain characteristics of the Hamamatsu intensifier, taken from [83].

4.1.3 Light sheet optics, lenses and filters

Peripheral components for the laser beam and the cameras are summarized below.

Light sheet optics

To convert the circular UV laser beam with a diameter of around 1 mm into a constant height light sheet, a combination of UV coated plano-convex spherical and plano-concave cylindrical lenses were used. For the flat flame calibration experiments, a spherical lens with a focal length of $f = 500$ mm and a cylindrical lens with $f = 25.4$ mm generated a light sheet with an effective height of around 13 mm. A larger light sheet of around 40 mm height was generated by a spherical and cylindrical lens of $f = 500$ mm and $f = -10$ mm, respectively, for the main reactive experiments and for the non-reactive experiments. An important property of the laser sheet is the minimum beam waist at the focus point. Assuming a Gaussian intensity distribution, the thickness $2\omega_0$ was estimated from [35]:

$$2\omega_0 = \frac{2\lambda_l f}{\pi\omega_l} \quad (4.2)$$

where λ and ω are the wavelength and light sheet thickness before focusing, respectively, and the subscript l denotes the laser properties. The variable f is the focal length of the lens given as 500 mm. Having an excitation wavelength around 282 nm and an initial laser beam diameter of around 1 mm yielded in a beam waist of around 0.09 mm.

Lenses

The choice of the camera lens was determined by the wavelength of the emission intended to be captured. For OH PLIF and OH* emissions in the range of 300 - 320 nm Nikon UV-

Nikkor lenses with a focal length of 105 mm and a maximum aperture of $f/4.5$ (f-number) were used.

For cold tracer experiments, the Andor camera was instrumented with a 35 mm focal length and $f/1.4$ Zeiss lens allowing magnifications in the range of 0.070 mm/pixel.

Filters

The light of the laser, which was used to excite the target molecules, might be scattered by other molecules (Rayleigh scattering) or by large objects like surfaces (Mie scattering). Especially the latter reflected intensity may be some orders of magnitude higher than the actual emission of the target molecule. Thus, the intensity values may be erroneous and more importantly the sensor of the detector can be damaged due to overexposure. To separate the scattered intensity of the excitation source from the actual emission and avoid its capturing, two strategies exist, namely temporal and spectral separation. The first method requires the knowledge of the temporal laser intensity and the temporal emission development. Using a photo-diode and a photo-multiplier, the time-resolved laser intensity and the time-resolved emission of the molecule can be captured, respectively. For the temporal separation in PLIF experiments, the detector delay needs then to be set beyond the declined laser curve. However, this method is recommended for lasers with small FWHM compared to the temporal emission curve, otherwise a major fraction of the signal might be lost. Further, this configuration reduces the flexibility as for example variations in laser energy yield in different laser delay times and consequently the detector has to be readjusted.

The spectral separation was suitable for the current study. Here, a band-pass filter was mounted in front of the camera lens and allowed the transmission of the emission spectrum only. Fig. 4.4 shows the properties of the band-pass filter used for the OH emission detection measurements. On the left, the emission spectrum of OH is showed together with the

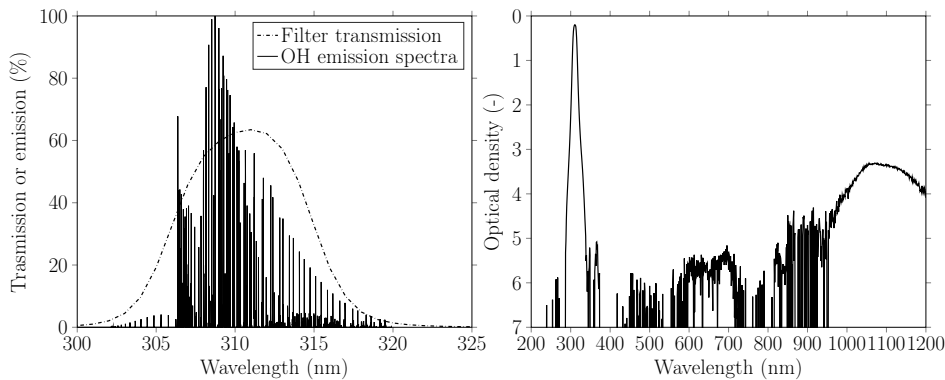


Figure 4.4: Properties of the band-pass filter for OH LIF. Left: filter transmission overlayed with emission spectra. Right: optical density of the band-pass filter.

transmission characteristics of the filter. On the right, the optical density (OD) curve is illustrated. This property is defined as:

$$\text{Transmission} = 10^{-OD} \cdot 100 \% \quad (4.3)$$

where the transmission value is taken in %. The OD is basically the exponent describing the fraction of transmitted signal. According to the filter specifications, the minimum OD

beyond 320 nm is 3, below 300 nm even 6. So in the latter spectrum range, $10^{-4}\%$ of the intensity was transmitted. The peak transmission was around 65 % at 310 nm.

The applied tracer for the cold flow analysis had an emission spectrum between 350 nm and 600 nm with its peak at around 420 nm. Thus, the camera was instrumented with an available long-pass filter with the transmission and OD properties provided in Fig. 4.5. In contrast to the reactive experiments, it was sufficient to block the scattered laser intensity, while the influence of the visible light spectrum was simply reduced by setting a short camera exposure time of 150 ns. In the reactive experiments on the other hand, the emission in the visible light spectrum of hot surfaces could not be suppressed only by setting a low exposure time as the intensity was sufficiently high and had a non-negligible effect which required the application of a band-pass filter.

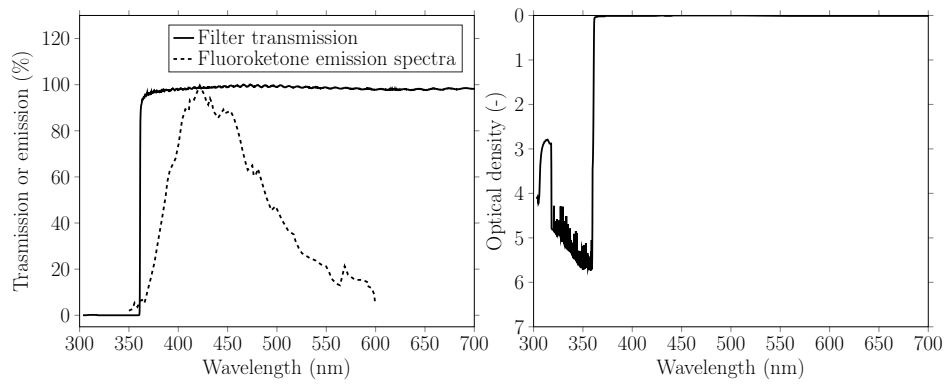


Figure 4.5: Properties of the band-pass filter for fluoroketone LIF. Left: filter transmission overlayed with emission spectra. Right: optical density of the band-pass filter.

4.2 OH LIF validation

The validation of the LIF method performed on a flat flame burner is presented in this chapter.

4.2.1 Flat flame conditions

Before applying the LIF method in the main experiment, a calibration and validation step was performed. Typically, a spatially homogeneous and steady state premixed flame is used to produce a sufficient concentration of OH for excitation. Suitable devices for the generation of calibration flames are Bunsen, Hencken and McKenna burners [47, 90, 115, 189]. A drawing of a McKenna burner is shown in Fig. 4.6. The burner consists of an inner volume for homogenization of the supplied gases. Fuel-oxidizer mixtures as well as separate fuel and oxidizer streams can be supplied. Then, the composition escapes through the upper sintered, porous matrix, which is water cooled to prevent thermal damage to the surface. The diameter of the inner core region is 60 mm. The burner has a second volume to connect an inert gas, which exits from an outer porous ring and shields the flame within the core region. The protective stream is of major importance for shielding fuel-rich flames from environment oxidizer. For the current investigation, a McKenna replica with same dimensions and properties of a McKenna burner was available at the institute. Gaseous CH₄ and

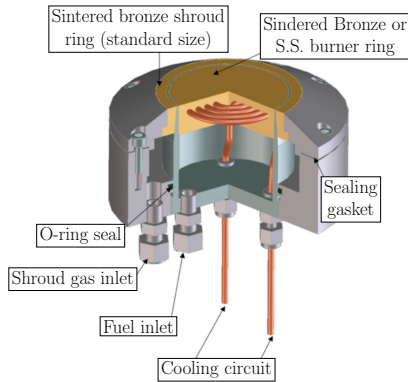


Figure 4.6: Sectional view of a McKenna burner [5], relabeled for this study.

air were mixed and supplied to the burner. A constant flow of 20 nl/min of N₂ protected the reaction zone. The streams were controlled by electronic mass flow controllers (MFC) from the manufacturer Bronkhorst. A constant cooling water temperature of 289.15 K was ensured by an external chiller. A summary of the cases investigated is given in Tab. 4.1. The aim was to test different stoichiometric conditions and generate different flame temperature levels. Due to heat losses to the cooled matrix and to the environment and due to relatively low fuel amounts, the obtained flame temperatures were below the adiabatic flame temperatures. Hence, numerical and experimental validation sources were employed. The

Table 4.1: Flat flame conditions, adiabatic temperature, Chemkin-Pro (CK) and TC results.

Case	CH ₄ (nl/min)	air (nl/min)	ϕ	T_{ad} (K)	T CK (K)	T TC (K)
1	1.10	15.00	0.70	1830	1694	1598 \pm 90
2	1.31	15.60	0.80	1990	1763	1669 \pm 100
3	1.73	20.63	0.80	1990	1826	1773 \pm 110
4	1.73	16.50	1.00	2220	1892	1857 \pm 126
5	1.73	13.70	1.20	2129	1841	1720 \pm 106
6	1.73	11.80	1.40	1972	1883	1740 \pm 109
7	3.42	32.40	1.00	2220	2050	2181 \pm 161

well-defined composition and geometric simplicity are key benefits of this flame configuration, which provide constant temperature and OH concentration in long-time experiments. Further, due to the rotation symmetry of the reaction zone, the condition at the centerline can be considered as 1D and the flame can be characterized theoretically. Knowing the boundary conditions (supplied mass flows, atmospheric pressure and 289.15 K flow temperatures), a 1D chemical kinetics calculation was performed in Chemkin-Pro [3] using the GRI-Mech 3.0 chemical mechanism [153]. The temperatures and the OH mole fractions along the height above the burner (HAB) are presented in Fig. 4.7. While the maximum of the OH mole fraction was located below a height of 2 mm, the maximum temperature was in most of the cases reached at heights larger than 2 mm. The temperature at HAB = 5 mm is added to Tab. 4.1 as T CK. Additionally, an uncoated TC type B with a spherical bead diameter of 1.1 mm (welded from two wires of 0.5 mm diameter) measured the flame

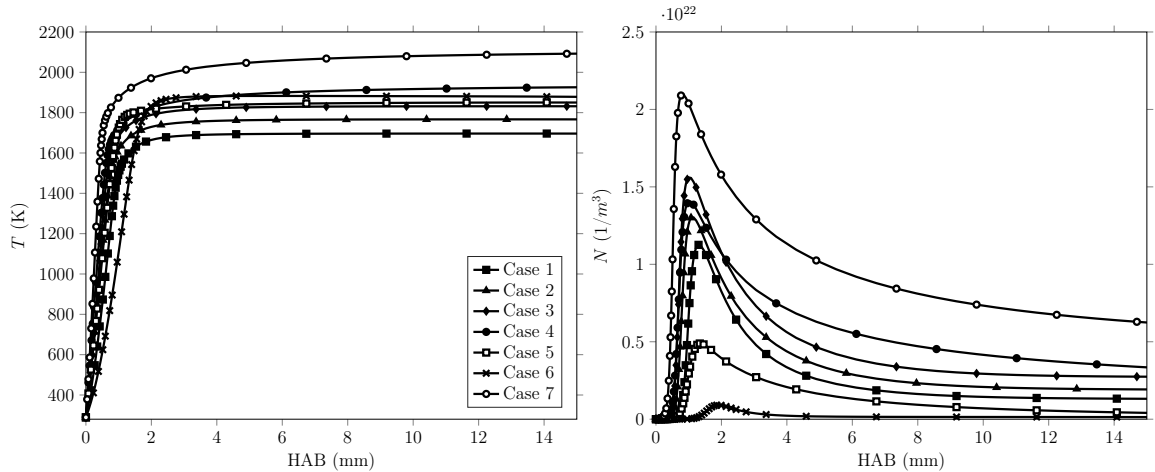


Figure 4.7: Simulated 1D chemical kinetics temperature and number density distribution along the height above the burner (HAB).

temperature at a HAB of 5 mm. As the TC was subject to radiation and convection heat transfer to the environment, the measured data was corrected using an iterative process in Python/Cantera [2]. The material data of the combustion products was based on the GRI-Mech 3.0. Cantera is an open-source, chemical kinetics tool similar to Chemkin-Pro. For the relevant equations and Nusselt correlation for the correction, the reader is referred to appendix G.1. The corrected TC data are found in Tab. 4.1 as T_{TC} . To account for systematic errors originating from TC bead diameter measurement and emissivity errors, a diameter variation of $\pm 20\%$ and an emissivity variation of $\pm 20\%$ were considered. The uncertainties yielded in an error of around 7 %. Except for case 7, the TC underestimates the temperature compared to the Chemkin simulations with a maximum deviation of around 8 %. The deviations were expected to result from the radiation correction and choice of Nusselt correlation. Interestingly, the temperature decreases from case 5 to case 6 as ϕ was lowered, while the Chemkin simulation and the TC measurement show a rise. A closer look to Fig. 4.7 reveals that the reaction zone of case 6 shifts further away from the surface compared to case 5 yielding in a lower heat loss and higher combustion temperature.

4.2.2 Flat flame optical setup

The optical setup for LIF validation is presented in Fig. 4.8 on the left. The laser beam was redirected to the height of the flat flame burner by special UV coated mirrors. For fluorescence scaling purposes a small fraction (around 8 %) was sent to an energy sensor using a fused silica plate. The circular UV laser beam was then converted into a light sheet with an effective height of around 13 mm using the optics discussed in section 4.1. A fraction of the light sheet was removed before and after crossing the flat flame and excited a diluted Rhodamine 6G ethanol solution for laser intensity attenuation determination purposes. An ICCD camera (PI MAX2) equipped with an UV lens and a band-pass filter was positioned perpendicularly to the light sheet to collect the emission from excited OH. A second ICCD camera (Andor) collected the emission from the dye solution.

The system was operated at 10 Hz and the images were collected in single-image mode. An on-chip accumulation was not applied. To increase the SNR and enable a frame rate

of 10 Hz, a 2×2 hardware pixel binning was performed. A magnification of around $250 \mu\text{m}/\text{pixel}$ was realized. The energy sensor and the cameras were connected to a computer. Energy data were saved as text files, while the 16 bit image files were saved as multi-page tagged image files (TIF).

4.2.3 Hardware synchronization

As the time scales in OH LIF are in the nanosecond range, a correct temporal synchronization of the hardware components was of major importance. Fig. 4.8 on the right describes the time synchronization of the system for the validation experiments as well as for the main experiment later. Generally, an experiment was performed in scan-mode, hence the

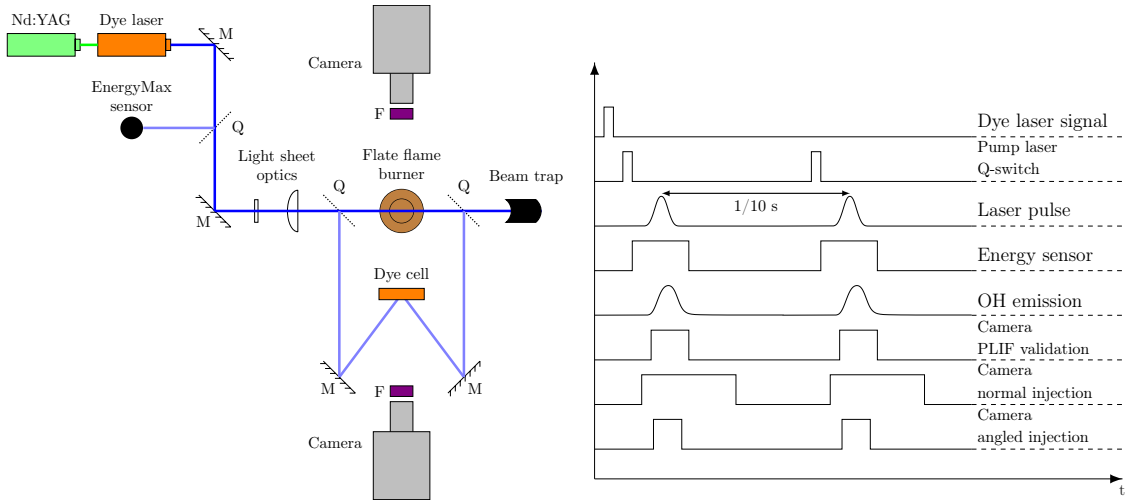


Figure 4.8: Left: flat flame calibration setup. Shortcuts: F is filter, M is mirror, Q is fused silica. Right: synchronization scheme for OH measurement.

triggering event originates from the dye laser. The pump laser was switched to external mode and awaited the trigger signal. As soon as the dye laser was launched, a measurement sequence at 10 Hz was started. Once a maximum population inversion was reached in the pump laser medium, the Q-switch changed and a pulse was released by stimulated emission shortly after. Additionally, a TTL-pulse was released by the Q-switch connection of the laser, which was connected to the energy sensor and to the cameras. The energy sensor was triggered without delay and recorded the laser signal energy for a sufficient time. To minimize the collection of OH* emission and background noise, an exposure time of 40 ns was chosen for the validation experiments. The injection experiments were conducted at 100 ns and 30 ns exposure times.

The exact delay period of the camera can be found by different approaches. A simple technical method is the synchronization of the camera to a photo-diode, which detects the released laser pulse. In this work, the delay time was found using a method based on the fluorescence detection without the requirement of additional devices. Here, a constant flame was excited and the fluorescence was collected with a sufficiently high exposure time, e.g. 400 ns, while a 0 ns the delay to the Q-switch signal was set. Then, the exposure time was gradually reduced until no further fluorescence signal was detected. This exposure time corresponded to the initial delay period. Depending on the intended exposure time (30 ns,

40 ns, 100 ns), the delay time was then modified to obtain the maximum time integrated signal.

4.2.4 Line selection

An important step before carrying out LIF measurements is the selection of suitable rotational lines for excitation and ratio forming to convert it into temperature. Two major rules have been proposed for the selection of line pairs by Seitzman et al. [175]. First, transitions isolated from nearby lines and second, transitions with N'' between 5 and 12 should be selected. As a laser has a non-zero spectral width (FWHM), excitation of nearby transitions may occur and the emission differs from calculated intensities. Hence, lines close to each other pose the threat of undefined excitation with high systematic errors. In [47, 115] lines with different distances were investigated and errors larger than 300 % were reported. Lines at the upper limit of $N'' = 5 - 12$ still provide good signal levels for the range of 1000 K - 3000 K, while increasing the lower limit leads to similar rotational numbers N' of the two lines and reduces the two-line fluorescence ratio dependency on the quantum efficiency.

A more systematic selection was carried out based on the temperature sensitivity. The temperature sensitivity on the fluorescence ratio can be determined by differentiating Eq. (3.18) and dividing by the fluorescence relation to obtain:

$$\left| \frac{dT}{T} \right| = \frac{kT}{|E_2 - E_1|} \left| \frac{dI_{ratio}}{I_{ratio}} \right| \quad (4.4)$$

This equation describes the sensitivity of temperature fluctuations on fluorescence fluctuations. Hence, the factor $|E_2 - E_1|/k = \Delta\varepsilon_{12}/k$ is referred to as temperature or slope sensitivity. Large energy gaps $\Delta\varepsilon_{12}$ lead to high sensitivity. Yet, a large ground-state energy, which is required for one line, results in a low population fraction and consequentially to a poor SNR and high uncertainties. On the other hand, large population fractions result in $\Delta\varepsilon_{12} \sim 0$ and that yields high SNR, but poor temperature sensitivities. According to [31, 175], a trade-off between sensitivity and uncertainty is aimed at by selecting two transitions with $\Delta\varepsilon_{12}/k \sim T_{max}$, where T_{max} is the maximum expected temperature in the experiment. It is recommended to choose a strong, less temperature-sensitive transition and a second, temperature sensitive transition. However, this criterion is not sufficient for a transition pair selection. A detailed analysis by Devillers et al. [47] showed higher precision of the measurement at energy gaps between 3000 K and 5000 K. Hence, the recommended upper and/or the lower limit of N'' had to be extended. After the determination of a specific N'' , one has to decide between the rotational branches P, Q and R. Depending on the application and expected level of OH concentration, R- and P-branches can be a better choice than the Q-branch. In case of high pulse energy and a high efficiency of the detection system, satellite branches such as P_{12} or R_{21} may be sufficient with regard to intensity level. Fig. 4.9 shows the relative intensity simulated for the individual branches at $T = 2000$ K. The magnitude of the intensity depends on the Boltzmann fraction and the Einstein coefficient for absorption B_{12} according to Eq. (3.12). B_{12} is proportional to the line strength factor or so-called Hönl-London factor $S_{J'J''}$:

$$B_{12} \propto \frac{S_{J'J''}}{2J'' + 1} \quad (4.5)$$

The factors specify the distribution of the total intensity among the different rotational branches. Analytical expressions for the calculation of the Hönl-London factors are reported in [96], while calculated values were accessed in LIFbase [129]. As seen in Fig. B.3,

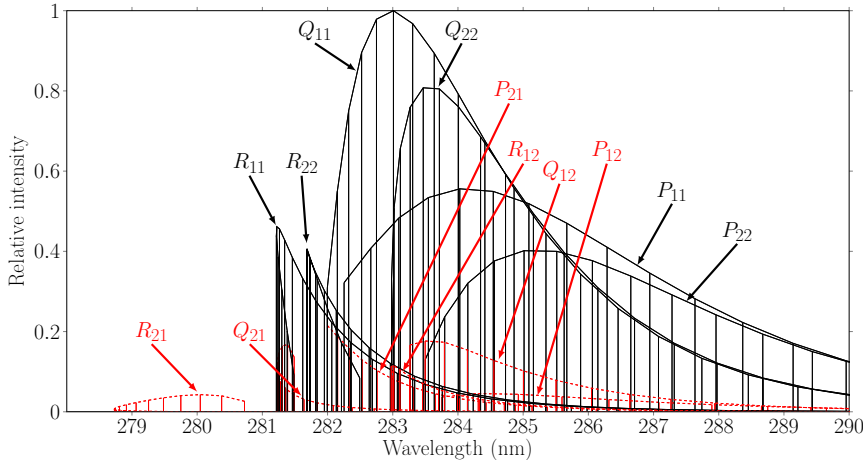


Figure 4.9: Simulated intensity for different rotational branches at $T = 2000$ K.

the line strengths of the individual branches correspond to the fluorescence intensities in Fig. 4.9. The Boltzmann distributions, calculated according to Eq. (B.24), and their first derivatives with respect to temperature vs. the rotational quantum number J'' are plotted on the first and second graph in Fig. 4.10. In the range of relevant flame temperatures for

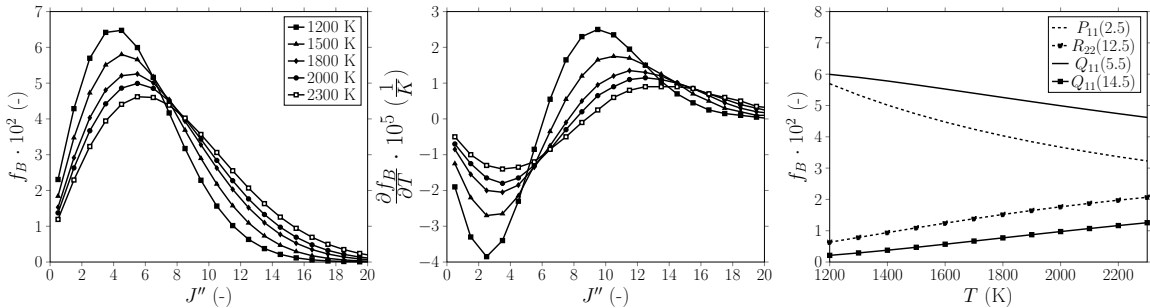


Figure 4.10: Left: Boltzmann distribution vs. J'' for different temperatures. Center: first derivative of Boltzmann distribution. Right: Boltzmann distribution vs. temperature for different rotational quantum numbers.

the current work, the maximum of $f_B(T)$ is around $J'' = 4.5 - 7.5$. With increasing temperature, the population of rotational quantum numbers $J'' > 8.5$ increases steadily, while the maximum temperature sensitivity shifts to J'' around 13.5. Based on the considered population distribution and the line strength factors, the Q -branch transitions yield in highest intensities, while $J'' \approx 13.5$ provides highest sensitivity.

Considering the specified criteria, different line pairs and line combinations may be suitable and preferred for PLIF thermometry. Giezendanner et al. [72] applied $R_{22}(13)/P_{11}(2)$ for the combustion in a pulsing gas turbine model and corrected the intensity for laser absorption. Devillers et al. [47] investigated a number of pairs and chose $R_{11}(12)/P_{11}(2)$ for high pressure internal combustion due to similar absorption characteristics of the transitions. Kostka et al. [115] studied different line pairs for an atmospheric Hencken burner and the transitions $Q_{11}(14)/Q_{11}(5)$ showed the best accuracy, whereas the pair $R_{22}(13)/P_{11}(2)$ underestimated the temperatures. There, constant premixed H₂/air flames of a wide range of

equivalence ratios were investigated by means of two-line and line-scanning techniques with quenching correction. The authors obtained quenching cross-sections of different collision partners of OH from [189]. Accuracies of 3.6 % and 4.1 % for the line pairs $Q_{11}(14)/Q_{11}(5)$ and $R_{22}(14)/P_{11}(2)$ were reported, respectively. While the results were impressive, the method required knowledge of the composition, which was unknown and determined from chemical kinetics calculation based on the operated condition (ϕ). Further, flames near adiabatic conditions were analyzed. Later, Richardson et al. [167] used the same pair ($Q_{11}(14)/Q_{11}(5)$) for the two-line spectroscopy of near-wall inverse diffusion flames without quenching consideration.

For the current study, the transition pairs $R_{22}(13)/P_{11}(2)$ (referred to as LP1) and $Q_{11}(14)/Q_{11}(5)$ (referred to as LP2) were selected and applied to the presented flat flame burner flames. The objective was to find the superior line pair for the main experiment. The Hönl-London factors of the Q_{11} transitions are more than twice as large as those of the P_{11} and R_{22} branches. The Boltzmann distributions for the temperature range of 1200 - 2300 K are shown on the third graph of Fig. 4.10. The population distribution of the *base line* $Q_{11}(5.5)$ reduced by $\approx 23\%$, while the population distribution of the *base line* $P_{11}(2.5)$ decreases by $\approx 43\%$ from $T = 1200$ K to 2300 K. In the same temperature range, f_B of $Q_{11}(14.5)$ increased by $\approx 490\%$ and was higher than the increase of f_B for $R_{22}(12.5)$, which was $\approx 227\%$. The properties of the individual transitions are summarized in Tab. 4.2. The energy gaps of LP1 and LP2 calculated from the ground state energies were 4694 K and 4705 K [38, 48], respectively, which yielded in similar temperature sensitivities. Each transition had sufficient spectral distance to neighboring transitions. The least distance was 0.52 cm^{-1} from the transition $R_{21}(23.5)$ to $R_{22}(12.5)$. However, the instrumental FWHM of the applied laser was around 0.33 cm^{-1} , see section 3.1.2, and the risk of exciting neighboring transitions was minor.

Table 4.2: Selected rotational lines for two-line PLIF thermometry investigation.

Transition	Position (nm)	B_{12} ($10^{17} \frac{\text{m}^3}{\text{J s}^2}$)	E_i (10^{-20} J)	$\frac{f_B(2300 \text{ K})}{f_B(1200 \text{ K})}$	Left neighbor	Spectral separation (cm^{-1})	Right neighbor	Spectral separation (cm^{-1})
$P_{11}(2.5)$	282.663	1.657	0.166	0.57	$R_{21}(23.5)$	2.54	$R_{11}(14.5)$	3.17
$R_{22}(12.5)$	282.639	1.571	6.65	3.27	$P_{21}(4.5)$	13.61	$R_{21}(23.5)$	0.52
$Q_{11}(5.5)$	282.750	2.772	1.08	0.77	$Q_{21}(14.5)$	4.38	$P_{21}(5.5)$	1.18
$Q_{11}(14.5)$	286.456	3.067	7.58	5.89	$R_{11}(21.5)$	2.41	$Q_{21}(21.5)$	2.30

Taking the ground-state energies E_i and the Einstein coefficients B_{12} from Tab. 4.2 and the line shape properties from 3.1.2, a so-called calibration curve was calculated using Eq. (3.18) to transform intensity ratios into temperatures. Fig. 4.11 shows the calibration curves for LP1 and LP2 with added polynomial functions (95 % confidence interval).

4.2.5 Time resolved measurement

The effective lifetime τ of the excited state is an important parameter for LIF measurements to synchronize the detection system in terms of delay and exposure time accordingly. Short exposure times may lead to loss of fluorescence signal, while high values lead to high background noise detection. The fluorescence lifetime depends on different aspects, such as temperature and (especially) pressure, because it affects the quenching rate and reduces the energy radiation. The natural lifetime τ_0 can be calculated from the inverse of the emission

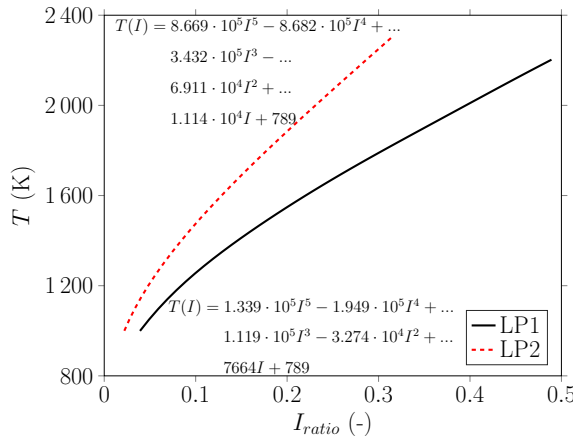


Figure 4.11: Calibration curves for LP1 and LP2. Polynomial functions included.

coefficient A , while the effective lifetime is obtained from the inverse of $A+Q$, as introduced in Eq. (3.16). Generally, a short pulsed laser is necessary to determine the time constant at atmospheric pressure experimentally, since the fluorescence lifetime reduces drastically and the exponential decay only occurs after the laser excitation has ended. Hence, the objective of the following measurement was solely the determination of the fluorescence period. Therefore, the flat flame burner was operated at a constant condition and the laser energy was set to a specific, moderate level to remain in the linear fluorescence regime. The exposure time of the camera was set to 5 ns and the delay was shifted successively 5 ns with respect to the laser pulse, while at each delay setting 100 images for time-averaging were captured. The temporal distribution of the fluorescence signal for a spatial averaged area of 10 x 10 pixels is shown in Fig. 4.12 on the left. The small number of measurement intervals led to a discontinuous curve. The second way to determine the temporal fluorescence decay is using a photo-multiplier, as seen on the right graph of Fig. 4.12. The device was equipped

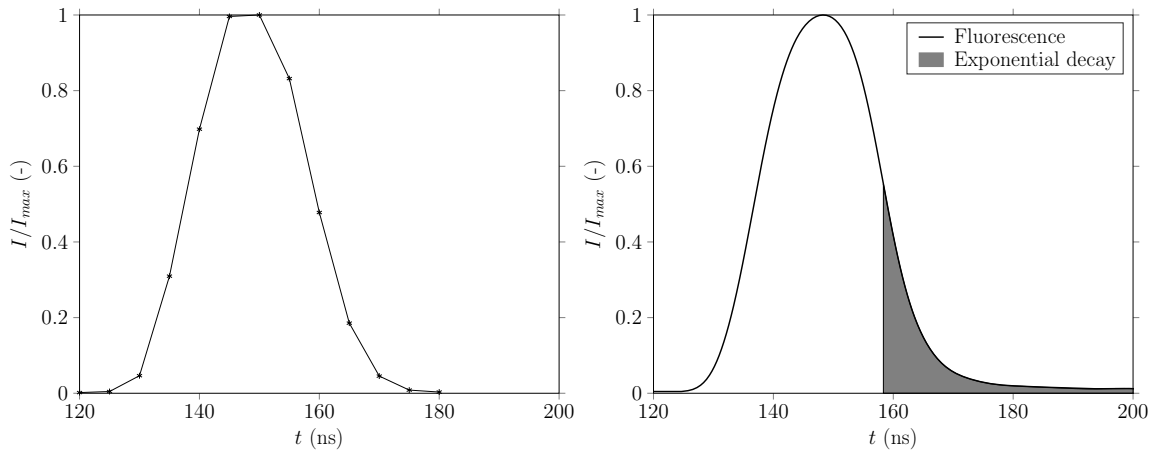


Figure 4.12: Time resolved signals. Left: LIF method. Right: multiplier method. The gate delay was around 120 ns.

with the same band-pass filter as the camera for the fluorescence detection and was positioned near the excited reaction region of the flat flame burner. Note that this method is a

non-spatial resolved approach and does not account for temperature variations. However, since the flame was almost homogeneous within the excited laser sheet of 13 mm height, the method could be applied to determine the time-resolved emission. The results of both methods were in good agreement, comparing the two curves.

The fluorescence period presented in Fig. 4.12 justified the selected exposure times shown in Fig. 4.2.3.

4.2.6 Fluorescence linearity

According to Eq. (3.12), the fluorescence was required to be in linear relation to the pulse energy of the laser. To ensure the linearity and avoid saturation, the OH of a constant flat flame was excited with increasing laser pulse energy. The experiment was conducted using the same sheet optics presented in 4.2.2. Fig. 4.13 shows the average fluorescence signal of a region of 20 x 20 pixels plotted against the measured pulse energy. Two different rota-

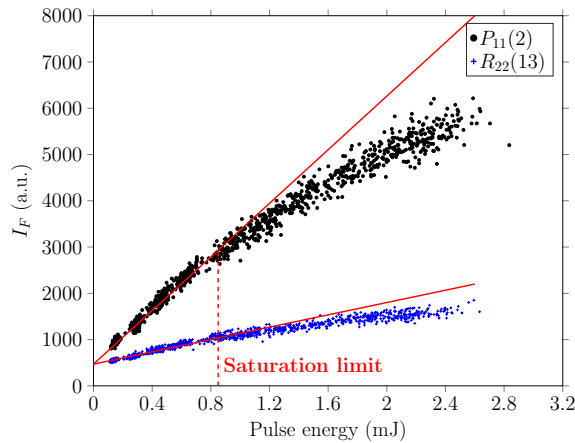


Figure 4.13: Fluorescence signal of excited flat flame OH over the pulse energy.

tional lines were excited therefore. Up to a pulse energy of around 0.8 mJ the fluorescence increases linearly according to the straight interpolation line. Thereafter, the transition to the saturation regime was observed. Hence, maximum pulse energies up to 0.8 mJ were set for the following experiments. It is generally advantageous to take pulse energies at the upper limit of the linearity to achieve a maximum SNR and image quality and lowest SNR error.

4.2.7 LIF thermometry

In the following subsections the LIF thermometry process and results are presented.

4.2.7.1 Post-processing routine

A number of post-processing steps recommended in literature [47, 71, 115] were applied to the raw images. For each rotational line, 100 images of the fluorescence signal and corresponding light sheets were recorded for time-averaging purposes and to increase the SNR alongside the laser energy data. The images were saved as multi-page TIF files, while the energy data were stored in text form.

Fig. 4.14 illustrated the procedure performed to obtain the final temperature distribution. The first step of the post-process was to eliminate the laser energy influence and to account for the shot-to-shot energy fluctuation. Thus, each fluorescence image was scaled by its accompanied energy value according to Eq. (3.12). As each single image was superimposed by an individual background noise of the detector, an average intensity value of 20×20 pixels from a region unaffected by the flame and by the laser was subtracted from the entire image. This step is referred to as noise removal. Some authors apply a background removal instead of noise removal, where an image without the flame is recorded and subtracted from the flame images and some authors remove a chemiluminescence image recorded with the same exposure time but without laser excitation. However, the noise removal proved to be suitable and sufficient for the current case. A background removal is practical for elimination of scattering. However, the light source passed through a reaction zone without particle, and reflections on surfaces were avoided. Further, the mounted band-pass filter blocked a major part of the laser intensity. Due to the short exposure time of 40 ns, no chemiluminescence intensity could be detected and the removal of this effect was redundant. To increase the SNR, a 3×3 (kernel size) Gaussian low-pass filter was applied to the images. The improvement of the SNR is seen in Fig. 4.2. Then, the 100 fluorescence images of each rotational line were time-averaged. To account for the spatial laser energy distribution, an average light sheet profile from the 100 light sheet images was determined using the intensity of around 10 pixels in width. The averaged fluorescence images were then scaled by the light sheet. In the same way, the laser intensity distribution after passing through the flame was determined. By means of both intensity distributions, the absorption correction of the laser intensity was performed according to the theory discussed in 3.1.5. Before determining the two-line intensity ratio, a lower cut-off limit of around 10 % of the maximum intensity was applied to the data. A similar procedure is found in literature [167].

This image post-processing routine was applied to the images of each rotational excited line. For the temperature calculation, the average images of the corresponding lines reported in Tab. 4.2 were divided pixel-by-pixel to obtain the fluorescence ratio I_{ratio} according to Eq. (3.18) and convert it into temperature using the calibration curves in Fig. 4.11.

4.2.7.2 Error analysis

LIF data are subject to different error sources, divided into two categories: systematic and random. Systematic errors affect the data consistently and cannot be reduced by averaging a number the measurement results. On the other hand, random/statistical errors are unpredictable and can be reduced by measurement repetitions and averaging of the same steady state incident. Here, the temporal average of n data reduces the error by $1/\sqrt{n}$ as demonstrated in the appendix G.2.

Generally, error sources affect the intensity of the corresponding excited line. Considering small, random and independent uncertainties ∂x_i , the total standard deviation σ_{I_F} of the fluorescence intensity I_F is according to the propagation of uncertainties [191]:

$$\sigma_{I_F} = \sqrt{\sum_i \left(\frac{\partial I_F}{\partial x_i} \sigma_{x_i} \right)^2} \quad (4.6)$$

where $\partial I_F / \partial x_i$ is the partial derivative and σ_{x_i} is the standard deviation of an particular error source. Further, the two-line LIF temperature is the result of the quotient of two

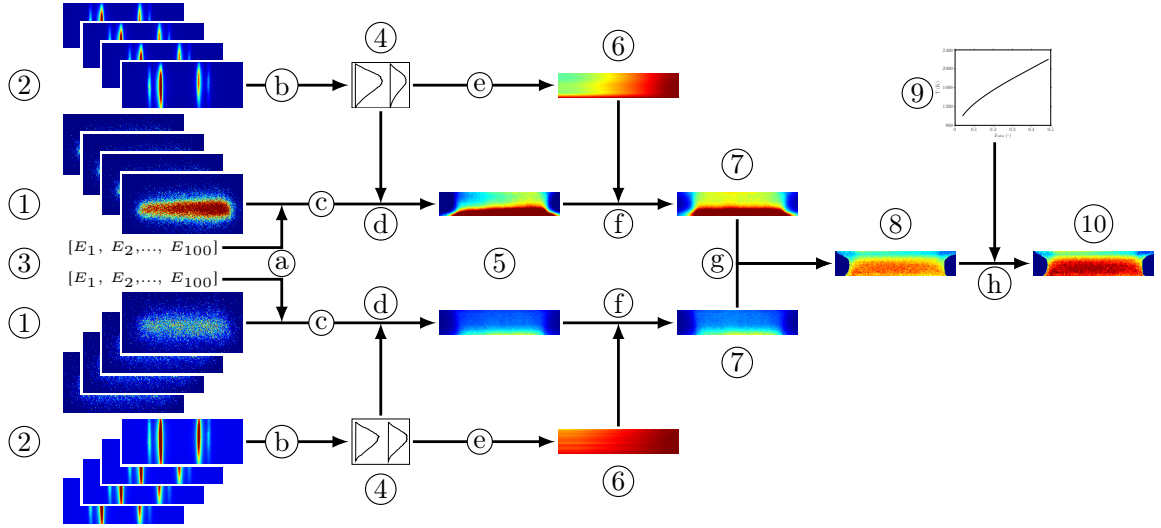


Figure 4.14: Flowchart of LIF post-processing. 1: raw intensity data set. 2: raw light sheet data set. 3: pulse energy vector. 4: extracted initial and attenuated light sheets. 5: averaged, light sheet corrected intensity distributions. 6: local laser intensity distributions. 7: attenuation corrected fluorescence intensities. 8: intensity ratio image. 9: calibration curve. 10: final temperature distribution. a: energy scaling. b: light sheet generation. c: geometrical scaling, noise removal, averaging. d: light sheet correction. e: local laser intensity calculation. f: absorption correction. g: calculation of intensity ratio. h: intensity ratio into temperature conversion.

intensities. Thus, the error increases by the factor $\sqrt{2}$ assuming equal errors of both lines 1 and 2 or the sum in quadrature of the two sets is applied. The standard deviation of the intensity ratio I_{Ratio} is then:

$$\sigma_{I_{Ratio}} = \sqrt{\sigma_{I_{F1}}^2 + \sigma_{I_{F2}}^2} = dI_{Ratio} \quad (4.7)$$

Thereafter, the obtained intensity variation was converted into temperature by means of the sensitivity relation Eq. (4.4). It is evident, that a large energy gap $\Delta\varepsilon_{12}$ yields in lower temperature variations and consequently in smaller errors. Following uncertainties reported in [36, 47, 58, 115] were considered for the LIF validation:

SNR error (random): Image quality is specified among others by the SNR. In the field of image processing and spectroscopy, it is calculated as the ratio of the signal to the standard deviation of the noise for a small number of pixels. The reciprocal of SNR was then used to calculate the temperature uncertainty.

Averaging error (random): The averaging error refers to the standard deviation intensity of the 100 images. It covers aspects like flame fluctuations and pixel intensity variations. Another issue arises from the averaging of fluctuating single intensity data and converting the result into temperature. A theoretical approach was used to demonstrate this relation. A theoretical temperature distribution was generated between 1200 - 2300 K from 0 - 20, which is shown in black color in Fig. 4.15 (overlapped

by the blue curve). This temperature distribution was superimposed by a zero-mean stochastic noise with a standard deviation of 1000 K. Then, $n = 300$ temperature distributions were calculated. Averaging the n number of profiles yielded in the blue curve, which represents a direct temperature measurement technique with n number of data. In another step, the 300 noisy temperature distributions were converted into intensity ratios using the calibration curve for $R_{22}(13)/P_{11}(2)$ in Fig. 4.11. The intensity ratio was related to the single intensity by Eq. (3.18). Setting $I_{F2} = \text{const.}$, one obtained 300 noisy intensities I_{F1} . Averaging the 300 intensities and reconverting the average intensity into temperature resulted in the red curve, which represents the average temperature determination from the two-line LIF thermometry. As the error curve (black dotted curve) shows, the deviation was around 2 % for temperatures between 1600 - 2300 K, while below 1200 K the error rose up to 6 %. The reason for the different error magnitudes was found in the form of the calibration curve, which was of linear nature in the range of 1600 - 2300 K. The non-linear regime below 1600 K increased the averaging error.

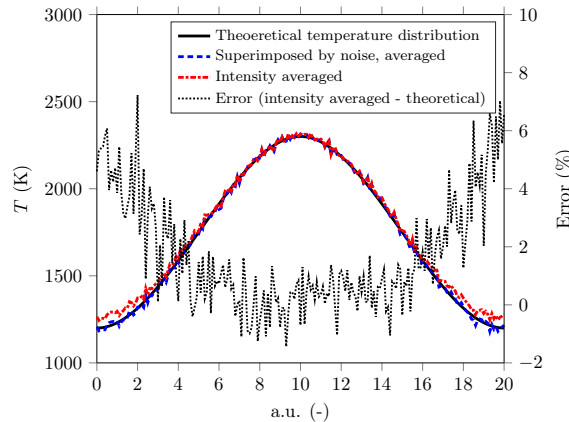


Figure 4.15: Theoretical temperature distribution (black). Superimposed temperature distribution by noise and averaged (blue). Noisy temperature distributions converted into intensity, averaged and reconverted into temperature (red). Black dotted curve is the error between red and black curves.

Laser sheet error (random): The 100 images were scaled by an averaged light sheet profile. However, the light sheet was subject to geometrical fluctuations and was a potential source of error. Hence, its standard deviation was determined and converted into temperature.

Laser pulse error (systematic): Each image was scaled by the corresponding measured energy. The accuracy of the energy sensor was specified as $\pm 2\%$ by the manufacturer.

Laser intensity attenuation (systematic): The absorption of the laser intensity by the OH molecule results in systematic errors in the fluorescence intensity in the beam direction. The error is passed on to the thermo LIF calculation in case of different attenuation of the two rotational lines. The impact on the temperature is determined from [47]:

$$\frac{1}{T} - \frac{1}{T + |T_{\text{error}}|} = \frac{1}{\Delta\varepsilon} |\alpha_1(x) - \alpha_2(x)|x \quad (4.8)$$

where x is the distance in the beam direction and α (1/m) is the integral absorption coefficient for the rotational lines. Generally, α depends on local properties as described by Eq. (3.20) and it is determined iteratively as discussed in section 3.1.5. Intensity profiles at a constant height were extracted from measurements, as the initial $I_F(x)$ in Fig. 3.5, and the temperature and number density of OH N_{OH} were obtained from chemical equilibrium simulation (Fig. 4.9) assuming constant distribution of OH molecules. Since the flame of the calibration burner had a diameter of around 60 mm corresponding to the diameter of the burner matrix, a distance of $x = 60$ mm for the attenuation was considered.

Further systematic errors arise from laser wavelength calibration and from uncertainties of the molecular coefficients to calculate the ground-state energies, which yield erroneous calibration curves (spectroscopic uncertainty). However, during each measurement a short excitation scan was performed to minimize the risk of dye laser calibration errors. Taking into account the uncertainty of the LIF would require an additional, independent measurement technique. Thus, the accuracy of the molecular data was taken for granted from literature.

4.2.7.3 Thermo LIF results

Fig. 4.16 shows the final two-line temperature fields for the cases named in Tab. 4.1. On the

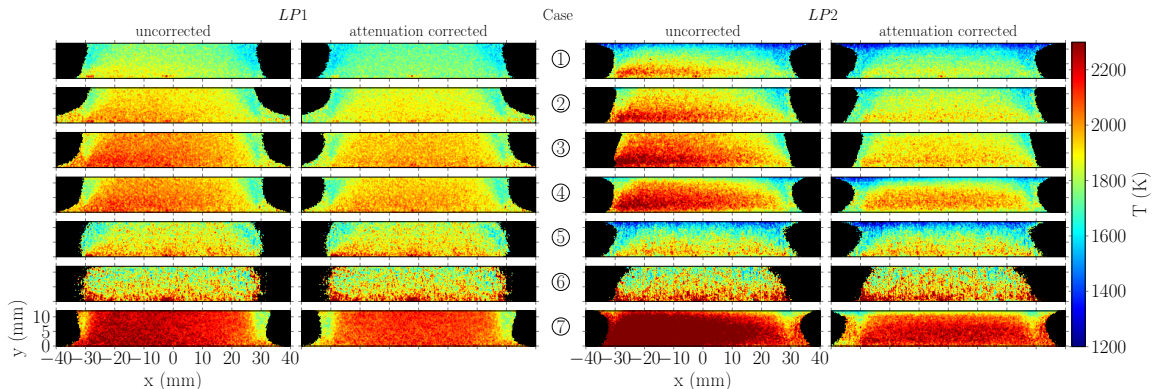


Figure 4.16: Thermo-LIF results. The two columns on the left correspond to the temperature fields of LP1, the two columns on the right are the results of LP2. On each second column, the absorption corrected temperature fields are shown. The beam direction was from right to left. Considered cases are arranged from top to bottom.

left side of the discussed figure are the raw and the attenuation corrected results for LP1, while on the right side are the results for LP2 sorted equally. The beam direction was from right to left throughout the cases. There were some significant characteristics among the cases and differences between the considered line pairs observed. As expected, the temperature increases from case 1 to case 4 since ϕ approached 1 and since additionally the fuel supply increased after case 2. Further, a homogeneous spatial temperature distribution is found. Changing to fuel-rich conditions, an apparent temperature drop is seen. However, the spatial temperature distribution seems *noisy* and is overlaid with inhomogeneous fluctuations. This is more pronounced for the condition with $\phi = 1.4$. The level of fluctuation appears to be lowest for case 7 (highest fuel amount, $\phi = 1.0$) which approaches adiabatic

flame temperatures. Another remarkable feature is the effect of the light attenuation. For both line pairs, a non-physical temperature increase in the beam direction is observed for the non-corrected temperature fields, as a stronger laser intensity absorption occurs for the lines $P_{11}(2)$ and $Q_{11}(5)$ compared to the respective second rotational lines. Thus, the intensity ratio increases which fakes a rise of temperature. The attenuation correction was addressed by the method discussed earlier and good results are achieved. Considering the results of each line pair separately, the absorption depends clearly on the number density of OH, because the attenuation is high for cases with $\phi \leq 1$, while the remaining cases hardly show any absorption effect. Theoretical number densities were presented in Fig. 4.7. Interestingly, the attenuation of case 3 (both line pairs) with $\phi = 0.8$ was slightly higher than that of case 4 with $\phi = 1.0$. A closer look to the corresponding number densities in Fig. 4.7 shows that in case 3 indeed a slightly greater peak number density was produced than in case 4. Comparing the two line pairs with respect to attenuation, it is obvious that LP2 is affected more significantly than LP1. The difference is particularly striking for case 7, which was subject to high intensity attenuation as the temperature even exceeds the adiabatic flame temperature (around 2220 K).

To analyze the attenuation for the current line pairs and cases in detail, a theoretical calculation was performed. Using the respective calculated number densities, rotational line specific properties and normalized intensity profiles from the cases 1 - 7, values around 0.01 - 0.03 for the constant C_1 for Eq. (3.20) were determined. In a second step, integral absorption coefficients with temperature and number density as parameters representative for the current cases were calculated and intensity attenuation for a distance of 60 mm were determined and as well as converted into temperatures by Eq. (4.8). Fig. 4.17 illustrates the results. Note that individual colorbars are used. $Q_{11}(5)$ exhibited highest attenuation, which

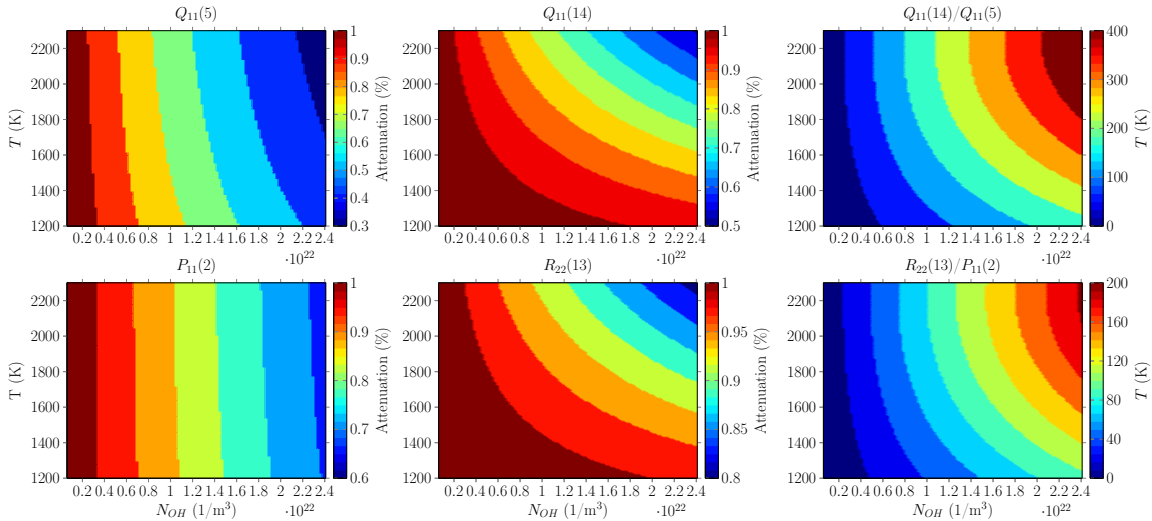


Figure 4.17: Calculated intensity attenuation and effect on temperature along a flame distance of 60 mm assuming homogeneous OH number density. Top: $Q_{11}(5)$ and $Q_{11}(14)$. Bottom: $P_{11}(2)$ and $R_{22}(13)$. First two columns contain intensity attenuation, the third column is the temperature error.

is around twice the magnitude of the attenuation of $Q_{11}(14)$. Obviously, the attenuation of the $Q_{11}(5)$ intensity depends preliminary on the number density and slightly on the

temperature. The intensity attenuation of $Q_{11}(14)$ on the other hand depends stronger on the temperature parameter. The large attenuation difference of the two lines produces temperature errors up to 400 K. The rotational lines of LP1 are generally subject to lower intensity attenuation and the difference is smaller than for LP2. This is attributed to the fact, that $\alpha \propto f_B B_{12}$, see Eq. (3.20) and Tab. 4.2. Consequently, a lower resultant temperature bias was obtained, which is around 200 K for the considered temperature and number density range.

For a detailed investigation, the average temperature of a 5 x 5 pixel region 5 mm above the burner surface at the center of the flame was extracted. The region is equivalent to 1.25 x 1.25 mm² and the spatial temperature standard deviation was below 5 %. The data was corrected for laser attenuation. The results are summarized in Tab. 4.3 and Tab. 4.4. Note, the statistical errors correspond to temperature calculation of single images and reduce by the factor \sqrt{n} , where n is the number of images (here 100). The maximum deviation of the PLIF temperature for both line pairs from the Chemkin temperature was around 7 %. Highest SNR is achieved for the transition $Q_{11}(5)$, while the lowest is for $Q_{11}(14)$. Moderate SNR is obtained for the transitions of LP1. Due to the low SNR of $Q_{11}(14)$, the resulting SNR error of LP2 is in general larger than the error of LP1. The poor SNR of $Q_{11}(14)$ is due to the spectral efficiency of the dye laser, as the pulse energy dropped at wavelengths around 286 nm (see Fig. 4.1). The remaining random errors of LP2 exceed likewise those of LP1. A drastic increase in random errors is found for fuel-rich compositions, which was attributed to the low SNR and mainly to the temporal standard deviation. The laser pulse error is basically negligible. As discussed earlier, LP2 is affected considerably more by attenuation than LP1. These findings were in good agreement to the 2D temperature distribution in Fig. 4.16. According to [115], LP2 was superior to LP1 for $\phi = 0.4 - 1.4$ and

Table 4.3: LIF calibration results. Line pair 1 (LP1) stands for $R_{22}(13)/P_{11}(2)$ with $P_{11}(2)$ as transition No. 1 and $R_{22}(13)$ as transition No. 2. Line pair 2 (LP2) is $Q_{11}(14)/Q_{11}(5)$ with $Q_{11}(5)$ as transition No. 1 and $Q_{11}(14)$ as transition No. 2. Part 1.

Case (ϕ)	1 (0.70)		2 (0.80)		3 (0.80)		4 (1.00)	
T CK (K)	1694		1763		1826		1892	
T TC (K)	1598		1669		1773		1857	
Transition	LP1	LP2	LP1	LP2	LP1	LP2	LP1	LP2
T PLIF (K)	1708	1721	1810	1808	1897	1843	1911	1903
SNR No. 1	8.3	10.7	8.3	10.6	8.8	11.2	8.4	10.7
SNR No. 2	5.7	4.9	6.0	5.0	6.4	5.3	6.2	5.2
Statistic. error (K)	152	172	167	195	173	192	183	200
SNR (K)	132	142	144	154	148	151	156	164
Standard dev. (K)	65	76	73	97	76	95	79	90
Laser sheet (K)	41	62	45	70	50	70	53	70
Pulse error (K)	3	3	3	3	3	3	3	3
Attenuation No. 1 (%)	16	35	18	40	21	46	20	43
Attenuation No. 2 (%)	4	11	6	15	7	19	7	19
Attenuation error (K)	75	169	90	202	111	247	103	234

no indication of poor SNR at fuel-rich conditions was found in the study. Errors around 100 K were determined for LP1 (4.1 %) in the temperature range of 1700 - 2300 K, despite

Table 4.4: LIF calibration results. Line pair 1 (LP1) stands for $R_{22}(13)/P_{11}(2)$ with $P_{11}(2)$ as transition No. 1 and $R_{22}(13)$ as transition No. 2. Line pair 2 (LP2) is $Q_{11}(14)/Q_{11}(5)$ with $Q_{11}(5)$ as transition No. 1 and $Q_{11}(14)$ as transition No. 2. Part 2.

Case (ϕ)	5 (1.20)		6 (1.40)		7 (1.00)	
T CK (K)	1841		1883		2050	
T TC (K)	1720		1740		2181	
Transition	LP1	LP2	LP1	LP2	LP1	LP2
T PLIF (K)	1837	1773	1720	1843	1997	2130
SNR No. 1	5.4	6.6	4.8	5.3	8.6	11.1
SNR No. 2	4.6	4.4	4.3	4.2	6.7	5.8
Statistic. error (K)	280	283	415	485	186	231
SNR (K)	205	183	197	219	160	188
Standard dev. (K)	183	204	363	427	73	100
Laser sheet (K)	53	69	41	68	62	89
Pulse error (K)	4	4	4	4	3	4
Attenuation No. 1 (%)	-	-	-	-	28	58
Attenuation No. 2 (%)	-	-	-	-	13	33
Attenuation error (K)	-	-	-	-	158	349

quenching correction. However, the authors applied the two-line method to H₂/air flames near adiabatic conditions, while in the current case non-adiabatic CH₄/air flames were used. The chemical reaction of CH₄ in air is more complex and produces a substantially larger number of species compared to H₂/air combustion. Hydrocarbon/air flames may lead to major quenching effects and lower SNR. An attenuation analysis was not part of the investigation in [115]. Premixed CH₄/air flames of different composition were investigated in [47] and similar SNR and error magnitudes were reported for fuel-rich conditions up to $\phi = 1.3$. Discrepancies up to 75 K were found for flame temperatures between 2100 K and 2240 K. However, the author operated a Bunsen burner near adiabatic conditions and averaged a significant amount of LIF images to improve the data quality.

On the basis of the performed investigation and obtained statistical and attenuation errors, LP1 was considered to be better suited for the main experiment despite the greater accuracy of LP2 as reported in [115]. Furthermore, LP1 offered an additional benefit compared to LP2, which was related to the employed laser system. The short spectral separation of $P_{11}(2)$ and $R_{22}(13)$ required only small motions of the resonator and the frequency doubling unit. Thus, similar spatial beam intensity distributions and consequently light sheets were expected, which minimized errors as the LIF data are highly sensitive to spatial intensity variations. The different light sheets are pictured in Fig. G.3, which were recorded on a dye cell. The light sheet of $Q_{11}(14)$ was broadened compared to the other laser profiles. Due to these differences, minor laser sheet errors occurred in the 2D temperature distribution in Fig. 4.16. Especially case 1, 4 and 5 show an unusual temperature decline in the region near $y = 10$ mm. Further improvement of the measurement technique can be made by including quenching effects and/or considering a calibration constant [47, 115]. Operating the burner at higher fuel/air supply and recording a greater amount of images for time-averaging could reduce errors.

4.3 Cold tracer LIF

A similar procedure as in the case of OH LIF was conducted to calibrate the fluoroketone LIF. The calibration required an environment with constant, non-fluctuating fluoroketone vapor with sufficiently high concentration (for OH calibration a steady flat flame was used). Therefore, a dye cell made of fused silica with a cross-sectional area of $20 \times 20 \text{ mm}^2$ was partially filled with liquid state fluoroketone. At atmospheric pressure and room temperature of 294.15 K, saturated vapor formed above the fluid, which was then excited by the UV laser and fluoresced. An excitation wavelength of 283 nm was selected, which was a trade-off between molecular absorption cross section and dye laser efficiency, see Fig. 3.7 and Fig. 4.1. The utilized hardware was discussed in section 4.1. Fig. 4.18 shows exemplarily the fluorescence emission from excited fluoroketone vapor. As the laser sheet entered from the left and its intensity was subject to molecular absorption, the fluorescence decayed in the beam direction.

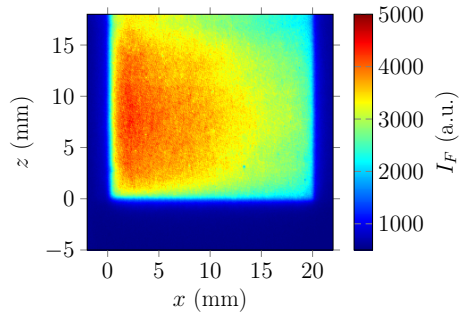


Figure 4.18: Tracer fluorescence in a dye cell. Laser enters from left. Liquid state $z < 0 \text{ mm}$.

The following calibration process covers the verification of the fluorescence linearity to excitation energy, determination of the time-resolved behavior and the molecular absorption characteristics.

4.3.1 Fluorescence linearity and time resolution

In order to determine the maximum laser energy and assure that the fluorescence shows a linear behavior to the selected energy according to Eq. (3.28), the vapor inside the cell was excited with increasing pulse energy. The resulting fluorescence of a selected region was then plotted vs. pulse energy, measured by an energy sensor, as seen in Fig. 4.19 on the left. Based on the best-fit-line, saturation was reached around a pulse energy of 1.4 mJ for the applied light sheet optics. Following measurement were then conducted below this value.

For the time resolved measurement, a constant camera exposure time of 5 ns was set, while the gate delay was successively shifted by 5 ns. For each setting, 100 fluorescence shots were captured and the energy-scaled, maximum normalized intensities ($\frac{I_{fl}/E_L}{(I_{fl}/E_L)_{max}}$) were plotted vs. fluorescence time. Fig. 4.19 on the right shows the transient development of the intensity. The fluorescence starts around 120 ns and lasts up to 230 ns. On the basis of this measurement an exposure time of 150 ns was set for the subsequent measurements. According to the general transient formulation of the fluorescence, Eq. (3.7), the emission decays exponentially after the incident excitation stopped and the effective radiation lifetime, Eq. (3.16), emerges from the natural lifetime in absence of quenchers and from the

quenching rate. Fitting an equation of the type $e^{-(t/\tau)}$ to the exponential fluorescence decay, resulted in effective lifetimes of $\tau = 18.59 - 19.19$ ns. According to Schulz et al. [173], typical values for organic molecules are 1 - 100 ns, which means, the lifetime in the current case was rather in the lower range. Lozano et al. [126] measured a lifetime of 4 ns for acetone, which was considerably lower than that of fluoroketone.

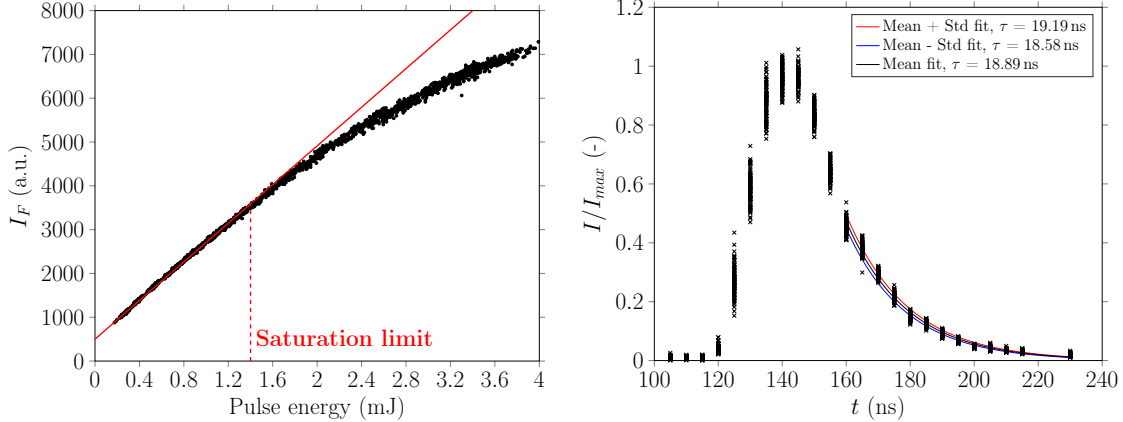


Figure 4.19: Left: scatter plot of fluorescence over pulse energy. Right: time resolved measurement and exponential fittings.

4.3.2 Laser absorption

For uniform density flows, the mixture fraction was synonymously considered as the relative concentration c/c_{max} [103], which on the other hand was related to mole fraction X and the normalized intensity fluorescence intensity I_{fl}/E_L as:

$$\frac{X}{X_{max}} = \frac{c}{c_{max}} = \frac{I_{fl}/E_L}{(I_{fl}/E_L)_{max}} \quad (4.9)$$

It is common practice to scale the intensity by the maximum intensity, which emerges in the region of maximum tracer concentration. In JICF analysis, where the jet flow is seeded, this region is directly at the outlet of the injection orifice. The relation in Eq. (4.9) is valid for spatially constant quantum yield, optical properties, temperature and pressure, see Eq. (3.28). Additionally, the fluorescence intensity is proportional to the laser intensity. However, due to molecular absorption the laser intensity was attenuated in the beam direction and Eq. (4.9) becomes valid, only if the local intensity was known, which in general not the case. Thus, a conservative analysis was performed to estimate the error.

The attenuation behavior of fluoroketone on the laser intensity can be characterized by two approaches. The number density of tracer molecules in the cell, Fig. 4.18, was determined from the temperature and the partial pressure, Eq. (3.30). According to $n = p_v/(RT)N_A$, where N_A is the Avogadro constant, the number density $n = 8.71 \cdot 10^{24} \text{ 1/m}^3$. Then, the absorption coefficient α_{abs} of fluoroketone was obtained from $\alpha_{abs} = n \cdot \sigma_{abs}$ and estimated as 0.0386 1/mm . The quantity σ_{abs} is obtained from the spectral absorption distribution in Fig. 3.7. A second approach is the determination of the absorption coefficient experimentally. According to the Lambert-Beer law in Eq. (3.27), the intensity decays exponentially in the spatial direction. Fig. 4.20 shows on the left exemplary normalized

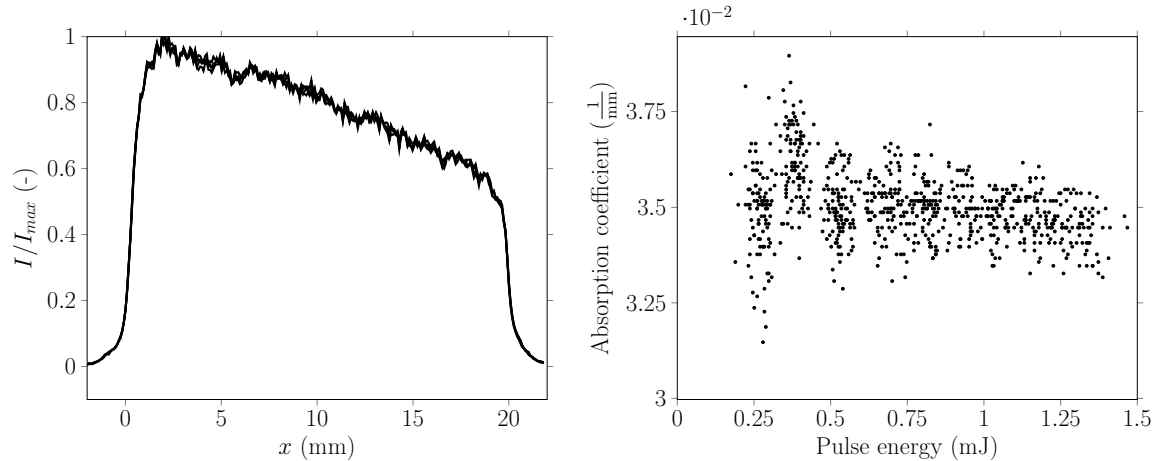


Figure 4.20: Left: spatial intensity distributions from a number of images at the same height (overlapping). Laser beam enters from left. Right: experimentally determined absorption coefficient. Average of 10 vertical pixels.

fluorescence intensities from Fig. 4.18. In order to improve the data quality, 10 pixels were averaged vertically. There is a clear slope observed originating from the laser intensity attenuation, because the cell contained homogeneously distributed fluoroketone vapor. Basically, the gradient of the curves represents the absorption coefficient. It is determined by solving Eq. (3.27) iteratively for the exponent until the intensity profiles become horizontal. The scatter plot of Fig. 4.18 presents the absorption coefficient of 800 profiles, extracted from the same number of images. The corresponding fluorescence images were obtained from different laser pulse energies. The dispersion decreases with increasing pulse energy, due to decreasing laser fluctuations. An average absorption coefficient of 0.035 mm^{-1} (std of 3 %) was obtained, which differs around 10 % from the theoretically estimated value of 0.0386 mm^{-1} . With regard to the main experiments, the maximum width of the saturated flow was below 1 mm. Based on the Lambert-Beer law and experimentally determined absorption coefficient, the corresponding intensity decay and consequently the error would be approx. 4 %. As an absorption correction could not be performed for the JICF experiments, this error was accepted.

Chapter 5

Test Bench

A description of the designed test bench and its main components is provided in this chapter. An isometric, 3D drawing of the test bench is shown in Fig. 5.1 together with a reference person. Photographs of the actual test rig from different angles are found in Fig. C.1 of the appendix. A 2D top view of the optical setup is presented in Fig. 5.2. The figure also

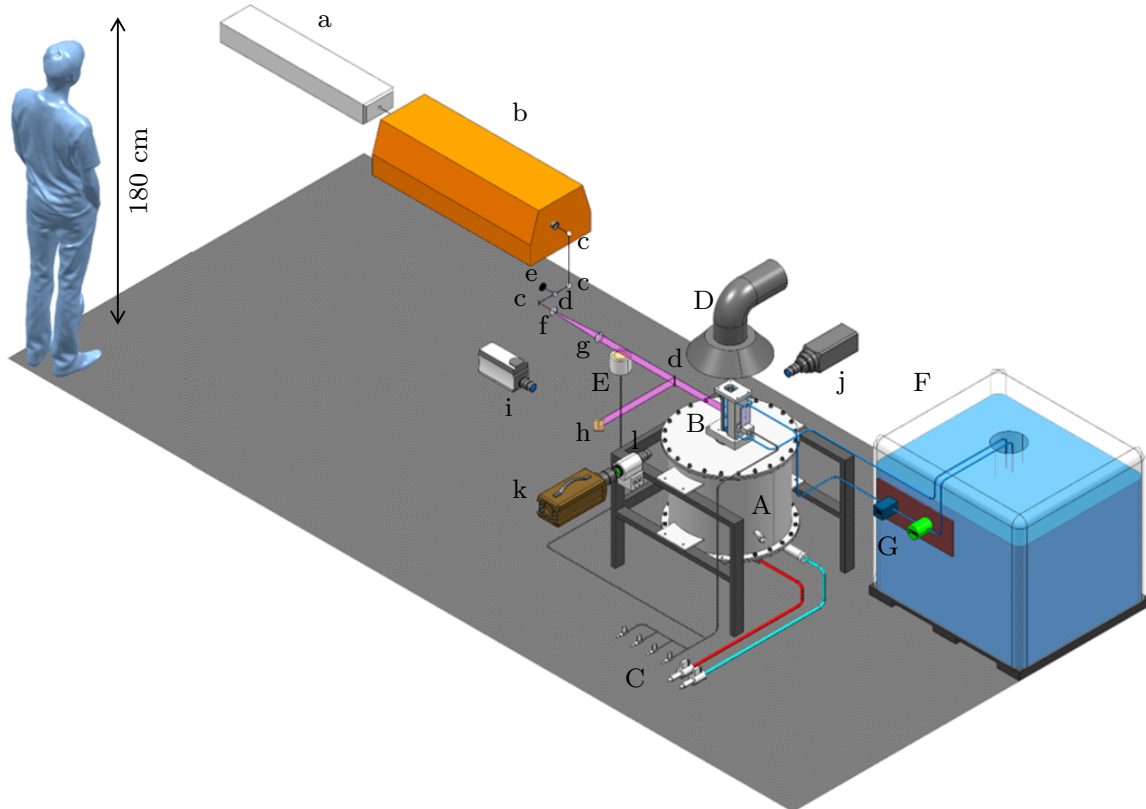


Figure 5.1: 3D illustration of the test bench: A: HGG. B: TS. C: MFC. D: exhaust system. E: flat flame burner. F: water reservoir. G: water pump and flow meter. a: Nd:YAG laser. b: dye laser. c: mirrors. d: fused silica. e: energy sensor. f: cylindrical lens. g: spherical lens. h: dye cell. i: Andor camera. j: PI MAX2 camera. k: Phantom camera. l: intensifier.

shows the indication of the front and side directions. The optical components were already

described in chapter 4.1 and the remaining components are discussed here. The hot gas generator and the test section are referred to as HGG and TS for convenience. Within the TS, chemical reaction took place between the injected fuel jets and the hot crossflow. OH* chemiluminescence imaging was conducted from the side direction, and in separate experiments, also from the front direction. For the OH PLIF diagnostic, a vertical light sheet entered from the front direction and excited OH radicals in the centerplane. The emission was then collected from the side view.

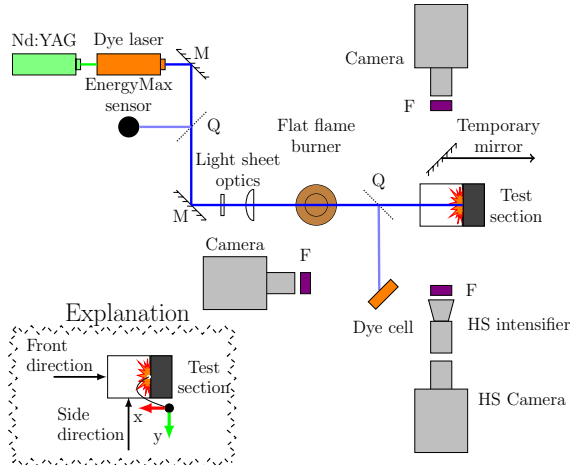


Figure 5.2: Schematic illustration of the main experiment from the top view. Shortcuts: F is filter, M is mirror, Q is fused silica.

5.1 Hot gas generator

The investigation of near-wall reacting fuel jets required hot, oxygen-rich exhaust gas. Thus, a HGG was designed and manufactured specially for this purpose by a third party [8]. Fig. 5.3 shows the structure and the internal parts of the HGG. The device was placed upright and gaseous air and fuel supply pipes were connected to the corresponding reservoir or chamber on bottom, as illustrated in Fig. 5.9. The specified amounts of air and fuel were injected separately through small tubes into the combustion chamber of octagonal cross section. To prevent a flashback, mixing took place only within the combustion chamber. Still, the tubes had a small diameter to ensure high flow velocities, which counter possible flashbacks in case premixed operation was intended. The mixture was ignited once by an external, removable electrode and continuous combustion took place as long as the fuel/air supply was maintained. To enhance mixing and increase the residence time of the composition, the chamber was filled with high-temperature tubular ceramic elements with a diameter and height of around 20 mm. Some of them are exemplarily shown in Fig. 5.3 part c. As a consequence, the volume of the combustion chamber was calculated to reduce from 3.084 l to 2.468 l. Then, the combustion products flowed through a flame breaker into a second chamber with a volume of 2.087 l. The flame breaker was basically a perforated plate and separated the combustion chamber, while the second chamber helped to homogenize the flow. Finally, the exhaust gas exited the device from a convergent nozzle with an inlet cross section of 80 x 80 mm² and outlet cross section of 50 x 50 mm², as indicated in Fig. 5.3. At the edges of the nozzle inlet, wake and recirculation regimes might form. Due to the shape

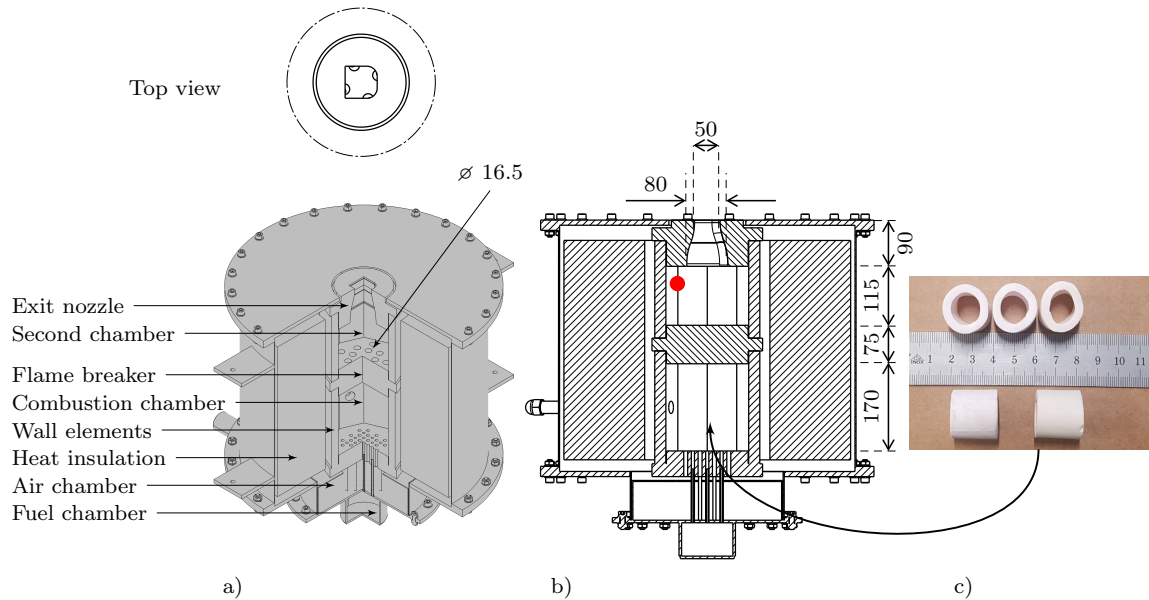


Figure 5.3: Hot gas generator. a: isometric view. b: cross sectional view. c: ceramic elements. Red dot indicates the position of the monitoring TC type B. Units in mm.

of the nozzle, the flow accelerated and these effects and remaining inhomogeneity within the flow were eventually mitigated. This was shown in the work of Fischer et al. [61], from which Fig. 8.64 was obtained. As seen on the top view of the HGG in Fig. 5.3, the flame breaker and the nozzle were positioned non-symmetrically to one another. This fact and the stochastically distributed ceramic elements inside the combustion chamber affected the spatial flow distribution and resulted in inhomogeneity.

The internal components which were exposed to the combustion products consisted of zirconium oxide. The melting point of this ceramic material is specified as $\sim 2950\text{ K}$ [37]. Especially, the low thermal conductivity of $\sim 1 - 3\text{ W}/(\text{mK})$ was of major importance to keep heat losses to a minimum level and achieve high gas temperatures. Additionally, several layers of aluminum oxide wool with a temperature specification of 1873 K and a micro porous layer of silicon dioxide provided further insulation. The outer structure of the device was made out of stainless steel. The internal structure was of modular design for modifying and replacing purposes. According to the specification, the device was designed for a power up to 60 kW , with an exhaust volume flow of $540\text{ m}^3/\text{h}$, which might be achieved by a supply of 100 nl/min CH_4 . Exhaust gas temperatures up to 2000 K should be possible. For the current study, up to 40 nl/min CH_4 was supplied and a mainstream temperature of around 1600 K within the TS was reached.

As illustrated in Fig. 5.9, the temperature of the supplied flows were measured by type K TC before entering the HGG. The exhaust gas temperature within the HGG was measured by a TC type B. The position of the sensor is indicated in Fig. 5.3. As the TC served for monitoring purposes rather than for accurate and fast response measurements, a ceramic sheathed sensor was selected to ensure long lifetime and slow degradation.

Except for the outlet nozzle and the ignition opening, the HGG was a closed device and did not allow optical access for measurement purposes. Thus, flow field measurement techniques such as PIV were inapplicable due to the internal structure and due to the fact

that those particles would have contaminated the internal structure of the HGG.

5.2 Test section

An optically accessible, water-cooled flow guide was designed from the special alloy Hastelloy C22 as the wall element and silica plates for the duct walls, as seen on Fig. 5.4. The main application field of this nickel-chromium alloy are thermally stressed components of gas turbines, such as combustion chamber, turbine blades and vanes, and rocket chambers due to its material characteristics like low thermal conductivity ($10 - 21 \text{ W}/(\text{mK})$ for $323 - 873 \text{ K}$) and corrosion resistance [6, 37, 122]. Same reasons led to its application in this study. For combustion investigation using OH* chemiluminescence and LIF, UV transmittance of the channel windows was required and therefore industrial fused silica was employed. High quality plates may provide better transmission and results, but the high demand in this study would have made it cost-inefficient. A mounting plate and an end plate helped to attach the test section to the hot gas generator and hold the test section components together. To account for thermal expansion and reduce thermal stress, pressure springs were used. As indicated in Fig. 5.4, the origin of the coordinate system in the presentation of results was defined to be at the exit of the center orifice.

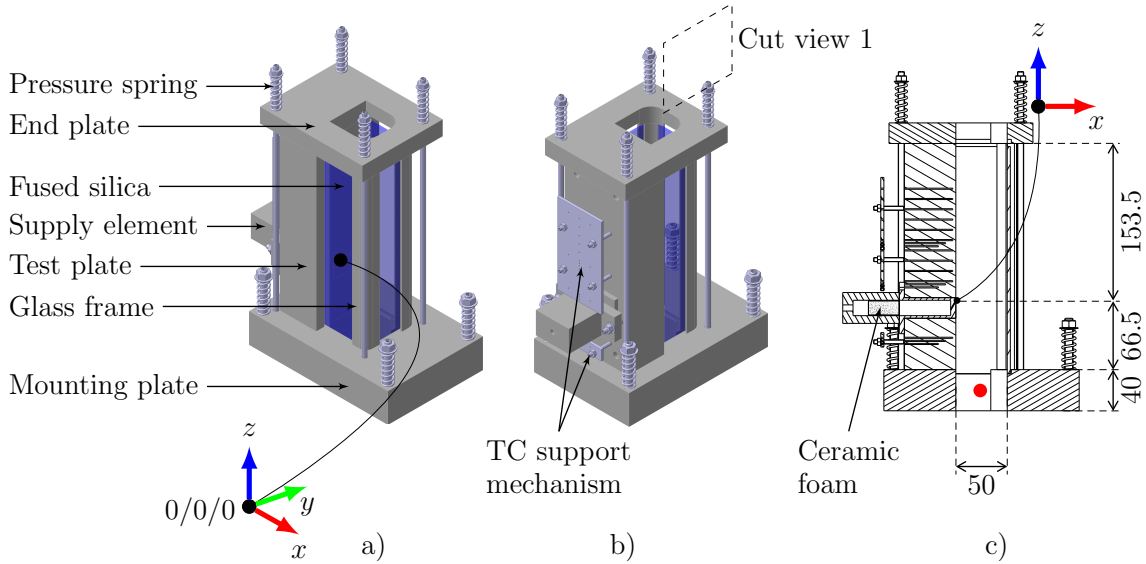


Figure 5.4: Assembled test section. Red dot indicates the position of the monitoring TC type B. Units in mm.

Fig. 5.5 shows the computer-aided design (CAD) of the test plate. The wall element was basically a vertically positioned, massive block of the dimensions $220 \times 86 \times 50 \text{ mm}^3$. The thickness of the block was necessary to generate a detectable temperature distribution within the plate, while the height was required to provide a sufficient throughflow time for the reaction to occur inside the channel. Two vertical grooves provided guidance for the fused silica plates and two vertical holes were machined for water-cooling. To measure the block temperature at different positions below the hot surface, a number of blind holes of approximately 1.1 mm diameter were drilled from the rear side to insert TC's of 1 mm diameter. A self-constructed spring system held the sensors in position and avoided vibration and

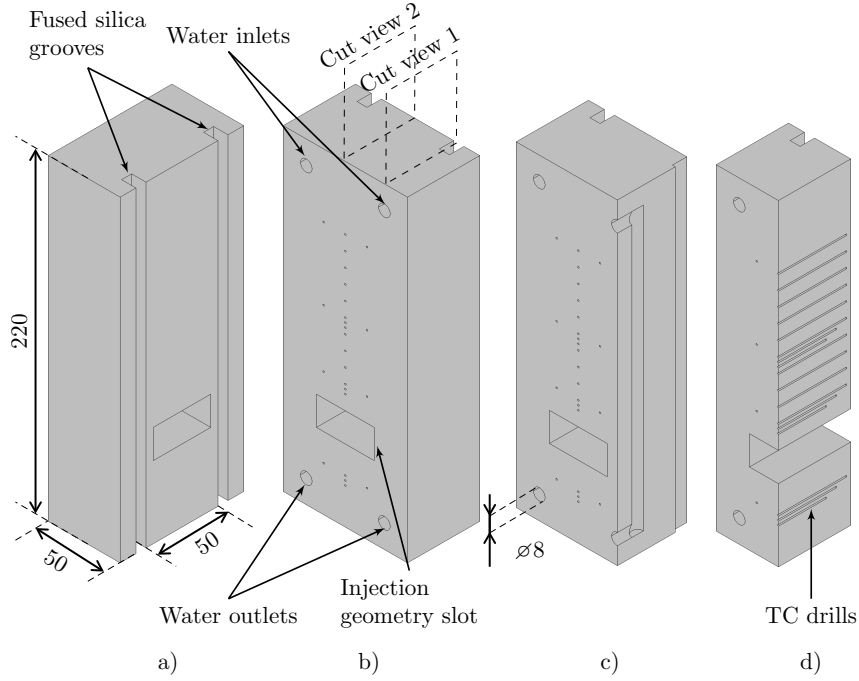


Figure 5.5: Test section block. a: front view. b: rear view. c: cut view 1. d: cut view 2. Units in mm.

mispositioning, as seen in Fig. C.2. The TC support plate applied pressure on the springs, which on the other end exerted a force on the TC. To enhance the contact between TC and material, high temperature heat-conduction paste was poured into the holes. The block served as the main component with a rectangular hole of side $35 \times 25 \text{ mm}^2$ to mount inserts with different injection geometries. A slot with five angled orifices at 30° to the crossflow and a slot with five 90° orifices to the crossflow were designed for this study. Fig. 5.7 and Fig. 5.6 show the insert drawings. The cold gas intended for injection was led to the slot, which offered expansion and homogenization space for the gas. A ceramic foam was placed inside the slot to ensure a homogeneous flow distribution. Thereafter, the gas exited the insert from the five orifices. The ratio of tube length to its diameter ensured a fully developed jet flow and avoided entrance effects according to Eq. (2.8) - Eq. (2.9). Laminar as well as turbulent jet flow conditions based on the jet Reynolds number were maintained. Detailed values are given later. As indicated in Fig. 5.4, the origin of the coordinate system was positioned at the exit of the center orifice. This convention is used throughout this work.

To access the main flow temperature during an experiment, an uncoated TC type B welded from two wires of 0.5 mm was positioned at the inlet of the test section at $x = 25 \text{ mm}$, $y = 15 \text{ mm}$ and $z = -86.5 \text{ mm}$ relative to the center orifice. The location is marked in Fig. 5.4. The sensor was replaced regularly due to degradation. Within the supply line of the insert, the temperature of the cold gas was measured before entering the injection geometry, as emphasized in Fig. 5.9. Though, for a more precise flow temperature measurement, a TC type K with a diameter of 1 mm was installed inside the injection geometry. The location is indicated in Fig. 5.6 and Fig. 5.7.

To estimate the thermal condition of the test plate, a simplified conjugate heat transfer

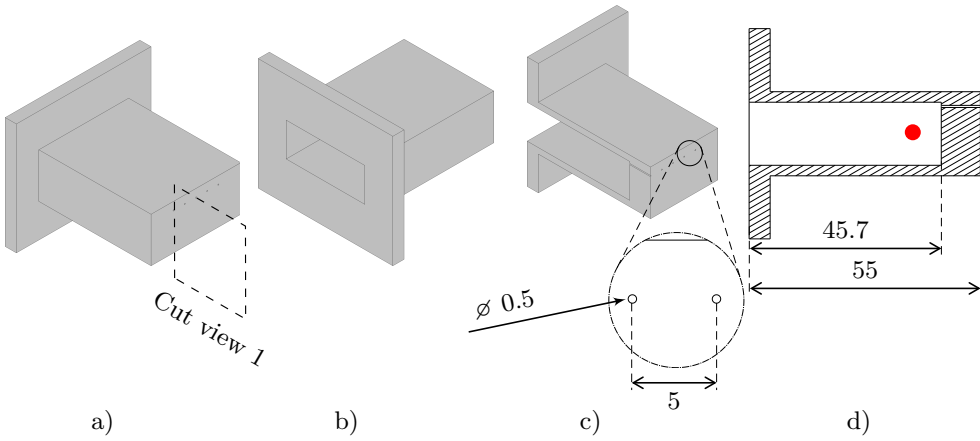


Figure 5.6: Injection slot. a: front view. b: rear view. c: cut view 1 with magnification. d: dimensioned cut view 1. Red dot indicates the position of the monitoring type K TC. Units in mm.

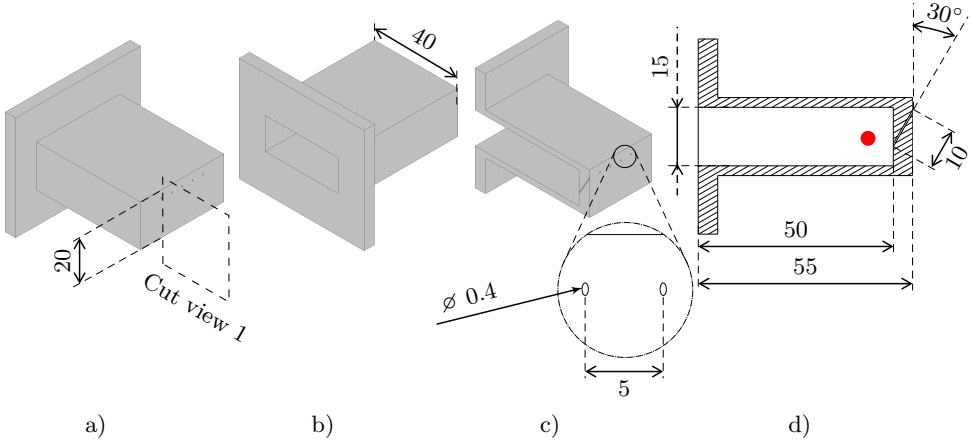


Figure 5.7: Injection slot. a: front view. b: rear view. c: cut view 1 with magnification. d: dimensioned cut view 1. Red dot indicates the position of the monitoring TC type K. Units in mm.

model was set up in the commercial tool Ansys Fluent [13] in the design process initially. The test plate was considered as a solid block with two straight cooling pipes of 6 mm diameter, without the insert gap. A representative cooling water velocity of 0.9 m/s at 300 K was set and a hot air stream with a velocity of 27 m/s and a temperature of 1600 K was applied to the hot side. The cooling water and air were established in counter flow manner. Structured meshes were used for the cooling water domain, the solid domain and the gaseous domain. An inert RANS simulation with the $k-\omega$ -SST turbulence model for the flow field was selected. Theoretical background of RANS simulation is found in the appendix D. Fig. 5.8 shows the temperature distribution on different planes of the plate. For a conservative thermal design, it was assumed, that the hot gas started at the beginning of the test block. Hence, a hot spot is observed there. Within a short distance, the temperature homogenizes in the downstream distance. The maximum temperature is around 700 K, which is far below

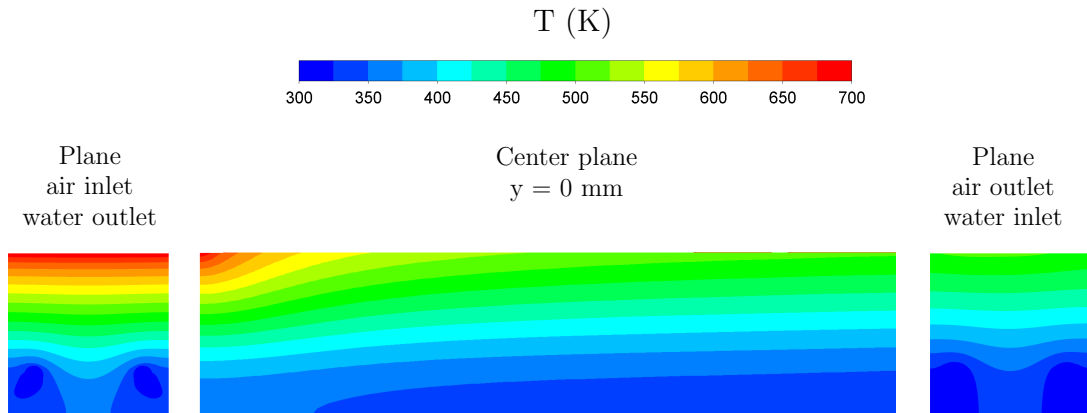


Figure 5.8: 2D temperature distribution from an inert RANS simulation of the test plate. Left: hot gas inlet plane. Center: center plane. Right: hot gas outlet plane.

the material melting limit of 1630 K [7]. Further, according to the cut planes, a spatially constant lateral temperature is observed for a sufficient distance and the effect of the cooling appears only within close proximity of the channels. Thus, the heat flux at the center plane normal to the surface can be considered as nearly 1D. Based on the simulation, the average water outlet temperature was 304 K, which is well below its boiling temperature and poses no risk to the experiment.

5.3 Peripheral components

A number of additional components were vital for the operation of the test rig. A summary is given below.

Gas supply and control

A diagram of the gas flows is shown in Fig. 5.9. The hot exhaust gas was generated from the combustion of CH₄. Alternatively, H₂ or C₃H₈ could be chosen if desired. To account for the considerable demand of fuel and ensure an uninterrupted operation, four bottles of gaseous CH₄ (50 l, 200 bar) were interconnected and supplied the HGG. The significant amount of required combustion air was provided by an in-house compressor. Within the scope of this work, near-wall reaction of CH₄, H₂ and C₃H₈ was investigated. CH₄ was tapped from the mentioned supply system, while H₂ (50 l, 200 bar) and C₃H₈ (33 kg, 7 bar) were incorporated additionally to the system. Each gas stream was individually controlled by an electronic MFC from Bronkhorst connected to a computer. Care was taken, that the MFCs were calibrated for the gas flow rates. According to the specification of the devices, the accuracy of the devices is 0.5 % of the set-value plus 0.1 % of the full scale value [4].

Exhaust system

During an experiment, large amounts of high temperature exhaust gas and reactive products emerged. Generally, various technical possibilities exist to cool down and dilute the exhaust

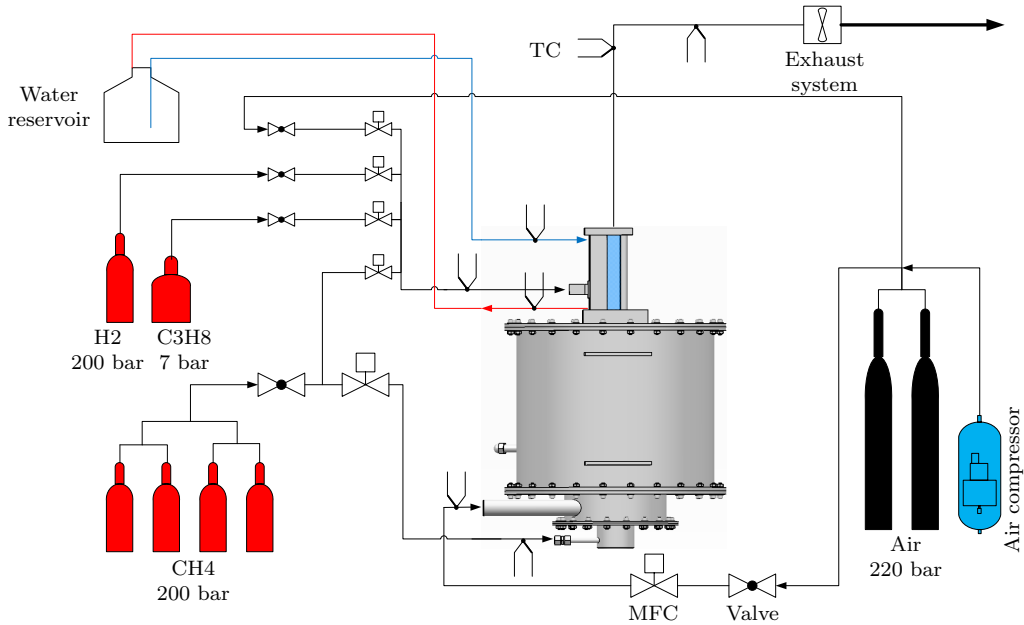


Figure 5.9: Schematic illustration of the gas flows. Some elements are labeled only once.

flow, such as water spray (atomization) to take advantage of heat capacity and heat of evaporation, N₂ injection or use of air excess. The most elegant solution for this test rig was the last method. Thus, an explosion-proof exhaust system with an extraction capacity of 3000 m³/h and temperature resistance of 673 K was installed. TC's within the exhaust pipe measured the temperature and ensured the safe operation of the system.

An inert RANS simulation was performed for a conservative thermal design of the exhaust system. Here, a hot air flow with a temperature of 2200 K and an average velocity of 60 m/s was led to the suction bell of the exhaust system with the mentioned extraction capacity. The ambient temperature was set to 300 K. To estimate the maximum suction pipe temperature, adiabatic thermal condition was applied there. The numerical simulation was conducted in Ansys Fluent, using a structured mesh and the *k-ω-SST* turbulence model. Fig. 5.10 shows the resulting velocity and temperature fields. Due to the exhaust capacity

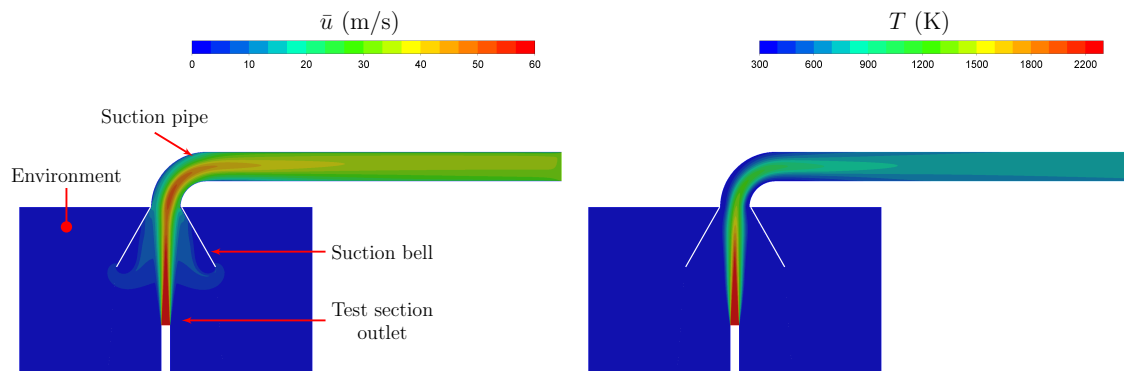


Figure 5.10: RANS simulation result of the test bench environment. Left: average velocity flow field. Right: temperature field.

additional air is taken from the environment, which mixes with the hot air and surrounds it. Hence, a direct contact of the hot gas to the suction pipe is prevented. And the large pipe diameter allows the hot gas to decelerate and to homogenize along the flow direction. According to the temperature field, the core temperature of the hot gas reduces to approx. 1200 K within the redirection, while relatively low temperature values emerge around the tube walls (around 300 K). As the flow homogenizes downstream, the near-wall temperature increases. The maximum pipe temperature was 723 K and the surface average flow temperature at the outlet was 725 K. These values are above the maximum allowed temperature of the system of 673 K, due to the assumed severe hot gas conditions. However, selecting realistic hot gas conditions of 1600 K and 27 m/s, led to average exhaust gas temperatures of 400 K at the outlet. Further, the exhaust pipe was subject of radiation and convective cooling, which lowered the temperatures additionally. Thus, a safe operation of the system was ensured.

Water cooling supply

The test section wall required active cooling to generate a temperature distribution within the component and protect it during long run-time experiments. Hence, a cooling circuit was established using a water reservoir of 1 m³. A pump pushed approx. 5.5 l/min water through the cooling drills of the test plate resulting in a velocity of around 0.9 m/s (at 293.15 K, 8 mm cooling pipe diameter). The water mass flow was measured by an electronic meter. The water backflow was led to the reservoir. The temperature rise during the operation was taken into account in the post-processing step, as the water inlet and outlet temperatures to and from the test section plate were measured.

Temperature data acquisition

A National Instruments cRio (9045) with TC temperature input modules of C series (9211, 9214, 9216) was used to acquire the temperature data from the TC. The accuracy of the modules is specified as < 1 K. The sample rate of the system depends on the number of connected sensors. Generally, the data of the 36 connected TC were recorded with a sample rate of 2.85 Hz.

Chapter 6

Inverse Heat Conduction Method

The thermal design of components exposed to near-wall combustion relies on the accurate and precise determination of heat transfer to the component's surface. The determination of the heat flux released by near-wall reacting fuel jets was of interest in the current study. Depending on the application, different possibilities exist to determine the heat flux experimentally. Heat flux gauges and local TC installations for heat flux calculation based on Fourier's law in Eq. (2.1) are 1D and provide limited information. Optical methods such as IR and temperature sensitive paints (TSP) require optical access to the surface and a precise calibration. Further, aggressive environments may damage the TSP. Another method found in literature is the inverse heat conduction (IHC). Here discrete local temperature data are used to reconstruct the unknown heat flux analytically. With increasing computational capacity and power, the method can be applied to complex geometries today. The principle of IHC, in general inverse heat transfer problem (IHTP), is presented in this chapter. For a detailed description the author refers to Ozisik [152], Okamoto [151], Colaco et al. [34] and Perakis et al. [155]. The IHC procedure is similar to that in the work of Perakis et al. [155], who determined the heat flux of capacitively cooled rocket chambers operated for few seconds.

6.1 Principle

Generally, heat conduction problems are divided into two categories: direct and inverse problems. In direct methods, the effects are calculated based on a given cause. The effects are physical phenomena like temperature and heat flux distributions within the geometry and the cause is the applied thermal boundary. In some cases, where geometrical forms (symmetrical, rotational, etc.) and the boundary conditions are of simple nature, the heat conduction problem can be solved using analytical expressions derived mathematically from Fourier's law. Heat transfer problems of complex 3D geometries on the other hand require numerical methods solved computationally. In contrast to direct problems, inverse methods deal with problems, where the cause is determined from known effects. For example, the temperature within a geometry is measured, while the thermal condition of the neighboring boundary projected onto the measured location is unknown and to be calculated. The IHC deals with this type of problem.

The objective of the inverse method is the minimization of the least square norm, also referred to as objective function. Within the scope of IHC, it describes the difference between the measured and the calculated temperature at a specific location. It is defined

as:

$$S(\mathbf{P}) = \sum_{i=1}^l [Y_i - T_i(\mathbf{P})]^2 \quad (6.1)$$

where Y is the measured temperature (effect), T is the estimated temperature, \mathbf{P} is the vector of N total unknown parameters and l is the total number of measurement positions, with $l = N$ in this work. The condition $l = N$ generates a determined problem, meaning that, each unknown parameter corresponds to a known temperature. The parameter vector \mathbf{P} in the field of IHC is the heat flux vector $\dot{\mathbf{q}}$ (W/m^2) of interest (cause). A better notation of Eq. (6.1) is provided by the matrix form as:

$$S(\mathbf{P}) = [\mathbf{Y} - \mathbf{T}(\mathbf{P})]^T [\mathbf{Y} - \mathbf{T}(\mathbf{P})] \quad (6.2)$$

where quantities in bold font are vectors and the superscript T denotes the transpose. The estimated temperatures $\mathbf{T}(\mathbf{P})$ originate from the solution of a direct problem, where \mathbf{P} is subject of optimization. To minimize the least square norm, the gradient of $S(\mathbf{P})$ with respect to the vector \mathbf{P} is set to zero:

$$\nabla S(\mathbf{P}) = 2 \left[-\frac{\partial \mathbf{T}^T(\mathbf{P})}{\partial \mathbf{P}} \right] [\mathbf{Y} - \mathbf{T}(\mathbf{P})] = 0 \quad (6.3)$$

The transpose of the partial derivative of T with respect to P is referred to as sensitivity or Jacobian matrix:

$$\mathbf{J}(\mathbf{P}) = \left[\frac{\partial \mathbf{T}^T(\mathbf{P})}{\partial \mathbf{P}} \right]^T = \begin{bmatrix} \frac{\partial T_1}{\partial P_1} & \cdots & \frac{\partial T_1}{\partial P_N} \\ \vdots & & \vdots \\ \frac{\partial T_l}{\partial P_1} & \cdots & \frac{\partial T_l}{\partial P_N} \end{bmatrix} \quad (6.4)$$

The elements of the sensitivity matrix, called sensitivity coefficients, can be approximated by applying a central difference or, as used in this study, by a forward difference scheme:

$$J_{ij} = \frac{\partial T_i}{\partial P_j} \cong \frac{T_i(P_1, P_2, \dots, P_j + \varepsilon P_j, \dots, P_N) - T_i(P_1, P_2, \dots, P_j, \dots, P_N)}{\varepsilon P_j} \quad (6.5)$$

where ε is recommended as 10^{-5} or 10^{-6} . Methods to determine \mathbf{P} iteratively are described in the following.

6.2 Governing equations

Different methods are proposed for the iterative determination of the parameters \mathbf{P} : Newton-Raphson (NR), Conjugate Gradient (CG) and Levenberg-Marquardt (LM) methods. The inverse calculation process is sometimes also referred to as optimization.

The NR method is based on the linearizing the vector of the estimated temperatures. According to the Taylor theorem, the estimated temperature can be represented by an expansion around the current point, which in case of an iterative method is the current iteration k :

$$\mathbf{T}(\mathbf{P}) = \mathbf{T}(\mathbf{P}^k) + \mathbf{J}(\mathbf{P} - \mathbf{P}^k) \quad (6.6)$$

Substituting Eq. (6.6) into Eq. (6.3) and solving for the unknown parameter vector \mathbf{P} of the next iteration leads to:

$$\mathbf{P}^{k+1} = \mathbf{P}^k + \left[(\mathbf{J}^k)^T \mathbf{J}^k \right]^{-1} (\mathbf{J}^k)^T [\mathbf{Y} - \mathbf{T}(\mathbf{P}^k)] \quad (6.7)$$

This expression, called Gaussian method and an approximation for the Newton-Raphson method, is then solved iteratively.

Generally, the iterative process is initialized with guessed parameters for the Jacobian matrix. It is possible, that in some cases the product of $\mathbf{J}^T \mathbf{J}$ becomes very small or even zero and instabilities occur, such that the NR method (Eq. (6.7)) is not applicable for the estimation of the parameter \mathbf{P} . Thus, the NR method is limited by the so-called *Identifiability Condition*, which requires a non-singular product of $\mathbf{J}^T \mathbf{J}$:

$$|\mathbf{J}^T \mathbf{J}| \neq 0 \quad (6.8)$$

Problems leading to very small or zero $\mathbf{J}^T \mathbf{J}$ are denoted as *ill-conditioned*. Especially heat transfer problems may cause such issues. The LM method overcomes this condition elegantly by introducing a positive scalar dumping parameter μ to Eq. (6.7):

$$\mathbf{P}^{k+1} = \mathbf{P}^k + \left[(\mathbf{J}^k)^T \mathbf{J}^k + \mu^k \Omega^k \right]^{-1} (\mathbf{J}^k)^T [\mathbf{Y} - \mathbf{T}(\mathbf{P}^k)] \quad (6.9)$$

where Ω is a diagonal matrix calculated from:

$$\Omega = \text{diag} \left[(\mathbf{J}^k)^T \mathbf{J}^k \right] \quad (6.10)$$

At the beginning of an iteration, a large value is assigned to the dumping parameter, e.g. $\mu^0 = 0.001$, to encounter the ill-condition state of the problem. Depending on the convergence condition of the objective function, the damping factor is handled differently. If the iterative process diverges, meaning the objective function rises, $S(\mathbf{P}^{k+1}) > S(\mathbf{P}^k)$, then μ is increased, e.g. $\mu^{k+1} = 10\mu^k$. In case of convergence, μ is reduced by a factor of 10. As the calculation advances to the solution, the LM method approaches the NR method, since $\mu \rightarrow 0$.

Another efficient approach suitable for linear and nonlinear estimation problems is the CG method. Here, the parameter for the next iteration is estimated based on the current parameter and a small step size in the direction of decent:

$$\mathbf{P}^{k+1} = \mathbf{P}^k - \beta^k \mathbf{d}^k \quad (6.11)$$

where β is the search step size, \mathbf{d} is the direction of descent. To assure convergence and minimization of the objective function Eq. (6.2), the direction of decent is calculated from a linear combination of the negative gradient at the current iteration and the direction of decent from the previous iteration:

$$\mathbf{d}^k = \nabla S(\mathbf{P}^k) + \gamma^k \mathbf{d}^{k-1} \quad (6.12)$$

where γ is the conjugation coefficient calculated by the Polar-Ribiere (Eq. (6.13)) or the Fletcher-Reeves expression (Eq. (6.14)):

$$\gamma^k = \frac{\sum_{j=1}^N \left([\nabla S(\mathbf{P}^k)]_j [\nabla S(\mathbf{P}^k) - \nabla S(\mathbf{P}^{k-1})]_j \right)}{\sum_{j=1}^N [\nabla S(\mathbf{P}^{k-1})]^2_j} \quad (6.13)$$

$$\gamma^k = \frac{\sum_{j=1}^N [\nabla S(\mathbf{P}^k)]_j^2}{\sum_{j=1}^N [\nabla S(\mathbf{P}^{k-1})]^2_j} \quad (6.14)$$

where $\gamma^0 = 0$ for both expressions. Finally, the search step size is calculated by:

$$\beta^k = \frac{[\mathbf{J}^k \mathbf{d}^k]^T [\mathbf{T}(\mathbf{P}^k) - \mathbf{Y}]}{[\mathbf{J}^k \mathbf{d}^k]^T [\mathbf{J}^k \mathbf{d}^k]} \quad (6.15)$$

The three methods were tested on a validation case and produced the same results. The LM and CG methods required the least iterations. Due to the implementation simplicity, the LM method was applied throughout the current study.

6.2.1 Stopping criteria

Heat transfer problems are classified in *well-posed* and *ill-posed* conditions. A well-posed problem has a unique, stable solution. The stability condition requires that the solution behaves stable under small variations of the input information. While direct problems are of well-posed nature, IHC problems belong to ill-posed categories. To provide the necessary stability to IHC, the inverse procedure is formulated in a well-posed manner. First, the iteratively estimated temperatures for the least-square norm Eq. (6.1) are obtained from direct calculations. Further, additional stability is required and introduced by applying appropriate stopping criteria to the inverse process, such as:

$$S(\mathbf{P}^{k+1}) < \varepsilon_1 \quad (6.16)$$

$$|\mathbf{P}^{k+1} - \mathbf{P}^k| < \varepsilon_2 \quad (6.17)$$

The tolerances ε are chosen according to the measurement accuracy of the experimental temperatures. The criteria in Eq. (6.16) is also called *Discrepancy Principle*. A possible stopping criterion is the variance obtained from the square of the standard deviations of the measured data, such as $\varepsilon = \sigma^2$. According to Ozisik [152], Eq. (6.16) is sufficient for the stability of the CG method, while the LM method involves the stopping criteria Eq. (6.17) in some cases, where the measurement contains random errors.

6.2.2 Calculation of the sensitivity matrix

The presented optimization methods require the calculation of the Jacobian matrix Eq. (6.4) for the inverse problem. The Jacobian matrix basically describes how the temperatures change with respect to the parameters, precisely how each temperature behaves when each heat flux parameter is altered. Thus, to determine the sensitivity coefficients using Eq. (6.5) a time-consuming procedure has to be conducted prior to the direct problem. For this forward difference, a guessed value is assigned to the parameters and the corresponding temperatures are obtained. Then, each (heat flux) parameter is varied one-by-one by a small quantity ε leading to altered temperature values. Hence, each optimization iteration involves $N + 1$ direct calculations for the Jacobian matrix, where N is the number of parameters. The time consumption increases the larger N becomes. Further, the efficiency of the method diminished for transient problems as the optimization is applied to each time-step. To overcome this issue and utilize the inverse methods for time-dependent problems, Perakis et al. [155] found, that while the iteration procedure advances to the solution, the sensitivity coefficients remain mostly unchanged as long as the position and number of measurements are constant. Hence, the Jacobian matrix was calculated once prior to the optimization process and used for each iteration and each time step.

6.3 Implementation routine

As shown in Fig. 5.5, the wall element of the test section was equipped with a number of TC at various lateral and axial locations to measure local pointwise temperatures. The major fraction, 11 of the 19 TC, was aligned at the centerline and the sensors were located around 3 - 4 mm below the surface. The exact coordinates are found in the appendix Tab. E.1 and in Tab. E.2. The numerical domain for the direct heat transfer calculation was a simplified geometry of the described wall element and is shown in Fig. 6.1. The water cooling channels were modeled as straight pipes, the block and injection slot were considered as a single domain. Further, the CAD drawing contains the assigned thermal boundary conditions to the individual surfaces. The external temperatures of water and cold gas for the forced convection were supplied by additional TC. To initialize the direct simulation for the first iteration, the heat flux to the thermally stressed surface, which faced the hot gas and near-wall reaction, was set to 0 W/m². The meshing, discretization of the domain and the direct heat transfer simulations were performed in the commercial finite-element method (FEM) tool COMSOL Multiphysics [194]. COMSOL is a graphical user interface tool, which enables the coupling and calculation of sets of partial differential equations describing different physics. Additionally, the software provides interfaces to other tools, such as to Matlab [138] through the module LiveLink [124]. It allows access to the case, modifications and most importantly external execution of the simulation and extract of results. This helps to parametrize calculations. Beside LiveLink, the heat transfer module was of interest for the current work to solve heat conduction problems. By the way, COMSOL contained an optimization module applicable to IHC problems. However, the defined objective function was spatial- and time-dependent, which was impractical for the present complex, long-term optimization. Further, the Jacobian matrix was calculated each iteration and thus, the algorithm was inefficient. For the current numerical domain, an unstructured mesh consisting of around 120000 elements was used. Local refinements were applied to improve the quality of the results. Simulations with different mesh refinements showed no significant dependency of the result on the mesh.

After the first direct simulation, the unknown heat flux released to the hot gas surface was attempted to be reconstructed by means of the introduced IHC concept. The implementation of the IHC algorithm is illustrated in Fig. 6.2. Here, the TC were projected onto the surface and a heat flux profile was iteratively optimized until the objective function satisfied an user-defined discrepancy. To calculate the Jacobian matrix, a constant heat flux (50000 W/m²) was applied to each of the surface positions. Then, a parameter vector \dot{q} based on Eq. (6.9) was estimated. As the heat flux vector consisted of single points, a heat flux profile was generated using piece-wise spline-interpolations, such as the Akima-interpolation [9], which has a discontinuous second derivative, uses only the neighboring points and damps non-physical, wavy behavior of the interpolated profile. The axial extrapolation was taken as constant. Since fewer sensors were installed in the off-center locations compared to the centerline, a special approach was necessary to interpolate a 2D heat flux profile, as proposed in [155]. Basically, additional points were added to the lateral positions missing a sensor and the heat fluxes were obtained as an average value of the neighboring locations, as illustrated in Fig. E.2, e.g. the average heat flux value of TC18 and TC19 was taken for the point at $y = -15$ mm, $z = 69.5$ mm. Further, two extrapolation types for the lateral heat flux from $|y| = 15$ mm to $|y| = 25$ mm were tested. In the current case, the flat plate geometry was heated for a long period of time and with an

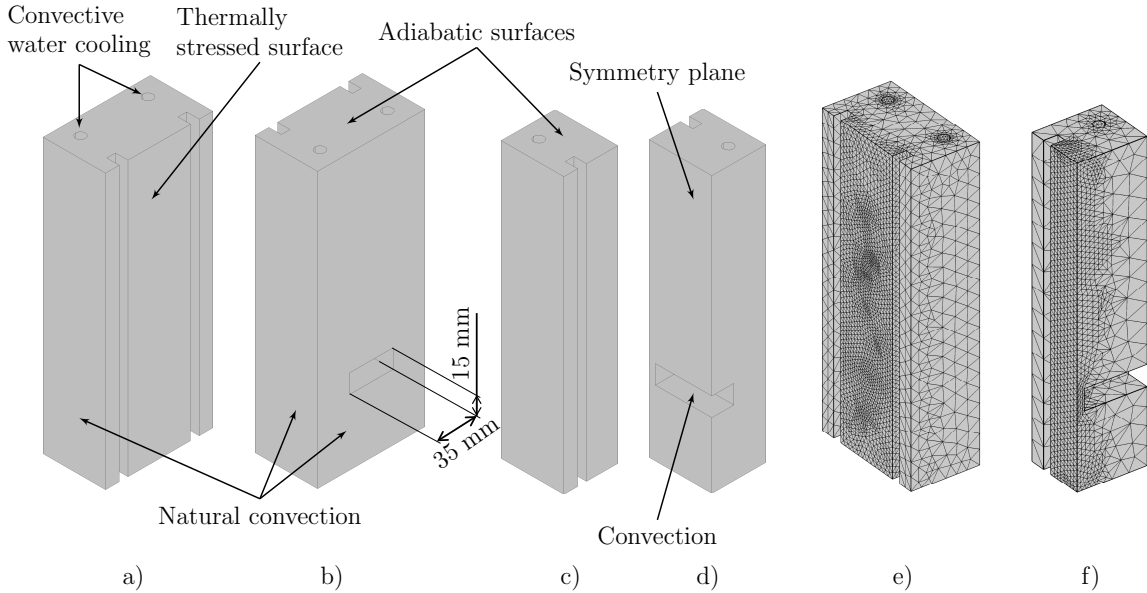


Figure 6.1: Heat transfer numerical domain. a: front view of full domain, b: rear view of full domain, c: front view of half domain, d: rear view of half domain, e: mesh of full domain, f: mesh of half domain.

approximately constant lateral heat flux distribution. The authors in [155] on the other hand applied a zero heat flux to the boundary, since the experiment was conducted for few seconds starting from room temperature. Thus, constant and zero heat flux conditions at $|y| = 25$ mm were compared in the following. For a 1D heat flux profile, only the sensors aligned at the centerline were considered and constant lateral heat flux was assumed. After assigning the heat flux to the surface, the direct problem was solved in COMSOL and the estimated temperatures were compared to the filtered experimental TC temperatures by means of the objective function. If the discrepancy was greater than the specified limit, another optimization iteration was performed. Otherwise, the IHC optimization proceeded with the next time step. The routine was executed to the last experimental time step.

6.4 Algorithm validation

For the validation of the optimization routine, a reference case with known boundary conditions and temperatures at the specified locations was necessary. Experimental setup of such a validation case would be challenging, thus theoretical cases were constructed. Therefore, two direct heat transfer simulations were performed with the domain in Fig. 6.1, where a time-dependent, 1D spatially varying heat flux in the vertical direction and a time-dependent, 2D spatially varying heat flux were assigned to the hot surface. The transient heat calculations were conducted for 160 s. Thereafter, the temperatures at the locations of Tab. E.1 and in Tab. E.2 were extracted with a rate of 1 Hz and filtered to 0.25 Hz. Then, the temperature and the heat flux distributions on the hot surface were reconstructed by means of the IHC. The optimization routines converged to a temperature discrepancy of 0.2 K at each TC position. The application of the stopping criteria Eq. (6.17) was not required as seen in the following results.

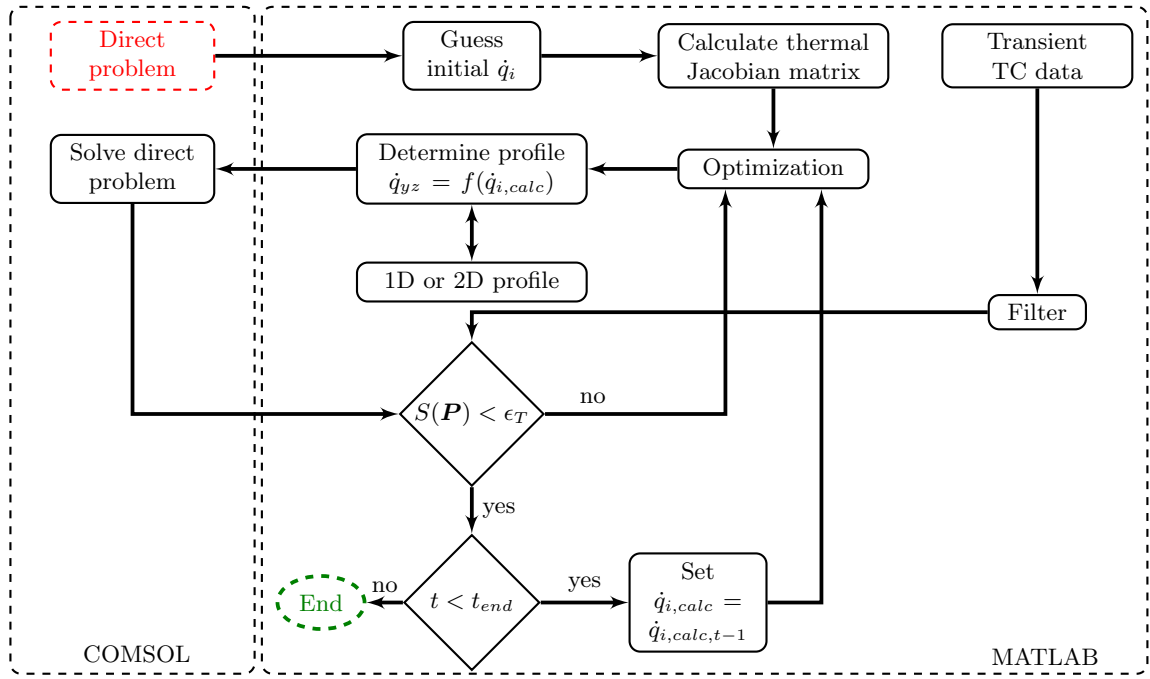


Figure 6.2: Calculation process of inverse heat conduction.

Fig. 6.3 shows exemplarily the transient heat flux at some locations on the geometry surface ($x = 0\text{ mm}$) from the direct and IHC simulation with constant lateral boundary condition. Except for TC11 with deviations around 20 %, the optimization process successively reproduced the heat flux up to a small discrepancy. The deviation at $t = 20 - 30\text{ s}$ was attributed to the filtering of the data. Around $t = 100 - 140\text{ s}$, some oscillations are observed on the TC11 and TC12 IHC curves. These instabilities were due to the ill-posed character of inverse problems and could be damped by the so-called *Tikhonov's regularization method*, where an additional term is introduced to the objective function in Eq. (6.1) which reduce the oscillations at cost of accuracy [151, 152]. However, the proper choice of the stabilization parameter might not be trivial. Thus, the small oscillations were accepted.

Centerline temperature and heat flux profiles are shown in Fig. 6.4. On the left and center column a direct case with 1D heat flux boundary condition was attempted to reconstruct using a constant and zero lateral boundary condition, respectively. On the right side, a 2D heat flux was applied and reconstructed iteratively using a constant lateral boundary. In all cases the optimization reproduced the direct temperature with a maximum deviation below 2 K in the interpolation range between the first and last axial TC and the results were in good agreement. Comparing the heat flux profiles from the cases with different lateral boundary types, an increased discrepancy is observed for the zero lateral heat flux boundary condition. Especially, around $z = 60\text{ mm}$ the optimized heat flux deviates from the direct profiles. For the cases with constant lateral heat flux extrapolation (1D and 2D heat flux), maximum deviations around 20 % at $z = 29.5\text{ mm}$ (TC11) occurs, likely due to instabilities and poor resolution. For the remaining positions, the errors are below 10 %. The reason for the large discrepancies of the adiabatic boundary condition is found in Fig. 6.5. Here, the lateral temperature and heat flux distributions are illustrated for

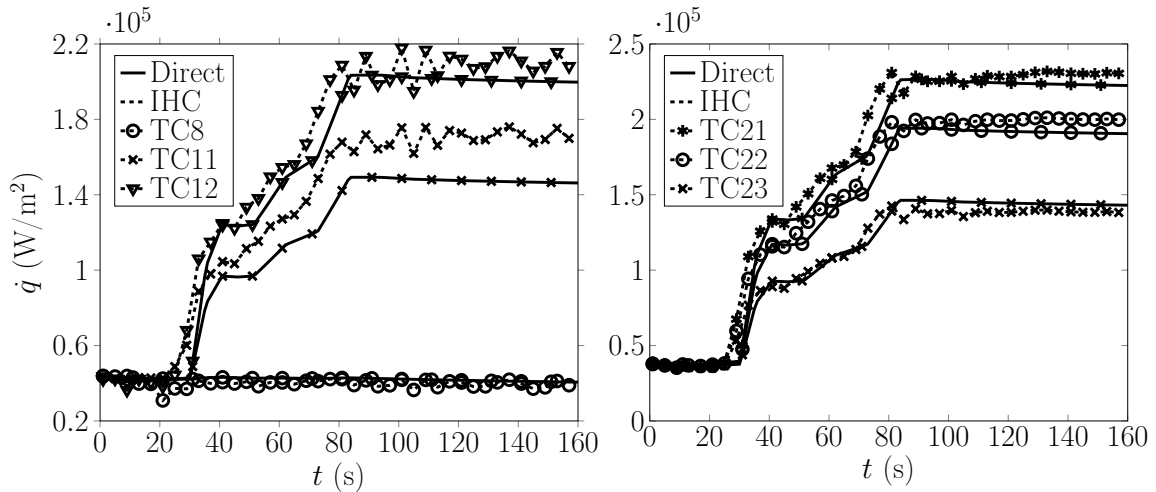


Figure 6.3: IHC validation. Transient heat flux data for different sensors projected on the surface for direct and IHC calculation.

the $t = 100$ s. The lateral locations at the level of $z = 93.5$ mm are added points for the interpolation, while the remaining levels contain actual sensors. The inversely determined results using a constant lateral boundary follow the specified temperatures and heat flux results largely. But the results of the case with zero heat flux boundary condition shows non-physical spatial oscillations, which was also found in the work of Perakis et al. [155]. This is attributed to the fact, that the spline-interpolation is constrained to zero heat flux at the boundaries, but requires larger values, which are provided at $|y| < 25$ mm and led to the oscillations. Integrating or averaging the heat flux profiles along the y -direction might lead to proper integral or averaged heat fluxes. 2D temperature and heat flux distributions at $t = 100$ s corresponding to Fig. 6.5 are provided in the appendix Fig. E.1.

Based on the conducted validation, the constant lateral heat flux boundary condition was considered more appropriate for the inverse calculation of the heat released to the test section wall.

6.4.1 Error analysis

Assuming the data was acquired from TC measurements, an error analysis was performed. The focus of the analysis was the effect of measurement errors on the final IHC results. As the Jacobian matrix was constant, the calculation was straightforward. A detailed description of some error sources and the conduction of the analysis is found in Perakis et al. [155]. The IHC based on TC measurement was subject to following, temperature-independent errors:

Sensor accuracy: The TC accuracy is generally specified by the manufacturer based on the type and tolerance class of TC. Type K TC of class 2 as applied in this work were specified with a accuracy of ΔT_a of ± 2.5 °C.

Sensor precision: The transient temperature data are superimposed by random noise originating from the TC and the data acquisition system (voltage conversion and amplification). An error of $\Delta T_p = 0.2$ °C was estimated from the standard deviation of measured data.

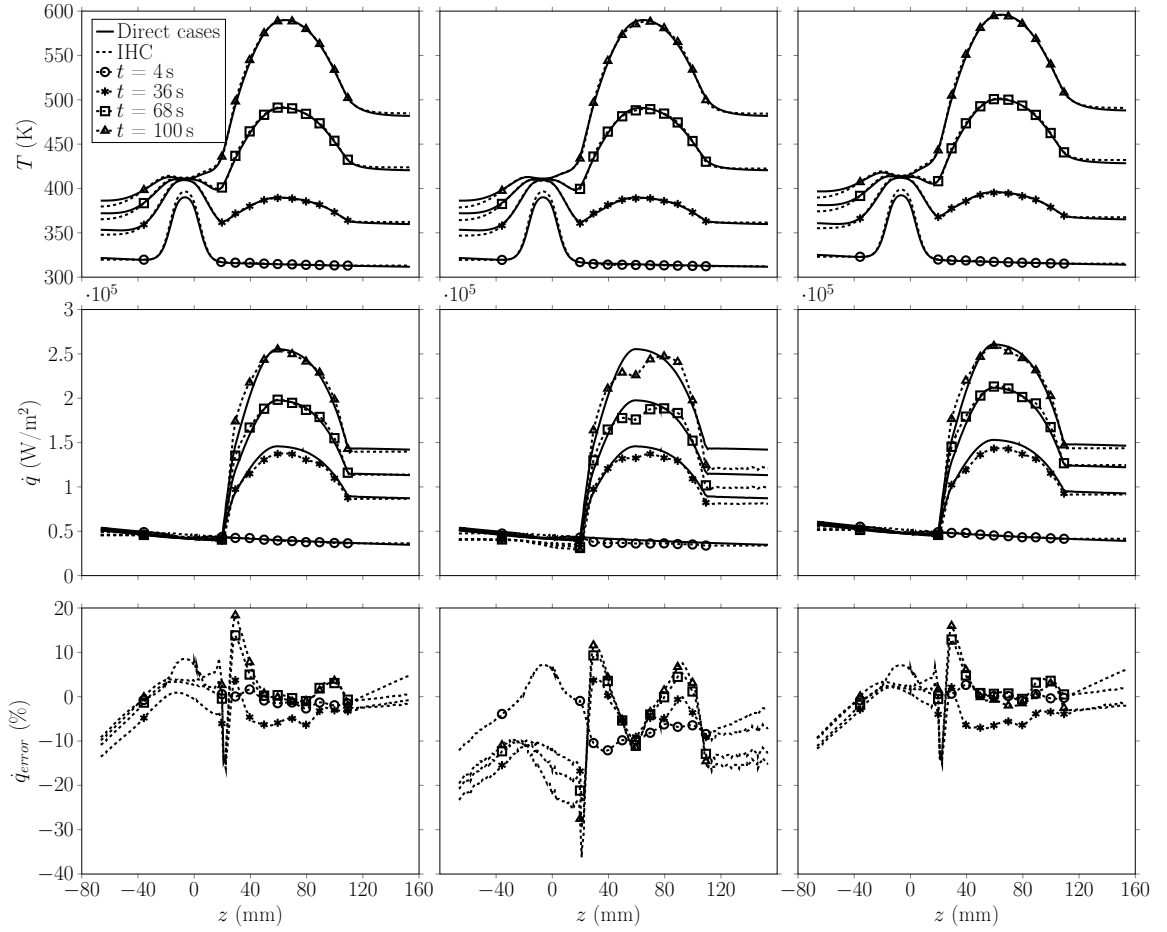


Figure 6.4: IHC validation. Centerline temperatures and heat fluxes. Left: 1D heat flux and constant lateral boundary condition. Center: 2D heat flux and zero lateral boundary condition. Right: 2D heat flux and constant lateral boundary condition.

Temperature module accuracy: According to the manual of the temperature module, the accuracy is $< 1^\circ\text{C}$. Thus, a systematic error of $\Delta T_{mod} = 1^\circ\text{C}$ was assumed.

Further, the heat flux augmentation depends on the temperature difference. Thus, each error source was multiplied by a factor of 2. The total temperature uncertainty is $\Delta T_{tot} = 7.4^\circ\text{C}$. According to the propagation of uncertainties and based on the linearization principle of the temperature, the heat flux error, \dot{q}_{error} , resulting from different inaccuracy sources was obtained from:

$$\dot{q}_{error} = \sqrt{(\mathbf{J}^{-1} \cdot 2\Delta T_a)^2 + (\mathbf{J}^{-1} \cdot 2\Delta T_p)^2 + (\mathbf{J}^{-1} \cdot \Delta 2T_{mod})^2} \quad (6.18)$$

Usually, it is of interest to express the error relative to a temperature difference ΔT_i , for example due to near-wall heat release:

$$\Delta \dot{q}_{rel,error,i} = \frac{\dot{q}_{error,i}}{\mathbf{J}^{-1} \cdot \Delta T_i} \approx \frac{\Delta T_{tot}}{\Delta T_i} \quad (6.19)$$

where i is the i -th sensor and ΔT is the calculated temperature difference between the state before and during the heat flux increase to the surface. The reciprocal function of Eq. (6.19)

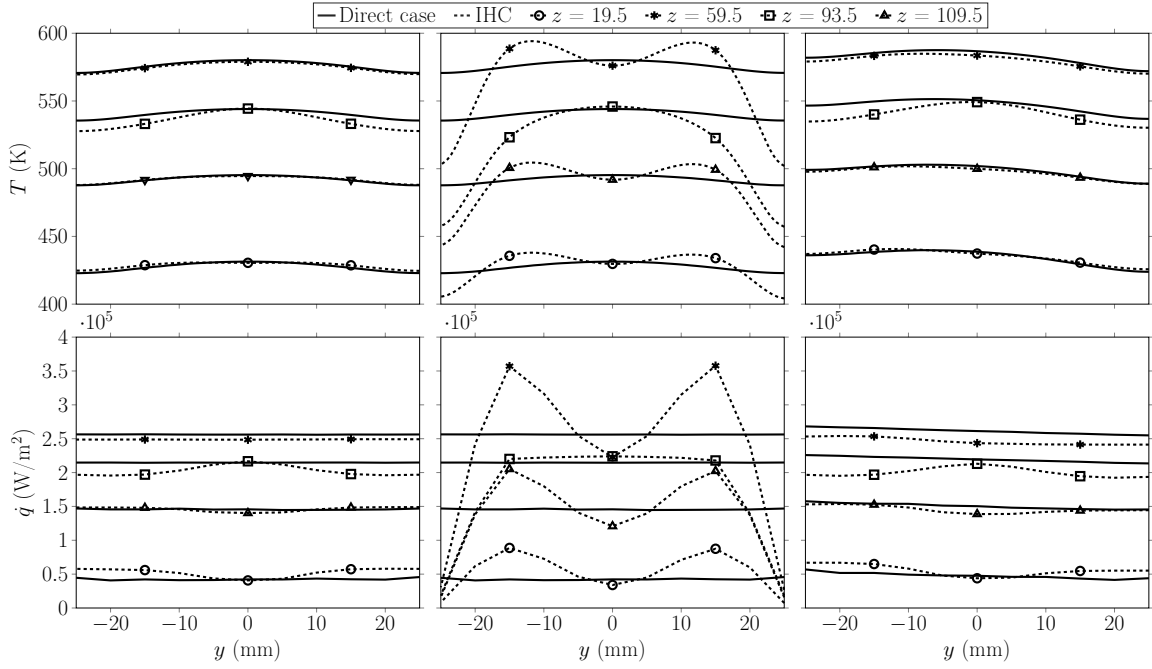


Figure 6.5: IHC validation. Lateral properties at $t = 100$ s. Left: 1D heat flux and constant lateral heat flux boundary condition. Center: 1D heat flux and zero lateral heat flux boundary condition. Right: 2D heat flux and constant lateral heat flux boundary condition.

is plotted in Fig. 6.6. Large errors around 15 % were expected at temperature differences up to 50 K. Thereafter, the error reduced to 7.4 % for temperature augmentations of 100 K.

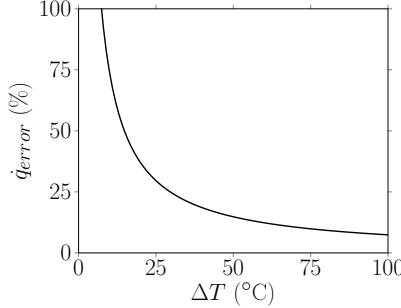


Figure 6.6: IHT error resulting from constant temperature deviations.

There are also errors, which depend on the actual temperature level and sensor position. Material data inaccuracy is one of this error type. Material data of Hastelloy C22 block was obtained from the manufacturer's data sheet [7]. However, inaccuracy of density ρ , heat capacity c_p and thermal conductivity k may exist and affect the IHC calculation. These properties determine the thermal diffusivity, $\alpha = k/(\rho c_p)$. Thus, two direct simulations with the same thermal boundary conditions, but one with altered conductivity of 5 % ($k_0 + \Delta k_0$), were performed and the temperature difference $\Delta T_k = T(k_0) - T(k_0 + \Delta k_0)$ was considered for the error analysis. Between the temperature range of 293.15 K to 600 K, discrepancies up to 7 K emerged, resulting from the temperature dependency of the material properties. Because of a lack of knowledge of the material property uncertainty, this error type was

unconsidered.

Another significant error source results from incorrect sensor positioning. The error magnitude is large for small temperature changes. To install the TC, blind holes were machined into the wall element with the locations summarized in Tab. E.1 and Tab. E.2. The exact determination of the x -location was challenging due to the small diameter and drilling depths. To estimate the effect of measurement inaccuracy, the temperature difference from two x -locations of the direct simulation was considered as: $\Delta T_x = T(x) - T(x + \Delta x)$, where Δx was set to 0.5 mm. Within the temperature range of 293.15 K to 600 K, the position changes resulted in errors up to 9 K.

Compared to the case of Perakis et al. [155] (capacitively cooled copper test section), the IHC calculation in this work resulted in larger errors, due to the low thermal conductivity of the Hastelloy material and consequently higher temperature gradients. Further, in the setup of Perakis' work, combustion of fuels with pure oxygen at elevated pressures were conducted, leading to significantly higher temperatures and heat fluxes and thus to lower relative errors, compared to the reacting jets in an air cross flow in this work.

Other neglected issues originate from potentially insufficient sensor-surface contact, wiring of the sensors and from the accuracy of the data acquisition system.

6.4.2 Stabilization procedure

Since the inverse heat conduction is of ill-posed character, it is prone to fluctuations in the input data (noise), location errors of the TC's, spatial resolution of the input data, material property discrepancies, interpolation schemes, inaccurate boundary conditions, insufficient sensor to surface contact, etc. Even the inverse recalculation of a predefined case leads to instabilities. These instabilities appear among other things as nonphysical spatial temperature and heat flux oscillations. Such an effect is shown in Fig. 6.7. The centerline surface

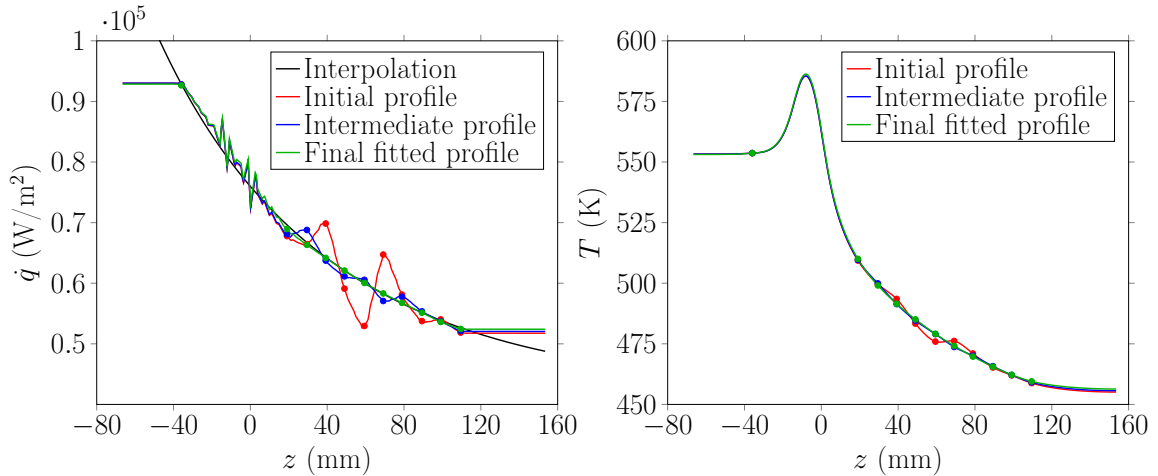


Figure 6.7: Effect of position variation. Left: heat flux profiles. Right: temperature profiles. Markers indicate sensor axial positions.

results correspond to the optimization process of experimentally obtained temperature data with the current geometry and sensors. Here, only hot exhaust gas streamed through the test section without secondary fuel injection. Performing the IHC as described so far with the TC at the locations given in Tab. E.1 and in Tab. E.2 yielded in the red curves. The

temperature profile exhibits a wavy shape and the instabilities are even more pronounced in the heat flux profile. To stabilize the procedure or rather smooth the profiles, the design of the test section and the experimental process were taking advantage of. First, the test section wall was basically a vertically aligned flat plate. Second, during the warm-up period of an experiment, only hot gas streamed over the flat plate surface leading to convective heat transfer. Generally, the convective heat flux \dot{q} is proportional to the heat transfer coefficient h , which is related to the local Nusselt number. According to Nusselt number correlations for forced convection [145], h is proportional to the local position along the plate by z^{-n} , where $n = 0.5$ for laminar flows and 0.2 for turbulent flows. Based on this fact, the wavy heat flux profile in Fig. 6.7 was corrected utilizing the position dependency of the IHC. In short, the instabilities which may result from different sources were converted into sensor location variations. The x -positions of the TC were altered iteratively until the heat flux profile converged to a predefined curve. This optimization scheme is described by the flow chart in Fig. 6.8. The routine works as follows:

- Solve the IHC problem considering a 1D heat profile and only the centerline TC for the warm-up period, e.g. up to 5100 s and extract the centerline temperature and heat flux profiles, see red curves in Fig. 6.7.
- Generate an interpolation curve assuming $h \propto z^{-n}$. The objective was to map the heat flux profile to the interpolation.
- Calculate a sensitivity matrix for the position variation, referred to as spatial Jacobian matrix. This was a time consuming step. Each TC x -location (TC8 to TC23 in Tab. E.1) was altered by an $\varepsilon_x = 10^{-5}$ m and the IHC process was performed for a number of time steps, e.g. 5000 s to 5100 s. The subsequent IHC calculation was necessary, as the thermal Jacobian matrix changed with varying x -location.
- After the variation of each x -location, a spatial Jacobian matrix was determined, based on Eq. (6.5). This matrix described how the heat flux at each location changed, when the x -location was varied.
- Finally, the first position variation was applied according to the NR, LM or CG method with the sole difference, that the x -locations were the parameter vector \mathbf{P} of interest.
- Perform the IHC again for 5000 s to 5100 s and compare the heat flux profile to the interpolation profile.
- If the spatial objective function $S_x(\mathbf{P}) < \varepsilon_x$, then the spatial optimization process was finished, otherwise another iteration was conducted starting from the beginning.

Generally, around 6 iterations were necessary and yielded in a maximum position variation of around 0.4 mm for TC16. The convergence process is demonstrated in Fig. 6.7. The heat flux profile approaches the interpolation. Thereafter, the entire IHC calculation was performed with the new x -locations.

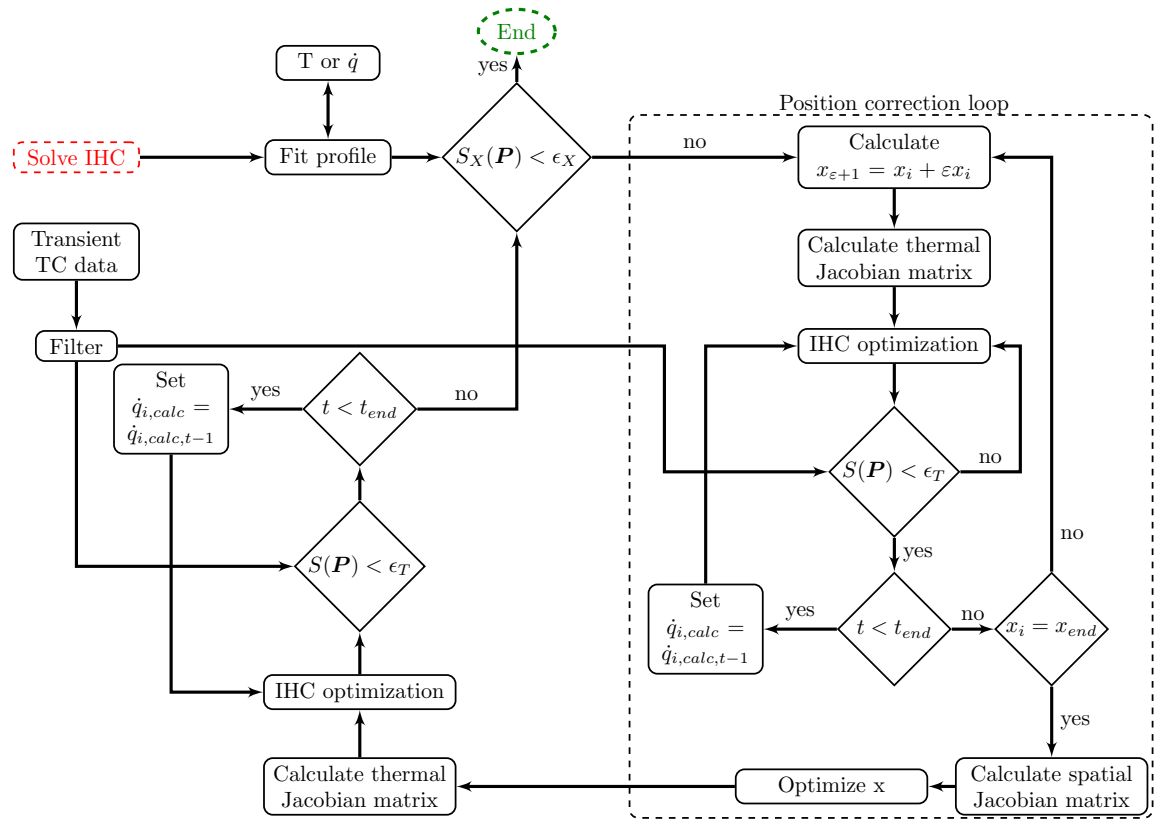


Figure 6.8: Calculation process of inverse position correction.

Chapter 7

CFD Setup

Experimental investigation generally provides access to only a small number of variables. The measurements might require sophisticated, costly techniques, which in turn are often applied non-simultaneously. With improving computational power and increasing capacity over the last decades, numerical simulations moved into the focus and present a meaningful approach to gain insight into specific properties, especially in combination with experimental data for validation. Therefore, additional combustion simulations were conducted for some selected cases to support the experimental findings. The fluid domain was meshed in ICEM, while the CFD simulations were performed in Fluent. Both tools are part of the commercial software Ansys [12]. The simulations were based on the Reynolds-averaged Navier-Stokes (RANS) equations - an approach to calculate mean flow characteristics. However, in a combustion process the transport equations for enthalpy and for the species have to be solved in addition. Further, as the density is subject to variation due to significant temperature change, the conservation equations are Favre-averaged, which is a mass-weighted averaging approach of the flow quantities. Though, the term *RANS* is not entirely correct. Nonetheless, it is used in this study to remain in accordance to the literature.

Over the last decades different RANS models have been introduced to simulate the mean properties of a turbulent flow field. Widely applied and popular RANS turbulence models are the two-equation models. Here, the turbulence is represented by two quantities, namely the turbulent kinetic energy k and the rate of turbulent energy dissipation ε [196]. Two additional transport equations are solved alongside the conservation equations for these properties. The models are often tailored for specific flow conditions and configurations. A recommended model for flows subject to pressure gradient, recirculation zones and to freestream mixing, with well resolved boundary layers without near-wall treatment by a law of the wall is the Menter shear stress transport (SST) $k-\omega$ -model. As the JICF configuration contains such flow complexities, this model was chosen without any modification of the model constants [196].

During a combustion process, additional energy is released to the system from chemical reactions and the species composition changes - some species are consumed while others are formed. Thus, the transport equations for enthalpy and species contain source terms, which are based on the reaction rate term $\dot{\omega}$ of Eq. (2.34). The main task in RANS combustion modeling is the appropriate physical description of these source terms and its coupling to the flow field, namely to the turbulence. An interesting straightforward model for non-premixed combustion which takes into account the turbulence-chemistry interaction is the Eddy Dissipation Concept (EDC) [123, 133]. This model is based on the energy cascade

approach, shown in Fig. 2.3. The basic idea is that in turbulent flows chemical reaction occurs in regions where turbulent kinetic energy is dissipated. It is assumed, that the large eddies break up into smaller eddies and the reactants mix on the small-scale, molecular level. Those regions are referred to as fine structures with a characteristic size in the order of the Kolmogorov length scale. Here, the fluid domain is divided into the reacting, fine scale volume fraction $\gamma^* = \gamma^3$ and the inert surrounding zone volume fraction $\gamma^0 = (1 - \gamma^3)$. The reacting time scale and length scales are described in terms of the turbulence properties k and ε , while the reaction rate is obtained from Eq. (2.34). Considering a PSR, the composition of the reacting volume is calculated. For a more stable and computationally efficient calculation, the reacting volume is treated as a PFR. Another benefit of the EDC is its ability to incorporate detailed chemical mechanisms like the GRI-Mech 3.0 [153] for CH₄ combustion, which may be important to account for different phenomena, such as ignition delay times. A chemical mechanism is a list containing the (intermediate) species and the elementary reactions, with associated rate and thermodynamic data. However, for each species introduced by the selected mechanism an individual species transport equation has to be solved accounting for the elementary reaction alongside the other conservation equations. This may lead to a complex system of equations and to high, inefficient computational efforts. A solution to reduced simulation time is to use reduced chemical mechanisms, referred to as skeletal mechanisms, where reactions almost at chemical equilibrium and species in quasi steady state are removed. In this work, the so-called Lu30 skeletal with 30 species and 184 reactions was used for CH₄/air and H₂/air CFD simulation, derived from the detailed GRI-Mech 3.0 with 53 species and 325 reactions [27, 127]. For C₃H₈/air CFD combustion simulations, a mechanism containing 37 species and 129 reactions reported in [135] and derived from the so-called San Diego Mechanism was used.

This chapter provides the details of the CFD simulations without modifications of the available models. A brief summary of the relevant theoretical background and governing equations is provided in the appendix D. For a further detailed, comprehensive discussion, the reader is referred to the corresponding literature [100, 159, 196, 198].

7.1 Numerical domain and settings

For the numerical simulation a structured mesh was used as presented in Fig. 7.1. The mesh corresponded to the fluid domain of the test section in Fig. 5.4 for normal injection, which was the subject of the CFD investigation. In order to reduce computational time, only a section of the original test section was considered. This included a reduced region upstream of the injection orifices and a reduced width of only 15 mm, which contained only 3 of the 5 nozzles. Thus, a symmetry boundary condition was applied to the lateral planes.

For accurate results near the surface, the k - ω -SST model required a mesh where the first grid point was located within the viscous sublayer. In terms of non-dimensional parameters, this corresponds to the dimensionless wall distance $y^+ < 1$. This is due to the fact, that the k - ω -SST model does not apply a wall function. Instead, the near-wall region is resolved. The downsides are increased computational time and in some cases convergence difficulties. y^+ depends on local flow properties and can only be estimated in advance to the actual simulations. Therefore, the original mesh was iteratively refined using the adaptive refinement option of Fluent. Here, after a user-specified number of iterations, Fluent checked the current local y^+ value of the hot surface and split those cells accordingly which did not meet the user-defined criteria $0.1 \leq y^+ \leq 1$.

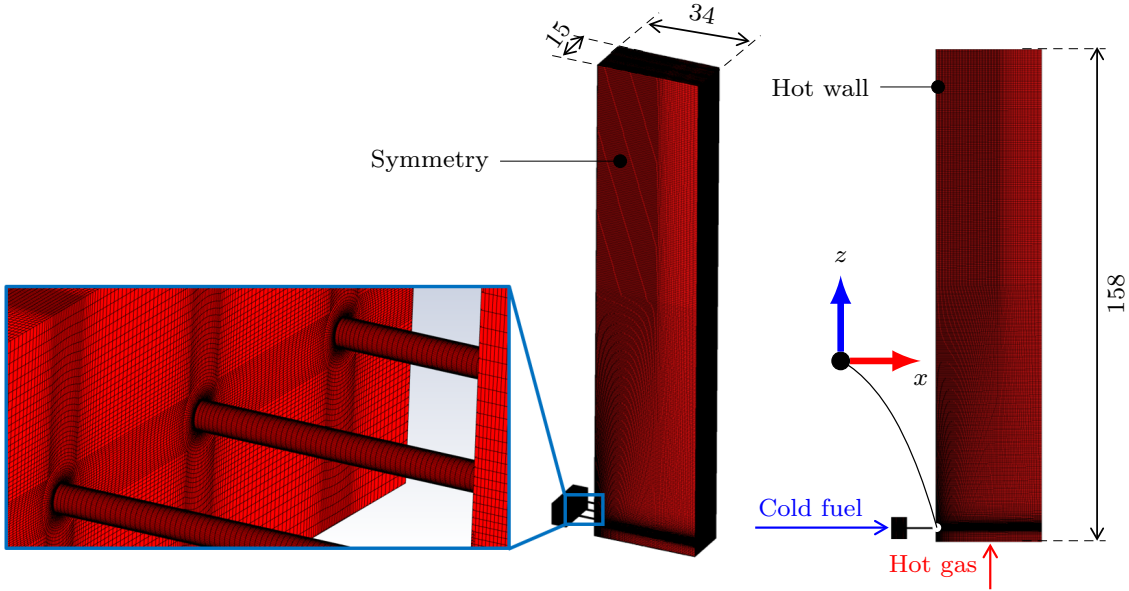


Figure 7.1: Domain for CFD simulations. Units in mm.

For the spatial discretization of the conservation equations in section D of the appendix, a second order scheme was selected. Convergence was monitored based on the residuals, which were in the range of $1e^{-4}$ to $1e^{-8}$, and based on monitoring points positioned at different locations of the domain. The absolute variations of the properties, namely temperature, velocity and OH concentration, were $< 1\%$ from iteration to iteration.

An important procedure in the field of RANS simulation is the mesh sensitivity analysis. For this purpose meshes with 3.9 M, 7.6 M, 14 M and 24 M nodes were tested for one of the cases. Temperature and OH mass fraction values of different monitoring points were plotted against the mesh node numbers, as shown in Fig. D.1 in the appendix. The mesh with 14 M nodes was selected as a trade-off between accuracy and computational time.

Chapter 8

Experimental and Numerical Results

This chapter provides the final experimental results obtained on the new test bench. First, non-reactive results are presented which served to characterize the inert flow field. Then, the corresponding near-wall experiments are analyzed by means of optical measurement results as well as by means of heat flux calculations. Some of the results were presented and published amongst others in [39, 40]. Reactive CFD simulations support the investigation. As described earlier, the origin of the coordinate system when plotting the data was shifted to the outlet of the center orifice. Further, the spatial coordinates were scaled by the corresponding orifice diameter. Using non-dimensional coordinates is a common practice to relate the dimensions of the problem to the size of the injection orifice. 2D averaged optical images resulted from the time-averaging of a number of instantaneous shots.

Numerical characterization of the crossflow and combustion modeling of a reacting jet using state of the art methods was conducted at the institute and published by Fischer et al. [61].

8.1 Non-reactive PLIF experiments

The setup introduced in section 5.2 and the described geometries in Fig. 5.7 and Fig. 5.6 were used for isothermal investigation of the jet flow field. Air was selected as the main flow fluid and as injection fluid. Fluoroketone was introduced only into the jet flow, acting as a carrier gas. The seeding of the tracer was realized by using the principle of a bubble column reactor. A closed vessel partially filled with liquid state fluoroketone was placed inside a water bath of constant temperature (293.15 K). Dry air was directed into the liquid part of the vessel, while fluoroketone containing air was removed from gaseous part of the container. The seeded air was then directed to the test section in Fig. 5.4 and discharged into the crossflow.

The idea behind this non-reactive analysis was to take advantage of the similarity concept and determine the crossflow characteristics and the jet structure under similar momentum ratios and main flow Re-numbers as in the reactive experiments. Thus, it was assumed:

$$Re_{d,i} = \left(\frac{\rho u_d}{\eta} \right)_i d_h = \left(\frac{\rho u_d}{\eta} \right)_r d_h = Re_{d,r} \quad (8.1)$$

and:

$$I_i = \left(\frac{\rho u_D^2}{\rho u_d^2} \right)_i = \frac{(\rho u_D^2)_f}{(\rho u_d^2)_r} = I_r \quad (8.2)$$

where i and r denote inert, isothermal conditions with air and reactive conditions, respectively, and f the reacting fuel properties. The variables d_h (51.32 mm) and D (0.55 mm and 0.4 mm) are the test section hydraulic diameter and the injection orifice diameter, respectively. The same geometry and configuration were used for the inert and reactive experiments. As the cold flow viscosity was lower and the density larger than in the reactive case, the crossflow velocity was subject of adjustment to maintain similar Re-numbers. At the same time, to obtain the same momentum ratio, the jet velocity was varied.

8.1.1 Crossflow characteristics

The characteristic of the crossflow plays an important role. Therefore, the HGG with mounted test section was supplied with a constant air mass flow and a hot-wire system with a 1D sensor in combination with a 3D motorized positioning system was utilized to measure the axial velocity distribution without injection. The system was operated in constant temperature mode, also referred to as constant temperature anemometry (CTA). Working principle and reviews of this method can be found in literature ([99, 148, 185, 187]). In short: The CTA uses the thermoelectric principle. Specifically, the temperature of the wire is kept constant above the environment temperature. Changes in the flow velocity lead to variations in the cooling effect of the wire and thus a relation between the heating voltage to the wire and the flow velocity can be derived based on the heat balance, which results in a calibration curve. The applied system (StreamLine with 1D probes 55P11 from Dantec Dynamics) was successfully applied and validated by Fischer et al. [62]. Fig. 8.1 shows the spatial pattern used for the discrete point measurements at an average, hydraulic diameter based main flow Reynolds number Re_d of around 7600. The mentioned figure corresponds to the top view of the test section, see Fig. 5.2 and part a of Fig. 5.3. The downstream position is described later. Additional measurements at different main flow Reynolds numbers were conducted for a smaller area, indicated by the red diamond and square shape markers. The coordinates were scaled by $D = 0.4$ mm. The probe was moved point-by-point and the instantaneous velocity was recorded for 5 s with a frequency of 50 kHz. Tab. 8.1 gives an overview of the

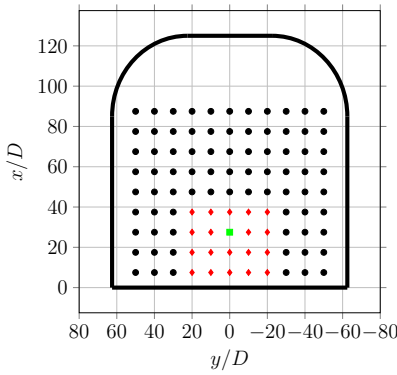


Figure 8.1: The discrete positions of the hot-wire measurements. Coordinates normalized by the angled orifice diameter $D = 0.4$ mm. Diamond shaped points were measured at different main flow velocity.

results for the square shaped marker. The velocity \bar{u} is the time averaged velocity, the Re-number Re_d was determined from the hydraulic diameter of the test section and supplied air flow. The turbulence intensity TI , integral length scale l_0 and the Kolmogorov length

Table 8.1: Crossflow boundary conditions of tracer experiments.

\bar{u} (m/s)	1.6	2.2	3.1	3.8	4.4	4.5	6.9
Re_d	5100	7600	10000	13000	15000	18000	28000
TI (%)	4.3 (4.6)	4.0 (4.6)	4.5 (4.7)	4.6 (4.7)	4.5 (4.8)	4.8 (5.0)	7.0 (6.7)
l_0 (mm)	9.8 (15.3)	11.0 (12.9)	12.8 (12.5)	7.5 (11.4)	5.6 (10.3)	6.8 (10.0)	7.6 (12.1)
l_k (μm)	572 (590)	458 (426)	360 (341)	261 (283)	223 (246)	220 (231)	129 (147)

scale l_k were determined from Eq. (2.15) - Eq. (2.18) using a code from Fischer et al. [62]. Explicitly, the TI was determined from the ratio of the standard deviation of the velocity and the time averaged velocity assuming isotropic conditions using Eq. (A.3), where n is the number of measured values, here $5\text{ kHz} \times 5\text{ s} = 250000$. Spatially averaged properties for the area marked by the diamond shaped markers are included in brackets. Up to a main flow Reynolds number of 18000 the turbulence intensity was between 4 to 5%. For the last case, the turbulence intensity increased to around 7%. This was probably due to higher influence of the flame breaker inside the HGG and its turbulence generation. The spatially averaged integral length scale (largest eddies) was in the range of 10 to 15.3 mm and seemed to correlate with the hole diameter of the flame breaker, which was 15.5 mm. With increasing Reynolds number the Kolmogorov length scale (micro scale) and thus the size of the smallest eddies was decreasing to a value of around $147\text{ }\mu\text{m}$. The development was in accordance with reported results in literature [169] and corresponds to the relations found in Eq. (2.18). These small scales pose a challenge for optical measurements when small scale resolution is required.

The 2D results corresponding to the complete pattern of measurement points shown in Fig. 8.1 for different downstream positions are presented in Fig. 8.2. The height $z/D = -166.25$ was located at the inlet of the test section, $z/D = 0$ was at the height of the injection orifice and $z/D = 83.75$ was downstream the injection location. As the time-averaged velocity plots indicate, there was a spatial inhomogeneity in the negative lateral direction. This flow structure was presumably caused by the ceramic elements within the combustion chamber and by the asymmetrical arrangement of the flame breaker holes as described in section 5.1. The ceramic elements might have led to different blockage of the flame breaker holes and to non-uniform flows through those. The velocity slightly homogenized in the downstream direction and the effect of the boundary layer formation seemed to manifest. A similar inhomogeneous distribution was found in the turbulence intensity spatial structure. Note, the high intensity values of 8% at the boundaries may be the result of flow detachment from the exit nozzle of the HGG. As the flow entered the exit nozzle of the HGG it faced the edge of the nozzle and formed a recirculation region, which generated turbulence. No significant turbulence decay such as a power law was observed in downstream direction compared to investigations by Roach [169] or Grzelak et al. [78]. However, these authors investigated initial turbulence levels around 10% behind grids over a range up to $1000 z/d$, with d as the wire diameter of the utilized grids. The energy spectra for the highest and the lowest Reynolds numbers at the position $y/D = 0$, $x/D = 27.50$ alongside the power law in green color ($E(\kappa) \propto \kappa^{-5/3}$, with κ as the wavenumber) for

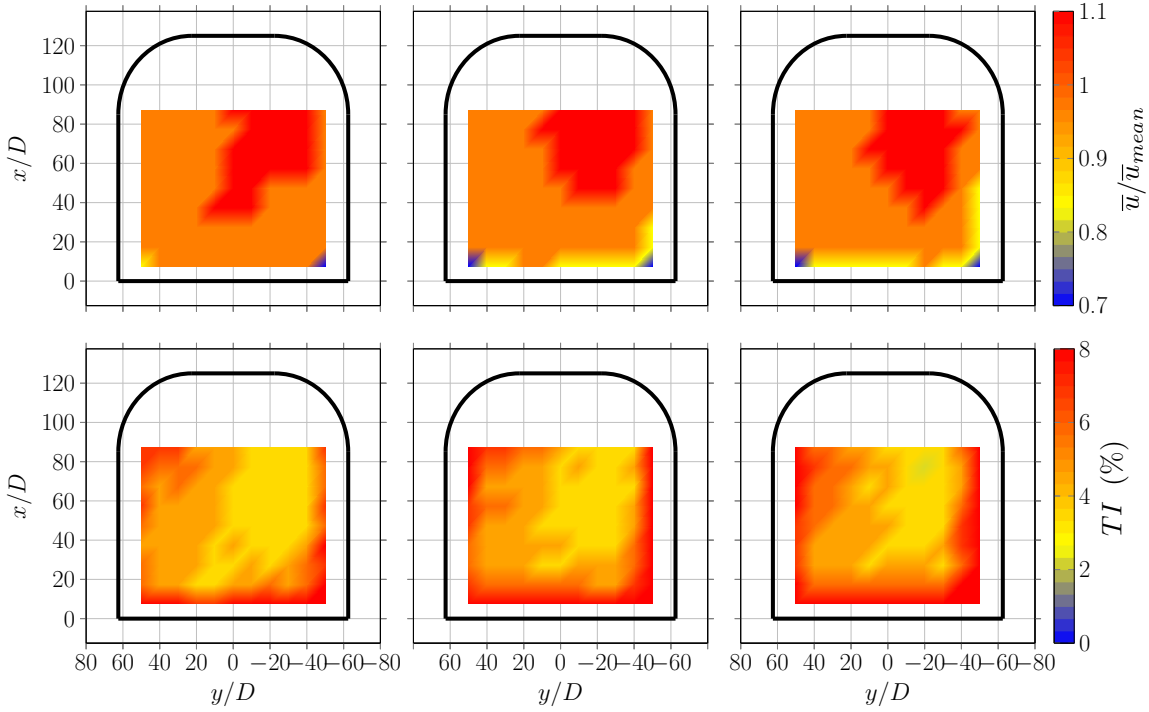


Figure 8.2: CTA results. Top row: normalized time-averaged velocities. Bottom row: turbulence intensities. Positions: $z/D = -166.25, 0, 83.75$. $D = 0.4\text{mm}$ is the orifice diameter.

the inertial range is presented in Fig. 8.3. The analysis was performed by a Fast-Fourier-

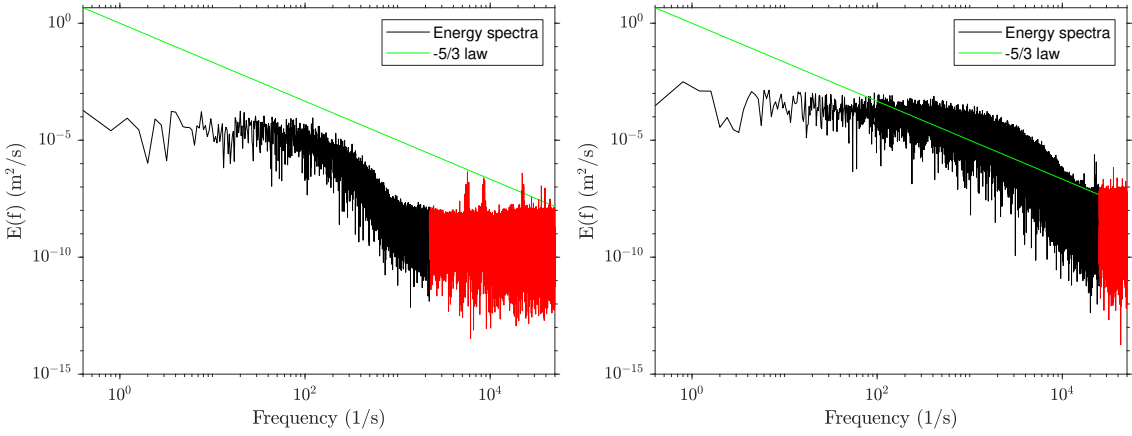


Figure 8.3: Energy spectra at $y/D = 0$, $x/D = 27.50$. Left: $Re_d = 5100$. Right: $Re_d = 28000$. No dominant peak is visible at low frequencies.

Transformation of time-dependent data, as described in [52]. The spectra, especially the inertial range of the energy cascade, shifted to higher frequencies with increasing Reynolds numbers representative for the presence of smaller scale eddies. Here, the maximum relevant frequencies were around $2 \cdot 10^4 \text{ Hz}$, while for the low Reynolds number it was around $2 \cdot 10^3 \text{ Hz}$. The high frequency regions with low energy and strong fluctuations above the relevant

frequencies are highlighted in red. These data values were the result of the high measurement frequency (50 kHz), low velocity fluctuations and of noise. Those do not contribute to the turbulent kinetic energy and could be removed by applying a low-pass filter, if desired. For the sake of completeness they are illustrated here. This behavior was also found in literature [52].

8.1.2 Injection conditions

The boundary conditions of the isothermal investigation with injection are presented in Tab. 8.2 in a summarized form. For a detailed presentation the reader is referred to F.1 of the appendix. The minimum main flow Reynolds number based on the test section

Table 8.2: Injection conditions of the PLIF tracer experiments.

Type	normal		angled		
I	2 - 20	1 - 40	40 - 300	10 - 300	2 - 300
$Re_{D,c}$	229 - 714	290 - 1826	375 - 1019	375 - 2031	300 - 3657
Re_d	15600	28400	7700	15400	28500
Re_z	60300	110000	3000	60000	110000

hydraulic diameter was 7700 (the Re-number based on the local z -coordinate starting from the inlet of the HGG nozzle up to the injection location is included) and above that of the reactive experiments, while the lowest momentum ratio was 1 for the normal injection. The deviation of the Reynolds number was attributed to the small orifice diameters D as further decrease in main flow Re-number required low injection mass fluxes to maintain the momentum ratio. At some point the mass fluxes would reach the lower limit of the mass flow controllers. Also, gravitational effects then may play a non-negligible role on the jet structure. Further, the smaller size of the discharged jet required higher optical resolution. The orifice diameter-based Re-number, except of one case, was found to be in the laminar region. The dimensions of the injection geometries taken from Fig. 5.6 and Fig. 5.7 yielded in a (L/D) of 16.9 and 25 for the angled and normal geometry, respectively, and considering the rule of thumb in Eq. (2.8) the lowest jet Re-number (229) resulted in a minimum value of $(L_{fd}/D) = 11.45$. For the turbulent angled jet, the minimum value according to Eq. (2.9) was 10 and in the current case it was 25. Thus, the velocity profiles of any case were considered as fully-developed. The fully developed flow condition was also validated numerically by Fischer et al. [61] for the angled jet at $I = 10$.

8.1.3 Resolution analysis of the tracer PLIF detection system

As mentioned, the jet orifices had diameters D of 0.4 mm and 0.55 mm. Small orifice dimensions create resolution difficulties for optical analysis. Smith et al. [182] intentionally chose an orifice diameter of 5 mm for normal injection to ensure at least 10 - 20 pixels in the core of the jet. As the authors reported, nozzle diameters of 2, 2.5 and 3.3 mm were too small. In fact, a review of various publications showed that the orifice diameters for this kind of investigation is around 2 - 10 mm and rather shifted to the larger dimensions to ensure the detection and resolution of small structures and vortices [23, 30, 56, 69, 81]. For a regular gaseous jet, Gerold [68] used an orifice diameter of 1 mm.

The minimum required system resolution depends on the Batchelor scale of the flow. As the isothermal JICF was conducted in air, the Batchelor and Kolmogorov length scales were assumed equal ($Sc \approx 1$) and Eq. (2.21) was evaluated. Further, β was set to 1. Due to unknown local jet velocity and diameter in the downstream direction, the calculation was based on the exit Re-number $Re_{D,c}$ from Tab. 8.2 assuming uniform spatial velocity distribution. This led to a conservative estimation of the length scale, as the discharged jet expands and reduces its velocity in general. Especially, the normal injected fluid experiences a 90° deflection, loses its momentum and approaches the crossflow velocity. Under these assumptions, the maximum Batchelor length scale was determined as 0.006 mm for the lowest momentum ratio of $I = 1$, while for the highest momentum ratio of $I = 300$ the scale even reduced to 0.001 mm. Two properties determine the actual resolution of the measurement system: the laser beam thickness and the spatial resolution of the detector (lens and camera resolution). According to section 4.1 the minimum beam waist was 0.09 mm. The spatial resolution of the applied detector system, described in the mentioned section, can be determined from the Rayleigh criterion, which specifies the minimum distance two objects can have to be resolved. However, the maximum possible resolution of lens was 0.07 mm/pixel and the pixel size of the camera sensor was 0.013 mm. So, considering the light sheet dimension and the detector properties, a spatial resolution of the smallest scalar scales was not achieved and a calculation of the Rayleigh value was redundant. There was a factor of 90 between the mixing length scale and the maximum dimension (beam waist). Thus, the following results served for qualitative and comparative purposes of injections from different geometries with focus on the global structure of the jets.

8.1.4 Data reduction and post-processing

For any considered and analyzed injection condition, 100 tracer LIF single shots with a frequency of 4 Hz were recorded. The data reduction process was basically the same as for the OH PLIF images. Each single image was scaled by the measured fraction of laser energy and by a time-averaged light sheet profile recorded before and after the experiment. The obtained data served as the basis for the subsequent post-processing step. To reduce noise and remove artifacts and Mie scattering, an averaged image of 100 background images without injection was removed from each data set. In order to convert the absolute intensity counts into mole fractions in accordance to Eq. (4.9), each intensity image was scaled by its intensity value at the orifice region. Here, highest intensity and thus tracer concentration was detected. Usually, an image may still contain noise from the detection device, which should not be mistaken for intensity information. Hence, a lower cut-off limit of 10 % was applied to all images ($X < 0.1 \rightarrow 0$).

Different methods and criteria were found in the literature to define the trajectory. Some authors extracted it from PIV data [30, 81] or from measured scalar concentration [69, 182]. Determination of the centerline from scalar properties, such as the concentration, required a special procedure. Note, that the jet and the CVP trajectories are distinct entities [30] and the visually determined centerline may be affected by the CVP. Fig. 8.4 (a) shows an averaged image of 100 single images after the data reduction procedure. In a first step, the well-defined angled jet was converted into a binary image and using an edge detection filter in Matlab, the enclosing boundaries were detected. The results are shown in Fig. 8.4 (b) and (c). Generally, a regular jet discharged into a quiescent environment is symmetrical and the line of maximum concentration is at its axis of rotation. However, the current jet did

not meet this condition and the centerline was not located *midway* of the outer boundaries. Further, the definition *midway* of the curves is not self-descriptive for a jet deflected by crossflow (along a vertical coordinate, horizontal coordinate or at a specific angle?). Hence, the enclosing curve facing the crossflow was isolated and served as the starting point for locating the trajectory. As seen on image (c), the contours exhibit a discontinuous shape. Thus, a fitting was applied to smooth the data. Then, the perpendicular line to the curve was found to each location of the enclosing curve, as illustrated on Fig. 8.4 (d). The averaged image was then sampled along each of the normal lines and the maximum intensities were extracted as seen on Fig. 8.4 (e). This initial maximum distribution was improved in a next step. For angled jets, Eq. (2.23) was utilized to find the best fit. Thereafter, an iterative process of locating the maximum intensity along the normal direction of the jet trajectory and fitting to those data was conducted. This is illustrated on the last part of Fig. 8.4, where the trajectory and its normal direction are indicated by s and n , respectively. For normal jets, the power law from Eq. (2.24) was fitted to the centerline by iteratively varying the entrainment coefficient A and the shape coefficient B . A least-square method was used for the fitting process. Around 3 - 4 iterations were required for convergence. A similar procedure to determine the concentration path was also found in literature [30, 69, 102, 182].

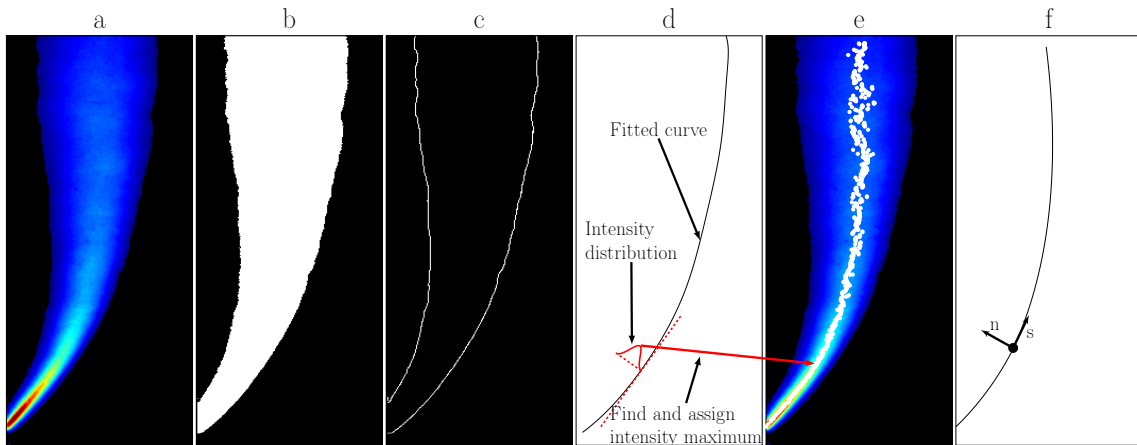


Figure 8.4: Tracer LIF image post-processing steps. a: isolated averaged image. b: binary image. c: enclosing contours. d: maximum intensity perpendicular to the upper contour. e: centerline maximum intensity, f: fitted centerline with path s and normal n direction.

8.1.5 Normal injection

Images of the normal jets in a crossflow with $Re_d = 28400$ are summarized in Fig. 8.5. From left to right the momentum ratio increases for each column as indicated. Instantaneous images are presented in the first two rows, while in the third row averaged images of 100 single images are shown. On single and averaged images high concentration cores and mixed regions are observed. With increasing I the width of the jet core grows in the direction normal to the crossflow. Directly after the deflection the concentration drops to values around 60 %. According to the single images, the core region is only slightly disturbed and the disturbances develop near the transition to the mixed region. As soon as the jet is deflected, it expands, the concentration further decreases and the jet boundaries

become wrinkled due to interaction with the crossflow and shear layer generation. Prior to the deflection point, also some jet material is entrained in the the crossflow leading to a broadened and asymmetrical shape of the jet core, which may be due to shear effects and CVP formation. Injection images in literature exhibit similar structure [182]. Gutmark et al. [81] identified even an inverse flow region beneath the jet area. Due to the orientation of the jet flow to the mainstream, there is a detachment from the surface already for the lowest I . For momentum ratios of 1 and 2 the jet reattaches, as seen on some images. Even for $I = 10$ for example, considering the second single image, the jet appears to reattach to the wall around $z/D \approx 35$ and the jet has an interesting S-shape resulting from global flow instabilities. This is likely due to the reattachment nature of normal jets at high momentum ratio as the interaction with the main flow intensifies. For the largest two momentum ratios, some seeded flow near the wall is observed, but the averaged images indicate a complete detachment from the surface.

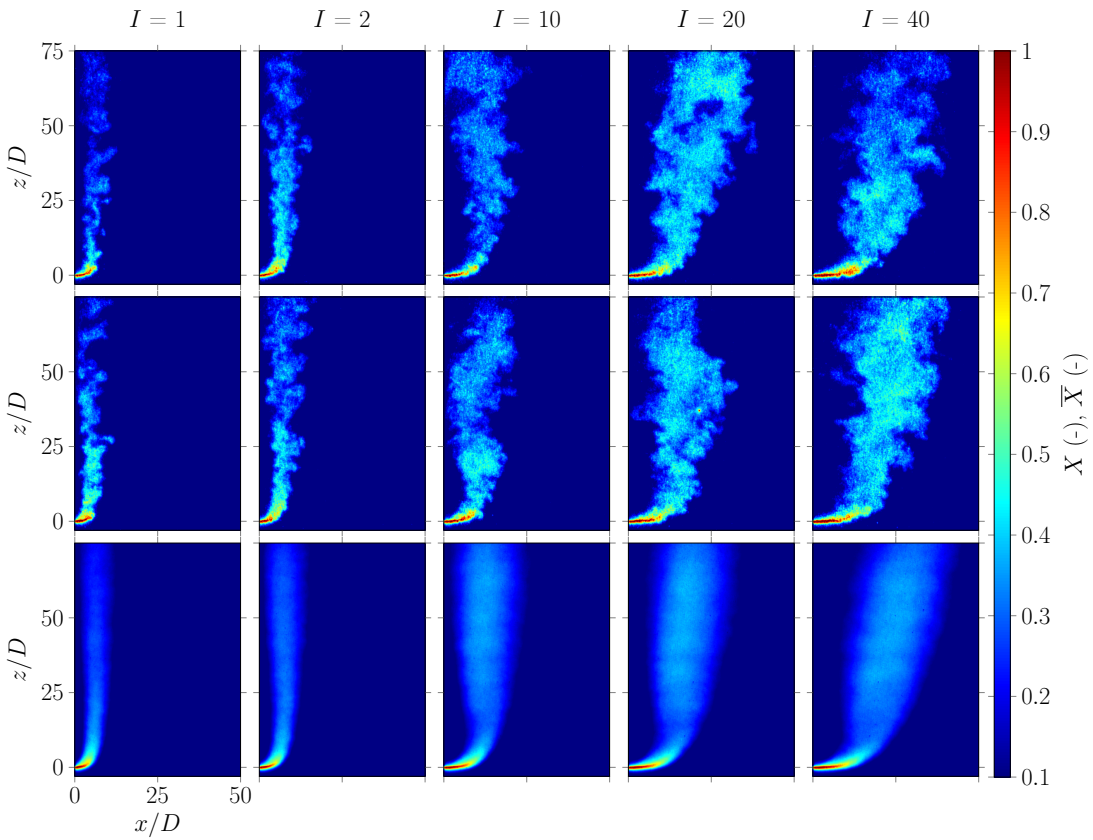


Figure 8.5: Tracer PLIF. Normal injection for different momentum ratios in a crossflow with $Re_d = 28400$. First and second column show randomly selected instantaneous images, third column contains averaged images of 100 instantaneous images.

The corresponding extracted concentration trajectories from the averaged images are presented in Fig. 8.6. Starting from left to right, the jet paths were scaled by D , \sqrt{ID} and ID , respectively, to find the best parameter. Scaling by the diameter solely did not result in any collapsing of the trajectories and there was no similarity observed. The dispersion was smaller for the scaling parameter ID . Beyond $I = 5$, the trajectories were approaching each other. However, the best result was obtained from the scaling parameter \sqrt{ID} , as reported

in many publications and discussed in chapter 2. Still, downstream of $z/(\sqrt{ID}) > 2$, dispersions increase. This can be attributed to different reasons, such as velocity trajectory vs. concentration trajectory, gravitational effects, jet velocity profile, discrepancies in the momentum ratio and eventually due to alignment problems of the laser light sheet. For momentum ratios above 5, a discontinuity was found in the trajectory. It was assumed that this occurred due to misalignment of the laser beam as the jet left the excitation sheet. However, the dispersion was mostly caused by the low momentum ratio trajectories. Recalling the main flow influence factors as mentioned in chapter 2, the trajectory had a higher penetration in the boundary layer in the free stream region. Considering the test section wall as a flat plate, the boundary-layer thickness $\delta_{99\%}$ was estimated from $\delta_{99\%}/z = 0.37Re_{z,\infty}^{-0.2}$ [172]. A scaled thickness of $\delta_{99\%}/D \approx 13$ was calculated. Hence, the trajectories from jets with $I < 10$ were most probably located within the boundary layer and this effect was not considered by the scaling parameters, as also reported in literature [30, 143]. Also trajectories found in the literature from different authors show a wide spread [143].

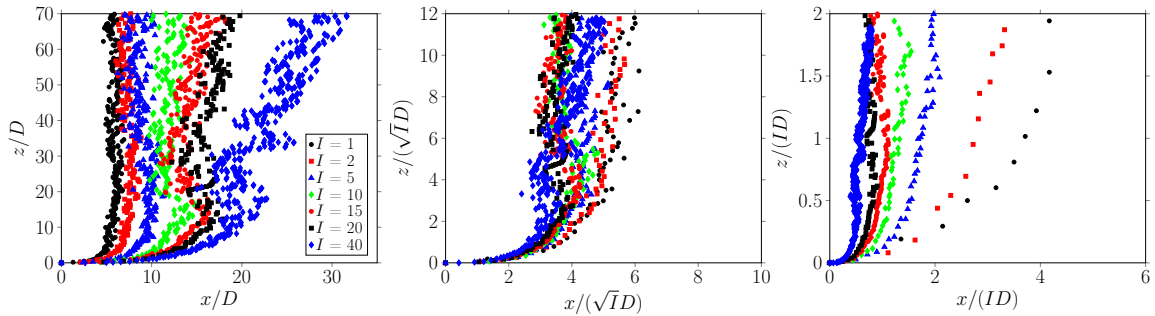


Figure 8.6: Tracer PLIF. Concentration centerlines for normal jets with different momentum ratios in a crossflow with $Re_d = 28400$. Dimensions scaled by D , \sqrt{ID} and ID .

Fig. 8.7 shows the trajectories for two different mainstream Re-numbers. Comparing the jet paths, an increased penetration of the crossflow by the jets is observed in case of low mainstream Re-number presumably due to the larger boundary layer thickness. Further, the two graphs show that the trajectories of high momentum ratios collapse best scaled by \sqrt{ID} but not the jet with low momentum ratio.

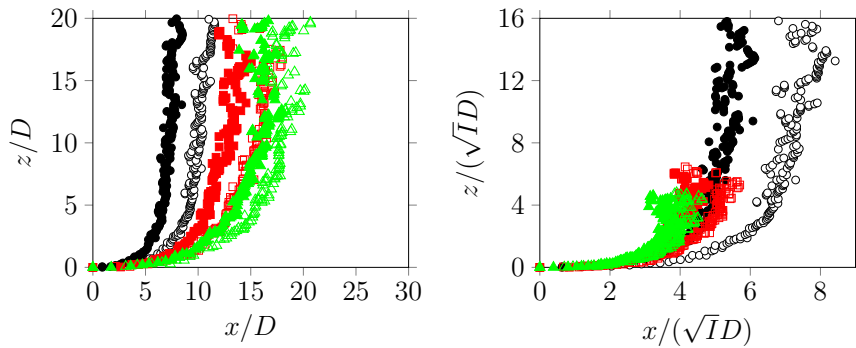


Figure 8.7: Tracer PLIF. Trajectories of three momentum ratios (black 2, red 10, green 20) and two mainstream Re-numbers $Re_d = 15600$ (empty markers), 28400 (filled markers). Results scaled by D and \sqrt{ID} .

An attempt was made to fit Eq. (2.22) to the extracted trajectories and determine the entrainment constant A and the shape constant B . These parameters are useful to describe the path of JICF and to find similarities. The result is shown in Fig. 8.8 for $Re_d = 28400$. The value of B was almost constant and ranged from 0.25 - 0.29 and was similar to reported values in the literature. The penetration constant A on the other hand showed a dependency on the momentum ratio. However, a wide range of values were reported in literature [102, 143, 146, 186]. An error calculation was conducted where the momentum ratio was varied by $\pm 20\%$. No significant changes appeared in the constant B , while the constant A changed by $\mp 8\%$ and had a value mostly above 2.6. This indicates that other factors need to be accounted for beside the momentum ratio, such as velocity profile and boundary layer thickness.

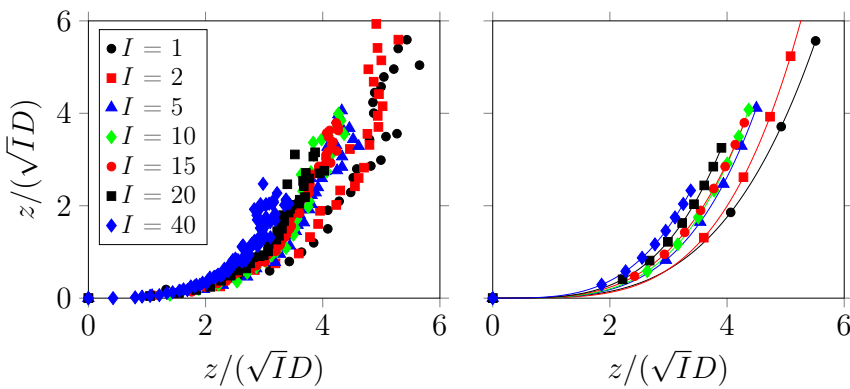


Figure 8.8: Tracer PLIF. Raw and fitted near-field trajectories of normal jets for $Re_d = 28400$ according to Eq. (2.22). $0.25 \leq B \leq 0.29$, while A decreases from 3.42 to 2.65 with increasing I .

For the analysis of the concentration development, the jet trajectory coordinate s was calculated from the x and z coordinate as $s_{i+1} = s_i + (\Delta x^2 + \Delta z^2)^{0.5}$ and the concentration was plotted vs. s . The results for different scaling parameters are shown in Fig. 8.9. There are basically three slopes observed. The first slope with the smallest gradient reflects the jet core length, the second and steepest gradient is the near-field region and the last slope is the far-field. These regions were referred to as vortex interaction region, near-field and far-field by Smith et al. [182]. The latter two regions were connected by the branch point. The best collapsing parameters were D and \sqrt{ID} , while ID scaling even dispersed the curves. The concentration decay in the near-field region seems to scale with $s^{-2/3}$ for low momentum ratio, while the slope approaches to s^{-1} scaling for higher momentum ratios. This may be attributed to intense flow interaction and mixing. After the transition to the far-field, the decay rate drops significantly. In fact, it was reported in literature, that the decay rate depends on geometry and flow conditions [69]. Smith et al. [182] and Gevorkyan et al. [69] conducted similar experiments with normal jets and acetone vapor as tracer. For the near-field trajectory the slope was between s^{-1} and $s^{-1.3}$, while the far field could be related to $s^{-2/3}$. In the present investigation, smaller decay rates were observed.

The PMF, sorted intensity values by size and distributed in discrete intervals, evaluated at different downstream positions z/D (horizontally) for $I = 2$ and 20 at a $Re_d = 15600$ and $I = 20$ for $Re_d = 28400$ is shown in Fig. 8.10. As mentioned initially, the resolution and the size of the jet were the limiting factors of this analysis. Only a small number of 10 - 20

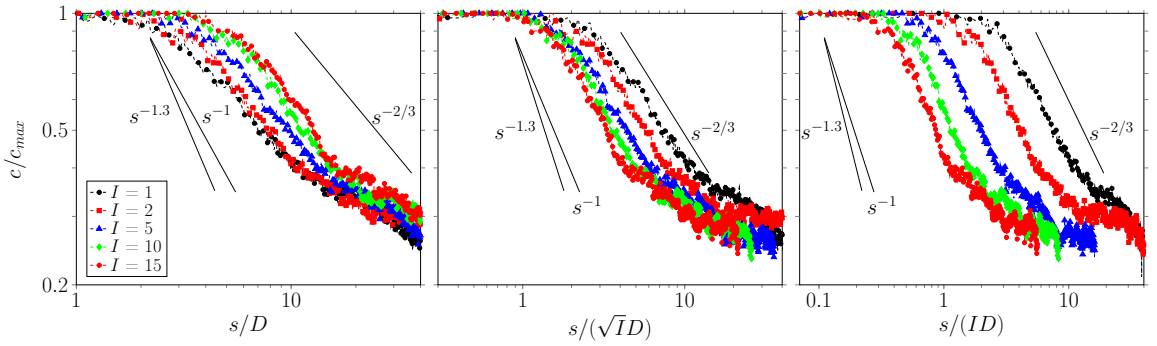


Figure 8.9: Tracer PLIF. Normalized concentration c/c_{max} along the centerline coordinate s in log-log form for $Re_d = 28400$. Data scaled by D , \sqrt{ID} and ID are shown. Power law curves added for reference.

pixels were located within the jet core and diminished the quality. The number of bins for the histogram was estimated as approximately 20. However, 32 bins showed a structured distribution. At the injection location, the PMF has peaks at 0 and 1. This reflected basically the non-mixed state, while values at 0 were rather noise. Going to the downstream direction, a peak develops, gets pronounced, shifts and approaches a final value, which is the mixed state. This structures were found in various publications [28, 49, 69]. Comparing the data of the two momentum ratios at the same crossflow Re-number, the difference was found negligible and marginal. Also an almost identical distribution was observed for the case with increased mainstream Re-number. The small sensitivity of gaseous mixing process on the Re-number was also observed by other authors [134]. The PMF peak shifts at $z/D = 10$ to ξ below 0.5 and the final mixture state of around 0.3 - 0.4 was reached between $z/D = 10$ and 20, which corresponds to the branch point and the far-field, see Fig. 8.9. Above $z/D = 20$ a mixed condition is assumed.

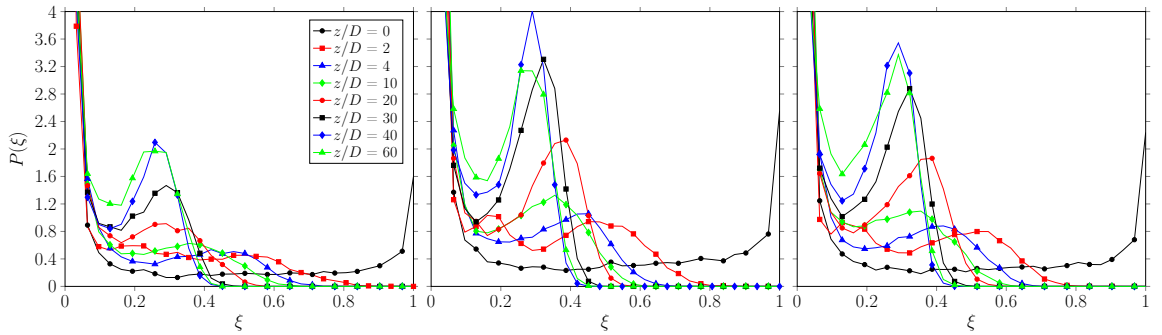


Figure 8.10: Tracer PLIF. Calculated PMF of normal injection for $I = 2$ (left) and 20 (center) at $Re_d = 15600$ and $I = 20$ at $Re_d = 28400$. Data was divided into 32 bins.

8.1.6 Angled injection

Injection experiments with the angled configuration were conducted and evaluated in the same way as the normal injection experiments in the previous section. Fig. 8.11 shows the images for momentum ratios between 2 to 300 at crossflow condition of $Re_d = 28500$. High

momentum ratios were tested to cover a wide range of values. The images are structured

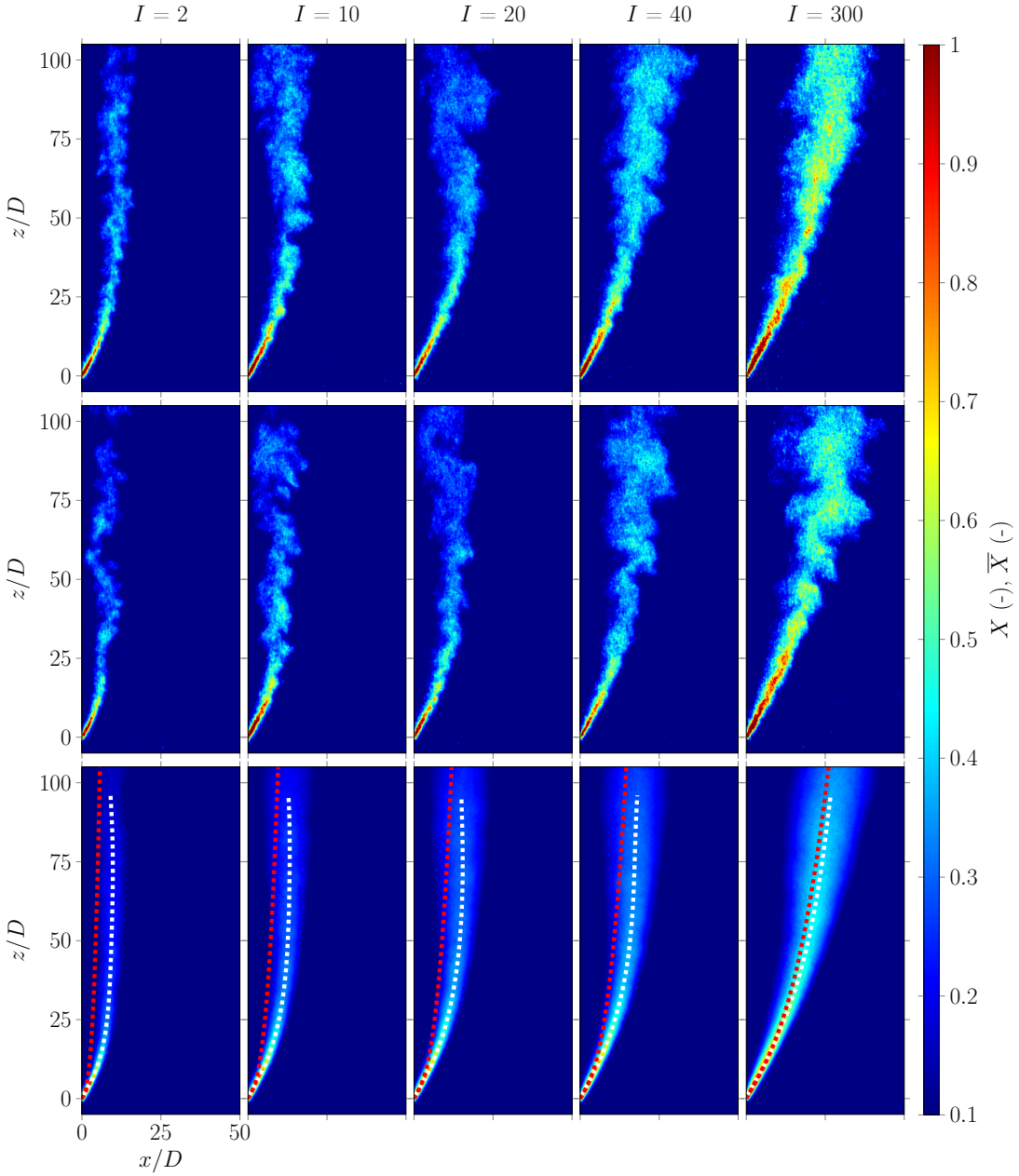


Figure 8.11: Tracer PLIF. Angled injection for different momentum ratios in a crossflow with $Re_d = 28500$. First and second column show randomly selected instantaneous images, third column contains averaged images of 100 instantaneous images. White trajectories are extracted from the images. Red trajectories are calculated based on Eq. (2.23).

and scaled identically as before. The jet exhibits a high concentration core and a subsequent mixed field. With increasing I , the stable core region becomes more pronounced, as observed on the single images. Jet detachment is seen even for the lowest momentum ratio of 2, which is in accordance to the literature mentioned in chapter 2. A clear reattachment is only observed on some instantaneous images for I up to 10 around $z/D > 50$. Due to the

angled configuration, the jet expands in the downstream direction steadily. In contrast to the normal injection, the shape of the concentration distribution in the core region is almost symmetrical. This is presumably attributed to the lower velocity difference between jet flow and crossflow and a weaker CVP generation process. In the far-field, the jet boundaries demonstrate similarities to tangential shear flows rather than to normal jets. The structure seems less wrinkled and more preserved. The highlighted trajectories are nearly independent of the momentum ratio up to $z/D = 10$, indicating an undisturbed and unaffected jet. In the downstream direction the penetration depth increases with the momentum ratio. Calculated trajectories according to Eq. (2.23) are also added to the averaged images. Large deviations are observed between calculated and extracted trajectories, while they match perfectly for $I = 300$. The jets with $I < 300$ penetrate further than theoretically predicted and those jets are laminar. One reason might be the jet velocity profile, which demonstrate higher core velocity and causes the deviation.

The extracted trajectories for different mainstream Re-numbers are summarized in Fig. 8.12. Due to lack of an appropriate scaling parameter, only the D scaling is presented

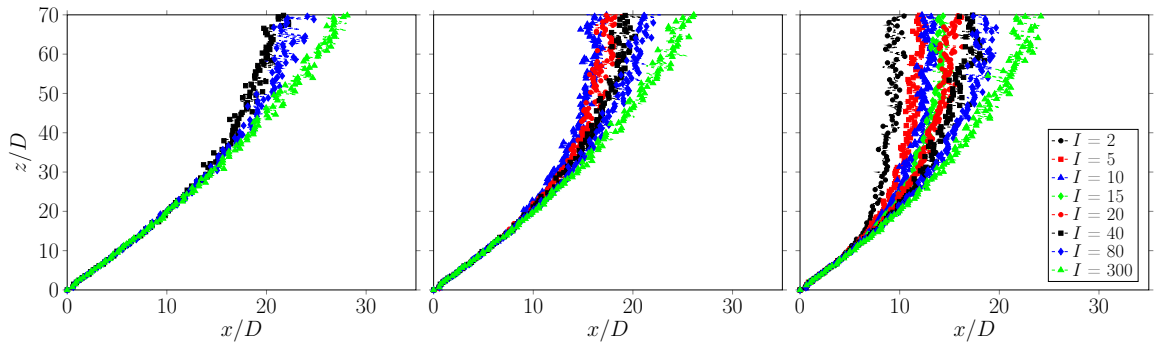


Figure 8.12: Tracer PLIF. Angled injection trajectories for $Re_d = 7700, 15400, 28500$.

in agreement to Eq. (2.23). With increasing main flow Re-number, the far-field shifts to larger x/D values and the penetration increases. The core region is less affected and the overall jet-crossflow interaction is less significant as for the normal injection. Comparing the trajectories to those of normal jets in Fig. 8.6, even though the penetration in the near-field and core region is smaller for angled jets, the penetration downstream at z/D was in the similar range. This is because the normal jet possesses initially a high momentum perpendicular to the crossflow and has the ability to penetrate further. As soon as the local momentum diminished, the jet was deflected and the horizontal penetration depth stayed constant. The angled jet on the other has a low penetration at the beginning, but due to smaller interaction the local jet momentum is preserved for a longer distance.

The normalized concentrations plotted vs. the scaled path coordinate s are presented in Fig. 8.13 on the first and second graph. As for the normal jets, the three regions are also observed here. However, some distinct differences occur. The size of the core region is for both configurations similar, as in both cases the initial maximum concentration of 1 sinks below $s/D = 10$. Compared to the normal jet, the concentration decay rate of the near-wall region is then smaller and corresponds to $s^{-1/3}$ and $s^{-2/3}$. Interestingly, the gradient decreases for increasing momentum ratio. Then, the branch or transition point to the far-field follows, which is significantly further downstream compared to normal injection and less pronounced. In fact, the angled jet has a smooth concentration decay along the trajectory

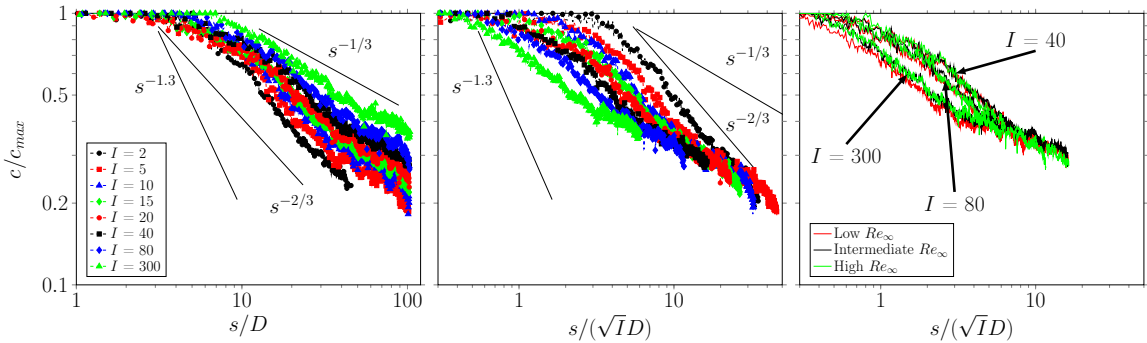


Figure 8.13: Tracer PLIF. Normalized concentration c/c_{max} along the centerline coordinate s in log-log presentation for $Re_d = 28500$ scaled by D (left) and by \sqrt{ID} (center). On the right: concentration centerlines for $Re_d = 7700, 15400, 28500$.

while the normal jet experiences a sudden change during the deflection. Trajectories with same momentum ratio but different mainstream Re-numbers are shown in the right graph of Fig. 8.13. There is no visible effect of the crossflow Re-number on the decay process. However, the curves show the reproducibility and good agreement of the experimental cases.

For the sake of completeness the calculated PMF at different downstream positions are given in Fig. F.1 of the appendix.

Some preliminary conclusion can be given at this point and some of the findings can be related to reactive experiments. Although the increase of mainstream Re-number shifted the trajectory of the jets towards the wall, the effect was small (normal jets were affected directly after the discharge, while angled jets were affected in the far-field) compared to the impact of the momentum ratio. Thus, the latter parameter is of more interest and is straightforward to alternate in the reactive experiments. Further, a noticeable effect of the Re-number on mixing was not observed, at least not for the tested conditions. The normal jets lost the momentum directly after the deflection and expanded, while the angled jets seemed more stable over a larger downstream range. Consequently, the tracer concentration of the normal jet flow was declining with a greater decay rate. Due to this enhanced mixing, normal reacting jets may promote the occurrence of chemical reaction more than angled jets for fuels which require extensive mixing, such as CH_4 . For highly reactive fuels like H_2 , there should be no significant effect. For both injection angles, jet cores of high concentration surrounded by mixed states were observed, which means that chemical reaction will most probably take place in those surrounding regions. The surface distance of the two different injection configurations might also be of importance for H_2 injection. Normal jets detached directly after the injection, which could shift chemical reactions away from the wall. Whereas angled reacting jets may remain in the proximity of the wall and release heat to the surface. The analytical trajectory reconstruction showed deviations from the actual path. However, the method is still a good approach for an initial estimation.

8.2 Reactive experiments

In this section, the results of the reactive experiments are presented. First, the determination of boundary conditions is discussed, followed by the optical results of normal and angled injections.

Fig. 8.14 shows exemplary a visual image of reacting JICF in the test section of this study. The image was recorded from the side direction corresponding to the PLIF image recordings during the normal injection of C_3H_8 into the crossflow.

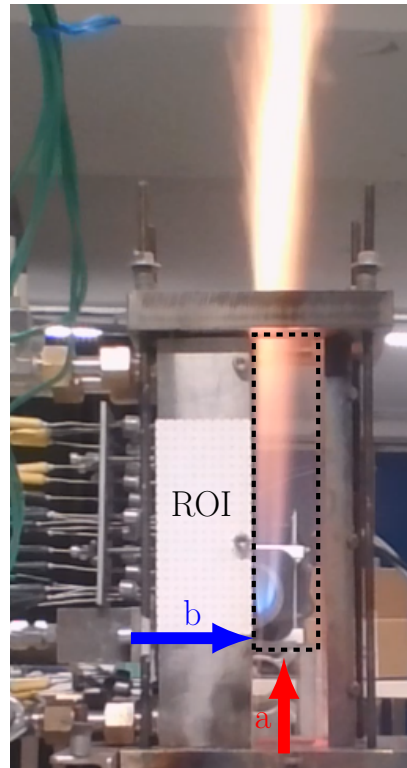


Figure 8.14: Visual view of reacting JICF in the current test section. a: crossflow direction. b: cold fuel direction. ROI relevant to optical diagnostics indicated by the dashed rectangle.

8.2.1 Operating condition

An exemplarily operation process to reach the desired HGG condition is visualized in Fig. 8.15. The upper graph shows the supplied fuel and air mass flows, the lower graph the resulting global fuel-to-air ratio ϕ and the exhaust gas temperatures measured within the HGG and at the inlet of the TS by TC type B, as indicated in Fig. 5.3 and Fig. 5.4. Radiation-convection correction was applied afterwards to the temperature data. The process is described in G.1. A gradual warm-up period was performed in order to protect the HGG internal components against thermal stress and to reach sufficiently high exhaust temperatures. Thus, the HGG was started at $\phi = 0.2$, which was continually increased towards 0.625. Temporally, conditions around $\phi = 0.77$ were also set to speed up the warm-up process. The experiments were conducted at $\phi = 0.625$ using 788.608 g/min of air and 28.698 g/min of gaseous CH_4 (6101/min of air and 401/min of gaseous CH_4 at normal condi-

tion). During the measurement period, the main flow temperature stayed at a quasi-steady state condition according to the TS TC. After the measuring period, the HGG was run down gradually by decreasing fuel-to-air ratio and reducing reactant mass flows.

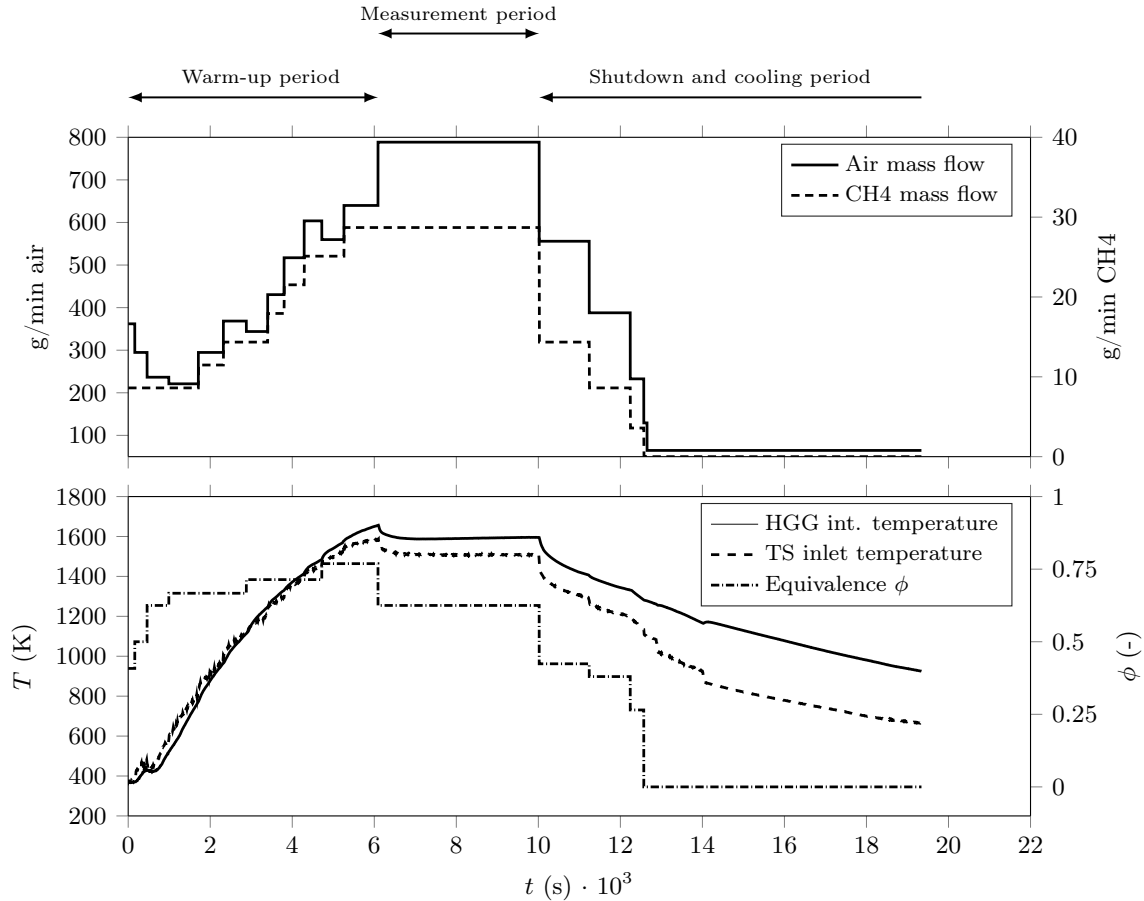


Figure 8.15: Top: supply mass flows of air and CH₄ for the HGG. Bottom: measured temperatures inside the HGG and at the inlet of the test section. Global equivalence ratio according to the supplied mass flows included in diagram.

The temperatures of the supplied gases to the HGG, of the cooling water and of the secondary gas are presented in Fig. 8.16. While the temperature of the supplied CH₄ was constant, the air temperature experienced a drastic reduction. This is attributed to the relation:

$$h_t = h + \frac{u_{air}^2}{2} \quad , \text{ for ideal gas: } T_t = T + \frac{u_{air}^2}{2C_p} \quad (8.3)$$

where h_t is the stagnation enthalpy and h is the static enthalpy and similar for the temperature T . u is the air velocity and C_p is the constant pressure heat capacity. Considering adiabatic conditions (constant h_t) and increasing the amount of air mass flow yields in higher air velocity and consequently the kinetic energy rises while the static temperature drops.

The cooling water temperatures, measured at the inlet and outlet of the TS as marked in Fig. 5.9, undergo an elevation of around 3 - 4 K while passing through the wall block.

The transient increase of the inlet temperature during the entire experiment was due to the fact, that the water was supplied by a closed circuit.

As indicated in Fig. 5.6, Fig. 5.7 and Fig. 5.9, the cold gas temperature was measured at two locations. Within the supply line, the temperature remained nearly constant, while it increased to values around 340 - 400 K inside the injection slot. During the cold gas injections, the temperature reduced up to 40 K depending on the type of gas and mass flow rate. It is notable, that the cold gas temperature within the injection geometry stayed constant without any significant variations (< 1 K) during each injection period - in some cases up to 600 s. Another temperature increase is expected inside the orifices of the injection geometry, which could not be measured. Based on the orifice length and the individual block temperatures obtained from the inverse heat conduction simulations, the jet exit temperature can be calculated.

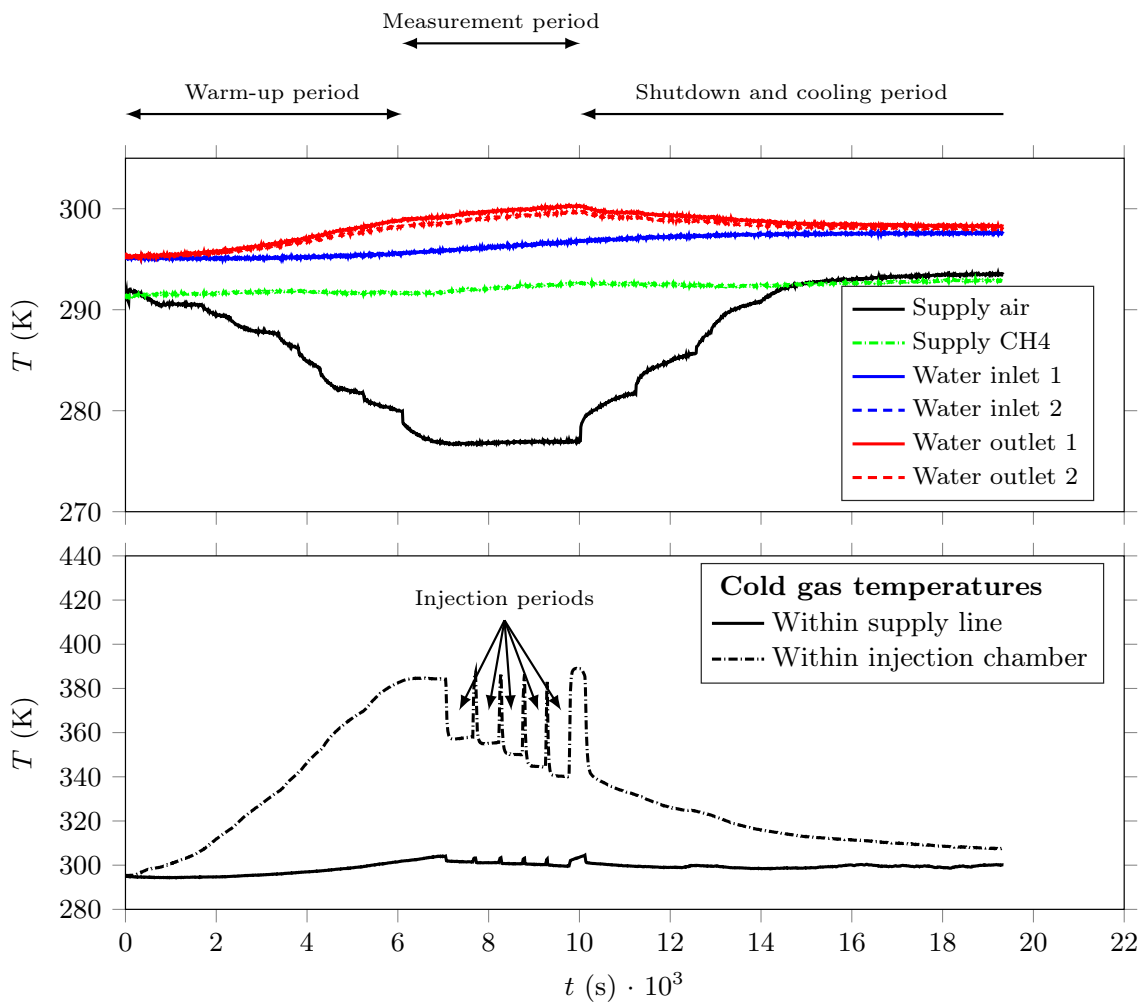


Figure 8.16: Top: supply gas temperature and cooling water inlet and outlet temperatures. Note, that the two water inlet and the two water outlet temperatures overlap. Bottom: measured temperatures of the injected gas within the supply line outside the TS and inside the chamber located within the TS.

As discussed in section 8.1.1, the main flow was subject to spatial inhomogeneity, prob-

ably due to the asymmetrical positioning of the HGG nozzle with respect to the internal components or the stochastically distributed ceramic elements within the combustion chamber, as seen in Fig. 5.3. Thus, the exhaust gas temperature at $z = -66.5$ mm was measured using a TC type B mounted on a linear translation stage. Fig. 8.17 on the left shows the discrete positions of the TC during the point-by-point measurement. The temperature of each position was recorded for 30 s with a sample rate of 90 Hz. A convection-radiation correction with a constant main flow velocity was applied to the data. Systematic errors around 7% were expected, similar to the measurements in section 4.2.1. The determination of the main flow velocity and material properties are discussed in 8.2.1.1. According to the 2D temperature distribution in Fig. 8.17, there is a shifted maximum similar to the cold flow velocity distribution in Fig. 8.2. However, the regions of interest such as the near-wall and y/D plane regions are nearly homogeneous. The spatially averaged temperature of the main flow was around 1600 K. The temporal standard deviation was negligibly small. Note, the main flow conditions may depend on environment temperature, supply gas temperature, operation period and degradation of the HGG. These factors impede exact reproduction of the conditions for each HGG operation. Thus, slight exhaust gas temperature variations might have occurred.

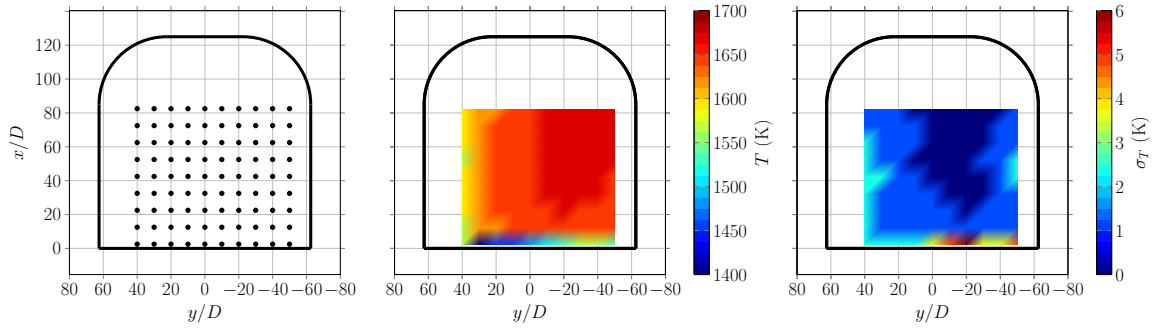


Figure 8.17: Left: TC measurement positions. Center: 2D exhaust gas temperature distribution. Right: standard deviation of temperature measurement.

8.2.1.1 Calculated main flow properties

So far, only the supplied mass flow rates of CH_4 and air to the HGG and the uncorrected temperature measured by the TC at the inlet of the TS were accessible and discussed. However, important missing quantities are the main flow velocity and density, which were especially of interest for the calculation of the momentum ratio. In contrast to non-reactive or cold flow test benches, measurement techniques like PIV or measurement devices like pitot tube were inapplicable. The HGG did not allow the introduction of PIV particles due to lack of access. Further, the particles would have contaminated the setup and especially hot particle would have stuck to the TS windows. And the author was unaware of the existence of pitot tubes for the mentioned temperature range. Thus, the density, the velocity and the composition of the exhaust gas were subject of theoretical reconstruction and calculation, as similarly applied in [167]. A schematic of the kinetic simulation model for the current work is shown in Fig. 8.18 using Chemkin-Pro symbols. The steady-state simulation starts with the supply of the reactant (CH_4 and air) mass flow rates (see 8.2.1) using the measures temperatures during the measurement period. The inlets represent a

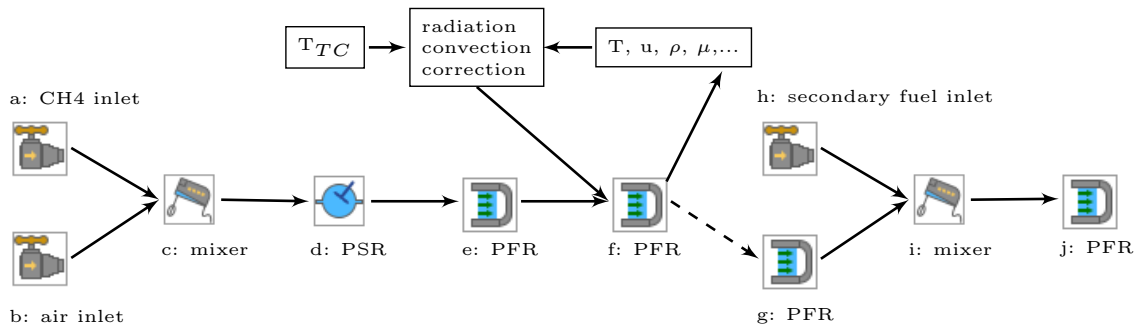


Figure 8.18: Chemical-kinetic simulation process. a, b: CH₄ and air supply to HGG. c: mixing within the combustion chamber. d: combustion process. e: secondary chamber of HGG. f: exit nozzle, mounting plate. g: test section up to injection slot. h: inlet cold fuel. i: mixing of exhaust gas and cold fuel. j: test section second part.

reservoir. Assuming high turbulence and perfect mixing on macro and micro scales the cold reactants were mixed and passed to a PSR. The reader is referred to corresponding literature for a detailed description of the reactor devices and the reactor models, such as to [3, 20, 107]. In short: a PSR represents a 0D system, where under the condition of mass, energy and species conservation the perfectly mixed reactive composition leads to chemical reaction. Corresponding species thermochemical data and reaction rate coefficients were obtained from optimized mechanisms, such as the GRI-Mech 3.0 [153]. The system was of transient nature, but for the sake of simplicity a steady-state calculation was performed for the current test bench. A PFR allows the simulation of a channel with defined cross-sectional area and additionally includes the momentum conservation in the axial direction, thus it is 1D. Similarly, the flow was considered homogeneous. Both reactor types can be adiabatic or non-adiabatic. After the chemical equilibrium was reached in the PSR, the product was led to a PFR, which represented the second chamber of the HGG. Thereafter, a PFR follows to represent the nozzle and the mounting plate in the current test bench. Here, the exhaust gas properties were extracted and used to correct the measured hot gas temperature T_{TC} for radiation-convection. The process was conducted iteratively, until the corrected temperature reached a constant value. Another PFR followed as the first part of the TS to the point of the injection slot. The exhaust gas was then mixed with an amount of secondary fuel to reach stoichiometric conditions and reacted within a last PFR. The condition of stoichiometry was based on the assumption that the reaction zone between the injected fuel and the exhaust gas corresponded to a diffusion flame. Since a PFR presumes a homogeneous mixture, the entire volume was taken as stoichiometric. Area-averaged properties of the PFR (g) allowed the calculation of different parameters and quantities, such as the momentum ratio, Reynolds number etc. The ignition delay length of the secondary fuel was accessed from the last PFR (j). Throughout the reactor network, an atmospheric pressure was considered.

The properties of the exhaust gas or vitiated air in PFR (g) for representative, corrected temperature of 1600 K is summarized in Tab. 8.3. As mentioned before, minor deviations might have occurred from experiment to experiment. According to the equilibrium kinetic simulation, the mole fraction of the remaining species, which are not listed in the table, was below 1 %. The diameter-based Re-numbers suggest turbulent main flow conditions, while the length-base Re-numbers indicate laminar flows assuming a flat plate. However,

Table 8.3: Crossflow conditions and properties of the reactive experiments.

ϕ	CH ₄ (g/min)	air (g/min)	T_h (K)	\bar{u} (m/s)	Re_d	Re_z	X_{N2} (%)	X_{H2O} (%)	X_{CO2} (%)	X_{O2} (%)
0.625	28.7	789	1600	26.5	5075	19600	74.1	12.3	6.1	7.4

the unstable nature and the shape of the secondary reactions in the following reactive experiments originated most probably from turbulent main flow conditions.

8.2.2 Secondary flow boundary condition

Tab. 8.4 presents the gaseous fuel injection conditions. Three types of fuels were injected into the oxygen-rich hot exhaust crossflow, discussed in the previous subsection, using the normal and the angled configuration. The average properties were determined from the injected mass flow rates and from the measured temperature by the TC within the injection geometry. The majority of the flow conditions was laminar except for some normal injections of C₃H₈.

Table 8.4: Boundary conditions of the reactive experiments.

Type	normal			angled		
Fuel	H ₂	CH ₄	C ₃ H ₈	H ₂	CH ₄	C ₃ H ₈
$Re_{D,c}$	162 - 761	364 - 1698	1032 - 6263	122 - 540	27 - 1215	598 - 2748
T_c (K)	366 - 340	358 - 340	348 - 327	380 - 364	361 - 351	354 - 342
\bar{u} (m/s)	45 - 187	16 - 66	11 - 60	50 - 210	16 - 73	9 - 40
I	0.9 - 16.8	0.9 - 16.9	1.3 - 41	1.1 - 19.6	1 - 19.3	0.9 - 17.2
M	0.5 - 2	1.5 - 6.8	3.1 - 18	0.6 - 2.7	1.5 - 7	2.5 - 11.3
VR	1.7 - 7.1	0.6 - 2.5	0.4 - 2.3	1.9 - 7.9	0.6 - 2.8	0.4 - 1.5
DR	0.3	2.6	7.6	0.3	2.5	7.3

The flow temperature was in the range of 327 K - 380 K, whereby the normal configuration yielded in lower temperatures due to the higher mass flow rates. As the momentum ratio was the parameter of interest and was intended to remain constant, the blowing ratio M , the velocity ratio VR and the density ratio DR varied. The parameters were calculated using the constant characteristic main flow properties in Tab. 8.3. The low density of H₂ resulted in highest average flow velocities up to 210 m/s and consequently in highest velocity ratios. Variations in the momentum ratio occurred and were difficult to prevent as the cold flow mass flow rates were calculated based on a nominal temperature prior to the experiments. Afterwards the values were corrected according to the actual temperatures.

8.2.3 Theoretical consideration

The first step of the reactive investigation consisted of a theoretical analysis of autoignition of the three fuels of interest: H₂, CH₄, C₃H₈. As these fuels at cold conditions were injected into a hot oxygen-rich crossflow in a channel of limited length, the chemical reaction was desired to occur within the channel. Specifically, the downstream distance in the TS after the injection location was 153.5 mm (see Fig. 5.4). However, due to the optical magnification and the field of view of the optical detectors a maximum distance of $L = 120$ mm was

considered. In this context, the ignition delay time (IDT) was an important characteristic parameter. Thus, a PSR was constructed in Chemkin-Pro with the main flow composition in Tab. 8.3 and with each of the named fuels with a global equivalence ratio of $\phi = 1$. Since the mixture temperature was a major influential factor in the current work (the pressure was assumed to be atmospheric), the IDT was evaluated depending on the temperature and plotted in the common type of presentation (abscissa $1000/T$ and ordinate logarithmic) in Fig. 8.19 on the left. The IDT was defined as the time period where the maximum OH concentration was reached. The GRI-Mech 3.0 was used for all three fuels and a second mechanism, derived from the detailed San Diego mechanism and optimized for C_3H_8 auto-ignition timing [135], was used for C_3H_8 , additionally. The latter case is indicated by SD. In the temperature range of 1000 - 2400 K the IDT of H_2 reduced only one order of magnitude and was in the range of 10^{-4} - 10^{-5} s. In comparison, the hydrocarbons showed significant higher IDT for the lower temperature range and decreased sharply as the temperature was increased. At temperatures around 1550 K, there is approximately an order of magnitude between the IDT of the fuels ($IDT_{CH_4} > IDT_{C_3H_8} > IDT_{H_2}$). The SD mechanism for C_3H_8 yields in similar IDT compared to the GRI-Mech 3.0 for temperatures around 1500 - 1600 K. The PSR is a 0D reactor without a length dimension. Thus, a PFR was setup to determine the ignition delay length (IDL), assuming the fuel amount was negligible and the velocity within the channel was basically determined by the exhaust gas mass flow (Fig. 8.18 PFR j). The molar fraction of some reactants, products and intermediate species, the temperature and the heat flux distribution plotted over the downstream direction are presented in Fig. 8.19 for stoichiometric CH_4 combustion. The peak location of X_{OH} corresponds to the location of maximum heat release and to the maximum gradient of the temperature, but the initialization of the reaction is not necessarily indicated by the X_{OH} curve. A similar lack of agreement between heat release rate location and OH concentration location was also discussed in chapter 2 (see Fig. 2.6). Here, the X_{CO} might be a better option.

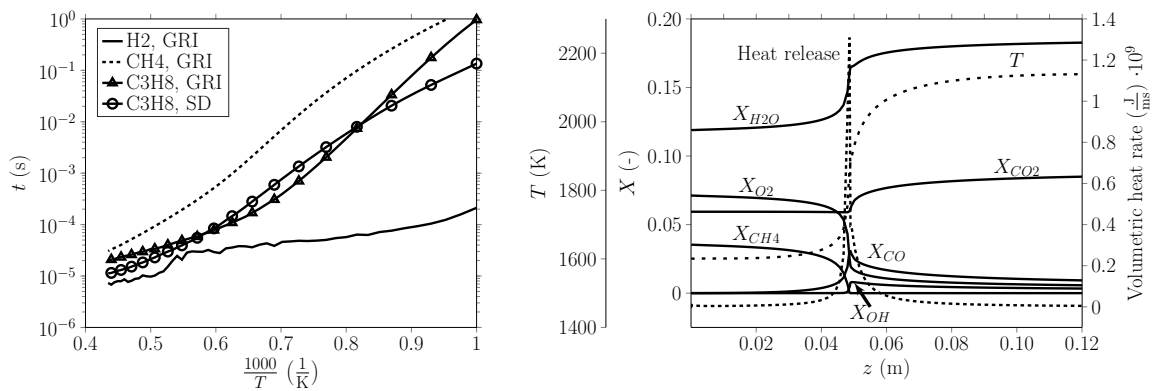


Figure 8.19: Left: ignition delay times for fuel/air at $\phi = 1$. Right: PFR reactor for CH_4 /air reaction and $\phi = 1$.

Injecting fuel into an oxygen-rich crossflow may form mixtures of different equivalence ratios. According to the reported empirical correlations in [100], the IDT depends on the fuel and oxidizer concentrations and increases when shifting the composition to fuel-rich regions. Thus, to estimate the reaction location relative to the test section downstream direction, the Damköhler number according to Eq. (2.46) was evaluated. The chemical time

scale τ_{chem} was considered as the period until the maximum heat release was reached, while the flow time scale was taken as the ratio of downstream length L to the average flow velocity \bar{u} (basically the period, the flow needed to exit the test section). The calculation results for the hydrocarbons are presented in Fig. 8.20. As the fuel-to-air ratio increases, the

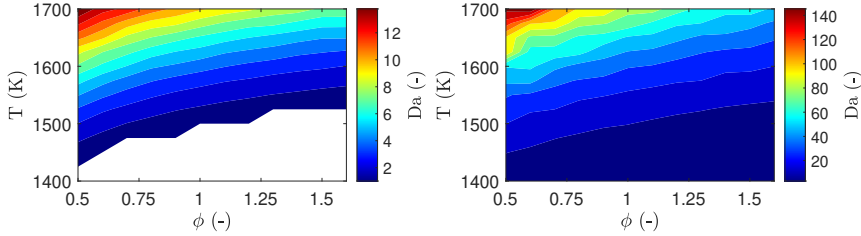


Figure 8.20: Left: Da-numbers for CH_4 . White area represents no reaction appearance. Right: Da-numbers for C_3H_8 .

Da-number declines and the IDL increases, which corresponds to reported IDT correlations based in the Arrhenius equation in [100]. For CH_4 , a lower temperature limit exists, below which no chemical reaction was expected within the channel. Note, that the color scales differ by a factor of 10. Consequently, the IDL of C_3H_8 may be ten times shorter than that of CH_4 . Assuming stoichiometric conditions and a temperature of 1600 K, the IDL of CH_4 was around 28 mm, while C_3H_8 required a distance of only 3 mm to react. The reason for the low reactivity of CH_4 is related to its molecular structure. CH_4 is the simplest stable C1 molecule and has a relatively high IDT compared to other hydrocarbons. Generally, the IDT is investigated for perfectly mixed compositions at different fuel-to-air ratios experimentally in shock tubes or numerically in a PSR. Analytic correlations are based on the Arrhenius equation Eq. (2.31) [198]. The pre-exponential factor is related to pressure and equivalence ratio or composition, while B depends on the effective global activation energy of the first order rate constants. B/T is predominant due to the exponential dependency of the IDT on the temperature. Experimental and analytical values for different fuel/oxidizer types and composition can be found in literature [42, 98, 122]. According to Holton et al. [98], CH_4 has a higher activation energy than C_3H_8 , basically due to the fact, that higher energy is required to breakup primary C-H bonds of CH_4 and to remove a H-atom than to breakup secondary C-H bonds of C_3H_8 [184]. H-atoms and radicals are necessary for sustaining a reaction chain. Comparing the elementary reaction paths of the two hydrocarbons directly for temperatures around 1600 K, the formation of methyl (CH_3) stands out for CH_4 and its primary radical, while the C_3H_8 decomposition produces other C2 and C3 species, which later trigger other reactions. According to Spadaccini et al. [184], CH_3 showed relatively high stability and low reactivity, while a variety of other radicals can be formed from larger hydrocarbons. At temperatures around 1500 K, the radical production from thermal decomposition of CH_4 may even be countered by CH_3 recombination. Hence, in technical devices with CH_4 combustion, H_2 or C_3H_8 may be added to decrease the IDT and establish a stable combustion [100].

The PSR and PFR calculations consider the chemical reaction of a perfectly mixed composition without the flow-chemistry interaction. However, the JICF is subject to turbulence and high strain rates. To estimate realistic temperatures of the reaction, a counterflow flame was constructed relating the reacting fuel JICF configuration to a flamelet approach. Here, a hot gas stream with the compositions in Tab. 8.3 and $T = 1620$ K was opposed to a cold

fuel stream. The cold fuel velocity was varied. Fig. 8.21 shows the normalized OH concentration plotted over the temperature with the strain rate as parameter. The strain rate was defined as the maximum gradient of the velocity [159]:

$$a = \left(-\frac{du}{dx} \right)_{max} \quad (8.4)$$

where x is the axial distance between the two streams and u is the velocity. The concentration is proportional to the number density, as $N_{OH} = N_A \cdot c_{OH}$, where N_A is the Avogadro constant. The H₂ maximum flame temperature decreased around 200 K, when the strain rate was increased by a factor of more than 10. The maximum expected temperature was around 2000 K. The CH₄ appeared to be more strongly affected by the strain rate and indicated temperature declines of approx. 200 K for increasing the strain rate of a factor of 3. Here, the maximum temperatures were around 1900 K. The C₃H₈ flame was more resistant to strain compared to the CH₄ flame. However, the maximum temperature here was slightly below that of CH₄. Interestingly, the OH concentration declined significantly with increasing strain for the hydrocarbons, whereas the OH concentration of H₂ flames seemed less affected by strain. This evaluation shows the stable nature of H₂ flames and the sensitivity of CH₄ flames to flow conditions.

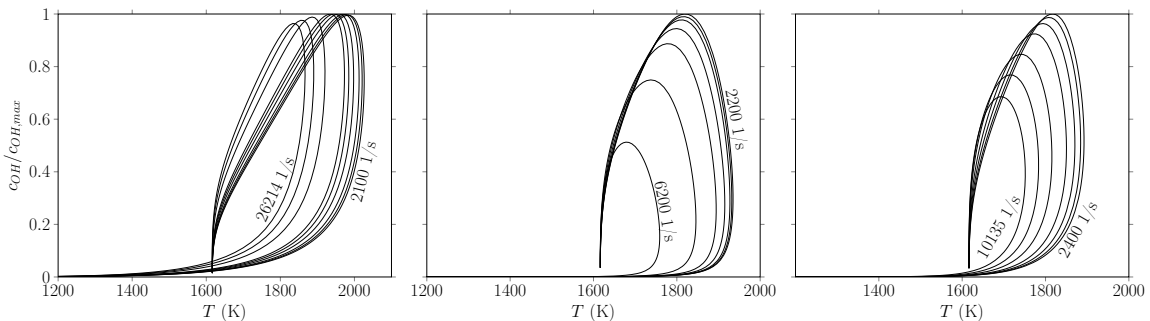


Figure 8.21: Strain rate calculation from counterflow diffusion flame simulation. Left: H₂. Center: CH₄. Right: C₃H₈.

Note, that the PSR/PFR analysis did not consider the macro and micro scale mixing times of the reactants. According to Poinsot et al. [159], diffusion flames can be decomposed into two sub-processes: mixing and combustion. During the mixing phase, fuel and oxidizer are transported by diffusion to the flame front and form a mixture, which reacts afterwards in the combustion phase. The flow turbulence and the diffusivities of the corresponding reactant affect the mixing time and hence the ignition position.

8.2.4 Optical data acquisition and post-processing

The experiments presented hereafter were conducted on the test bench illustrated (Fig. 5.1) with the optical setup in Fig. 5.2 as soon as the HGG reached the intended condition. To get an idea of the reaction zone of the individual orifices, additional OH* chemiluminescence experiments were conducted by aligning the OH* measurement devices to the front direction. This configuration did not allow simultaneous LIF measurements. 300 OH* images at a frame rate of 7500 Hz were recorded for each injection experiment. A maximum exposure time of 120 μ s was set for a sufficient signal intensity at even small cold fuel amounts. During

the experiments, an offset correction was carried out by the built-in function of the Phantom camera, where the aperture closed and the residual intensities were removed. This removal helped to decrease background noise, brightness inhomogeneities and pixel artifacts. Later during the post-processing step, a second background removal was performed to remove additional noise. A distortion correction was applied to the OH* images as the mounted lens and the intensifier-camera coupling optics exhibited a so-called *pincushion* distortion, where the image magnification increases away from the image axis. In order to calculate the system specific correction parameters and transformation matrices in Matlab's distortion toolbox [192], a series of chessboard images at different angles were recorded in advance. By means of those parameters, experimental images were undistorted afterwards. Fig. 8.22 shows exemplarily a raw image and a corrected image of the TS equipped with calibration paper.

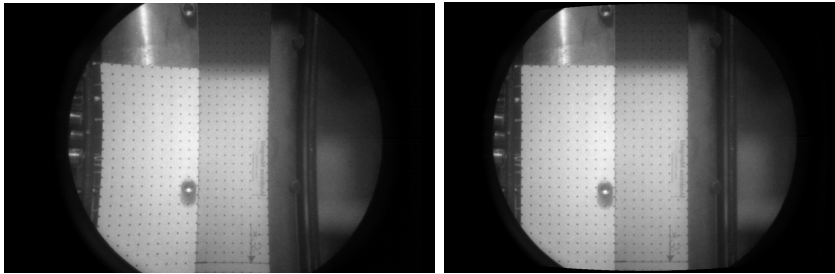


Figure 8.22: Distortion correction. Left: raw image. Right: undistorted image.

For the PLIF investigation, the laser light sheet was aligned to the center orifice. The LIF and OH* chemiluminescence systems were triggered in a time-shifted manner to avoid interference. Before the excitation of the reaction zone during the experiments, the dye laser required wavelength calibration. Hence the beam was led through a flat flame. A temporary mirror helped to collect the emission of the flat flame OH. In order to account for the geometric laser intensity distribution, the light sheet was recorded before entering the TS. However, the exhaust gas contained a sufficient, homogeneously distributed concentration of OH and this enabled the extraction of an average light sheet directly from the OH images. This procedure simplified the post-processing routine and helped to reduce systematic errors, such as different camera magnification and geometric allocation of the light sheet. Fig. 8.23 illustrates exemplarily the process of generating a light sheet and scaling the intensity data. As seen in the center image, there is only a slight difference between the light sheet obtained from the intensity image and obtained from the dye cell. Due to lack of access to the laser beam after passing through the reaction zone, an absorption correction was not possible. 298 images for all rotational lines of LP1 were recorded and the excitation was performed successively using pulse energies around 2 mJ. A saturation measurement was conducted in advance to ensure fluorescence linearity. Local saturation may still occur due to the inhomogeneous light sheet. Except for the absorption correction, the data was post-processed according to the flowchart in Fig. 4.14. Since the crossflow contained a non-negligible amount of OH, a cut-off limit was applied to the averaged intensity image data. The magnitude of the limit was in the range of the main flow intensity.

The origin of the coordinate system in the following results was shifted to the location of the center orifice for convenience, as mentioned before.

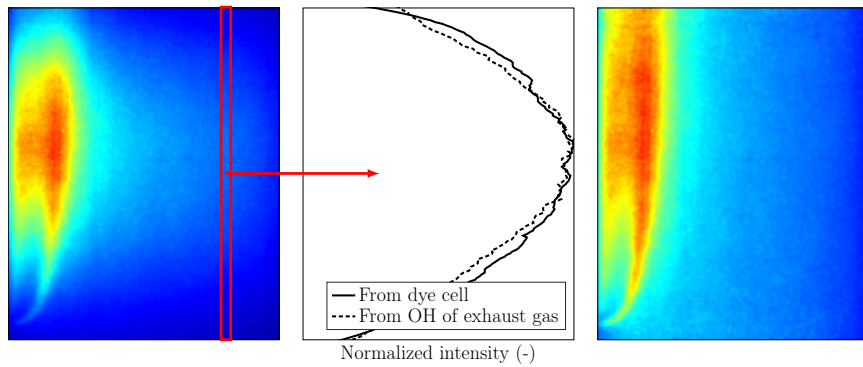


Figure 8.23: Light sheet correction. Left: averaged raw PLIF intensity. Center: intensity distribution obtained from dye cell and obtained from red rectangle. Right: PLIF image corrected by laser light sheet.

8.2.5 Normal injection results

The optical results for normal fuel JICF are presented in this section. To provide a better overview, OH* chemiluminescence and OH PLIF data are presented in two subsections.

8.2.5.1 OH* chemiluminescence

The following OH* images were recorded with the same camera and intensifier settings summarized in section 4.1. A trade-off between minimum gain factor for small fuel injection and thus low emission and maximum gain factor for large fuel flow rates and high emission, which might lead to pixel saturation, was made. Different gain factors were chosen for OH* recordings from the front and the side direction, see Fig. 5.2, as in the latter case the emission in the line-of-sight was higher due to the 5 aligned orifices and pixel saturation occurred sooner. The emission from the side direction was intensified with a factor of 800, while the emission from the front direction allowed an intensifier factor of 880. The luminous gain curve is found in Fig. 4.3. The intensity count scale of OH* images ranges from 0 to 255. OH* recordings of the crossflow before the fuel injection yielded intensity counts around 2, indicating no significant or low reactions.

Fig. 8.24 shows 7 instantaneous OH* images recorded successively at 7500 Hz and an averaged image from 300 images of H₂ injection with $I = 16.8$. Instantly after the injection a large reaction zone appears and anchors to the injection nozzle, despite the fact that the jet had an average velocity of around 187 m/s (eventually higher local velocity as the flow is presumably laminar). The main reaction zone is located in close proximity to the wall and is constrained to the region of $z/D = 0$ to 40. Afterwards, the reaction decreases gradually downstream. It is apparent from the single images that small fluctuations occur around $z/D = 50$, while larger instabilities are observed around $z/D = 100$ and grow downstream, likely due to the growth of shear layer effects. The time-averaged image shows no major difference to the time-resolved single images, which is an indication for the stable character of the flame. Time-averaged images and temporal standard deviations of H₂ injections with different momentum ratios are presented in Fig. 8.25. Chemical reaction occurs throughout the cases directly at the injection location without any visible IDL. The intensity level increases with increasing fuel amounts and the near-wall reaction zone expands gradually. Due to the main reaction location, the flame structure can be categorized as jet-like [88]. The

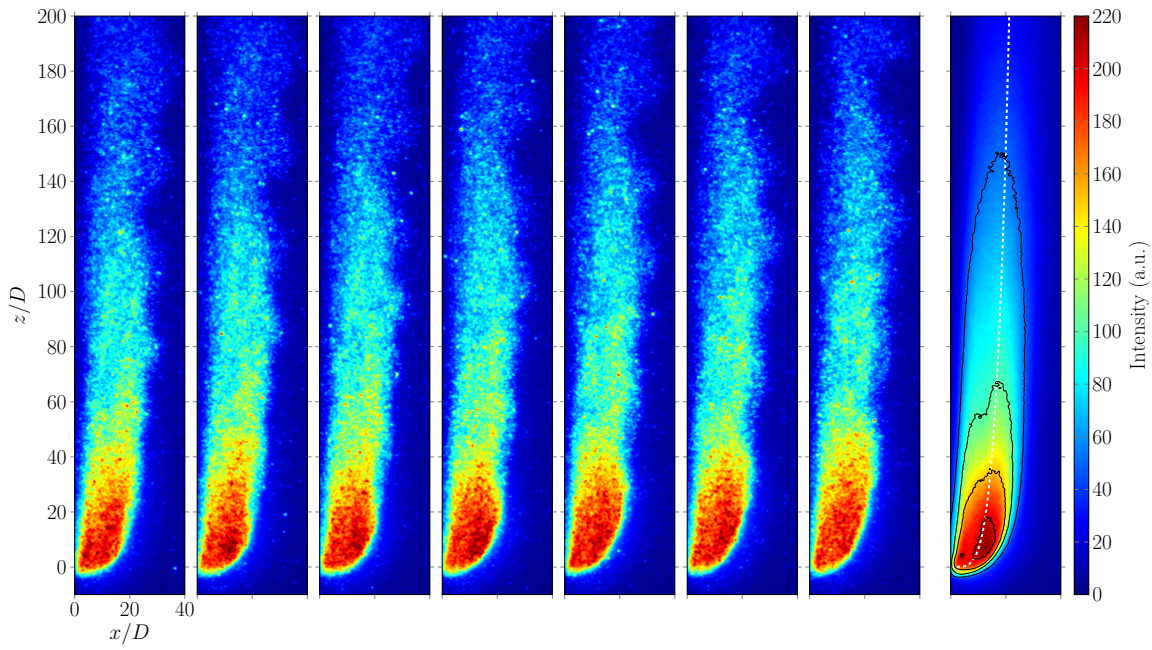


Figure 8.24: OH* chemiluminescence from H_2 injection at $I = 16.8$. 7 instantaneous and an averaged image from 300 single images. Dashed white line is the trajectory.

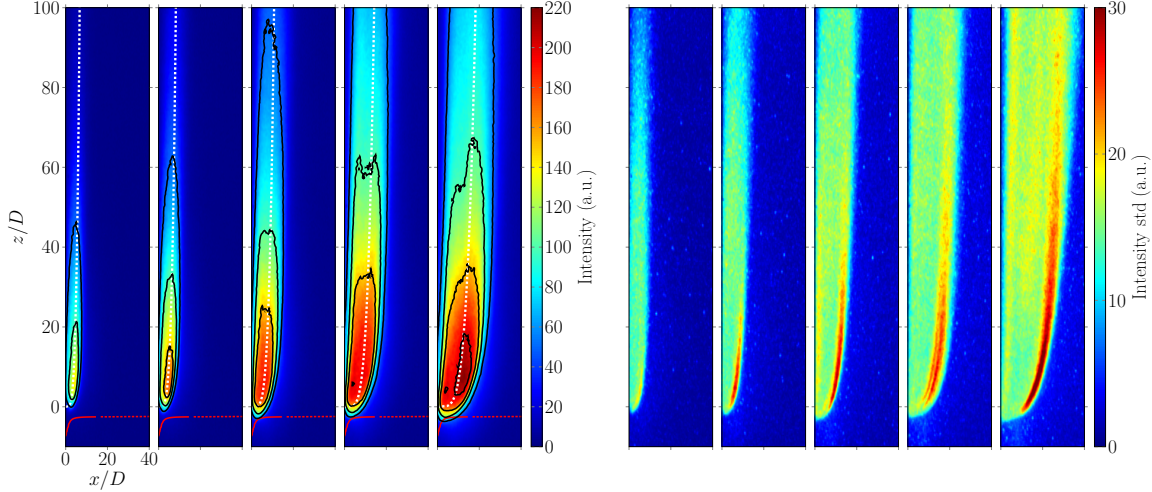


Figure 8.25: Left: averaged OH* chemiluminescence recordings from H_2 injection. Right: corresponding standard deviations. $I = 0.9, 1.8, 4.3, 8.6, 16.8$. Velocity profile in red. Solid part indicates boundary layer. Dashed white line is the trajectory.

temporal standard deviation shows low values around the main reaction zone and indicates high stability. As the momentum ratio is increased and the jet starts to deflect from the wall, the windward side is subject to enhanced fluctuations. This instability effect was also observed by Hasselbrink et al. [87] and explained with increased turbulence intensity verified by velocity data. Up to a momentum ratio of $I = 4.3$ the major part of the reaction zone, especially the stable region, occurs near the surface within the boundary layer, which is drawn as solid red line and has a thickness of $\delta_{99\%} = 8 \text{ mm}$ or $\delta_{99\%}/D = 14.5$. The

velocity profile close to the injection orifice was obtained from inert CFD simulations of the HGG at $T = 1430\text{ K}$ alongside a representative wall temperature profile, discussed in section 8.4 of this chapter. Note that the profile corresponds to the cold flow measurements in Fig. 8.2. The reconstruction of the jet trajectory is based on Eq. (2.24). The coefficient A and exponent B were determined from visually matching the trajectory to the main reaction form, similar to the procedures made in literature for non-reactive jets [136], due to lack of concentration or jet velocity information. In contrast to [186], the factor A was in range of 2.2 - 2.4 and B was 0.21 - 0.23 and both were smaller than the non-reactive values in section 8.1.5. The calculated trajectories represent the overall path of the jet. Deviations were observed around the main reaction zone, likely due to the expansion of the gas due to chemical reaction.

OH^* images of the highest CH_4 momentum ratio are presented in 8.26. The flame structure and shape differ substantially from H_2 flames. In contrast to H_2 flames, the

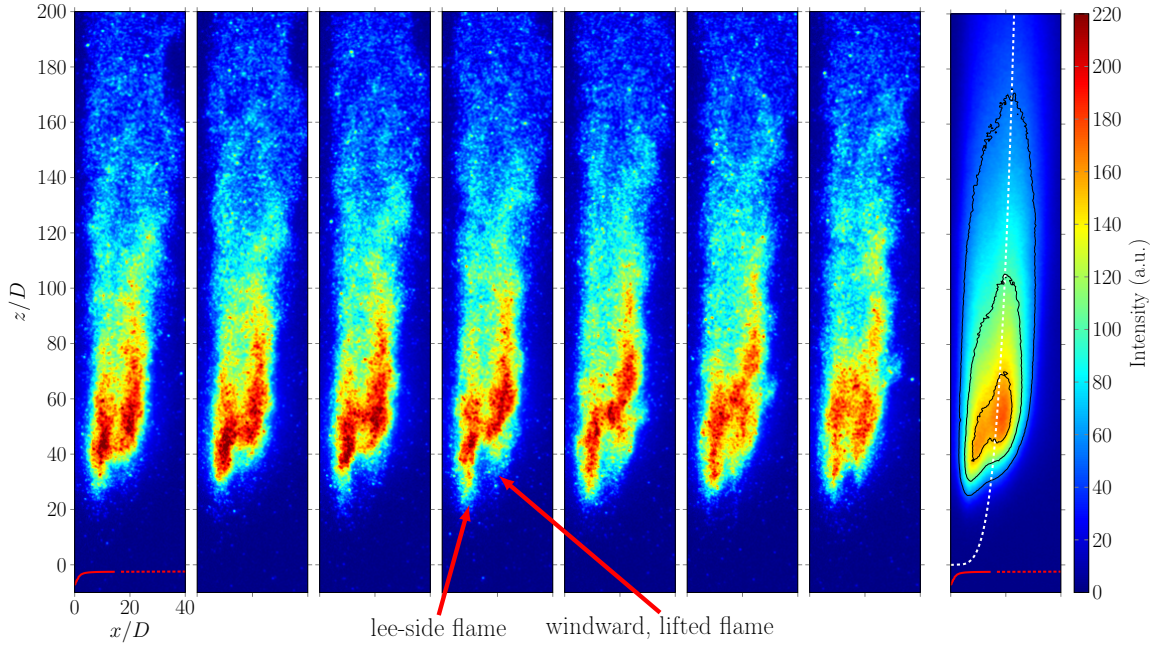


Figure 8.26: OH^* chemiluminescence from CH_4 injection at $I = 16.9$. 7 instantaneous and an averaged image from 300 single images. Velocity profile in red. Solid part indicates boundary layer. Dashed white line is the trajectory.

reaction zone is anchored to the wall instead of to the orifice and the entire shape of the flame is subject to fluctuations. Further, a significant IDL is apparent and the flame stabilizes at around $z/D = 30$. Then the main reaction ranges up to $z/D = 120$. Despite the fact, that the method is a line-of-sight integration of the intensity and the 5 orifices were horizontally aligned, two reaction zones are clearly visible. On the windward side, the fuel jet and the exhaust gas react on the contact interface, while apparently oxygen-rich main flow is transported to the region beneath the jets by CVP and chemical reactions occur on the lee-side. On some images, the two reaction streaks seem also to get in contact and merge. As clearly seen on the instantaneous and on the averaged image, the lee-side reaction zone is located further upstream than the windward one and agrees to the findings in [186], that the lee-side reaction zone is stabilized by the low velocity region near the wall. Taking

into account the velocity profile drawn before the orifice, the lee-side reaction occurs indeed mostly within the boundary layer. Averaged OH* images for different CH₄ injections are shown in Fig. 8.27. For the cases with $I = 0.9$ and 1.8 the reaction zones appear to reattach

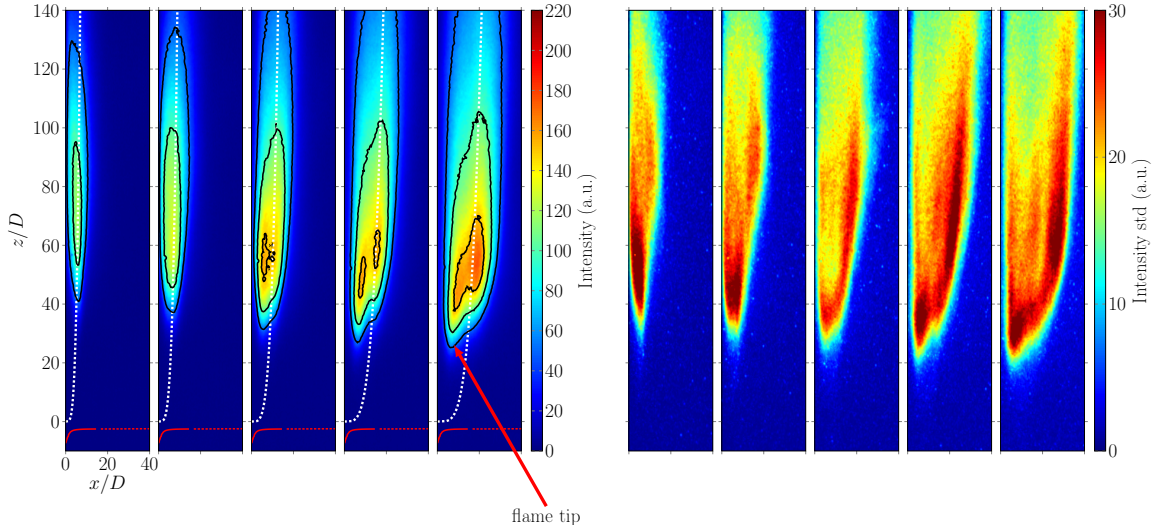


Figure 8.27: Left: averaged OH* chemiluminescence recordings from CH₄ injection. Right: corresponding standard deviations. $I = 0.9, 1.8, 4.4, 8.7, 16.9$. Velocity profile in red. Solid part indicates boundary layer. Dashed white line is the trajectory.

to the wall around $z/D = 60 - 100$ and are located inside the boundary layer. Further increase of I leads to expansion of the reaction zone and to increased separation of the main reaction from the wall. The double flame structure is also recognizable from $I \geq 8.7$, with the lee reaction appearing further upstream. With increasing momentum ratio, the entire reaction zone shifts upstream and the IDL decreases. Richardson et al. [167] made the same observation for inverse diffusion flames and explained this effect by enhanced mixing due to the JICF interaction. The standard deviations of the intensities, considered as an indicator for stability, show regions of high fluctuation on the flame tip (different from H₂ flames) and on the windward contact zone. The fluctuation levels of Fig. 8.27 are noticeably larger than the levels in Fig. 8.25, despite the fact that the absolute intensities of the H₂ flames are higher than those of CH₄ flames. As the fuel reacts far downstream the injection and the jet structure is dismantled, the shape is more wake-like. The optically determined trajectories, calculated based on Eq. (2.24), agree well with the shape of the flame. The factor A is 2.2, while the exponent B is 0.24.

Finally, OH* images of C₃H₈ injection with $I = 41$ are given in Fig. 8.28. The shape of the reaction zone, which is anchored downstream the injection, demonstrates strong similarities to the CH₄ flames. The overall structure is subject to fluctuations and the double reaction streaks appear. However, the windward reaction seems further upstream in contrast to that of CH₄, but still more downstream than the lee reaction, presumably due to boundary layer effects. The main reaction zone is limited to the downstream regions around $z/D = 60$, while on some instantaneous images there are also reaction kernels detaching from the main reaction and moving downstream, similar to CH₄ JICF. Due to the low spatial resolution and line-of-sight integration of the OH* method, a quantitative evaluation was not performed. However, broken and shredded flames were also identified in the literature

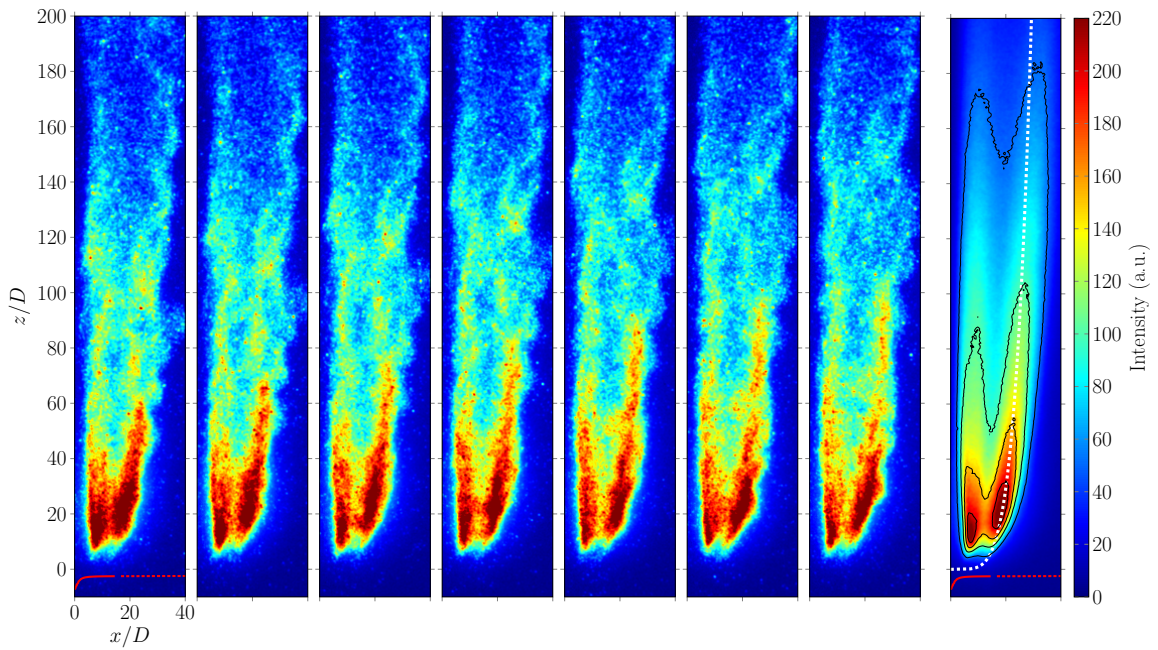


Figure 8.28: OH* chemiluminescence from C_3H_8 injection at $I = 41$. 7 instantaneous and an averaged image from 300 single images. Velocity profile in red. Solid part indicates boundary layer. Dashed white line is the trajectory.

on LIF images for high-speed JICF configurations [139]. The shape of the reaction zone corresponds to a transition form between jet- and wake-like, as the jet shape is still apparent. Averaged OH* images for different momentum ratios are presented in Fig. 8.29. The IDL are clearly smaller than those of CH_4 flames and similarly with increasing momentum ratio the IDL decreases. The double reaction zone structure starts to appear at $I = 6.5$ and it is well pronounced for $I = 13$. The lee-side reaction is always located within the boundary layer. The standard deviation images indicate large regions of instability on the windward side beginning with $I = 2.6$. Also the flame tip is subject to fluctuations. However, the fluctuation level is mostly lower than that of CH_4 . As previously outlined, the trajectories were calculated with A from 2.3 to 2.6 and B from 0.2 to 0.22. The trajectory seems to deviate from the jet path for the cases with higher momentum ratio.

To locate the main reaction zone in the downstream direction and relate the OH* signal to heat release rate, the intensities from the averaged images in Fig. 8.25, Fig. 8.27 and Fig. 8.29 were integrated in the x -direction using $I(z) = \int I(x,z)dx$. The integral intensity was then converted into heat release rate by Eq. (2.47). The lower heating values for H_2 , CH_4 and C_3H_8 are 119.96 MJ/kg, 50.03 MJ/kg and 46.34 MJ/kg [121], respectively, and the fuel mass flow rates are summarized in Tab. F.4. The scaling factor A_{OH^*} was obtained from $\int I(z)dz$. Since in some cases the injected fuel did not fully react within the test channel, the intensity $I(z)$ was extrapolated linearly to cover the entire heat release, as found in [139]. The conversion of OH* intensity to heat release rate was performed for comparative purposes despite the concerns discussed in section 2.7.4 regarding indication of spatial heat release rate from OH*. Additionally, a vertical intensity integration $I(x) = \int I(x,z)dz$ was performed. The results for the three fuels with different momentum ratios are in Fig. 8.30. With increasing H_2 fuel amount the reaction zones expand vertically and

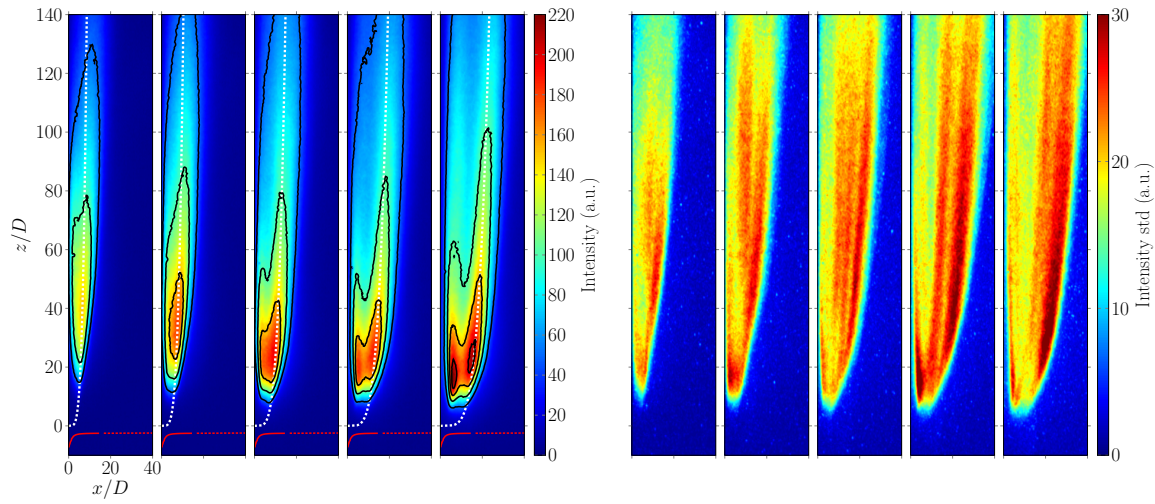


Figure 8.29: Left: averaged OH* chemiluminescence recordings from C₃H₈ injection. Right: corresponding standard deviations. $I = 1.3, 2.6, 6.5, 13, 25.4$. Velocity profile in red. Solid part indicates boundary layer. Dashed white line is the trajectory.

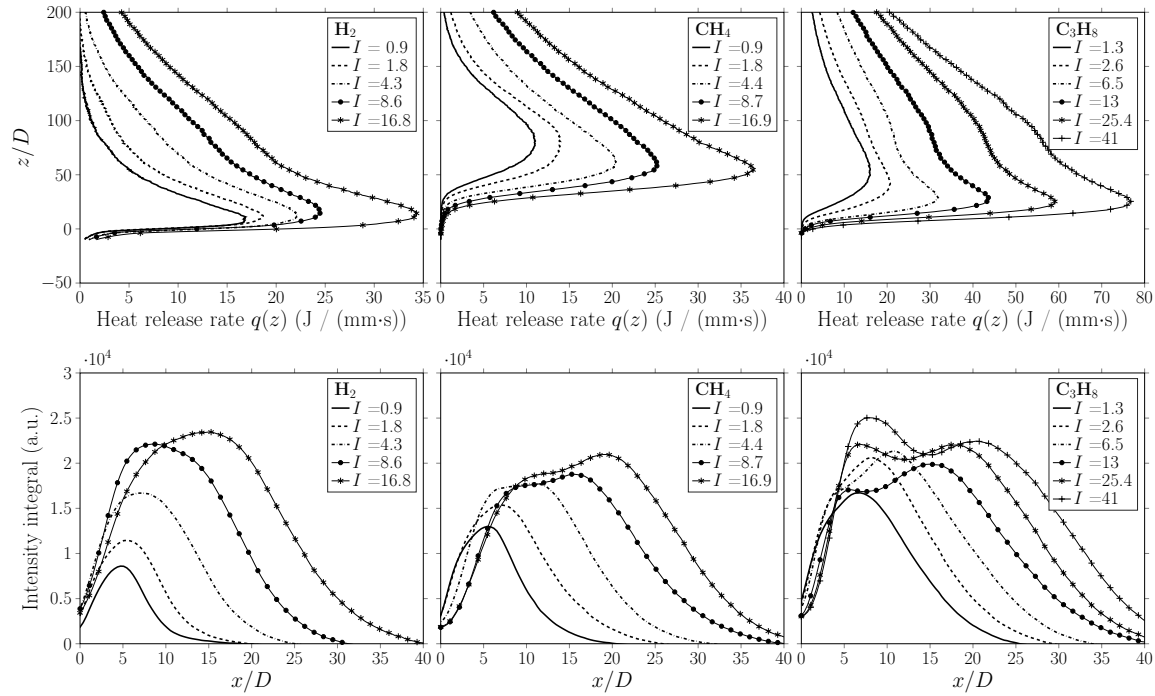


Figure 8.30: Normal injection. Top: heat release rate calculated from the intensities integrated horizontally. Bottom: intensity integrals in the vertical direction.

horizontally. While the horizontal location shifts away from the wall, the downstream peak is at a fixed location. The heat release curves appear scaled with increasing fuel mass flow rates. As mentioned before, the reaction zones of the hydrocarbons shift upstream and the flame wall distances increase with increasing momentum ratio. The double structure is also pronounced for the cases with high momentum ratio ($I \geq 4$), as two intensity peaks appear

in the horizontal intensity integrals. Comparing the peak heat release rates, H₂ and CH₄ are on similar levels, while the C₃H₈ fuel leads to higher heat rates for momentum ratios above 6.5.

The IDL of the hydrocarbons defined as the downstream location of the peak heat release rate and as the location of 10 % of the peak are plotted vs. the momentum ratio in the first graph of Fig. 8.31. The error bars indicate the standard deviation from the single images. The area A_{OH*} normalized by the maximum $A_{OH*,max}$ is plotted against the fuel mass flow rate \dot{m}_f , since $A_{OH*} \propto \dot{m}_f$ rather than $\propto I$. Finally, the right graph of Fig. 8.31 compares the normalized flame length l/D depending on the mass flow rate. The flame length was defined as the downstream distance from IDL 10 % to the position of 90 % heat release rate in Fig. 8.30. Due to the significant IDL of the hydrocarbons in the current study, the IDL defined from 10 % intensity increase was suitable. For both hydrocarbons, the IDL reduce

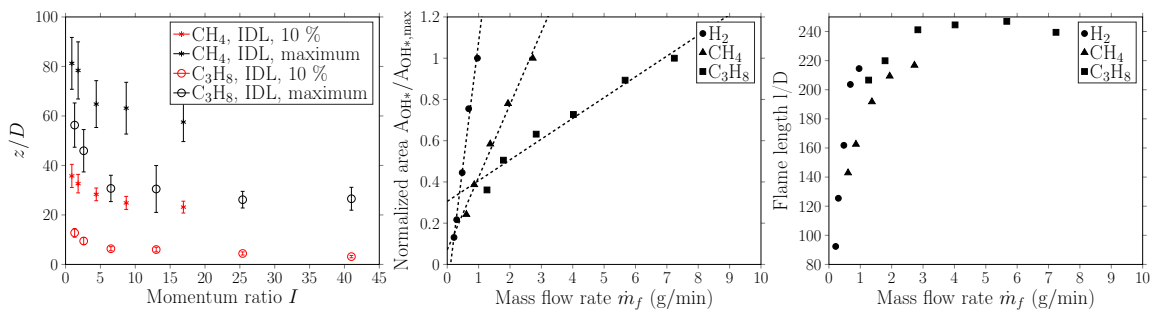


Figure 8.31: Normal injection. Left: ignition delay length for hydrocarbons. Center: normalized integral heat release rate. Right: flame length.

and approach $z/D = 20$ for CH₄ and $z/D = 3$ for C₃H₈ based on 10 % intensity increase. The values are smaller than predicted by the PFR calculations in Fig. 8.20. For example, the Da number for stoichiometric CH₄/air at 1600 K is 4.3 and the IDL scaled by D is 51, while for C₃H₈ under the same conditions the Da number was 37 and thus the IDL was 6. This kind of deviation between experimental and simulation data was also observed in [63] and justified by the mixing enhancement and increased interaction of JICF. The maximum based IDL's are around 60 and 26 for the two fuels, respectively. The error bars, defined as the standard deviation of the IDL from single images, indicate lower fluctuations for C₃H₈ in most cases. The normalized area ($A_{OH*}/A_{OH*,max}$), representing the normalized total heat rate, shows a linear relation to the fuel mass flow rate, as highlighted by the linear interpolation curves, and is a good indicator for the integral heat release rate. This was shown for H₂ JICF in [139], for CH₄/O₂ co-flow in [89] and here it is demonstrated for two hydrocarbon and hydrogen JICF flames. Comparing the gradients of the curves in the second graph of Fig. 8.31, H₂ combustion yields in the highest heat release for the same fuel mass rate compared to the hydrocarbons, followed by CH₄. This trends agrees to the lower heating values of the fuels. A linear behavior of the flame length on the other hand could not be observed. Especially, C₃H₈ demonstrates an unclear development. This is due to different reasons for the current transverse JICF. First, the jet experiences a redirection by the crossflow which distorts the actual flame length. Second, the mainstream turbulent condition and the JICF increase mixing and interaction. Those in turn intensify reactions. An increase in fuel mass flow rate results in further enhanced mixing and intense reaction, as seen from the IDL positions and on the intensity images, but not necessarily to a linear

extension of the flame.

Some selected OH* images from the front side of the test section are presented in Fig. 8.32. Every H₂ fuel jets is visible and well pronounced for low and high momentum

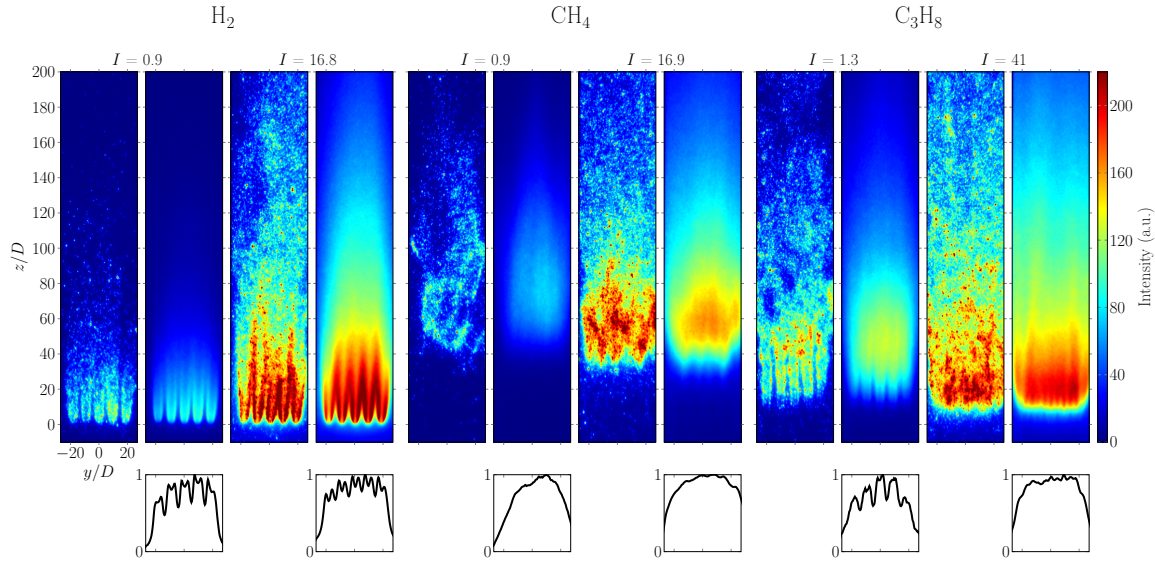


Figure 8.32: OH* chemiluminescence recordings from the front direction of normal fuel JICF. For each momentum ratio, an instantaneous image and an averaged image of 300 single images are shown. Vertical intensity integrals are given on the bottom.

ratio, as additionally highlighted by the vertical intensity integral curves below the 2D intensity images. The individual jets merge after a distance of 15 - 20 (z/D). Similar to the side view recordings, the H₂ flames appear stable. In contrast, the CH₄ jets with low momentum lead to chaotic and shredded reaction zones of unstable nature. There is no indication of a jet structure, as described by Andreopoulos et al. [11] with *no memory of the jet*. Higher momentum ratios stabilize the reaction zone. Yet, the jet structure is hardly present anymore. Finally, the C₃H₈ fuel jets at low momentum are well pronounced, while increasing the momentum ratio results in a homogenization of the flame tip region due to enhanced mixing and interaction. Similar to H₂ and CH₄ fuels, the major amount of the fuel reacts within a short distance. Comparing C₃H₈ jets to H₂ jets, an increased lateral spreading is observed for this hydrocarbon. The observation is analogous to film cooling applications, where the cooling effectiveness improves with increasing density ratio DR due to lateral distribution [181]. The DR in the current case are summarized in Tab. 8.4. The DR of the hydrocarbons are greater by at least a factor of 8. The total heat release rates equivalent to the results in Fig. 8.31 were also determined for the recordings from the front direction and showed same linear behavior as those from the side direction.

8.2.5.2 Planar laser-induced fluorescence

LIF diagnostics was conducted for the reactive JICF conditions listed in Tab. 8.4. Fig. 8.33 presents the LIF intensity images of the lowest and highest momentum ratio of H₂ injection. The following intensity images are evaluated from the rovibrational line $P_{11}(2)$. The maximum laser frequency of 10 Hz did not allow time-resolved measurements, thus single shots are randomly selected. As the crossflow was generated from CH₄/air combustion, the

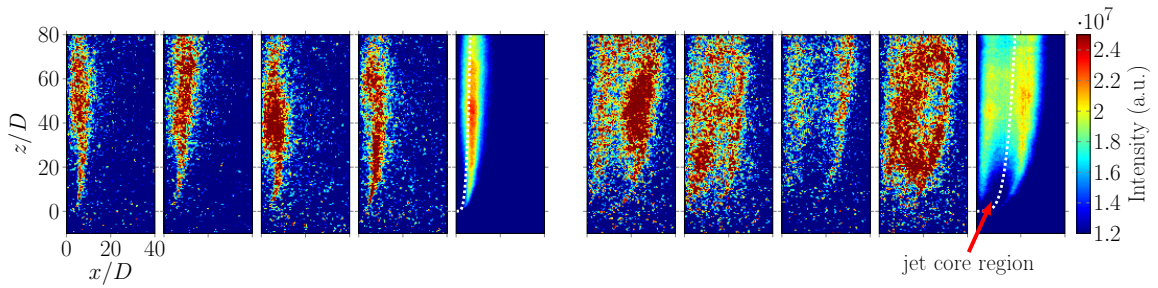


Figure 8.33: LIF of H_2 flames consisting of 4 single shots and an averaged image from 298 single images. Left: $I = 0.9$. Right: $I = 16.8$.

exhaust gas presumably contained OH radicals. In contrast to OH^* chemiluminescence detection, the equilibrium OH is excited and the emission is detected by the LIF measurement technique, as perceptible on the instantaneous images. However, the high OH concentration in the secondary reaction zone originating from the fuel injection could be distinguished from that of the main flow. The intensity ratio between mainstream and reaction zone was around 3 - 7 depending on the fuel and mass flow rate. Impurities of the silica plates and laser scattering may adversely affect the data quality, since the band-pass filter had an OD of 6 and transmits small fractions of the laser intensity. Despite the rather low spatial resolution due to binning, lens type and Gaussian filtering of the data, some characteristic features were observed. The low momentum jet detaches from the surface and reattaches around $z/D = 30$. In the downstream direction, the jet expands, especially at the reattachment region, as seen on the single images. The jet structure is well reflected on the averaged image. The trajectory determined with the same parameters given in 8.2.5.1 ($A = 2.2 - 2.4$, $B = 0.21 - 0.23$) leads to a good agreement and minor discrepancies. Increasing the momentum ratio to 16.8 leads to the formation of the two reaction streaks. As the jet exits the nozzle, crossflow air flows around the normal jet. Air is presumably transported to the near-wall region by vortices, which then reacts with the fuel on the lee-side. The near-wall reaction occurs almost directly after injection, as observed on the averaged image. As the laser sheet excites the centerplane of the center jet, the two reaction layers appear. On some images, the reaction zones merge due to the turbulent nature of the flow. In the injection region of the averaged image, the fuel jet core is evident before the transition to chemical reaction starts. There, the determined trajectory passes through this jet core. Despite the higher fuel amount, the intensity level of the averaged image of $I = 16.8$ is lower than that of $I = 0.9$, while the intensity of the single images have same magnitudes. This is presumably due to the fact, that the high momentum jet is less stable and the corresponding shot-to-shot spatial fluctuations result in lower averaged intensities.

Averaged LIF intensity images, two-line temperatures and random errors from SNR and fluctuations converted into temperature are presented in Fig. 8.34 for different H_2 momentum ratios. For the two-line LIF thermometry, two rotational lines were excited successively and converted into average temperatures under the assumption that the reaction zone was steady-state. With increasing momentum ratio, the jet lifts from the surface. The lee-side reaction is quite pronounced already from $I \geq 4.3$ and high intensity levels are detected near the wall. The average temperatures for lowest fuel flow rate is in the range of 1600 - 1700 K. With raising fuel amounts up to $I = 8.6$, temperatures above 1800 K are determined. A further fuel increase reduces the temperature level slightly. A gradual temperature increase

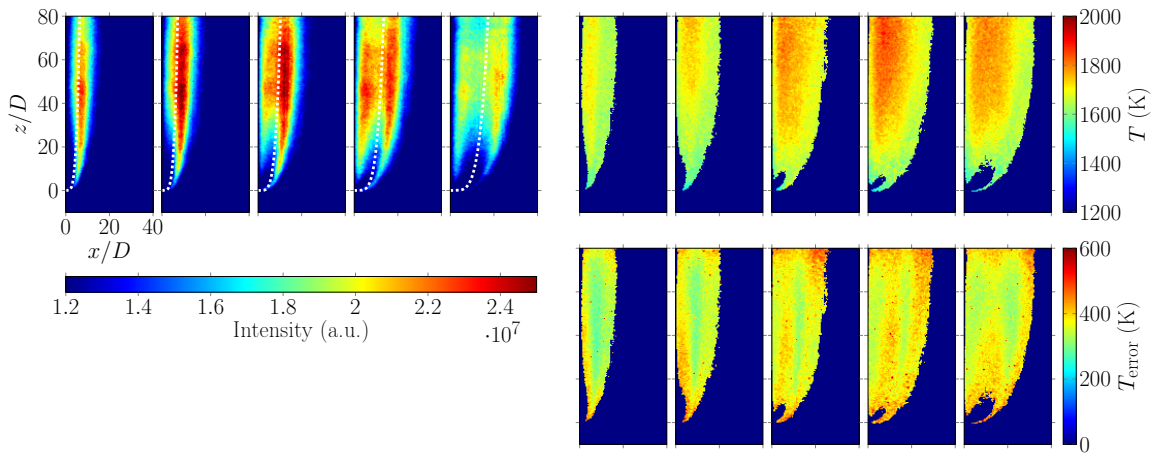


Figure 8.34: LIF of H_2 flames. Left: averaged images. Top right: two-line temperature. Bottom right: two-line temperature errors. $I = 0.9, 1.8, 4.3, 8.6, 16.8$.

downstream of the injection location is also observed. The temperature distribution does not necessarily correspond to the OH PLIF intensity images due to the fact, that the intensity of $P_{11}(2)$ depends not only on the OH number density, but also on the temperature, as discussed in section 4.2. The temperature error images correspond to single intensity images and reduce by the factor \sqrt{n} where n is the number of averaged images. The data correlates to the intensity images. Regions of high intensity result in lower temperature inaccuracies. Generally, in the main reaction zones the accuracy of the temperature measurement is higher. Compared to the theoretically predicted temperatures by the 1D simulation in Fig. 8.21 the experimentally determined temperature level is lower.

Instantaneous and averaged LIF images of CH_4 jets are shown in Fig. 8.35. At low

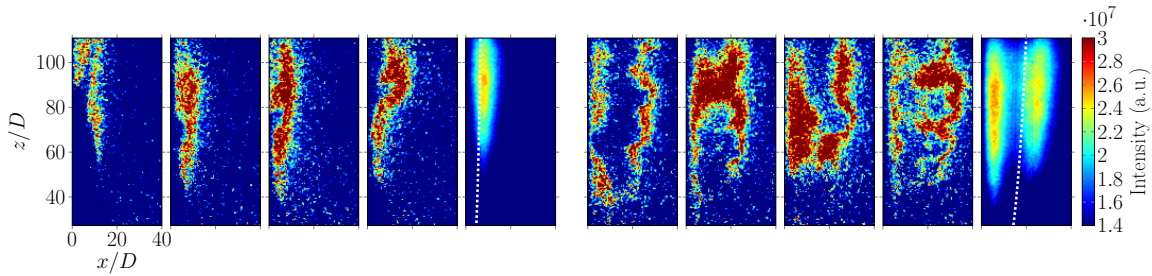


Figure 8.35: LIF of CH_4 flames consisting of 4 single shots and an averaged image from 299 single images. Left: $I = 0.9$. Right: $I = 16.9$.

momentum ratio, mostly a single continuous reaction layer of different shape forms, while the double flame structure appears for $I = 16.9$. It is noticeable, that this structure is more wrinkled and deformed compared to the flames of $I = 0.9$. This behavior was also observed by Hasselbrink et al. [87] for fuel JICF with low vs. high velocity ratio. Also straight flames, continuous flames, broken flames (multiple islands) and merging structures of the two layers are visible on the single images, similar to investigations in literature [87, 186]. Compared to the high momentum ratio H_2 flames, the reaction layers of the CH_4 flame are more separated. And according to the OH^* data, the lee-side flame is further upstream, likely stabilized by the boundary layer. Similarly to the H_2 fuel jets, the two reaction layers occur

already at $I = 4.4$, as seen on Fig. 8.36. With increasing momentum ratio, the windward

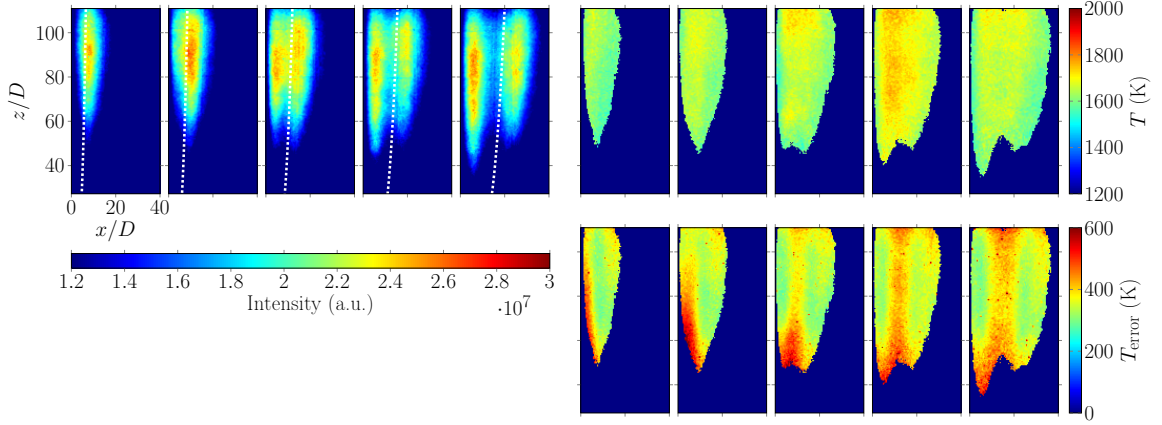


Figure 8.36: LIF of CH_4 flames. Left: averaged images. Top right: two-line temperature. Bottom right: two-line temperature errors. $I = 0.9, 1.8, 4.4, 8.7, 16.9$.

flame shifts further downstream, which may be due to turbulence and instabilities. The calculated and inserted trajectories agree well to the general form of the reaction zone with little deviations. At the lowest fuel rate, the temperature is around 1600 K. Increasing the fuel amount to $I = 8.7$ leads to temperature values around 1750 K and declines slightly with a further fuel increase. A spatial temperature distribution is not clearly observed, probably due to the large IDL and advanced mixing state. High temperature errors were determined for regions of low intensity and regions subject to instabilities, like the flame tip area. The experimental temperature level of the CH_4 flames is also lower than predicted by simulations in Fig. 8.21.

Finally, LIF images for two different momentum ratios of C_3H_8 are shown in Fig. 8.37. Even for the low momentum ratio case, the flame appears unstable and forms different

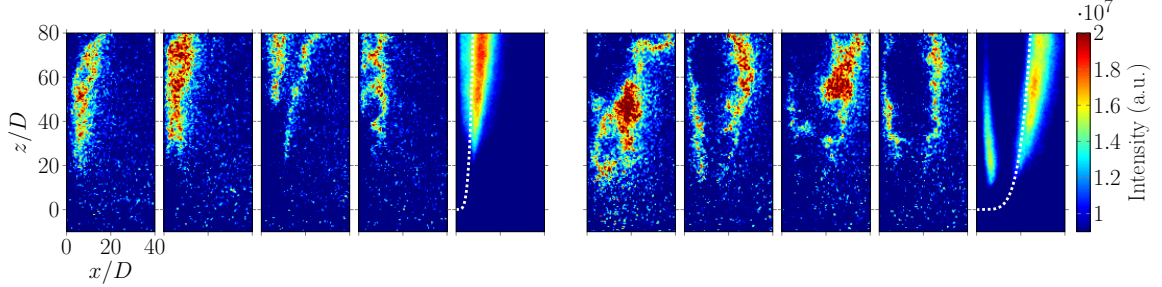


Figure 8.37: LIF of C_3H_8 flames consisting of 4 single shots and an averaged image from 298 single images. Left: $I = 1.3$. Right: $I = 41$.

shapes (single flame, double flames, wrinkled). At $I = 41$, the flame becomes shredded, broken and chaotic. Compared to H_2 and CH_4 flames, the C_3H_8 reaction layers are more dismantled. On the instantaneous shots as well as on the averaged image, a small lee-side reaction and a large windward reaction zone establish. This is observed for different momentum ratios, as seen in Fig. 8.38. A lee-side reaction develops for $I = 2.4$ already and is quite pronounced at $I = 6.5$. It is for all cases smaller than the windward reaction zone and the two layers are significantly separated. With increasing momentum ratio, the

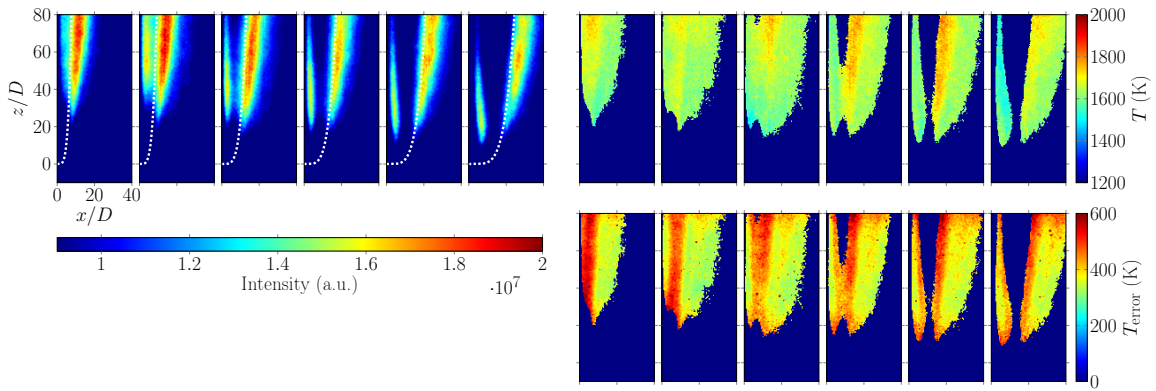


Figure 8.38: LIF of C_3H_8 flames. Left: averaged images. Top right: two-line temperature. Bottom right: two-line temperature errors. $I = 1.3, 2.4, 6.5, 13, 25.4, 41$.

reaction shifts upstream, as seen on the OH^* recordings. The temperature is around 1600 K to 1700 K. There is no notable increase when the fuel amount is altered. Since the reaction zone is subject to great instabilities and fluctuations, the resulting temperature errors are significantly above the errors of the two previous fuel types. Compared to the 1D simulations and results in Fig. 8.21, the experimentally determined temperatures are again lower than expected. The maximum temperatures are in the range of 1800 - 2000 K at low and moderate strain rates for the used fuels here. Interestingly, compared to the premixed flat flame burner experiments in section 4.2, where lean and stoichiometric conditions reached SNR values around 8 and fuel-rich conditions were even far lower ($P_{11}(2)$), the flame front of the reaction zone from the injection experiments exhibited SNR values around 12 and in some cases up to 14, independently of the fuel type and momentum ratio.

In contrast to the diffusion flames in this study, the inverse diffusion flames found in the work of Richardson et al. [167] and presented in Fig. 8.39 did not show lee-stabilized and windward flames, independently of the geometry and blowing ratio m . The authors injected cold air into a fuel-rich hot main flow. There, the flames appear rather as premixed, with high intensity cores. Though, the main reaction zone shifted upstream and reduced the IDL with increasing the blowing ratio m .

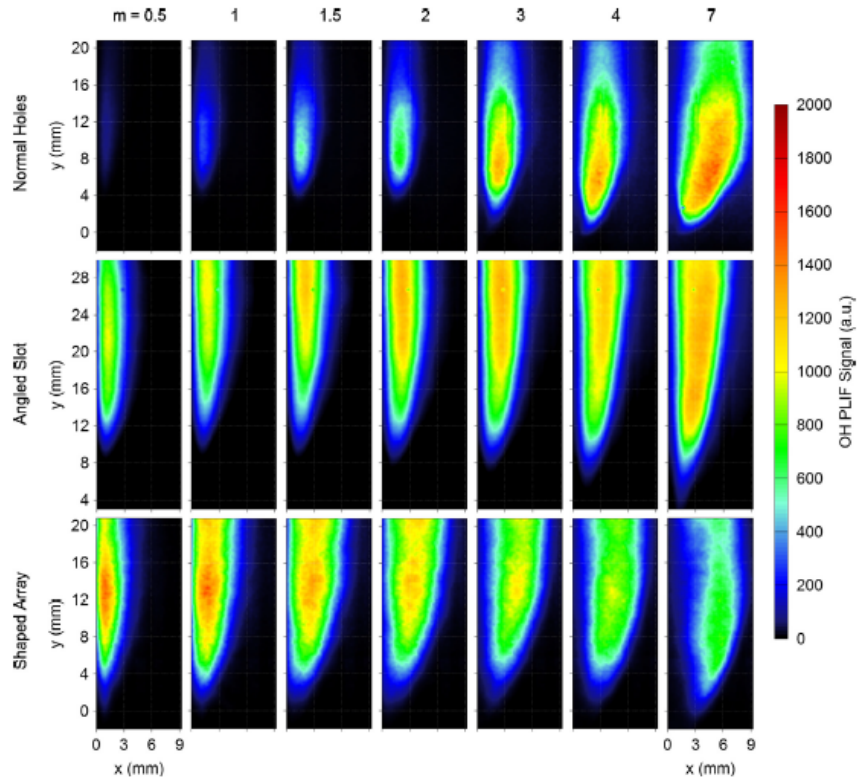


Figure 8.39: OH PLIF results for different geometries and blowing ratios m . Result from Richardson et al. [167].

8.2.6 Angled injection results

The orifice of the angled 30° JICF experiments had a diameter of $D = 0.4$ mm. Thus, for equivalent momentum ratios to the normal jets with a diameter of $D = 0.55$ mm, lower fuel amounts were injected. Consequently, the global reaction of the angled JICF may be less intense.

8.2.6.1 OH* chemiluminescence

Averaged OH* images for the three fuels subject to investigation are shown in Fig. 8.40 side-by-side. Identical hardware settings were applied as in section 8.2.5.1. The detailed momentum ratios are listed in Tab. F.5. The illustration reveals different characteristics. As experienced from the normal JICF, the angled H₂ jets ignite near the injection location and basically anchor to the orifices. Perhaps, the angled jet exhibits a small, but negligible IDL due to its angle and thus similar orientation as the crossflow. The flames reflect the jet-like structure of the reaction zone. With increasing fuel amounts a gradual vertical extension of the wall-attached flames are observed. Depending on the fuel amount, the reaction zone is confined to well defined region. In comparison, the CH₄ jets react after a considerable IDL and anchor to the surface. With increasing I , the reattachment point of the lifted jet and the main reaction zone shifts slightly upstream. However, for the highest momentum ratio, a clear reattachment is not observed. The flame remains lifted. It is notable, that the peak intensities are lower than those of H₂ flames. Changing to C₃H₈, a reaction zone develops

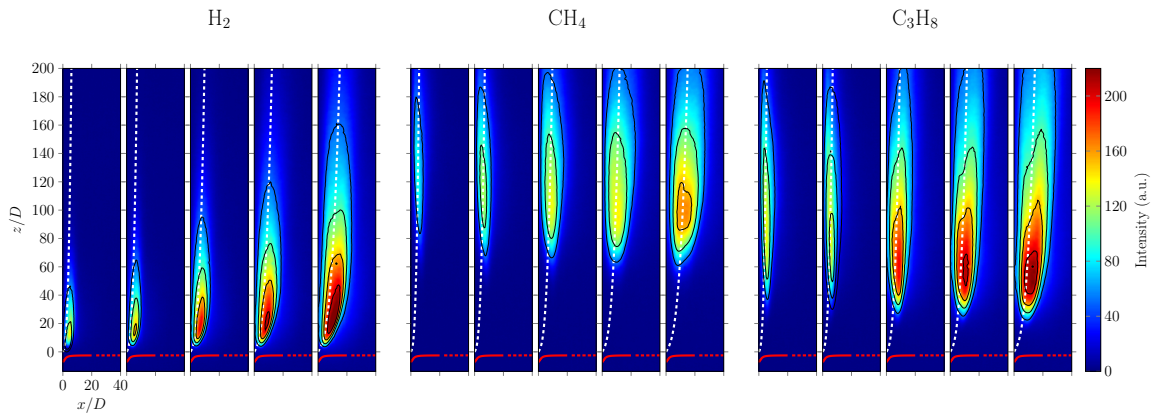


Figure 8.40: Averaged OH^* chemiluminescence images. Left: H_2 with $I = 1.1 - 19.6$. Center: CH_4 with $I = 1 - 19.3$. Right: C_3H_8 with $I = 0.9 - 17.2$. Velocity profile in red. Solid part indicates boundary layer. Dashed white line is the trajectory.

attached to the major part of the surface which also moves upstream with increasing I . The peak intensities are on the level of those of H_2 flames. Trajectories were determined from the analytical expression in Eq. (2.23) and are included to the intensity images in Fig. 8.40. The simplicity of the equation with only the injection angle and the momentum ratio as parameters makes it especially appealing. In general, the trajectories correspond well to the overall shape of the flames except for the main reaction and core area. The deviation in this region is likely due to expansion of the reactive flow which causes the centerline to move away from the surface and is not described by the analytical trajectory function perfectly (the expression was found in literature for non-reactive jets). Due to the steep injection angle, the trajectory and the main part of the reaction are located within the boundary layer with a scaled thickness of $\delta_{99\%}/D = 20$.

Spatial heat release rates determined based on Eq. (2.47) and integral intensities from the OH^* data are summarized in Fig. 8.41. The chemical reaction of the H_2 flames is completed within the test section, as the heat release rates decline to zero in the downstream direction. With rising momentum ratio, the flame extends downstream and the maximum of the heat release rate shifts downstream from around $z/D = 10$ to $z/D = 40$, in contrast to the normal H_2 flames which remained at a constant position. The maximum heat release is in the range of $7 - 10 \text{ J}/(\text{mm}\cdot\text{s})$. While the H_2 heat release curves experience a steep ascent at the ignition location, the CH_4 reaction zone shows a bell-shaped curve. A slight upstream shift is observed in the maximum locations at increasing I . At low fuel rates, the C_3H_8 heat release rate resembles the CH_4 flames. The maximum heat release rate of the hydrocarbon flames is around a factor of $2 - 3$ higher than that of H_2 flames. For all fuels, the width of the reaction zone increases and the peak location shifts from $x/D = 5$ to 15 , but remains within the boundary layer.

The IDL length, the normalized integral heat release and the flame length of the angled fuel injection are summarized in Fig. 8.42. The momentum ratio does not affect the IDL of CH_4 based on maximum location and as well as 10 % indicator significantly, while the normal injection showed a favorable effect of I on IDL. In contrast, the C_3H_8 flame maximum location shifts from approx. $z/D = 105$ to 65 when I varies from 0.9 to 17 . But the IDL based on 10 % increase is hardly affected (from $z/D = 30$ to 20). Further, the IDL of the

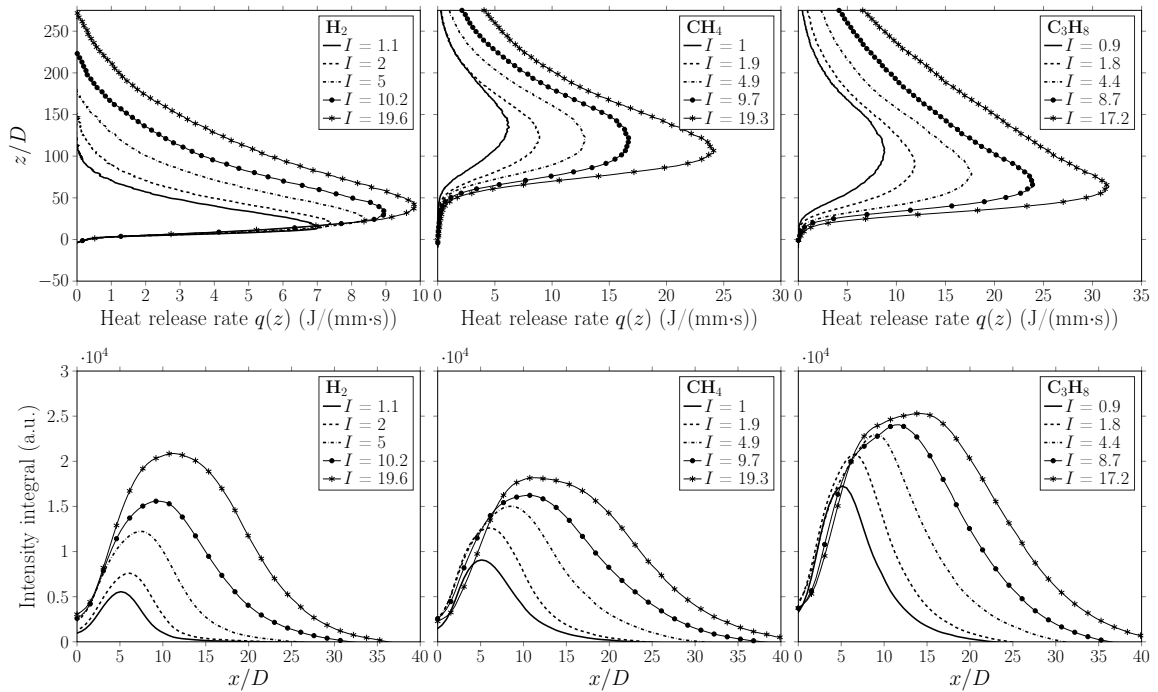


Figure 8.41: Angled injection. Top: heat release rate calculated from the intensities integrated horizontally. Bottom: intensity integrals in the vertical direction.

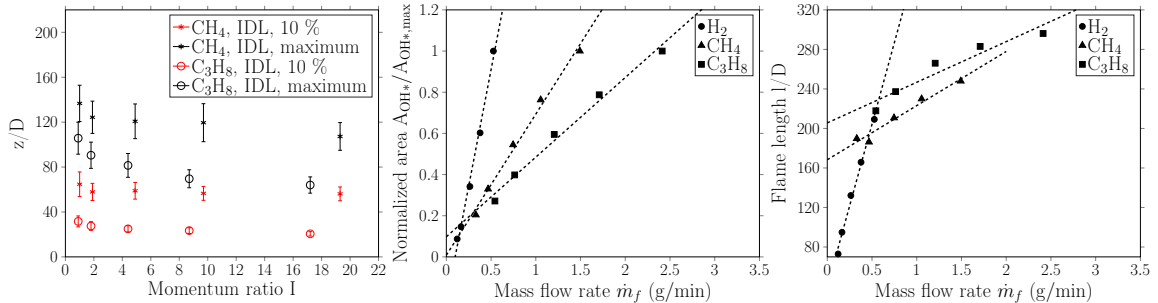


Figure 8.42: Angled injection. Left: ignition delay length for hydrocarbons. Center: normalized integral heat release rate. Right: flame length.

angled flames are notably larger than those of transverse flames due to the orifice orientation. As demonstrated for the normal jets, the integral heat release depends linearly on the fuel mass flow rate also for angled injection, which means that this property is independent of the injection configuration. While the flame length of the normal injection did not correlate with the mass flow rate, a linear tendency is observed for angled H_2 and CH_4 injection up to a certain degree. This might be attributed to the fact, that the angled H_2 and CH_4 jets do not experience a strong deflection and exit the orifices with velocities around 50 to 210 m/s and 16 to 73 m/s (Tab. 8.4), respectively. Thus, the flames take stable shapes and resist largely the interaction with the main flow.

OH^* chemiluminescence images from the front direction are shown in Fig. 8.43 for the lowest and highest momentum ratio. The H_2 single flames are clearly visible. At the lower momentum ratio, the individual fuel jets fully react and do not merge, while increasing the

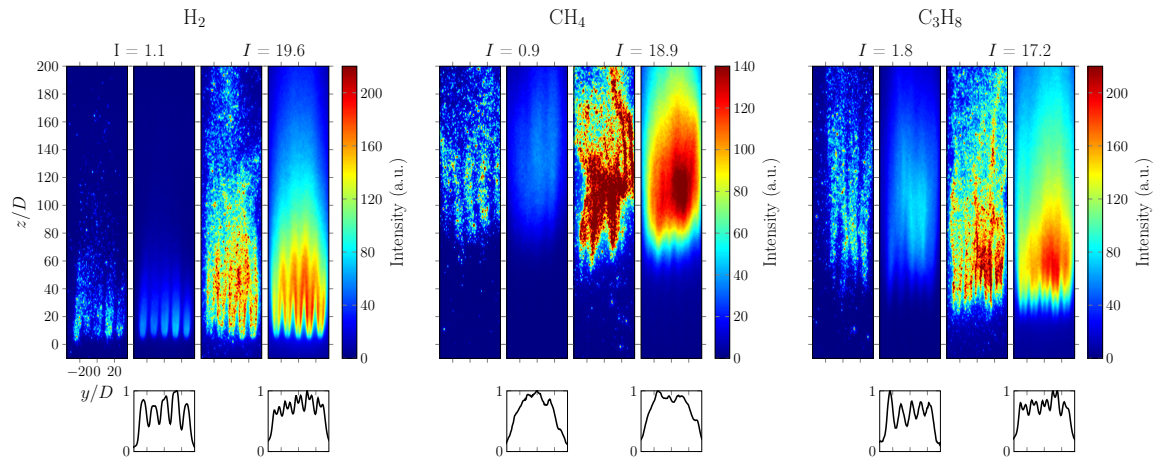


Figure 8.43: OH* chemiluminescence recordings from the front direction of angled fuel JICF. For each momentum ratio, an instantaneous image and an averaged image of 300 single images are shown. Vertical intensity integrals are given on the bottom.

momentum ratio to 19.6 the reaction zones get in contact around $z/D = 35$ and cover the surface entirely. The CH₄ flames show a different picture. Some individual jet structures appear in the single images of both momentum ratios. However, time-averaging 300 images results in a blurred and smeared shape, especially for $I = 18.9$. The low momentum C₃H₈ flames reflect the jet structure along the complete downstream distance, while at $I = 17.2$ the jets appear initially, but after a short distance merge to a homogeneous reaction film. Compared to the normal injection cases, the jet structures of the angled injection for all three fuels are more pronounced due to two reasons. First, the normal jets experience an enhanced mixing due to the orientation and intense flow interaction. Second, the orifice distance to diameter ratio P/D (hole spacing) of the normal configuration is 9.1, while that of the angled geometry is 12.5. Reducing the spacing allows the jets to merge further upstream.

8.2.6.2 Planar laser-induced fluorescence

Fig. 8.44 presents two LIF intensity instantaneous images and a time-averaged image (of 298 single images) of the rotational line $P_{11}(2)$ for each of the investigated fuels. The H₂

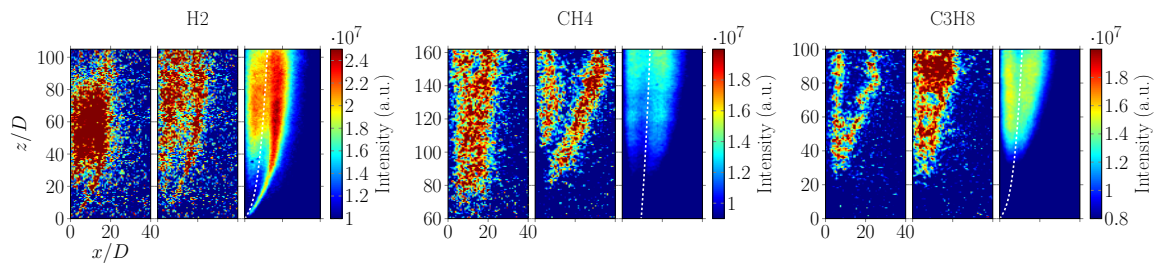


Figure 8.44: LIF of angled fuel flames consisting of 2 single shots and an averaged image from 298 single images. Left: $I = 19.6$. Center: $I = 19.3$. Right: $I = 17.2$.

flame reacts instantly after injection despite average jet velocities around 210 m/s. Due to

its high momentum ratio, the jet detaches from the surface. On the single images, a reaction streak develops along the jet shape on the windward jet-crossflow interface, but also along the wall a reaction zone develops. As the mainstream gases flow around the jets, fuel is transported downstream due to shear effects and react after mixing. The intensity of this reaction zone increases gradually in the downstream direction, observed on the averaged image. The hydrocarbon flames show similar double structures, only further downstream due to the IDL. However, compared to the H_2 flame, the CH_4 reaction zone exhibits hardly a jet shape, while some jet structures are found in case of the C_3H_8 flame. The low intensity of the CH_4 averaged image compared to the corresponding single shots is attributed to the unstable nature of the reaction zone. The analytically determined trajectory deviates from the H_2 jets, as seen before on the OH^* image, while for the hydrocarbons a good agreement is found. This observation is made for different momentum ratios in Fig. 8.45. The superimposed trajectories for non-reactive jets agree well with the general shape of the reaction zones. The H_2 flames detach from the surface with increasing I and the windward

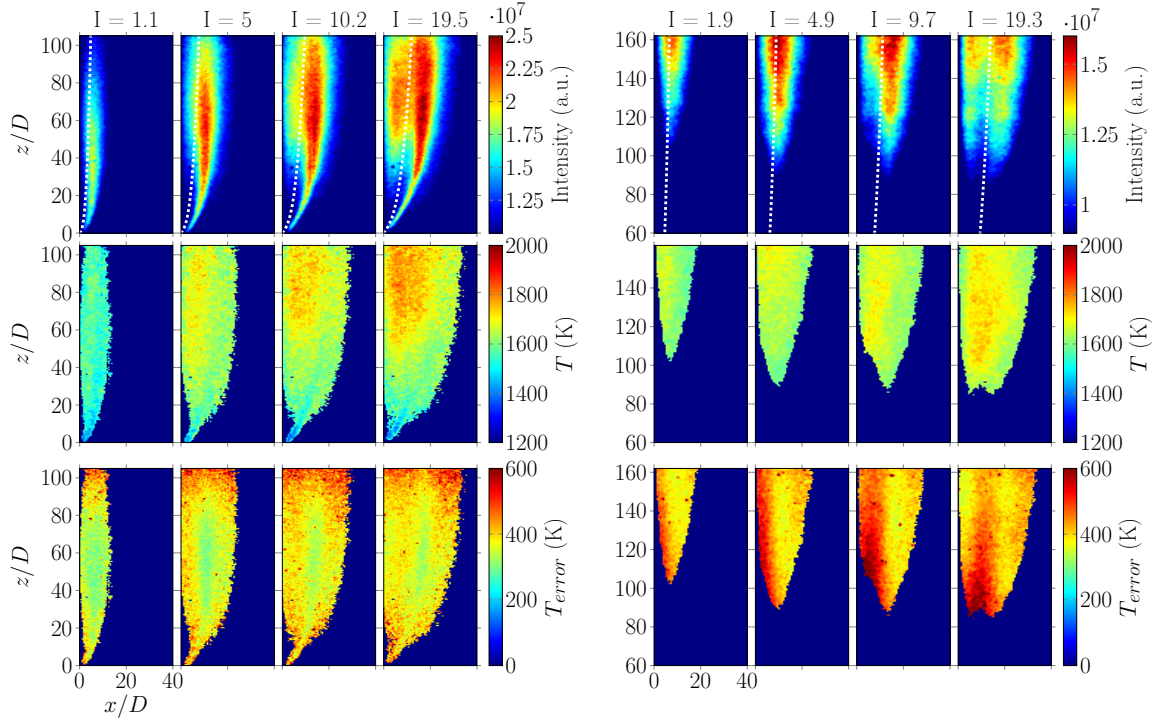


Figure 8.45: Left: H_2 . Right: CH_4 . Top: averaged intensities. Center: two-line temperature. Bottom: temperature errors.

reaction as well as the lee-side reaction enhances. The splitting of the reaction zone into two regions is observed in the same manner for the CH_4 flames. The H_2 flame temperature is around 1600 K for the lowest fuel rate and shows a homogeneous spatial distribution. As the fuel amount is increased, the temperature reaches values around 1800 K gradually in the downstream direction. Colder regions are also perceptible directly after the injection. Compared to the normal injection in Fig. 8.34, the temperature level of angled H_2 flames is slightly lower, while the flame temperature distribution of the normal injection is more homogeneous. This might be attributed to the fact, that the transverse fuel jets are subject to higher mixing and interaction and thus more intense reaction. As the core of the flames

in Fig. 8.45 are stable and experience lower fluctuations, the temperature errors are around 300 K and small in that region, while especially on the edges the errors raise to values around 500 - 600 K. The CH₄ flame temperature of angled fuel jets is quite similar to the temperature of the normal flames in Fig. 8.36. The maximum temperature level is around 1700 - 1750 K for the highest fuel rate. The reason for the similarity might be due to the IDL. The angled and normal CH₄ fuel jets travel a significant distance, during which they can mix with the crossflow and eventually react. The low reactivity of CH₄ compensates the enhanced mixing effect of the normal jet compared to the angled configuration. In contrast, the H₂ flames ignite directly and the mixing affects the reaction intensity. Compared to the H₂ flame temperature, the CH₄ temperature is subject to larger errors caused by the unstable nature of the flame.

As mentioned at the beginning, there was no access to the light sheet after passing through the reaction zone, due to the wall element of the test section. Thus, an absorption correction of the laser intensity was not possible. However, an estimation of the absorption error based on the flame thickness can be given. The width of flames on the single images is mostly around 5 mm and on the averaged reaction zone it is around 16 mm. From the counterflow simulations in Fig. 8.21 the largest number density of OH was determined for H₂ flames as $4.6 \cdot 10^{22} \text{ 1/m}^3$ and the temperature was 2050 K. According to the theoretical background in section 4.2, especially to Eq. (4.8), the temperature error would be 37 K and 96 K for the specified flame thicknesses, respectively. As the number density of OH for CH₄ and C₃H₈ flames was around 50 % of that of H₂ flames, the maximum temperature error might be below 50 K consequently. Another source of error is quenching, which was unconsidered due to lack of knowledge of the local reaction zone composition of the collision partners of OH and temperature. Including these sources of error in future investigations may improve the results significantly.

The optical results so far helped to localize and characterize the reaction zones by means of IDL, wall distance, integral intensities and heat release rates, and the overall shapes. The heat release effect of the reacting jets on the wall is subject of the next section.

8.3 Heat flux results

The reacting fuel jets in the oxygen-vitiated crossflow released significant amounts of heat due to exothermic reactions. As the combustion was in close proximity to the surface, part of the heat was transferred to the wall, which was determined by means the inverse heat conduction method and based on discrete temperature measurements within the wall block. IHC simulations were conducted on the numerical domains e) in Fig. 6.1. A 2D heat flux profile with lateral variations was optimized. Prior to those calculations, the spatial stabilization procedure presented in section 6.4.2 was conducted on the smaller, symmetrical domain f) first, and final IHC simulations were conducted with the new determined TC positions.

The simulations were performed on a local computer, with a 1.80 GHz, 8 physical core CPU and 64 GB of RAM. A direct simulation iteration took around 90 s.

8.3.1 Boundary conditions and data processing

During an experiment, the inlet and outlet cooling water temperatures and the temperature of the cold gas within the injection slot were measured by TC, as exemplarily shown in

Fig. 8.16. Additionally, discrete temperature measurements at various locations of the test section wall were conducted by the 19 implemented TC, as discussed in chapter 6. The data recorded with a sample rate of 2.85 Hz was subject to noise. Further, the run-time of an experiment in combination with the sample rate resulted in a large number of time steps, which for the direct IHC was inconvenient, an inverse calculation for the transient case would be inefficient. Thus, a Savitzky-Golay filter [164] was applied to smooth the data and to reduce the measurement points and consequently the number of temporal optimization steps. A 5th order polynomial with a frame length of 11 (subsequent data points) helped to reduce the sample rate to 0.1 Hz. Fig. 8.46 shows the transient temperature of a TC. Steep slopes emerged during the injection and combustion of fuel near the surface. Turning off the injection and thus the combustion resulted in a temperature drop. As the enlarged sections highlight, the filtering did not significantly alter the initial measured data. Gradients and sudden changes are still covered by the filtered curve. Additionally, an injection period conducted for around 500 - 600 s and reduced by the filtering to 50 - 60 time steps, was still sufficient for the inverse heat analysis.

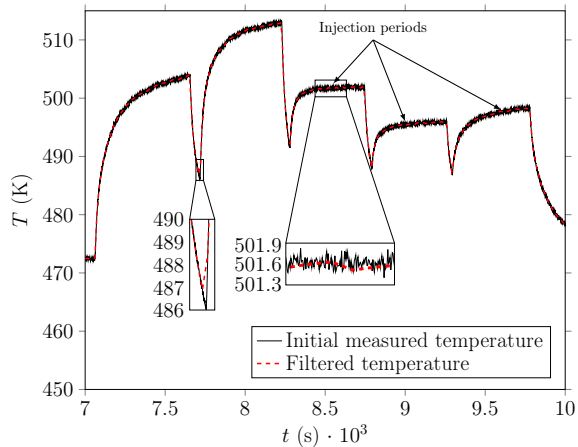


Figure 8.46: Measured and Savitzky-Golay filtered transient temperatures.

For the IHC simulations, the known boundary conditions were applied to the domain as characterized in Fig. 6.1. A representative reference temperature of $T_\infty = 300\text{ K}$ and the geometry height of 220 mm were set for the natural convection on the vertical surface. As the ambient temperature around the test section slightly increased, this value was reasonable. According to the cooling water setting, reported in chapter 5, the flow condition was turbulent. Thus, the tube diameter D_t (8 mm) based Nusselt number $Nu_{D_t} = 0.027 Re_{D_t}^{0.8} Pr^n (\eta/\eta_s)^{0.14}$ was applied, where n is 0.3 or 0.4 for heating or cooling, respectively, and η is the dynamic viscosity of water [194]. The subscript s indicates properties evaluated at surface temperature. Therefore, the reference local water temperature $T(z)$ was linearly interpolated between the measured inlet and outlet temperatures. For the reduced block domain, a symmetry boundary condition was selected for the x - z -plane. The bottom and top surfaces, which were connected to the mounting and end plates, see Fig. 5.4, were considered as adiabatic.

8.3.2 Normal injection

Fig. 8.47 shows some exemplary IHC results of a complete experiment period. On the

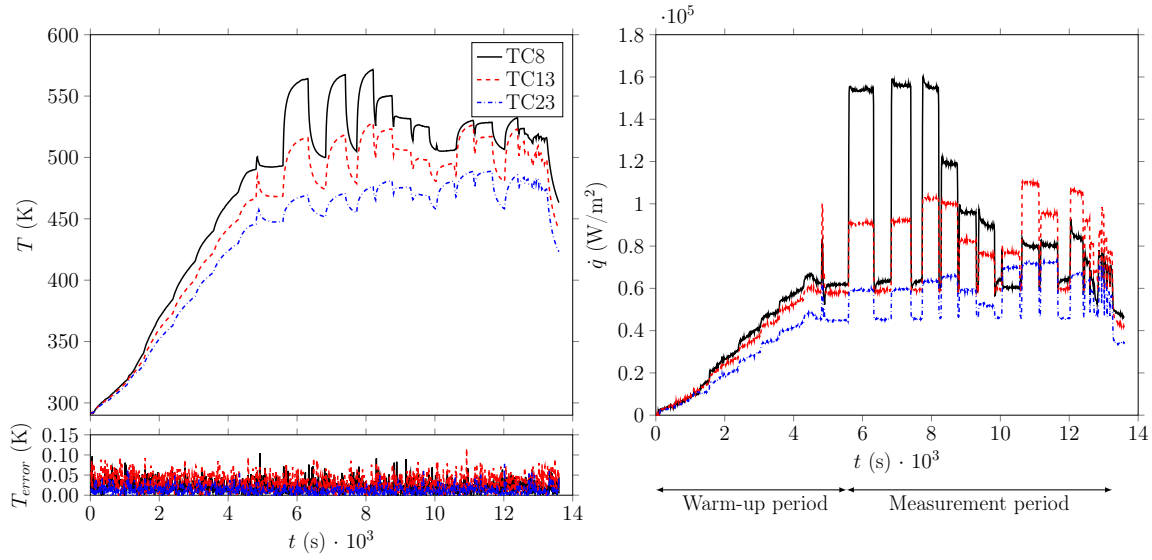


Figure 8.47: IHC results. Left top: temperature profiles at TC positions. Left bottom: temperature discrepancy. Right: surface heat fluxes at projected TC positions.

left graph the recalculated transient TC temperatures are presented, while the right graph contains the corresponding surface heat fluxes (surface locations where the TC are projected onto). According to the error graph on the bottom left, $T_{\text{error}} = |T_{\text{measured}} - T_{\text{calculated}}|$, the measured temperatures were reproduced to an accuracy of smaller than 0.15 K for the three selected TC. The maximum discrepancy for the 19 TC was set to 0.2 K. As discussed before, the data consists of a warm-up period, a measurement period and finally the cool down phase, which is not explicitly indicated in the figure. Within the measurement period a number of peaks in the temperature and heat flux graphs are observed. Each peak occurred due to fuel injection at a constant momentum ratio and the subsequent combustion. These periods are referred to as injection periods. It is obvious, that at the end of the warm-up period a steady-state condition was reached, since the temperature and heat flux profiles reach a constant level. Different temperature and heat flux magnitudes were determined in this period for the selected TC according to the locations. Further downstream locations were subject to lower thermal loads, as the boundary layer increased in the downstream direction, while the convective heat flux experienced the inverse effect.

The IHC surface results of four selected centerline TC positions during H₂ injection are presented in Fig. 8.48. Note, the origin of the abscissa was shifted for reasons of convenience. For each momentum ratio, a constant fuel mass flow was injected for a period of time resulting in near-wall reacting jets and heat release to the surface. Initially, the temperature profiles experience a steep gradient, which shortly after decline and the temperatures consequently approach a constant value. In most cases, a steady-state temperature was not reached, as this required longer injection and cooling periods. Moreover, the heat fluxes are of interest, which is presented on the right graph of the discussed figure. Here, the profiles demonstrate that the injection period was sufficient. During the combustion, the heat fluxes reach a nearly constant level. After turning off the injection, the heat loads reach pre-injection values, whereas the temperatures drop rather slowly to a constant condition and require longer cooling time. In agreement with the optical results and the location

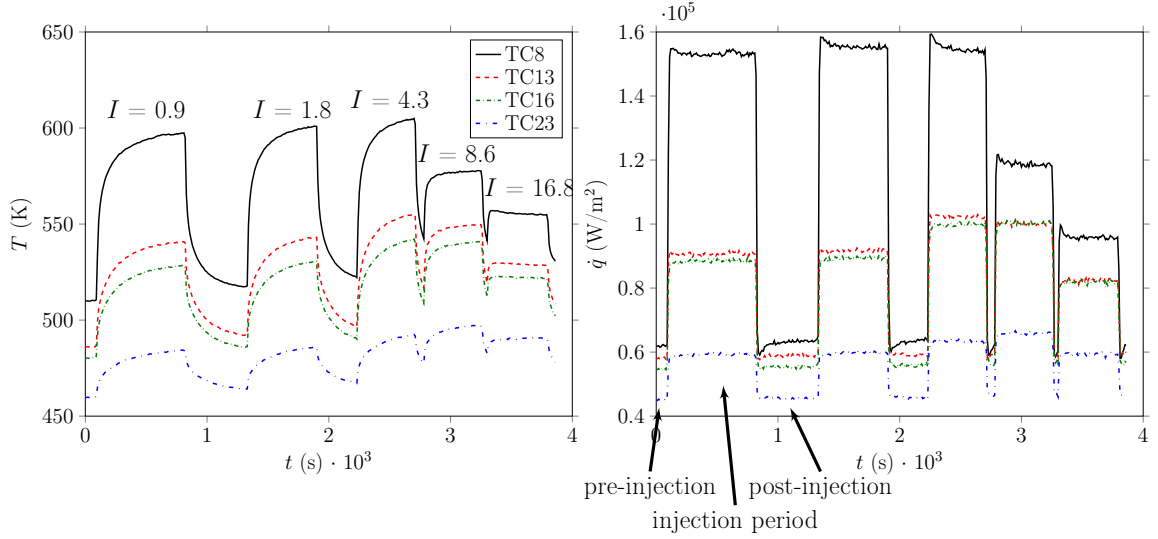


Figure 8.48: Transient IHC results for H_2 injection. Locations correspond to TC projected onto the surface. Left: temperature profiles. Right: heat flux profiles.

of the reaction zone, the highest thermal elevation occurs near the first TC location and gradually decreases in the downstream direction. Interestingly, despite the increased H_2 fuel amount up to $I = 4.3$, the heat release does not significantly increase. Slightly higher levels are observed downstream of TC13 for $I = 4.3$. Heat elevations around 150 % were found at TC8 location. Further increases of I resulted in significantly lower heat fluxes to the surface (100 % and 65 % for $I = 8.6$ and 16.8, respectively), even though the heat release rate according to Fig. 8.30 gradually increased and the reaction zone covered more area of the plate surface, see Fig. 8.32. Thus, the heat flux decline might be attributed to the detachment of the jets from the surface. Especially for $I = 8.6$, the heat flux at the location of TC8 is lower than for the previous momentum ratio cases, while similar heat releases are detected at the remaining TC locations. Apparently, the reaction zone detaches first and reattaches further downstream. Going to $I = 16.8$, reduced heat fluxes are observed on the entire locations.

2D temperature distributions for the pre-injection case and for the H_2 injection at $I = 4.3$ are presented in Fig. 8.49. Before the injection, peak temperatures are observed around the slot, due to the gap and lack of water cooling effect. Apart from that, the surface temperature shows a homogeneous lateral distribution on the surface ($x/D = 0$). On the $y/D = 0$ plane, a strong temperature gradient develops due to the heat load to the $x/D = 0$ plane, the water cooling and the low thermal conductivity of the material. According to the z/D planes, a temperature distribution symmetrical to the y/D plane is obtained. Peak values are located along the centerline, which might be an appropriate region for the evaluation of IHC data. During the injection period, the region near the injection location was affected mostly due to the anchored H_2 flame to the orifices. The thermal effect declined in the downstream direction. On the $x/D = 0$ some inhomogeneities in the off-center regions are found. These irregularities are actually more pronounced on the corresponding heat flux distribution in Fig. 8.50. Here, the surface normal heat flux for different conditions according to the individual image title is presented. As discussed in chapter 6, the heat flux values for those lateral locations, which were missing sensors, were averaged from the neighboring

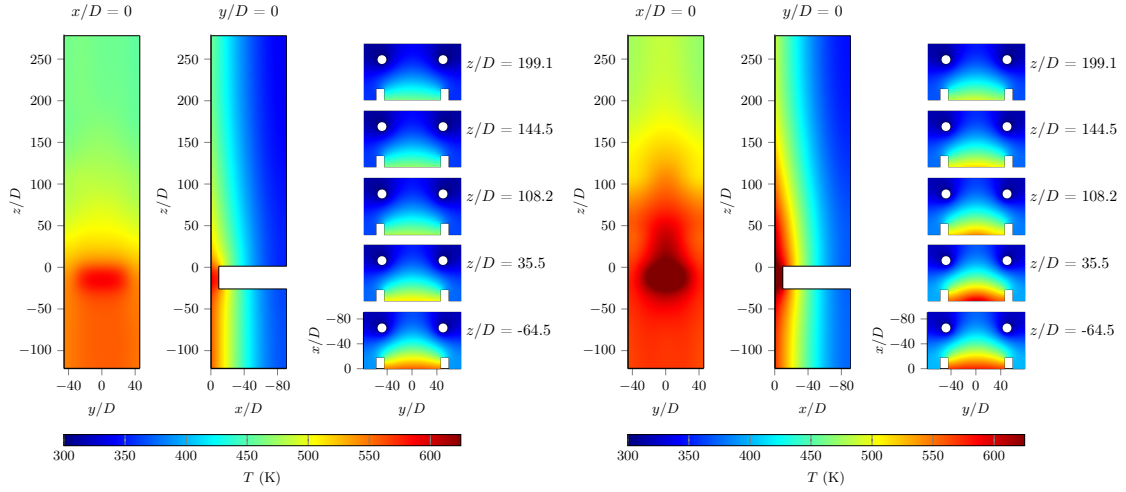


Figure 8.49: 2D temperature distribution for H_2 injection at $I = 4.3$. Left: before injection. Right: during injection.

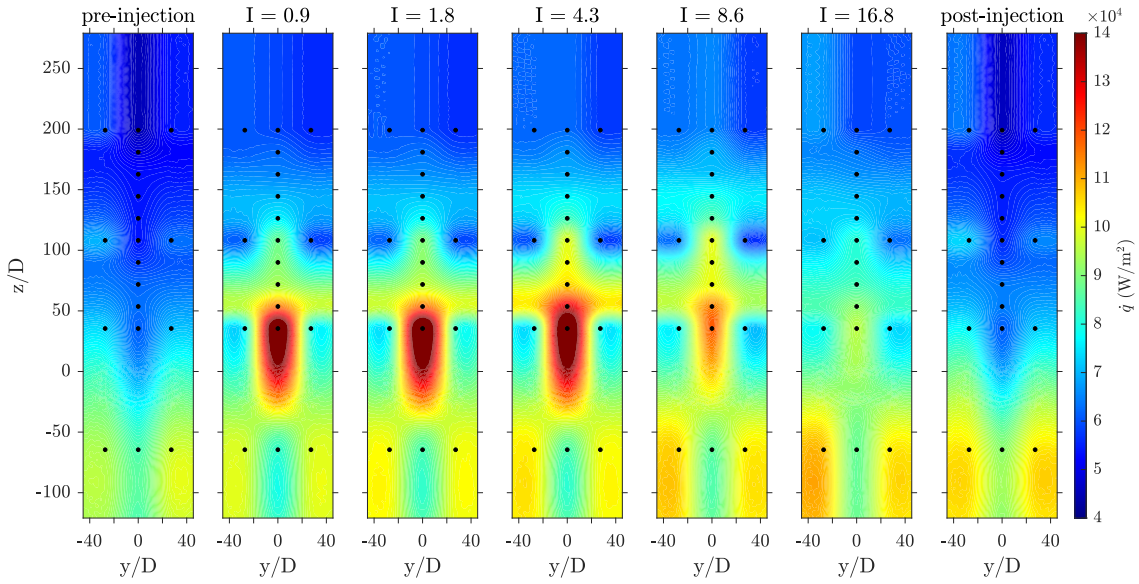


Figure 8.50: 2D surface heat flux for H_2 injection.

TC locations. Thus, lateral regions downstream of TC8 ($z/D = 35.5$) without a sensor are subject of spatial heat flux variations. However, along the centerline, a sufficient number of TC were arranged to detect the temperature elevation. As seen on the transient discrete location data in Fig. 8.48, the heat loads increased up to $I = 4.3$, then reduced significantly. Note, that similar pre-injection (before $I = 0.9$) and the post-injection states (after $I = 16.8$) emerge despite the intervening combustion periods. Meanwhile, only the inlet region heated up. Non-physical lateral heat flux fluctuations due to the nature of the interpolation scheme are also observed in the study of Perakis et al. [155], as illustrated in Fig. 8.51. While the lateral temperature distribution showed a rather smooth behavior, the heat flux curves were subject of strong fluctuations, which did not necessarily project the location of the

injectors and did not represent local conditions accurately.

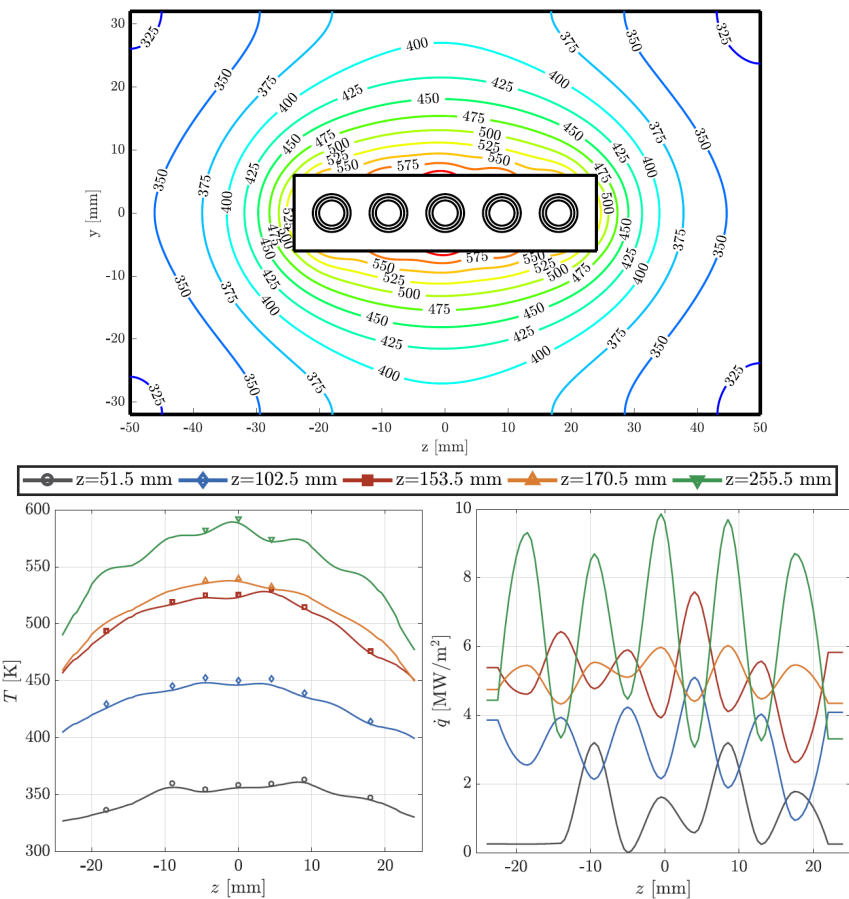


Figure 8.51: Left: cross sectional view to show the arrangement and z - y -locations of the co-flow injectors at the center. Right: lateral temperature and heat flux distribution from IHC simulation. Markers indicate measured values. The legend of the graphs should indicate the flow direction x instead of z . The temperatures were from 1 mm below the hot surface, while the heat fluxes were on the surface. Coordinate z corresponds to the lateral coordinate y in this study. Images extracted from Perakis et al. [155].

Axial heat flux distributions along the centerline are presented in Fig. 8.52. Since the fuel was injected through 5 horizontally aligned orifices and additionally the IHC was subject to lateral fluctuations, the surface heat flux $\dot{q}(y,z)$ was laterally averaged from $y = -15$ mm to $y = 15$ mm. This calculation corresponds to an IHT calculation with constant lateral heat flux assumption. However, the averaging was on the cost of the spatial resolution of the data. To determine the non-dimensional heat flux augmentation due to near-wall reaction, Eq. (2.5) seemed as an appropriate basis for the current experimental data. Further, the non-dimensional parameter $\Delta\dot{q}$ in percentage could be utilized for comparison purposes of heat flux augmentations resulting from different fuel amounts and different fuel types injected. Here, \dot{q}_{react} was obtained from the injection period, while \dot{q}_{inert} was taken from the pre-injection period, see Fig. 8.48. In the discussed figure, the centerline heat flux, laterally averaged heat flux and the heat flux parameter for the averaged profiles of H₂ near-wall reaction are shown. In general, the averaged heat flux values are lower than those

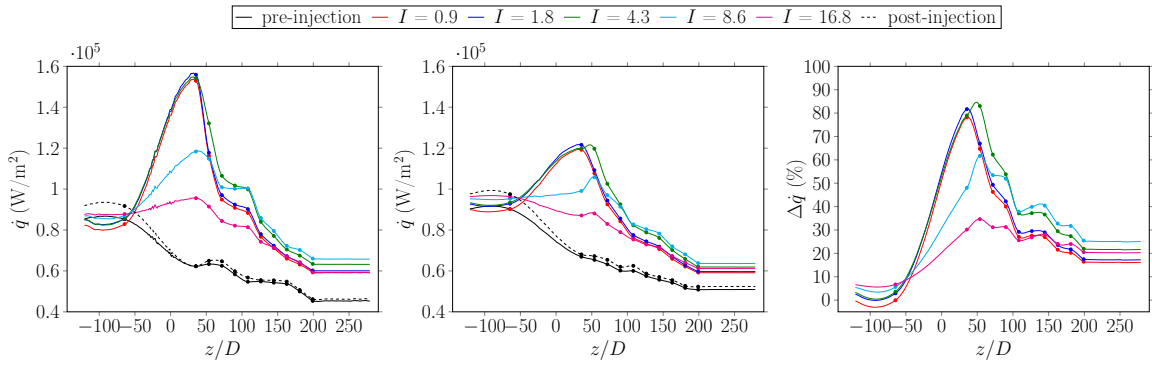


Figure 8.52: Centerline IHC results for normal H_2 injection. Left: centerline heat flux. Center: area averaged heat flux. Right: heat flux increase according to Eq. (2.5) for the lateral averaged data. Solid points indicate TC positions.

on the centerline. At the location of the first TC, the highest heat elevation is detected, which then declines in the downstream direction. For the first three momentum ratios, the maximum augmentation based on the averaged profiles is around 80 %. For $I = 8.6$ and 16.8, the increase is around 60 % and 30 %, respectively. Note, the overall pre- and post-injection profiles are in good agreement.

Selected transient IHC results for normal C_3H_8 jets are shown in Fig. 8.53. An analysis

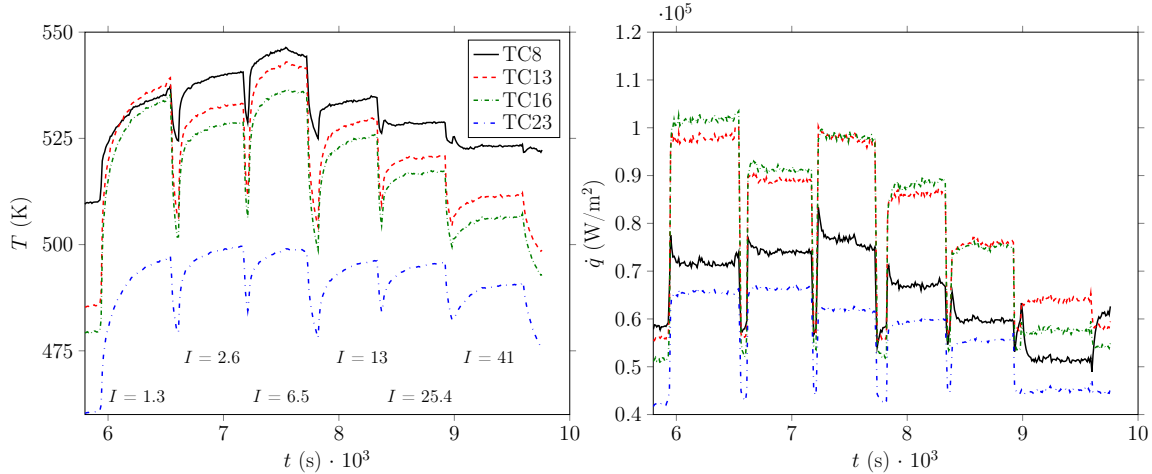


Figure 8.53: Transient IHC results for normal C_3H_8 injection. Locations correspond to TC projected onto the surface. Left: temperature profiles. Right: heat flux profiles.

of the heat release from the hydrocarbons is more difficult than from H_2 . The heat augmentation depends on the distance of the reaction zone from the surface and on the amount of injected fuel, beside the type of fuel. However, increasing the momentum ratio and hence the amount of fuel led to an increased tendency of detachment of the reaction zone from the surface. Further, the hydrocarbons exhibited an IDL, which in turn depended on the momentum ratio and fuel amount (and fuel type). In Fig. 8.53, highest heat augmentation for $I = 1.3$ is detected around TC13 and TC16, while the first position shows a small increase due to the IDL and the increase around the last location is also small, as most of the injected fuel was oxidized according to Fig. 8.30. Furthermore, based on the mentioned

figure, H_2 and C_3H_8 have similar peak heat release rates for their individual lowest I . However, the maximum surface heat flux increase for H_2 was around 150 %, while that of C_3H_8 is only 100 %. Apparently, the ignition location has a major effect on the surface heat load. Proceeding to $I = 2.6$, lower heat flux compared to the previous case is observed around TC13 and TC16. This might be attributed to detachment effects. The remaining locations experience similar heat loads to $I = 1.3$. At $I = 6.5$ the heat flux around TC13 and TC16 increases again. A closer look at the optical data in Fig. 8.29 and Fig. 8.38 reveals that first, the reaction zone is shifted downstream and second, a clear lee-side reaction emerged which might have caused the heat augmentation. Additional increase of I results in gradually decreasing heat loads, despite the potentially available energy, see Fig. 8.30. Actually, for $I = 41$, the heat augmentation was almost negligible, at least on the centerline locations. Here, especially the first position (TC8) experiences no significant heat loads. Note, the optical and the IHC data were from the same experiment in order to avoid inconsistencies.

For the sake of completeness and as an example, the 2D surface heat flux distributions resulting from the C_3H_8 near-wall reactions are provided in Fig. 8.54. The overall appearance

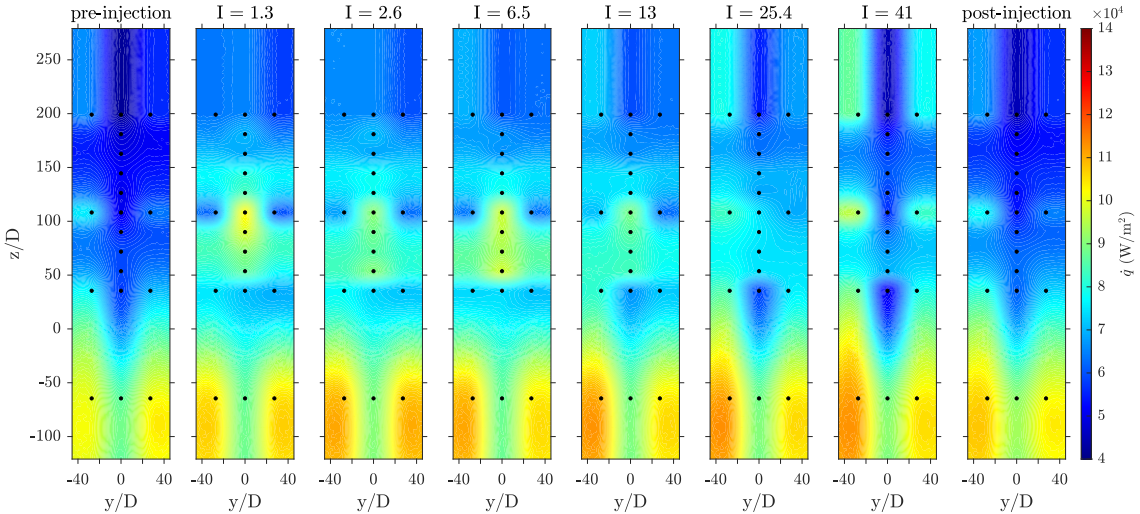


Figure 8.54: 2D surface heat flux for normal C_3H_8 injection.

of the heat inhomogeneities is similar to the discussed case in Fig. 8.50. However, starting from $I = 13$ to $I = 41$ the thermal loads around $z/D = 35.5$ decline. At the same time, the lateral locations at $z/D = 108.5$ and 199.5 were exposed to higher heat loads.

The corresponding axial heat flux profiles of C_3H_8 injection evaluated in the same manner as the IHC for the discussed H_2 injections are summarized in Fig. 8.55. Compared to the H_2 injection cases, the locations of maximum heat release are further downstream of the injection orifice. With increasing I it shifts upstream from $z/D = 100$ to $z/D = 50$. As seen on the transient data, the case with smallest momentum ratio and consequently lowest fuel rate causes the largest heat loads due to the close distance of the combustion to the surface. The maximum averaged heat augmentation was approx. 50 - 60 %, while the minimum was around 20 %. According to the optical results in Fig. 8.29 and Fig. 8.38, the reaction zone shifts upstream with increasing I and at the same time detaches further from the surface, according to the intensity integrals in Fig. 8.30, which may explain the significant heat flux reduction and that the first TC downstream the injection, TC8, still

detects thermal changes.

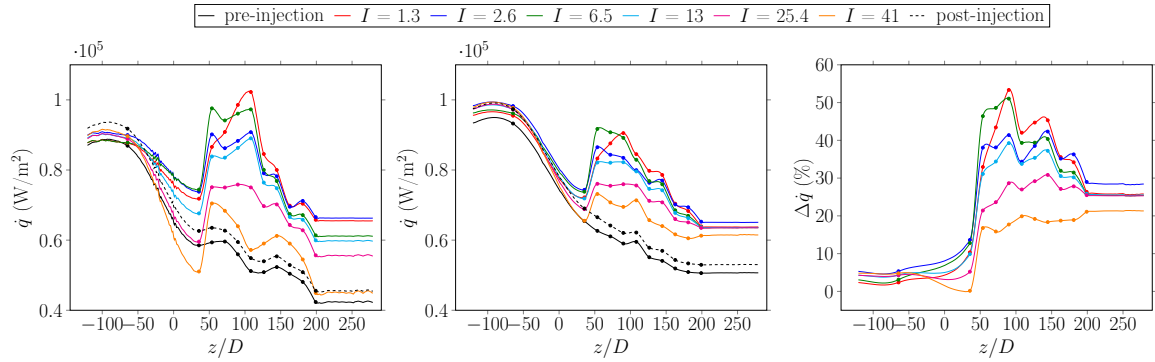


Figure 8.55: Centerline IHC results for normal C_3H_8 injection. Left: centerline heat flux. Center: area averaged heat flux. Right: heat flux increase according to Eq. (2.5). Solid points indicate TC positions.

Finally, IHC transient results for the second hydrocarbon, CH_4 , are found in Fig. 8.56. Similarly to the C_3H_8 cases, the first TC downstream the injection, TC8, is exposed to

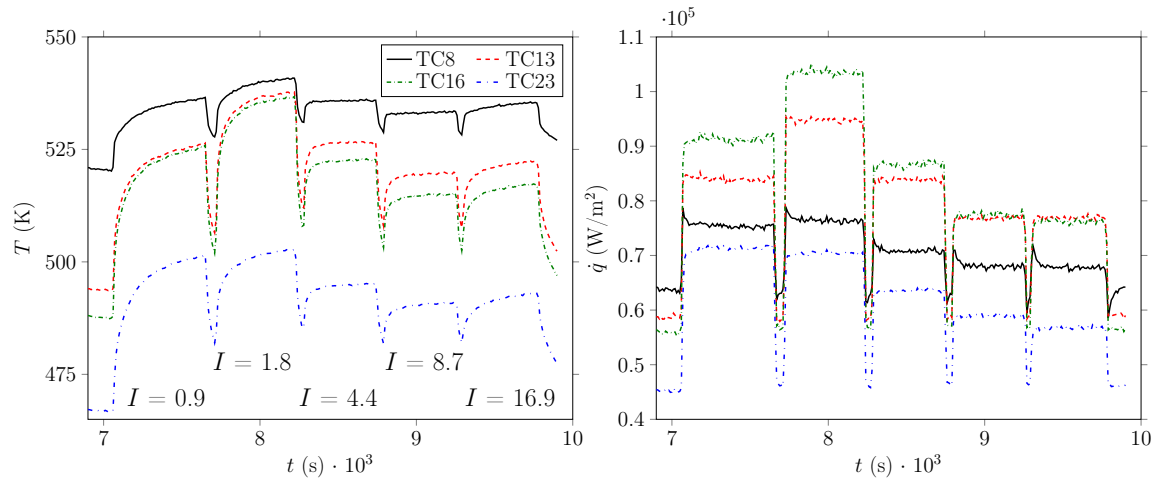


Figure 8.56: Transient IHC results for normal CH_4 injection. Locations correspond to TC projected onto the surface. Left: temperature profiles. Right: heat flux profiles.

the least thermal loads due to the IDL, while TC16 experiences the highest thermal effect, followed by TC13 and TC23. From $I = 0.9$ to 1.8 , the surface heat release around TC13 and TC16 increase significantly, but remain constant on the other locations. The maximum augmentation for this momentum ratio is around 80 %, which is lower than that of both other fuels. A further elevation of I results in lower thermal effect to the wall and for the last two cases, the heat flux stayed almost constant. For a better analysis of the heat flux development, Fig. 8.57 contains the axial data. Indeed, the maximum heat flux is detected for $I = 1.8$, which for the averaged case was just around 40 %. At the same time, the location of the peak has shifted upstream from $I = 0.9$ to 1.8 , which corresponds to the optical data in Fig. 8.27. The location of the peak heat release rate according to Fig. 8.30 was further upstream compared to the location of maximum heat flux and differed slightly.

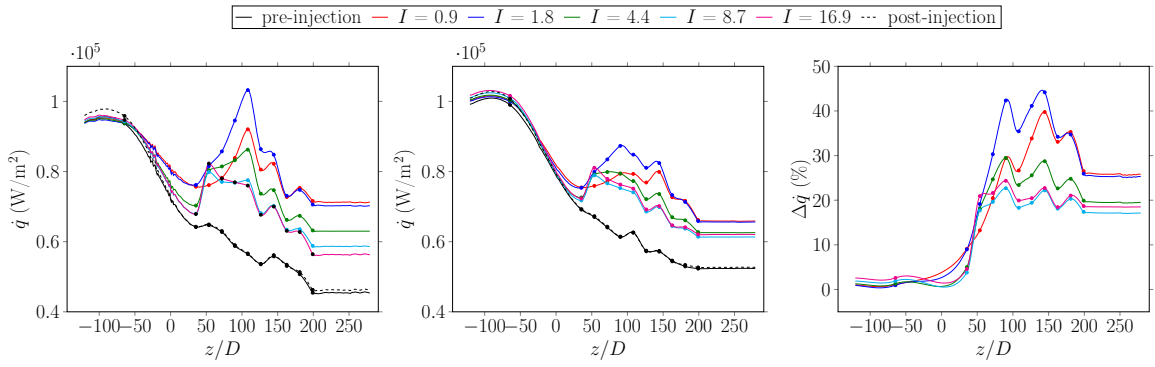


Figure 8.57: Centerline IHC results for normal CH_4 injection. Left: centerline heat flux. Center: area averaged heat flux. Right: heat flux increase according to Eq. (2.5). Solid points indicate TC positions.

This might be attributed to the fact, that the fuel jet reacts during the detachment phase and the reaction products reattach and cause the heat augmentation further downstream. Despite the increase in heat release rate due to the amount of fuel according to Fig. 8.30, the axial heat flux profiles of $I = 8.7$ and 16.9 appear to have an almost identical shape. The heat flux increase approaches a relatively constant value of around 20 % in the downstream direction and interestingly, the vertical intensity integrals for this two specific cases in Fig. 8.30 demonstrat the same gradient on the surface.

Based on the IHC data in combination with the optical results some conclusions can be drawn. The reacting normal jets produce a complex near-wall flow and the resulting heat flux to the surface depends on different aspects. First and foremost, the normal jets in the considered momentum ratio range detach from the surface and in some cases eventually reattach downstream. Due to the injection angle relative to the freestream, the jet fluid is exposed to high strain. H_2 seemed mostly insensitive to the strain and momentum ratio in the current condition and ignited directly. Apparently, stable anchored flames, see Fig. 8.25, with small distance to the wall release the highest heat flux. In comparison, the hydrocarbons are less stable and anchor in the mainstream somewhere downstream the orifices. Thus, significantly less heat augmentation on the surface is determined for the reaction of these fuels. Another important factor is the momentum ratio. Its increase results in separation of the secondary flow from the wall and consequently reduces heat transfer to the surface. However, there is a counteracting effect. The elevation of the momentum ratio is realized by increasing the fuel amount and hence, the total energy, which might result in higher heat flux. For H_2 injection, an increase of I caused only a reduction of the maximum heat flux, while for the hydrocarbon injections heat flux augmentations with varying I is observed. Further, increasing I contributes to the stability and the lowering of the IDL of the hydrocarbons, which in turn favors the surface heat transfer. However, as observed for CH_4 , the location and magnitude of the maximum heat flux approaches a constant value in case of large I . According to Fig. 8.30, the H_2 and CH_4 jets show similar heat release rates, but the H_2 flames cause significantly higher surface heat fluxes. It is obvious that the ignition location and stability of the flames are of major importance for the surface heat transfer. This is further confirmed by the fact, that the highest C_3H_8 fuel mass flux generated peak heat release rates twice as large as for H_2 and CH_4 , but lower surface heat flux.

8.3.3 Angled injection

IHC calculations for the angled injection cases were conducted in the same way as for the normal cases before. The results of the two configurations can be compared in a qualitative manner, but due to the different orifice diameters and different fuel mass flow rates, only a qualitative comparison is considered.

Fig. 8.58 shows selected transient surface temperature and heat flux results. The location

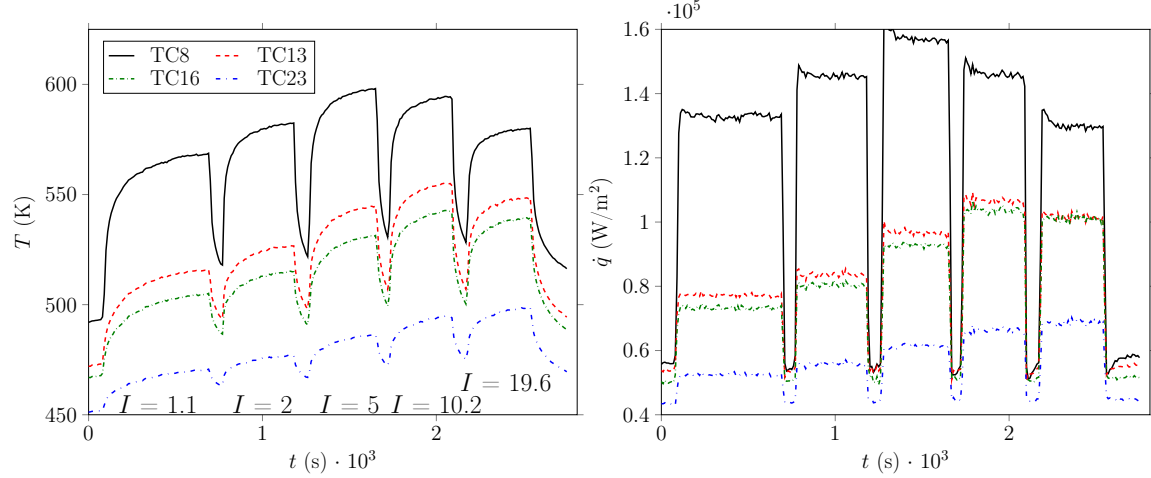


Figure 8.58: Transient IHC results for angled H_2 injection. Locations correspond to TC projected onto the surface. Left: temperature profiles. Right: heat flux profiles.

of TC8 is exposed to highest thermal loads. As the momentum ratio increases to $I = 5$, the heat augmentation at TC8 rises gradually from around 140 % to 150 %, then declines as I is further increased to 19.6. Whereas in the remaining locations, mostly a continually increase of heat flux was detected with increasing I . This might be explained by the injected amount of fuel vs. the downstream shift of the reaction zone. According to Fig. 8.41, the location of the maximum heat release moved downstream as I was increased, while for the normal H_2 injection the location of the maximum heat release rate stayed constant due to intense jet-crossflow-interaction. According to the axial heat flux profiles in Fig. 8.59, the maximum heat flux increases from $I = 1.1$ to 5, then it reduces slightly, which is in agreement to the transient data in Fig. 8.58. Compared to the normal injection profiles in Fig. 8.52, the peak value reduces from 100 % to 70 - 80 % from moderate to high momentum ratios. In case of normal injection, it reduces from 80 % to 30 %. Interestingly, the angled injection of H_2 fuel results in a maximum average surface heat augmentation of approx. 100 %, while for the normal injection the increase is around 80 %. This is despite the fact, that the normal injected H_2 mass flow rate is twice as large as angled injection and the heat release rate is even up to three times higher. The reason therefore is probably due to the low detachment tendency and wall proximity of angled jets.

The transient and the spatial results for C_3H_8 are provided in Fig. 8.60 and Fig. 8.61. Here, from $I = 1.8$ to $I = 4.4$, the maximum surface heat release increases and the location of the peak shifts slightly upstream. This is in agreement with the optical results. Other than that, the general shape of the profiles is similar to those of normal injection, see Fig. 8.55, with the difference that the injected mass flow rates and the heat release rates are twice as low as those of the normal injections, according to Tab. F.4, Tab. F.5 and Fig. 8.41.

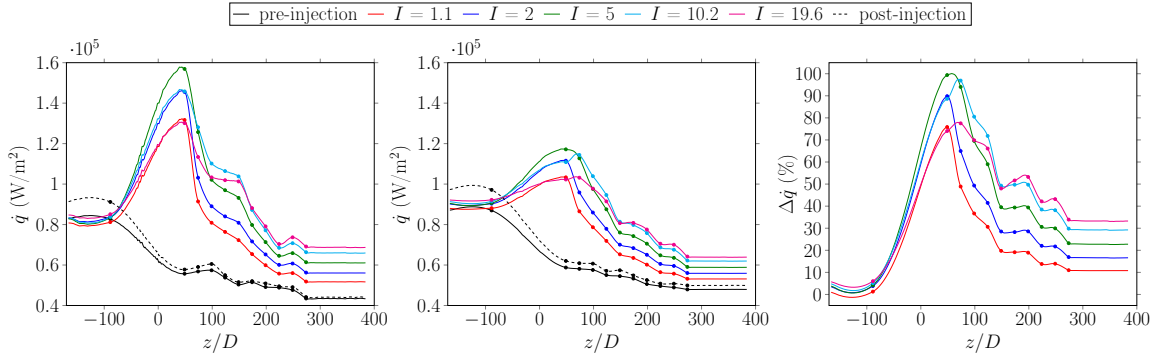


Figure 8.59: Centerline IHC results for angled H_2 injection. Left: centerline heat flux. Center: area averaged heat flux. Right: heat flux increase according to Eq. (2.5). Solid points indicate TC positions.

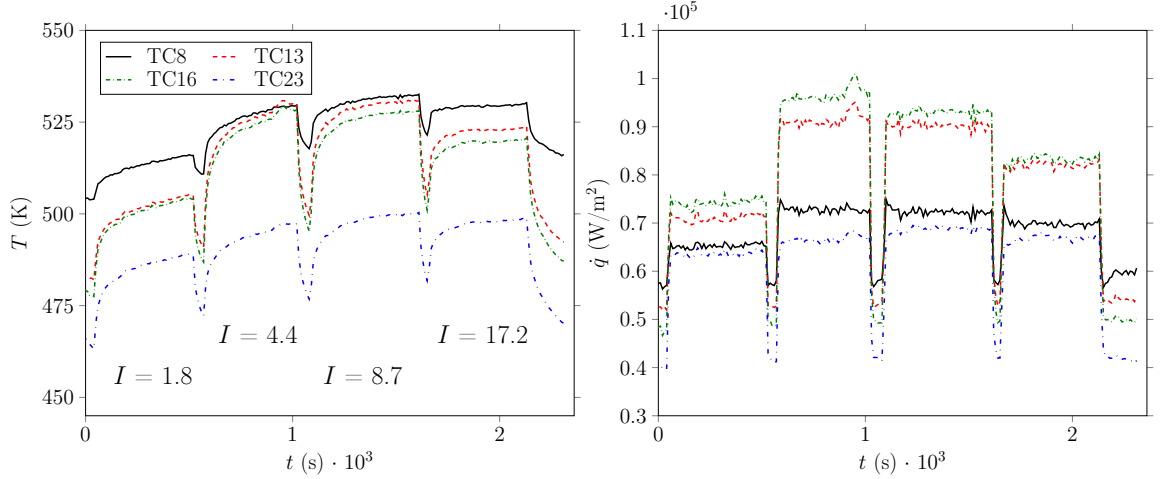


Figure 8.60: Transient IHC results for angled C_3H_8 injection. Locations correspond to TC projected onto the surface. Left: temperature profiles. Right: heat flux profiles.

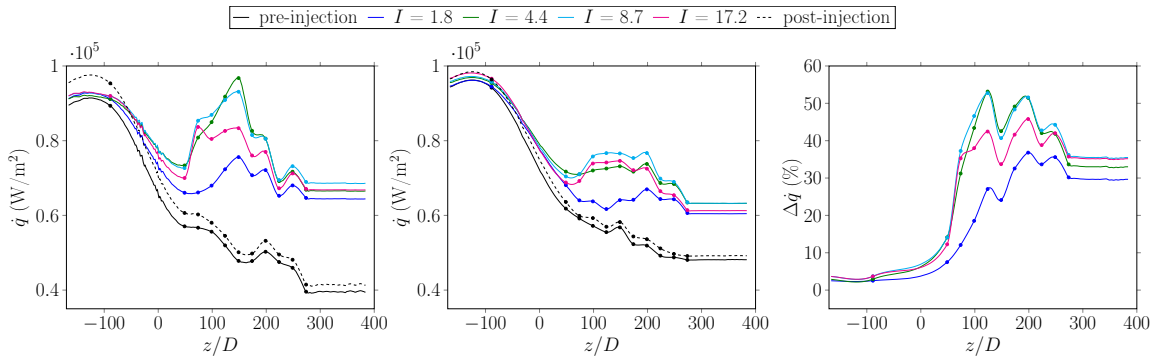


Figure 8.61: Centerline IHC results for angled C_3H_8 injection. Left: centerline heat flux. Center: area averaged heat flux. Right: heat flux increase according to Eq. (2.5). Solid points indicate TC positions.

IHC results of angled CH₄ injection are presented in Fig. 8.62 and Fig. 8.63. For the lowest momentum ratio, the peak thermal effect is detected far downstream around the last TC position. Increasing the momentum ratio leads to elevated heat release and to an upstream shift of the maximum location. This is attributed to the fact that the reaction zone moved upstream due to enhanced jet-crossflow-interaction and due to increased injected fuel rate. The maximum heat transfer to the wall is caused at $I = 9.7$. Some distinct differences

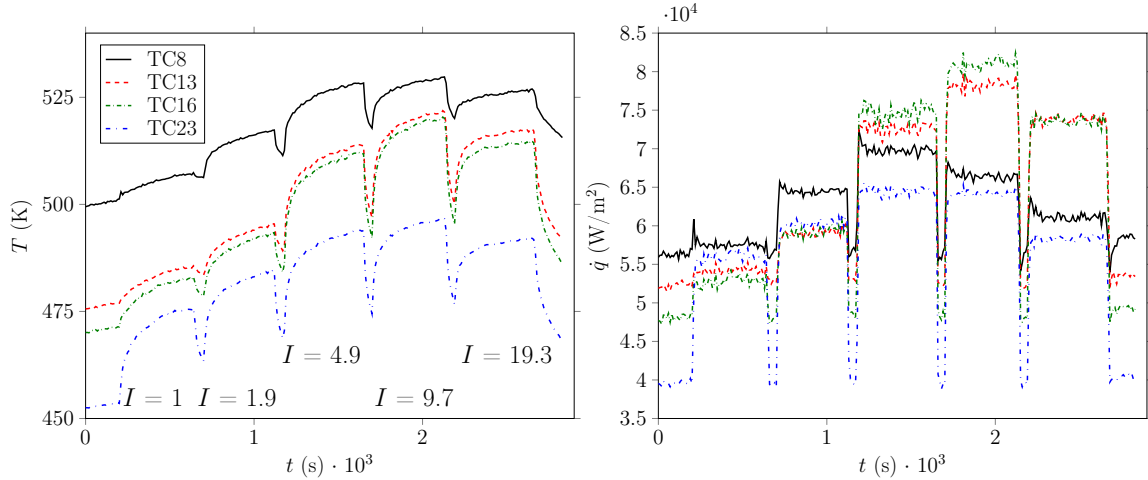


Figure 8.62: Transient IHC results for angled CH₄ injection. Locations correspond to TC projected onto the surface. Left: temperature profiles. Right: heat flux profiles.

are found between the axial profiles of angled and normal CH₄ injection. While in Fig. 8.57 the downstream position of the maximum heat augmentation remained nearly constant and the maximum heat flux tended to reduce with increasing I , the situation is different in Fig. 8.63. Here, the locations of the maximum shifts upstream, while at the same time the surface heat transfer increases with I . And similarly to the previous fuel types discussed, despite the lower injected angled fuel rate, relatively high thermal loads to the surface are observed.

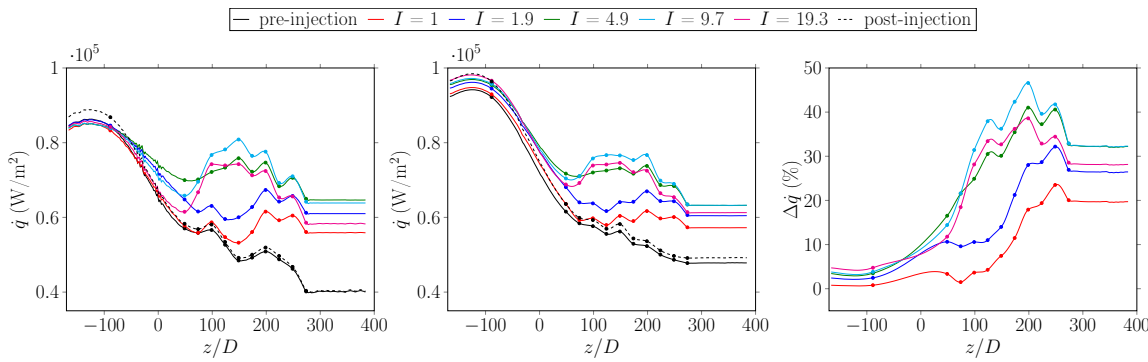


Figure 8.63: Centerline IHC results for angled CH₄ injection. Left: centerline heat flux. Center: area averaged heat flux. Right: heat flux increase according to Eq. (2.5). Solid points indicate TC positions.

In conclusion, the angled IHC data are in good agreement with the conclusion from optical data. The location of the heat flux shifts upstream and, in most cases, the heat

transfer to the surface rises with increasing I , in contrast to the first considered injection configuration. Further, compared to the normal injection, the surface heat release from reacting angled jets are generally speaking similar, even though lower mass flow rates were injected in the angled configuration. This is attributed to the narrow distance of the reaction zone to the surface, as the angled jets are less prone to separation and detachment. This is another indication, that the surface distance of the reaction zone is of major significance for the heat transfer.

The provided IHC method and the heat transfer data might be of interest for the determination of heat transfer coefficients based from an analogous procedure as in Eq. (2.6). The non-dimensional heat flux increase is the counterpart of the NHFR and can be formulated as:

$$\Delta \dot{q}_s = \frac{\dot{q}_{react}}{\dot{q}_{inert}} - 1 = \frac{h_{react}(T_{ref} - T_w)}{\dot{q}_{inert}} - 1 \quad (8.5)$$

Using an appropriate reference temperature T_{ref} , e.g. the maximum combustion temperature expected, the reactive based heat transfer coefficient h_{react} might be obtained. Additionally, the wall temperature T_w is also provided by the IHC.

8.4 CFD results

This section presents the CFD analysis conducted for the normal injection. First the boundary conditions are discussed, then the final reactive results follow.

8.4.1 Boundary conditions

The flow field within the HGG and the TS was investigated by Fischer et al. [61] by means of inert large eddy simulation (LES). The fluid domain for the numerical simulation consisted of a short part of the combustion chamber, the entire second chamber and the fluid domain of the mounted TS according to Fig. 5.3 and Fig. 5.4. The inlet temperature was set to 1430 K, while the mass flow and composition correspond to the values reported in Tab. 8.3. The deviation of the mainstream temperature from the experimental temperature results from the fact that the simulations were conducted prior to the experiments. Even though the temperature is lower compared to that of the actual experiment with 1600 K, no significant effect on the flow field was expected from the deviation. Except for the TS surface with a constant temperature profile from the IHC experiments, adiabatic boundary conditions were assumed. The longitudinal section through the domain is shown in Fig. 8.64. A non-homogeneous velocity field was observed within the second chamber evolving from the jets coming out of the flame breaker. Inside the convergent nozzle the jet flows were merged and the flow homogenized quickly. According to the extracted wall normal velocity profiles, the flow seems to be fully developed at the injection location P_5 (compare P_5 to P_3 and P_4). The cross sectional velocity and turbulence intensity distributions are found in Fig. 8.65. The velocity field showed no inhomogeneity in the center region. Likewise, the TI exhibited constant values around 3 - 6 % in the core. Approaching the wall, corresponding velocity and turbulence intensity profiles developed as expected. Compared to the cold flow hot-wire measurements shown in Fig. 8.2, the velocity field from the LES simulation was more homogeneous, but the TI fields were in a similar range. The reason for the velocity field inconsistency might be due to the ceramic elements within the combustion chamber, which probably led to unequal flows through the flame breaker exit holes. This inequality could

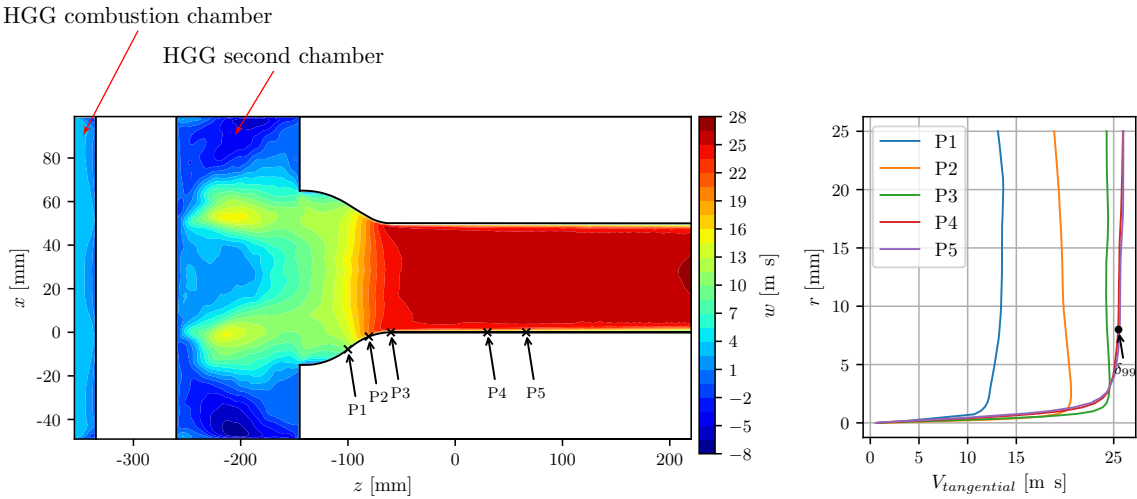


Figure 8.64: Inert LES simulation results of the HGG and test section inlet region. Left: velocity field within the HGG on the plane $y = 0$. Compare to Fig. 5.3. Right: wall normal velocity profiles. w is the velocity magnitude u in the current study, while r corresponds to the distance normal to the surface. The injection location is at P_5 . Images taken from Fischer et al. [61] and adapted.

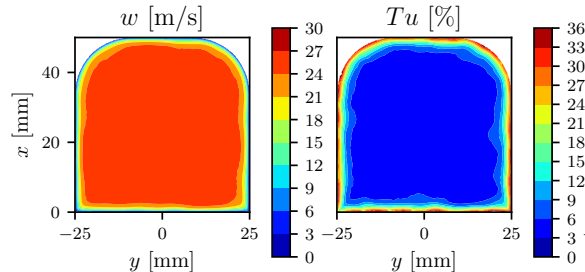


Figure 8.65: Cross sectional LES results of the test section near the injection location. w is the velocity magnitude u , Tu is the turbulence intensity TI in the current work. Images taken from Fischer et al. [61].

not be taken into account in the LES simulation. However, the LES results reflected the experimental findings.

For the reactive RANS simulations, the velocity profile of Fig. 8.65 was applied to the inlet of the fluid domain in Fig. 7.1 with a constant TI of 5 %. The main flow temperature T_h was set to 1620 K with the composition in Tab. 8.3. For each simulated case, the corresponding 2D temperature profile from the IHC was patched on the hot wall surface. The boundary conditions of the injected fuels are summarized in Tab. 8.5. The injected mass flow rates correspond to the reported values in Tab. F.4, but for 3 injection nozzles instead of 5.

Table 8.5: CFD boundary conditions of normal injection cases.

Fuel	H ₂	CH ₄	C ₃ H ₈
T_c	346	345	335
\dot{m} (g/min)	0.41	1.16	2.41
I	8.6	8.7	13

8.4.2 Results

The numerical simulations allowed insight into different properties of the physical problem. In order to stay consistent with the experimental results the focus was on the shape of the reactive jets. Fig. 8.66 shows an isometric view of a reactive CFD simulation and visualizes the planes of interest. The fuel injection chamber is not shown in the following images. However, fully-developed jets were observed at the location of injection, which indicated a sufficient length-to-diameter ratio of the fuel injection nozzles. This observation was also made by Fischer et al. [61] applying LES. The longitudinal view helped to determine the

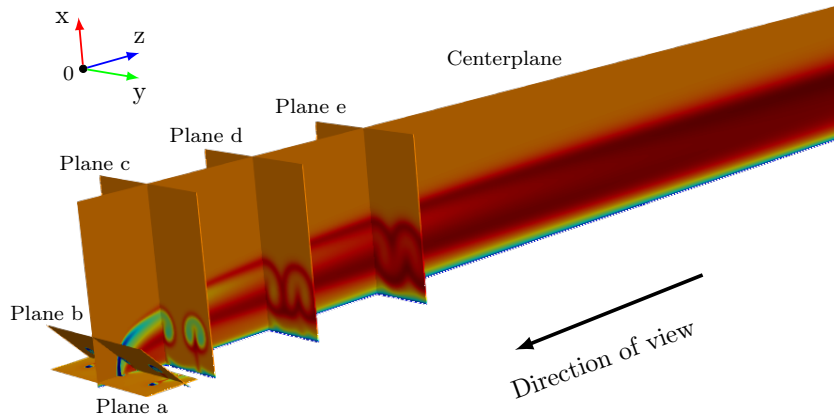


Figure 8.66: Locations of the considered planes shown on an isometric view.

downstream position of the reaction zone and the view corresponds to the PLIF images, while the cross sectional views reveal the development of the fuel jets, observed from the indicated direction of view.

Fig. 8.67 provides cross sectional temperature and OH molar concentration distributions of H₂ injection. Plane a is located at $x/D = 0.9$ parallel to the y - z -plane and the flow enters from the top of the image. According to the streamlines the mainstream flows around the jets and meet at the stagnation point, where a recirculation zone forms. On the windward side a slight increase of OH concentration is observed (hardly recognizable). Around the point S and downstream the jets a trace of high temperature and OH concentration is generated due to fuel being removed by the main flow. Apparently, sufficient mixing takes place here. On plane b, which incorporates the x - y -view, chemical reaction is present beneath the jet which corresponds to the trace in plane a. The shape of the CVP is clearly visible on the temperature image of plane b and corresponds to the schematic illustration in Fig. A.1. The CVP transports high temperature matter to the lee-side and into the core of the jets. Due to the near-wall combustion the thermal boundary layer is affected and disturbed which

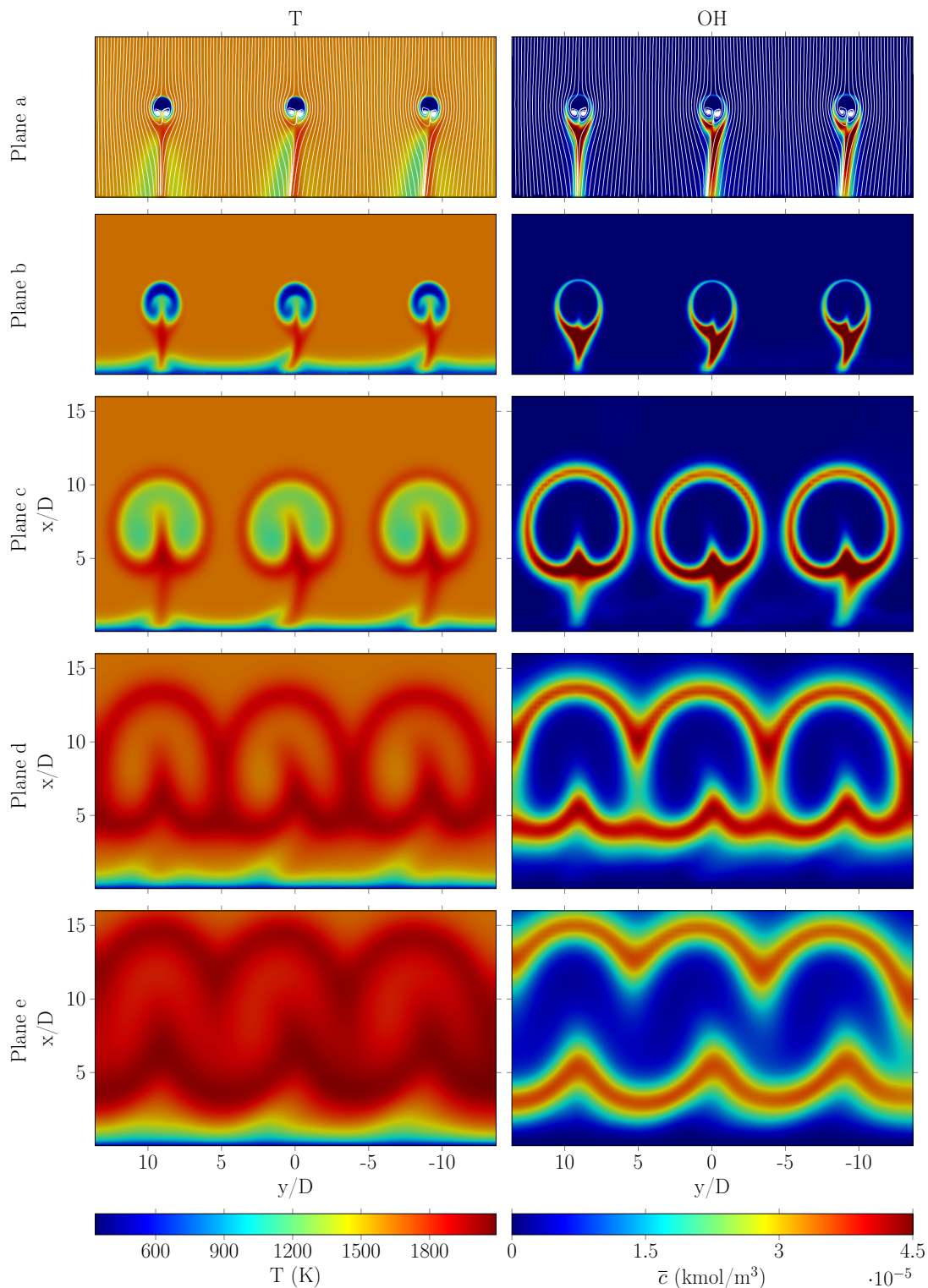


Figure 8.67: H_2 simulation results. Left: temperature. Right: OH molar concentration. Plane a contains velocity streamlines.

probably leads to enhanced wall heat transfer beside the heat release of the reaction. Plane c shows basically a similar situation to that in plane b. Here, the jets are further expanded, increased chemical reaction is found on the jets' outer surface and the core temperature has raised from ≈ 600 K to > 1200 K. Further downstream, the individual jets merge until finally two reaction sheets, namely one on the lee-side and one on the windward side, are formed, while the core temperature increased to > 1800 K, but the OH concentration drops successively. Apparently, the near-wall fuel was consumed, as there is no chemical reaction in the proximity of the surface left on plane d and e. The shape of the hydrocarbon fuel jets was similar, except for the fact, that an IDL existed and the OH formation occurred downstream the injection.

The situation on the centerplane is presented in Fig. 8.68 by means of temperature and OH molar concentration. Similar to the OH PLIF images, a double structure appears, which

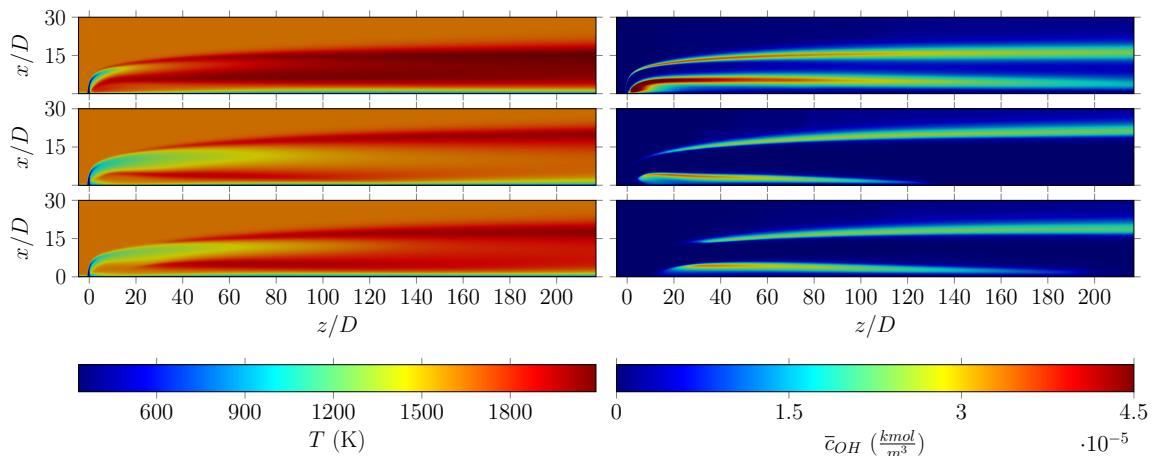


Figure 8.68: CFD simulation results. Left: temperature. Right: OH molar concentration. Top row: H₂. Center row: C₃H₈. Bottom row: CH₄.

is attributed to the fact, that the centerplane cuts through the center jet and visualizes the windward and the lee-side reactions. The numerical simulations result in maximum temperatures of 2091 K, 1985 K and 1995 K for H₂, C₃H₈ and CH₄ injections, respectively, and correspond to equilibrium temperatures in a PSR. After a short distance downstream the injection location, the H₂ fuel produces an almost homogeneous, high temperature region, whereas the C₃H₈ fuel shows the most confined shape and the reaction is limited to a thin layer around 15D away from the wall. The maximum temperatures are around 300 - 400 K higher than determined experimentally by the two-line PLIF thermometry. The reason therefore was amongst others, the EDC model takes into account the effect of turbulence on mixing, but it does not consider strain effects. The over-prediction of reaction temperatures by the EDC model was also observed in [123]. Fig. 8.21 showed, that the temperature decreased with increasing strain rates. Further, the combustion model does not incorporate heat losses of the chemical reaction, as the EDC relays on an adiabatic, constant-pressure reactor, see D. Comparing the OH concentration on the lee regions of the different fuels, it is notable, that H₂ generates the largest near-wall and lee-side reaction zone, followed by CH₄ and lastly C₃H₈ jets. One reason might be the higher momentum ratio of the C₃H₈ which leads to a more strongly lifted jet. However, the small lee reaction zone with this fuel is also observed on PLIF images for different momentum ratios, compare

Fig. 8.38 to Fig. 8.34 and Fig. 8.36. This might be attributed to the high DR of C_3H_8 /main flow relative to that of the other two fuels, as specified in Tab. 8.4. With increasing DR less fuel is removed from the fuel jet when the mainstream impinges on it, similarly to non-reacting jets. Another distinctive feature of the hydrocarbon jets is that chemical reactions take place further upstream on the lee region compared to the windward side. This phenomenon was observed for the hydrocarbon jets in Fig. 8.38 and Fig. 8.36 and in the literature for H_2 jets in hot crossflows [186]. It was argued, that the low velocity region beneath the jet and near the surface provided stability to the reaction zone. Fig. 8.69 provides a closer look to the H_2 injection location superimposed by streamlines. On the

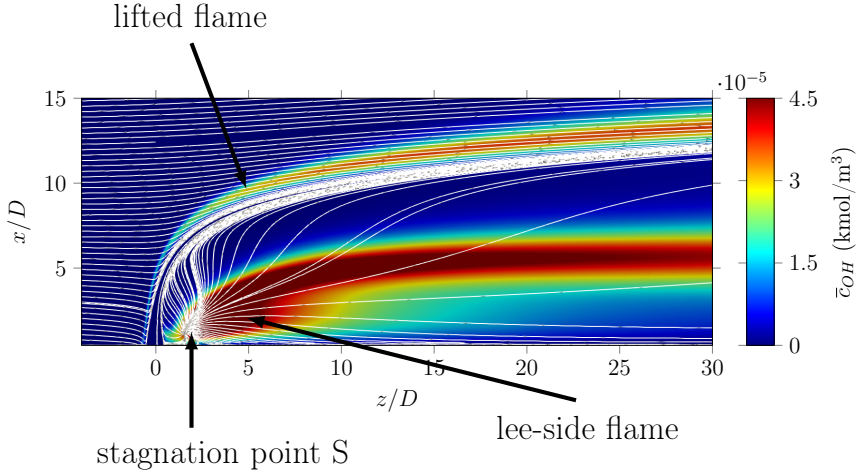


Figure 8.69: Magnified view of H_2 injection with added streamlines.

lee-side of the H_2 jet, the fuel ignites around the stagnation point S apparently. It seems, that sufficient mixing took place there. This point indicates the presence of out-of-plane streamlines and a recirculation zone. It was referred to in the literature as unstable focus or saddle point [81, 146]. High OH concentration is found in the numerical result of Fig. 8.69 in contrast to the corresponding OH PLIF case in Fig. 8.34. Also for the C_3H_8 jet, the ignition appears to originate from the mentioned point S , considering the magnification in Fig. 8.70. However, the two hydrocarbons of interest have a significant IDT and thus a IDL is present here.

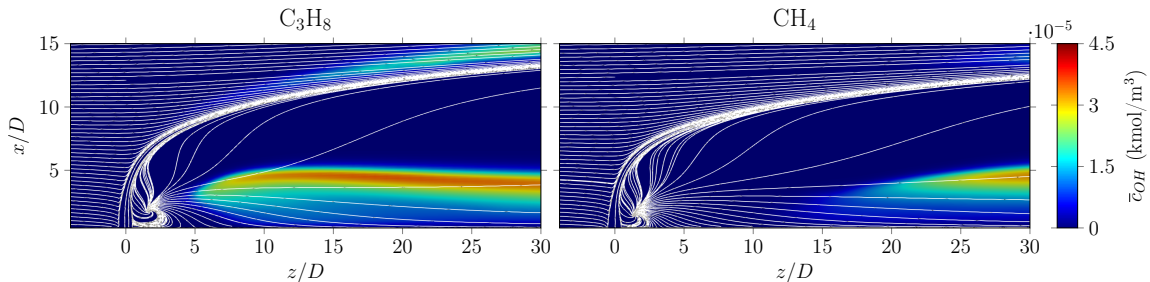


Figure 8.70: Magnified views with added streamlines. Left: C_3H_8 injection. Right: CH_4 injection.

In order to determine the IDL of the 3D reacting fuel jets and relate the simulation to the

OH^* measurements, the line-of-sight integration and averaging of a number of planes were performed. Therefore, the heat of reaction $\Delta\bar{H}$ ($\propto \bar{\omega}_T$) and the OH molar concentration were spatially averaged. The parameter $\Delta\bar{H}$ is calculated as:

$$\Delta H = \sum_{i=1}^N h_i^0 (\nu_i'' - \nu_i') \quad (8.6)$$

where h^0 is the standard enthalpy and N is the number of species. $\Delta\bar{H}$ used even though it may be inaccurate in RANS. Further, an attempt was made to determine the OH^* concentration $\bar{c}_{\text{OH}*}$. Generally, two approaches are reported in literature for $\bar{c}_{\text{OH}*}$: implementing corresponding elementary reactions for OH^* formation and consumption like Eq. (2.41) to Eq. (2.45) into the reaction mechanism or in a post-processing step [59, 158]. The first method is an accurate approach, but requires the knowledge of thermodynamic data and a special procedure of the simulation. The second method was proposed for the determination of the OH^* concentration in a post-processing step assuming thermal equilibrium [158]:

$$\frac{\bar{c}_{\text{OH}*}}{\bar{c}_{\text{OH}}} = \exp \left(-\frac{\Delta g_{mf}^0}{R_m T} \right) \quad (8.7)$$

where R_m is the universal gas constant and Δg_{mf}^0 is the molar Gibbs standard state enthalpy of formation, which is obtained from:

$$\Delta g_{mf}^0 = \frac{hc}{\lambda} N_A \quad (8.8)$$

Here N_A is the Avogadro constant and the λ is set to 308.5 nm as the dominant wavelength of the spontaneous emission. However, this approach is strictly valid for $> 2700 \text{ K}$, where thermal excitation is the dominant mechanism generating OH^* . For conditions $< 2700 \text{ K}$, chemical excitation occurs additionally and plays a non-negligible role. Nonetheless, this approach is used in the current work, similar as in [158] to demonstrate the results. The spatially averaged data is shown in Fig. 8.71. Comparing the ignition delays, H_2 reacted

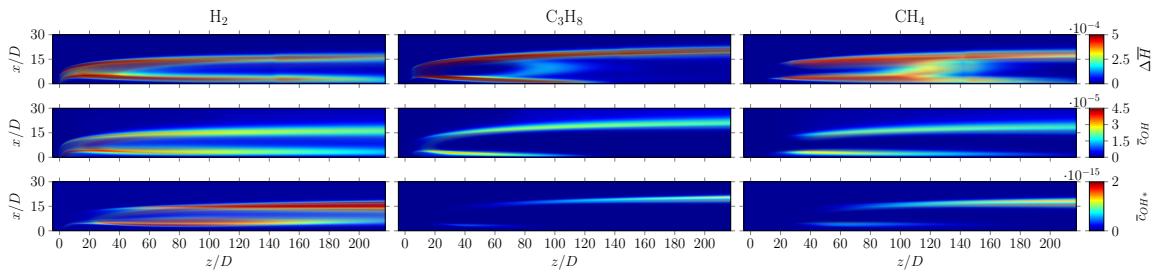


Figure 8.71: Line-of-sight averaged CFD results. Top row: heat of reaction (W). Center row: OH molar concentration (kmol/m^3). Bottom row: OH^* molar concentration (kmol/m^3).

directly around the injection location, while C_3H_8 and CH_4 ignited further downstream around $z/D \approx 5$ and 15, respectively, according to the heat release. Experimentally, IDL of around 6 and 25 were determined for the two fuels from 10% OH^* intensity increase in Fig. 8.31. In Fig. 8.71, regions of high $\Delta\bar{H}$ correspond to regions of high OH concentration. In case of H_2 this region is located near the injection orifice and in general the highest heat

release rates are observed directly after the ignition. Further downstream, a constant and homogeneous distribution of $\Delta\bar{H}$ and \bar{c}_{OH} develops. Despite the fact, that the properties were averaged in the line-of-sight direction, the two reaction streaks are still distinctive and rather more pronounced than experimentally found in Fig. 8.25, Fig. 8.27 and Fig. 8.29. This might be due to the turbulent nature of the experimental combustion region. Further, the OH* images were line-of-sight integrated intensities of 5 jets instead of 3. On the last row of Fig. 8.71, the OH* concentrations obtained from the post-processing step are provided. For all fuels, the OH* does not indicate the ignition position correctly and the OH* concentration increases downstream in contrast to the heat release, OH concentration and the experimental findings. The inconsistency was largest for the C₃H₈ reaction due to its relative low temperature compared to the other fuels. As the temperature is located in the exponent of Eq. (8.7), it affects highly the OH* concentration. Thus, the OH* from post-processing was found to be least useful to indicate the ignition position for conditions < 2100 K. Considering Fig. 2.6, the change in temperature as well as the increase of OH concentration might be suitable.

Since the main flow temperature was subject to uncertainty like systematic errors, simulations with $T_h = 1570$ K were conducted additionally. The centerplane properties are provided in the appendix in Fig. F.2 and Fig. F.3. The maximum temperatures were in the same order of magnitude as for the previously discussed case with $T_h = 1620$ K. However, the IDL of CH₄ shifted to $z/D \approx 20 - 25$. Numerical simulations for angled injection were performed in a similar manner and the results are shown in the section F.4 of the appendix.

The general structure of the reaction zones is in good agreement with the single OH PLIF images. However, as the main flow in the experiments was subject to fluctuations and the reaction zone was highly turbulent, the windward and lee-side flames merged downstream the injection as observed on the PLIF images. These fluctuations remained unconsidered by the simulations due to the time-averaging principle of RANS modeling. As pointed out, the reactive mixture is modeled as a steady-state PFR in the EDC approach. Here, strain-effects on the flame by turbulence are not taken into account, which affect the reaction chemistry and lead to non-equilibrium conditions. Further, the PFR and RANS models assume mean flow properties, which may significantly deviate from actual transient and fluctuating conditions and alter the chemical reaction rates. Thus, the EDC overestimates the combustion temperature. Alternative approaches for more realistic conditions are the steady flamelet theory and LES simulation. However, due to the fast chemistry assumption, the flamelet model fails to predict ignition delays, as seen in the study of Pohl et al. [158]. Using subgrid-scale modeling (in LES) to resolve small-scale time and spatial fluctuations may produce most accurate results and is investigated in [61] for the current test bench. These fluctuations affect the local reaction chemistry and should be considered. In [61] the authors also found, that for angled CH₄ with $I = 10$, the crossflow temperature was of major importance, whereas the turbulence intensity did not play a significant role, at least not for the conditions in this study. The IDL and the overall results were in good agreement to the current experimental study. However, the numerical study using LES and detailed combustion modeling required much higher computational efforts.

Chapter 9

Conclusions

In this study, reacting fuel jets in crossflow were investigated. A test bench was designed specifically for this purpose. A hot oxygen-vitiated exhaust gas serving as mainstream was generated by the combustion of gaseous CH₄/air and was led to a test section. Within the test section, gaseous H₂ and the hydrocarbons CH₄ and C₃H₈ were injected individually into the crossflow through normal or angled orifices. Different momentum ratios I were tested. At mainstream temperatures around 1600 K, the fuels reacted near the surface. In a first step, the crossflow and the JICF were characterized at ambient temperature. Hot-wire anemometry was applied for the mainstream characterization, while PLIF was used to excite the tracer, which was introduced to the jet flow. This enabled the visualization of the jet. In the main combustion experiment, the reacting jet structure was investigated qualitatively by means of OH* chemiluminescence and OH PLIF. Further, the average reaction zone temperature was determined by the two-line PLIF thermometry. A number of TC's was installed inside the test section wall to measure the temperature at different locations during the near-wall combustion of reacting jets. The provided data was then used to numerically reconstruct the thermal condition of the wall by the IHC method and determine the heat loads. To support the optically obtained results, 3D reactive CFD simulations were performed.

Following aspects were observed for the measurement techniques:

- For cold flow visualization, the selected fluoroketone is a good alternative to acetone. It is inexpensive, of low toxicity and its high vapor pressure leads to high seeding density in the carrier gas. It has a broad absorption spectrum with a sufficiently large absorption cross section. The latter leads to high fluorescence signal. It is beneficial for laser diagnostics, as the absorption and emission spectra are widely separated. The intensity of the excitation source could be blocked by standard band-pass or long-pass filters. Compared to acetone, the excited state has a significantly higher lifetime at atmospheric pressure.
- The OH* chemiluminescence detection is a straightforward line-of-sight technique for combustion analysis. In the current application, it was employed to localize and characterize the global reaction zone. The OH* intensity signal was used only as an approximation of the spatial heat release rate. As reported in literature, the location of maximum heat release in laminar diffusion flames does not necessarily correspond to the location of maximum OH* concentration. In turbulent diffusion flames, the situation is further complicated by the effect of turbulence-chemistry interaction.

- OH concentration detection by LIF is a sophisticated technique, which requires a tuneable UV laser and a synchronized UV sensitive detector with a mounted band-pass filter. For qualitative analysis, the method was well suitable for the current study. The excitation of rotational lines within the vibrational branch $v'' = 0$ to $v' = 1$ and subsequent broadband detection is a common practice in literature. For optically thin media and concentration measurement, the line $Q_{11}(5)$ is preferable over $P_{11}(2)$, due to reasons of laser attenuation, lower temperature sensitivity and thus higher signal.
- Having established an OH LIF setup, it is only a minor step to the two-line OH LIF thermometry, if steady state conditions can be assumed, the temperature vs. intensity ratio is linear and the excitation of the selected rotational lines are performed successively. Assuming thermal equilibrium, same OH number density, similar quenching, and spectrally independent optical properties, the ratio of the two intensities obtained from the excited rotational lines is related to the temperature based on the Boltzmann distribution. The line pair $R_{11}(12)/P_{11}(2)$ was preferred over the line pair $Q_{11}(14)/Q_{11}(5)$, because $R_{11}(12)/P_{11}(2)$ had wavelengths closer to each other and had rather similar absorption characteristics. The latter is of interest, when laser intensity attenuation cannot be accounted for. The method was validated on a calibration burner and satisfactory results were reached. It is recommended to record a high number of images, here 100 - 300, for each rotational line, as the low SNR otherwise causes high random errors. If possible, quenching should be considered to reduce systematic errors, according to literature. For highly turbulent combustion, a double laser-detector system should be taken into consideration for two-line thermometry. However, the complexity increases notably and the low SNR remains. Further, a system with a repetition rate of more than 10 Hz and with higher detector resolution is preferable for the current case.
- The IHC is an useful method to determine the heat flux to locations, which otherwise are not accessible. Further, the method is able to provide 2D temperature and heat flux information in theory. Practically however, different aspects need to be considered related to the data acquisition and the IHC method itself. First, temperatures measured by TC are subject to systematic errors. Those might be large relative to the measured temperature variations, depending on the type and class of TC and positioning inaccuracies. Here, for temperature variations around 25 K, the errors in heat flux are at least 25 %. Second, the IHC is usually ill-posed and thus sensitive to temperature fluctuations like noise or small positioning errors. This may produce instabilities and require special treatment. Here, a TC position variation was applied to the profiles obtained during the warm-up time. Third, the method is well suitable to reconstruct transient thermal conditions. However, high time resolution combined with long total runtimes and large number of sensors lead to inefficient and time-consuming simulations. Finally, one of the largest downside of the method is its low spatial resolution. Too many sensors reduce the efficiency of the method, while the opposite affects the spatial resolution and the selected interpolation may produce non-physical shapes.

Based on results from these measurement techniques, following observation of gaseous fuel jets in oxygen-rich exhaust flow were made:

- Gaseous H₂ jets ignited directly at the injection location due to the reactivity of the

fuel. Flames anchored to the orifices were observed. C_3H_8 showed a small ignition delay length, while CH_4 reacted at a significant distance downstream the injection orifices.

- Especially for CH_4 fuel, with increasing momentum ratio I , the ignition location moved closer to the injection location despite expected increase in strain rates. This observation was reported in the literature for inverse-diffusion flames. It is assumed, that the elevation of momentum ratio enhances mixing and thus accelerates ignition.
- Lowest flame position stability was observed for CH_4 flames and highest for H_2 flames. One of the reasons is attributed to the fact, that H_2 jet ignites directly, where the local momentum ratio was higher compared to CH_4 jets, which lost and dissipated its momentum downstream.
- With increasing I , a double structure reaction zone was found on the PLIF center-plane images for both injection angles and also on some OH^* images. It was more pronounced for normal injection. The lee-side and the windward side reactions appeared, because the fuel jet ignited on the interface with the mainstream. Oxygen found its way to regions beneath the jet due to the formation process of the CVP. This was supported by OH^* images from the normal hydrocarbon injections. Further, in the PLIF setup, the laser sheet then cut through the jet and the reactions facing the main flow and the wall side were visualized.
- The lee-side flame was located further upstream than the windward reaction. Apparently, the near-wall low velocity region stabilized the reaction.
- The integral OH^* intensity showed a linear behavior to the fuel mass flow rate for all three fuels. As an approximation, the OH^* intensity was related to the heat release rate.
- On single PLIF images, shredded and wrinkled shapes were observed for hydrocarbon jets, especially at high I .
- Two-line PLIF temperatures were significantly lower than estimated from calculated counterflow diffusion flames. The deviation was higher for the hydrocarbons than for H_2 . Including quenching effects in the postprocessing may improve the results.
- H_2 fuel resulted in highest wall heat fluxes, followed by C_3H_8 and lastly CH_4 . Generally speaking, the detected heat fluxes were lower for the highest I , basically due to the fact, that the reaction zone shifted from the surface.
- The location of the heat flux peaks correlated to some degree with the location of the reaction zone.
- Despite lower fuel rates injected in the angled configuration, wall heat fluxes comparable to and in some cases higher than in the case of normal injection were determined.
- EDC simulations were able to reproduce the shape of the reaction zone and to predict an ignition delay length. However, the temperatures were higher than experimentally determined. Flamelet models could provide more accurate results, but would perhaps fail to predict any ignition delay. LES subgrid models to account for small scale fluctuations might be the most accurate approach.

Appendices

Appendix A

Additional Theoretical Background

A.1 Vortex structure of JICF

- Horseshoe vortices: on the upstream side of jet exit an adverse pressure gradient is imposed on the incoming boundary layer. Its displacement and separation lead to the formation of *horseshoe* vortices. The vortices wrap around the jet and extend downstream along the wall.
- Counter-rotating vortex pair (CVP): the initiation of this kidney shape vortex is believed to originate from the superposition of two mechanisms. Firstly, the initial jet flow forms vortex structures having their maxima at the orifice wall. They get reoriented by the crossflow and result in streamwise vortices. This type of vortex generation plays a role for velocity ratios $VR \leq 0.5$. Secondly, the velocity gradient at the jet interface leads to shear layer vortices, which are bent over, fold and contribute to the CVP formation. The rolling up, tilting and folding of the shear layer vortices are illustrated in Fig. A.1. Fearn et al. [57] were the first to determine the position, strength and diffusion character of the CVP in downstream position in the two dimensions perpendicular to the path of a turbulent jet. The kidney shape vortex was measured quantitatively by hot-wire anemometry by Andreopoulos et al. [11] and visualized both in water and in air test channels by Kelso et al. [108]. The drawing on

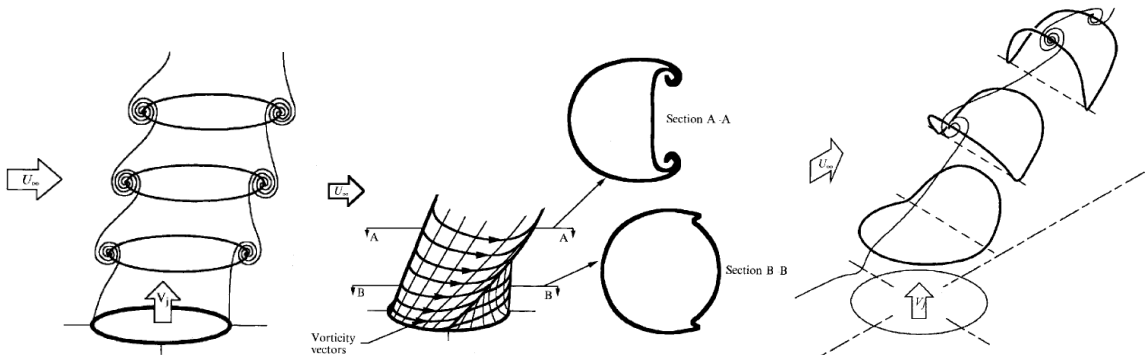


Figure A.1: Schematic illustration of the CVP generation. Left: roll-up vortices. Center: shear layer vortex generation and reorientation. Right: tilting, folding and superposition. Drawings taken from [108].

the right side of Fig. A.1 shows the superposition process. The leading side parts are tilted, while the lee-side vortex is tilted and folded and finally an alternating vortex structure is generated. The initial symmetrical jet transforms into an asymmetrical structure during the deflection process.

- Jet shear-layer vortices: this type of vortex is located at the leading side of the jet and forms on the windward interface between the jet and the crossflow resulting from the Kelvin-Helmholtz instability. According to Kelso et al. [108], the structure appears around 3 jet diameter after injection. They grow in the downstream direction.
- Wake vortices: as the crossflow passes around the transverse jet, it experiences an adverse pressure gradient similar to the horseshoe vortex generation but on the leeward side. Beneath the jet on the leeward side, the laminar boundary layer separates and likely generates a vortex system, vertically oriented and connecting the downstream region of the jet to the boundary layer.

A.2 Statistical data analysis

For the analysis of data, different statistical tools were utilized in this study. An overview is given below.

A.2.1 Mean, standard deviation and variance

For averaging n number of data, the arithmetic mean was used as:

$$\bar{x} = \frac{1}{n} \sum_{i=1}^n x_i \quad (\text{A.1})$$

To quantify the average dispersion or the average deviation of the n data, the standard deviation was calculated as:

$$\sigma = \left(\frac{1}{n-1} \sum_{i=1}^n (x_i - \bar{x})^2 \right)^{1/2} \quad (\text{A.2})$$

For example, the RMS velocity fluctuation and the turbulence intensity for 1D measurements were calculated as:

$$u'_{rms} = \left(\frac{1}{n-1} \sum_i^n (u_i - \bar{u})^2 \right)^{0.5} \quad \bar{u} = \frac{1}{n} \sum_i^n u_i \quad TI = \frac{u'_{rms}}{\bar{u}} \quad (\text{A.3})$$

A.2.2 Probability density function

The PDF was calculated as [182]:

$$p(\xi)d\xi = \text{Probability}(\xi - \varepsilon \leq \xi \leq \xi + \varepsilon) \quad (\text{A.4})$$

with the normalization condition:

$$\int_0^1 p(\xi)d\xi = 1. \quad (\text{A.5})$$

Eq. (A.4) gives the probability to find the mixture fraction of ξ within the range $\xi \pm \varepsilon$. The mixture fraction $\xi = 1$ corresponds to the first fluid in its unmixed stage, $0 < \xi < 1$ is the mixed state and $\xi = 0$ describes the unmixed state of the second fluid. The average mixture fraction or first moment of $p(\xi)$ is [33]:

$$\bar{\xi} = \int_0^1 \xi p(\xi) d\xi \quad (\text{A.6})$$

Experimentally, the mixture fraction is often determined from optical data, such as PLIF intensities. As the data are discrete rather than continuous, the correct term is *probability mass function* (PMF). A PDF can be approximated by a PMF for a sufficient quantity of available data [125]. For optical data, the intensity values of pixels in a region of interest (e.g. along a line) are basically sorted by size, distributed in discrete intervals and the number density of each interval is the spatial PMF of the corresponding intensity level. This representation is also referred to as histogram and the interval width is termed as bins. The appropriate number of bins can be estimated from $n_{bins} = \min(\sqrt{n}; 10\log(n))$, where n is the number of evaluated data [125]. Number of bins of 32 to 256 and bin sizes around 0.01 to 0.031 are reported in literature [56, 113, 125]. Generally, the information content increases with the number of bins. However, with a large number of bins the PMF representation may yield in a ambiguous structure. To increase the amount of data and thus the quality of the PMF, the spatial PMF is averaged over a number of temporal data [49, 69, 182]. For a detailed discussion on PDF of turbulent flows the reader is referred to the corresponding literature [28, 33, 113, 182].

Appendix B

Spectroscopy of Diatomic Molecules

Molecule, from the Latin word *molecula* and derived from *mōlēs* ('mass'), refers to a group of di- and poly-atoms chemically bonded. Even though the basic components of a molecule are atoms, the properties of the resulting molecule can not be obtained by simply *summing up* or *extrapolating* the atomic properties. Therefore, the basic principle of molecular spectroscopy based on di-atomic molecules is explained in this section to the certain extent which is necessary for this work. For a detailed explanation the reader is referred to [38, 44–46, 48, 50, 82, 92, 93, 95–97, 111, 117, 132, 141].

B.1 Molecular energy quantification

The simplest molecules consist of two atoms of the same element, also referred to as homonuclear, such as H₂, O₂ and N₂. The diatomic structure is held together by a covalent bond, which is basically a shared pair of electrons between the atoms. The next category is the heteronuclear molecule, like NaCl (known as table salt), NaI, KBr, CO or OH. In case of different magnitude of electronegativity values the ionic bonding is of importance. In contrast to the atom, additional energy states beside the electronic state (*el*) exist for the molecule, which are associated to the inner degrees of freedom, namely: rotation and vibration.

In the 1920s Louis de Broglie stated that matter, e.g. electrons, may have wave-like characteristics (*matter waves*). Later, Erwin Schrödinger postulated an universal partially differential equation, the so-called *Schrödinger equation* - the fundamental equation of quantum mechanics, to characterize the states of matter. The solution of the equation allows for the quantization of energy based on the eigenvalue *E*, referred to as total energy, and the corresponding eigenfunction. The eigenfunction is a solution of the wave function Ψ . Schrödinger successfully applied his postulate to determine the hydrogen energy levels and therefore the frequencies of the spectral lines. Max Born interpreted the square of the wave function, $|\Psi|^2$, of a particle as a proportionality factor to the probability density of locating the particle at a specified position. A major simplification of systems consisting of multiple particles, such as electrons and nuclei, is the Born-Oppenheimer (BO) approximation. This approach allows for an analytical calculation of the quantum mechanic processes of a molecule. Due to the higher mass of nuclei and their slower dynamics compared to electrons, the two particle categories can be considered as decoupled and a separation of the total wave function is performed. Further, the nuclei motion is divided into rotation, vibration and rotational-vibration-interaction. Finally, the decoupled wave function for a particle, e.g. a

molecule, is:

$$\Psi = \Psi_{el} \cdot \Psi_{vib} \cdot \Psi_{rot} \quad (\text{B.1})$$

and the corresponding total energy is obtained from the distinct energies:

$$E = E_{el} + E_{vib} + E_{rot} + E_{trans} \quad (\text{B.2})$$

where the magnitudes of the individual energies are:

$$E_{el} \geq E_{vib} \geq E_{rot} \geq E_{trans} \quad (\text{B.3})$$

The translational (*trans*) energy is included and mentioned here. It affects the Doppler broadening of the spectral line. However, this energy type is not quantized and omitted later. Each molecular energy can be related to its temperature within the statistical thermodynamics and in case of equilibrium, the same temperature sets in. According to Eckbreth [50], nonequilibrium effects are dissipated within few hundred collisions, where the mean collision time is around 1 ns for combustion at 1 atm. This leads to equal vibrational, rotational and translational state temperatures.

As mentioned, the total energy of a molecule is subject to quantization. This requires the knowledge of the corresponding quantum numbers, namely: n of the electronic, v of the vibrational and J of the rotational mode. Generally, the energy is specified in the unit cm^{-1} in literature and referred to as *term energy*, which is obtained by dividing E from Eq. (B.2) by hc . The expression for the term energy is then as follows:

$$T(n,v,J) = T_{el}(n) + G_{vib}(v,n) + F_{rot}(J,v,n) \quad (\text{B.4})$$

Note, that the vibrational and rotational term values contain electronic and electronic, vibrational quantum numbers for the sake of precise assignment of each term energy. Meaning, for an electronic state multiple vibrational state exist and each vibrational level contains a number of rotational states.

A short summary of the calculation of term energies is given in the next subsections.

B.1.1 Vibrational energy

The molecular vibration is modeled as two non-spinning masses connected by a spring (*dumbbell model*). First, the oscillation is described by the dynamics of a *harmonic oscillator* using a parabolic potential function around its equilibrium position. A quantized solution for the Schrödinger equation is obtained as:

$$E_{vib} = h\nu(v + \frac{1}{2}) \quad (\text{B.5})$$

or as term energy:

$$G_{vib}(v) = \omega(v + \frac{1}{2}) \quad (\text{B.6})$$

where $v = 0, 1, 2, \dots$ is the vibration quantum number. The assumption of harmonic oscillator is valid for small displacements (small vibrational amplitudes and v) of the nuclei from the equilibrium position. However, for large displacement the potential deviates from the harmonic oscillator motion and requires anharmonic characteristics as:

$$G_{vib}(v,n) = \omega_e(v + \frac{1}{2}) - \omega_e X_e(v + \frac{1}{2})^2 + \omega_e Y_e(v + \frac{1}{2})^3 + \dots \quad (\text{B.7})$$

The vibrational constants (ω_e , $\omega_e X_e$, $\omega_e Y_e$) of OH are listed in various publications ([38, 48, 86, 97, 130, 141]).

B.1.2 Rotational energy

The rotational energy is derived from the *rigid rotor* model. Consider a diatomic molecule as two masses attached to each other by a massless rigid connection without vibrational effects and assume constant nuclei distance. The rotor spins around its center of mass and the solution of the Schrödinger equation for the eigenvalue E_{rot} depends only on angular momentum and the moment of inertia I :

$$E_{rot} = \frac{\hbar^2}{8\pi^2 I} J(J+1) \quad (\text{B.8})$$

and the corresponding term energy is:

$$F_{rot}(J, v, n) = BJ(J+1) \quad \text{where } B = \frac{\hbar}{8\pi^2 c I} \quad (\text{B.9})$$

B is termed rotational constant. It can be seen, that this solution of the Schrödinger equation and thus the rotational energy is quantized with quantum number $J = 0, 1, 2, \dots$. Generally, the *rigid rotor* model does not reflect reality and increasing J leads to higher rotational energy and due to the centrifugal force the nuclei distance increases and changes the moment of inertia. To account for that effect, a correction term with the so-called centrifugal distortion correction D_e is introduced. Additionally, rotation and vibration modes occur simultaneously and coupling needs to be account for as vibration alters the moment of inertia and consequentially the rotational energy. Hence, the rotational and the centrifugal distortion constants are modified to:

$$F_{rot}(J, v, n) = B_v J(J+1) - D_v J^2(J+1)^2 + H_v J^2(J+1)^2 - \dots \quad (\text{B.10})$$

where D_v is a correction term called centrifugal distortion constant and defined as:

$$\begin{aligned} B_v &= B_e - \alpha_e(v + \frac{1}{2}) + \gamma_e(v + \frac{1}{2})^2 - \dots \\ D_v &= D_e + \beta_e(v + \frac{1}{2}) \end{aligned} \quad (\text{B.11})$$

the subscript e refers to the equilibrium position of the nuclei. B_v is several order of magnitudes larger than D_v . Values of the molecular constants are tabulated in the literature ([38, 48, 86, 97, 130, 141]).

B.1.3 Electronic state

According to the Bohr model, an electron resides at defined, quantized orbitals which are an integer multiple of Planck's constant. As mentioned, the BO approach can be applied to consider energetic state of electrons separately from nuclei. The eigenfunctions Ψ of electrons of an atom are characterized by the principal quantum number n and the azimuthal or orbital angular momentum quantum number l . However, the energy levels may degenerate in the presence of an magnetic field, and the magnetic quantum number m_l and the spin quantum number m_s are introduced. Degeneracy refers to same energetic levels with different quantum characteristics. The quantum numbers basically refer to the space where the electron is most probably to find, as according to the Heisenberg Uncertainty Principle, momentum and position cannot be both predicted. Quantum numbers relevant for the description of atomic orbitals are:

Quantum number n :

The principal quantum number $n = 1, 2, 3, \dots$ characterizes the energy of an electron and basically defines the size of the orbital and thus the distance of the electron from the nucleus.

Quantum number l :

The azimuthal quantum number $l = 0, \dots, n - 1$ defines the shape of an orbital and is denoted by Roman letters as $s(l = 0)$, $p(l = 1)$, $d(l = 2)$, $f(l = 3)$, etc.

Quantum number m_l :

The magnetic quantum number $m_l = l, l - 1, l - 2, \dots, -l$ with $2l + 1$ orbitals specifies the orientation of the orbital in space.

Quantum number m_s :

According to the Pauli Exclusion Principle, two electrons with same n, l, m_l must have opposite spins, specified by $m_s = +1/2$ or $-1/2$ leading to different orientation of the spin axis. Thereby is m_s the spin-quantum number and s is the magnitude of the electron spin and always $+1/2$ for an electron. In some cases, s is referred to as spin-quantum number.

In contrast to atoms, diatomic molecules are of linear structure and lack of spherical symmetry. Due to the potential of the two nuclei, a precession of the outer, non-fully occupied orbital electron about the internuclear axis sets in. Hence, l is not a *good* quantum number anymore (it is not sufficient anymore to describe the state of the system) as interaction with the Coulomb potential occurs, but the projection of m_l onto the internuclear axial (z -projection) is introduced as a new quantum number λ . Using vector addition, a total orbital angular momentum quantum number for multi-electron molecules is introduced to describe the z -projection of the total angular momentum \vec{L} as:

$$\Lambda = |M_L| = \sum_i \lambda_i = \left| \sum_i m_{li} \right| \quad (\text{B.12})$$

where $\Lambda = 0, 1, 2, 3, \dots = \Sigma, \Pi, \Delta, \Phi, \dots$. The nomenclature in molecular spectroscopy is based on Greek symbols rather than Roman letters in atomic spectroscopy. For single-electron characterization of molecules, lowercase Greek letters $\lambda = \sigma, \pi, \delta, \phi \dots$ are used. States with $\Lambda > 1$ are doubly degenerated due to the direction $|M_L| = +M_L, -M_L$. Further, considering independent spin and angular momentum precession for small molecules as the spin-orbit coupling is weak compared to the coupling of l to the internuclear axis, in a multi-electron system mutual coupling between electrons emerges and another component of the total momentum results from the sum of individual electron spins, calculated from $\vec{S} = \sum s_i$ and takes values $S = 0, 1/2, 1, 3/2, \dots$. A quantum number describing the z -projection of the spin-orbit coupling is introduced as:

$$\Sigma = S, S - 1, \dots, -S \quad (\text{B.13})$$

Note, Σ should not be mistaken for the term description $\Lambda = \Sigma$ and for the sigma sign for summation. Based on Eq. (B.13) a total number of $2S + 1$ energy levels, the so-called *spin multiplicity*, are possible. The total spin \vec{S} and the total orbital angular momentum \vec{L} lead to a resultant angular momentum referred to as \vec{J} with its projection quantum number Ω :

$$\Omega = |\Lambda + \Sigma| \quad (\text{B.14})$$

This leads to the conclusion, that the characteristic quantum numbers to describe the electronic state are n , Λ , Ω , S .

B.2 Hund's cases

So far the electronic mode and the molecular rotation mode were treated separately. However, coupling between these two modes play an important role. Generally, there are five coupling possibilities termed as *Hund's case (a) - (e)*. For OH, only *case (a)* and *case (b)* are relevant:

Hund's case (a):

In this case, \vec{L} and \vec{S} are coupled strongly to the internuclear axis and precess rapidly and independently (faster than molecular rotation) about it and the coupling of \vec{S} and the angular momentum of the nuclear rotation \vec{N} is weak. \vec{N} is oriented perpendicular to the internuclear axis. This condition is met for $\vec{L} \neq 0$ and the projection quantum number Ω is well-defined. The resultant total angular momentum \vec{J} is then:

$$\vec{J} = \vec{\Omega} + \vec{N} \quad (\text{B.15})$$

This condition is valid for small molecular rotation and the corresponding quantum number $J = \Omega, \Omega + 1, \Omega + 2, \dots$

Hund's case (b):

If \vec{S} couples weakly or does not couple at all to the molecular axis and consequentially Ω is not *well-defined* anymore, then \vec{L} and \vec{N} sum up first to an angular momentum \vec{R} defined by a new projection quantum number R . The total angular momentum is finally obtained by coupling \vec{K} and \vec{S} :

$$\vec{K} = \vec{L} + \vec{N} \quad \text{and} \quad \vec{J} = \vec{K} + \vec{S} \quad (\text{B.16})$$

where $J = K + S, K + S - 1, \dots, |K - S|$. The coupling types are illustrated schematically in Fig. B.1. $\Lambda = 0$ state and large rotational N tend to be of Hund's case b as seen in section B.3.

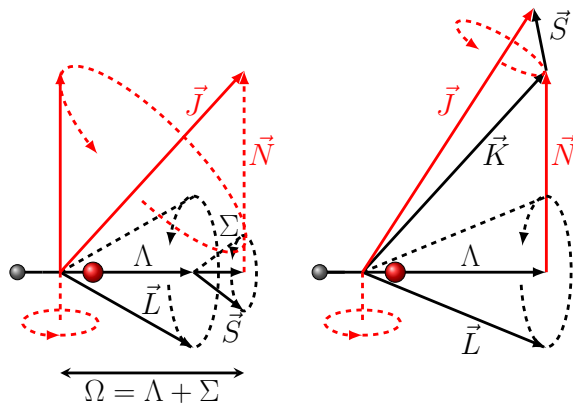


Figure B.1: Hund's cases. Left: Hund's case (a). Right: Hund's case (b).

B.3 Characterization of the OH molecule

As described in the previous subsections, the molecular energy state is determined by the electronic configuration. Based on the *LCAO* (*Linear Combination of Atomic Orbitals*) the ground state configuration of OH termed by the individual electron notation is:

$$X^2\Pi : (1s\sigma)^2(2s\sigma)^2(2p\sigma)^2(2p\pi)^3 \quad (\text{B.17})$$

The notation indicates the position of the electron and corresponds to the terminology (n l λ). The superscript specifies the number of electrons within each orbital, respectively. A σ orbital allows 2 and a π orbital 4 electrons. Unoccupied orbitals are those of interest, also referred to as *LUMO* (*Lowest Unoccupied Molecular Orbital*), while in contrast *HOMO* (*Highest Occupied Molecular Orbital*) refers to the last fully occupied orbital. The 3 electrons of the $2p$ need different m_l and m_s quantum numbers, as according to the Pauli Exclusion Principle, each electron must have unique quantum numbers. Here $m_l = -1, -1, 1$ or $1, 1, -1$. From Eq. (B.12), it follows $|\Lambda| = 1$ and therefore a Π state. Due to the single unpaired electron, the spin quantum number is $|S| = 1/2$ and from $2S + 1$ a state multiplicity of 2 emerges. The doublet structure is also referred to as *Λ -doubling* in literature. Finally, the projection quantum number $\Omega = 3/2$ and $1/2$ are obtained, leading to the sub-states $^2\Pi_{3/2}$ and $^2\Pi_{1/2}$. A last notation is necessary to label the electronic state. The ground state is indicated by X and the excited states by A, B, C, \dots and the final ground states are $X^2\Pi_{3/2}$ and $X^2\Pi_{1/2}$. Due to the non-zero Λ and S quantum states, Hund's case (a) may apply to this state. However, OH belongs to *intermediate* or *transition* cases between (a) and (b), as \vec{L} couples more to \vec{N} for large rotational quantum number and \vec{S} decouples from the internuclear axis. The rotational energy of the doublet structure of Π is defined by the manifolds F_1 and F_2 :

$$\begin{aligned} F_1(J'') &= B_v \left[(J'' + \frac{1}{2})^2 - \Lambda - \frac{1}{2} \left(4 \left(J'' + \frac{1}{2} \right)^2 + Y_v (Y_v - 4) \right)^{0.5} \right] - D_v J''^4 \\ F_2(J'') &= B_v \left[(J'' + \frac{1}{2})^2 - \Lambda + \frac{1}{2} \left(4 \left(J'' + \frac{1}{2} \right)^2 + Y_v (Y_v - 4) \right)^{0.5} \right] \\ &\quad - D_v (J'' + 1)^4 \end{aligned} \quad (\text{B.18})$$

where $Y_v = A/B_v$ is the spin-orbit coupling term. Typically, Hund's case (a) is specified depending on $J = N + 1/2$ and $J = N - 1/2$ for $\Pi_{3/2}$ and for $\Pi_{1/2}$, respectively. The double primes $''$ indicate the ground state. According to Coxon [38] the spacing between the F_1 and F_2 splitting is around 126 cm^{-1} for the lowest rotational number.

The first excited state of OH, termed as A , is obtained by exciting an electron from the HOMO orbit $2p\sigma$ to $2p\pi$ and forming an occupied shell. Following electronic configuration describes the excited state:

$$A^2\Sigma : (1s\sigma)^2(2s\sigma)^2(2p\sigma)^1(2p\pi)^4 \quad (\text{B.19})$$

The unoccupied orbital $2p\sigma$ with its remaining electron results in a $|\Lambda| = 0$ (as $n = 2, l = 1, \lambda = 0$) and thus the Hund's case (b), which applies to all N . Similarly to the ground

state, a doubling state appears leading to two rotational terms, described by F_1 and F_2 as:

$$\begin{aligned} F_1(N') &= B_v N' (N' + 1) - D_v N'^2 (N' + 1)^2 + \frac{1}{2} \gamma N' \\ F_2(N') &= B_v N' (N' + 1) - D_v N'^2 (N' + 1)^2 - \frac{1}{2} \gamma (N' + 1) \end{aligned} \quad (\text{B.20})$$

The primes ' indicate the excited state. Note, Eq. (B.20) corresponds to Eq. (B.10) apart from the third term, which accounts for the rotational energy splitting by the constant γ .

B.3.1 Selection rules and notation

As the applied measurement techniques in this study are based on energetic transition of OH, the so-called *transition rules* or *selection rules* for electronic, vibronic and rotational transition need to be briefly outlined. Variations of the quantum numbers are indicated by a Δ and traditionally the excited state is ranked first.

The total angular momentum and thus the rotational transition in terms of Hund's case (a) is restricted to:

$$\Delta J = -1, 0, 1 \quad \text{where} \quad J' = 0 \leftrightarrow J'' = 0 \quad (\text{B.21})$$

The symbol \leftrightarrow indicates forbidden transitions. If Hund's case (b) is selected, then $\Delta N = N' - N'' = -2$ to 2 is also possible for satellite branches, resulting from the definition $J = N \pm 1/2$. Capital letters P, Q, R are usually assigned to transitions $\Delta J = -1, 0, 1$. $\Delta N = -2, 2$ correspond to O, S , respectively. The introduction of N was necessary to further classify the coupling (Hund's cases). Additionally, the *parity* (symmetry (+) or asymmetry of the molecular wave function) must be reversed during the transition as $+ \leftrightarrow -$. The electronic transition obeys following selection rules:

$$\Lambda = -1, 0, 1 \quad (\text{B.22})$$

and with the restriction $\Delta S = 0$ on the spin multiplicity, it results in transitions like:

$$^2\Sigma \leftrightarrow ^2\Sigma \quad ^2\Sigma \leftrightarrow ^2\Pi \quad ^2\Pi \leftrightarrow ^2\Pi \quad (\text{B.23})$$

where $^2\Sigma \leftrightarrow ^2\Pi$ is relevant for this work. Finally, the vibrational transition may be characterized. During electronic transition, the vibrational quantum number can also change. But compared to electronic and rotational transition, there are no selection rules restricting the vibrational transition. Δv is not a limiting factor and $\Delta v = 0, \Delta v = 1, \Delta v = 2, \dots$ are all allowed possibilities. However, the strength and thus the relative intensity or the fluorescence is determined by the *Franck-Condon* factors. Within an electronic state, transitions of $\Delta v \pm 1$ are strongest. Based on the assumption that the nuclei position may not change significantly during an electronic transition due to higher momentum of inertia of nuclei compared to electrons, the Franck-Condon principle states that vibrational transitions are most probable for states with matching nuclei velocity and position. Thus, the absorption and emission processes are indicated as vertical lines or arrows in potential curves of molecules, see Fig. 3.3. From a quantum mechanical point of view, the highest transition probability is maintained for the largest overlap of the vibrational wave function. Remember, the probability density of the electron location is obtained from the square of the wave function. Fig. B.2 illustrates graphically the 12 possible transitions for OH between $^2\Sigma \leftrightarrow ^2\Pi$.

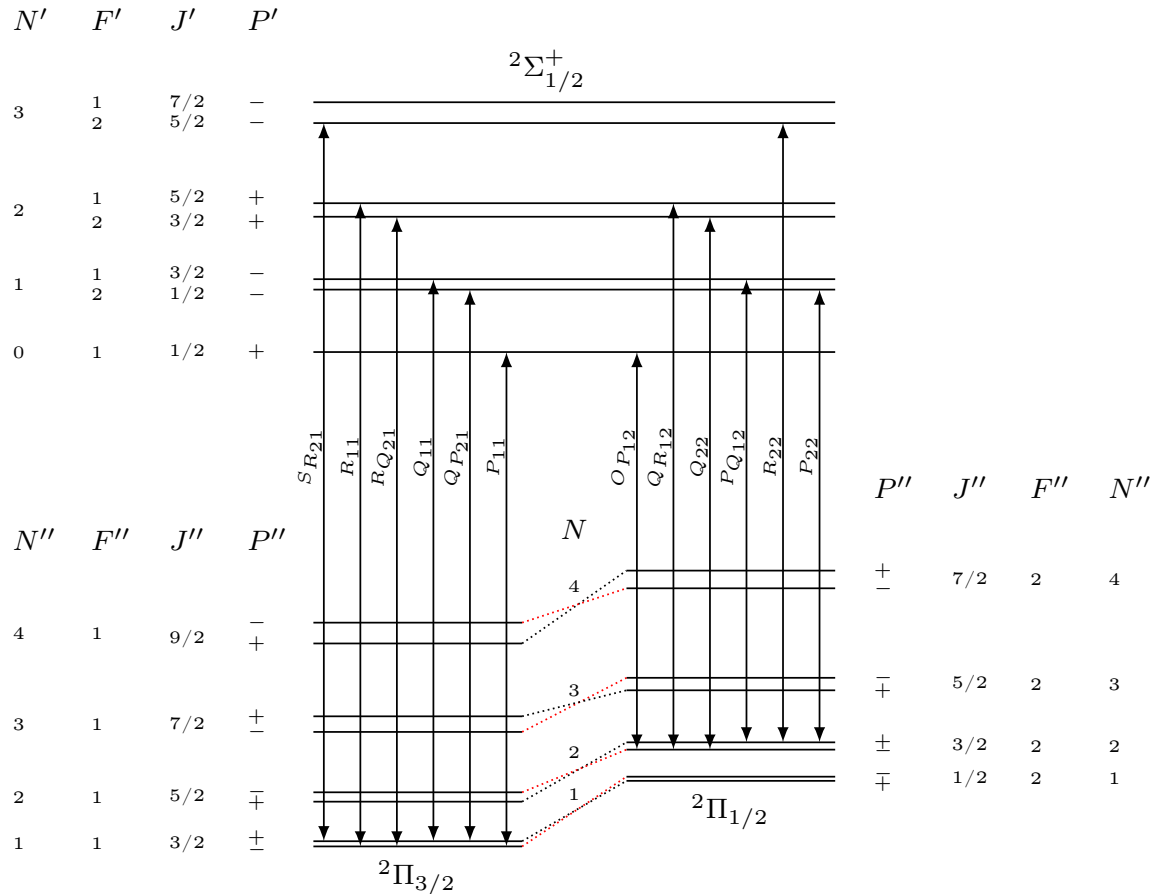


Figure B.2: Rotational transition structure according to [50, 86] for $^2\Sigma_{1/2}^+ - ^2\Pi$. Notice the conversion of Hund's case (a) to Hund's case (b). P' is the parity.

B.3.2 Population of energy levels

In the previous section the energies of individual states were quantum mechanically quantified. However, methods are necessary to convert the molecular energy levels into macroscopic properties, i.e. into temperature. Considering a group of N molecules and assuming thermal equilibrium (equilibrated electronic, vibrational and rotational modes), the number N_i molecules having a certain energy E_i (instead of certain quantum state) is given by the Boltzmann probability distribution $f_B(T)$, used in statistical mechanics. The function for the relative population is expressed as:

$$\frac{N_i(n,v,J)}{N} = \frac{g_i(2J+1)e^{E_i/kT}}{\sum_i g_i(2J+1)e^{E_i/kT}} = \frac{g_i(2J+1)e^{E_i/kT}}{Q(T)} = f_B(T) \quad (\text{B.24})$$

where g_i is the degeneracy of the i -th state, which for the ground state of OH $^2\Pi$ is $(2S+1)2 = 4$ due to spin splitting and Λ -doubling and $(2S+1)1 = 2$ for the excited state Σ . k is the Boltzmann constant and $Q(T)$ is the so-called partition function (sometimes named Z for the German term *Zustandssumme*). This, basically a normalization factor, is of major importance as it relates the line strength to temperature and sums up every possible conditions. The energy levels of a molecule could be well separated in Eq. (B.2)

and treated independently. Hence, the partition function is divided into individual partition terms:

$$Q(T) = Q_{elec}(T)Q_{vib}(T)Q_{rot}(T) \quad (\text{B.25})$$

The general equations for partition functions of the electronic mode is $Q_{elec} = g$ and for the rotational and vibrational modes are:

$$Q_{rot} = \sum_J (2J + 1)e^{-F(J,v,n)/kT} \approx \frac{1}{1 - e^{\omega_e/kT}} \quad (\text{B.26})$$

$$Q_{vib} = \sum_v e^{-G(v,n)/kT} \approx \frac{kT}{B_v} + \frac{1}{3} + \frac{1}{15} \frac{B_v}{kT} + \frac{4}{315} \left(\frac{B_v}{kT} \right)^2 + \dots \quad (\text{B.27})$$

The vibrational approximation is based on the harmonic oscillator. For high temperatures, the rotational approximation reduces to the first term $\frac{kT}{B_v}$.

B.4 Hönl-London-factors

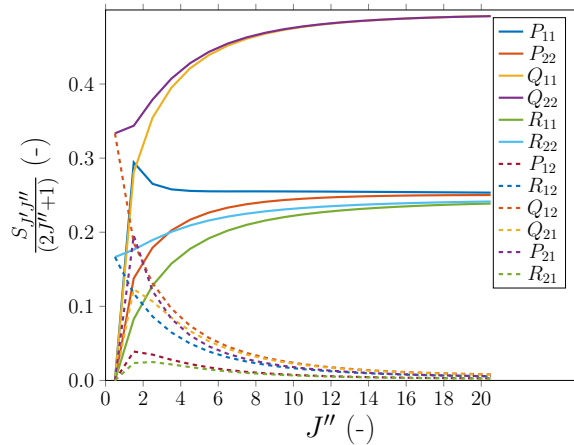


Figure B.3: Hönl-London factors for OH.

B.5 Line shape and broadening

B.5.1 Natural line broadening

The natural line broadening is mathematically described by the Lorentzian profile given in Eq. (B.28):

$$g_N(\nu) = \frac{1}{\pi} \frac{\Delta\nu/2}{(\nu - \nu_0)^2 + (\Delta\nu/2)^2} \quad (\text{B.28})$$

where $\Delta\nu$ is the full width at half maximum (FWHM) and ν_0 is the central wavelength. The natural broadening corresponds to the lifetime τ :

$$\Delta\nu = \Delta\nu_n = \frac{1}{2\pi\tau c} \quad (\text{B.29})$$

For a lifetime of 50 ns for OH, the natural broadening is $< 8 \cdot 10^{-4} \text{ cm}^{-1}$ and can be neglected.

B.5.2 Collision broadening

The collision of a molecule with an emitting molecule increases the uncertainty in the emitted energy, hence it leads to a broadening line shape. This type of broadening is also known as pressure broadening and depends preliminary on the density/pressure. The line shape is also described by a Lorentzian profile (Eq. (B.28)). The pressure broadening is investigated in a various number of publications. In [177] the authors found, that the broadening is linearly dependent on pressure in the range from 50 Torr to 1 atm. The air-broadening of the $P_{11}(2)$ for OH was given as 0.2 cm^{-1} . Since, the interaction of the molecules is complex, an empirical parametric equation for the FWHM $\Delta\nu_C$ is defined as [165]:

$$\Delta\nu_C = \sum_i 2\gamma_i(T)p_i = p \sum_i x_i 2\gamma_i(T) \quad (\text{B.30})$$

where p_i is the partial pressure, x_i the mole fraction and $2\gamma_i \text{ cm}^{-1}/\text{bar}$ the broadening coefficient of the species i . The latter can be approximated from reference measured coefficients by Eq. (B.31) [165]:

$$2\gamma = 2\gamma_{ref} \cdot \left(\frac{T_{ref}}{T} \right)^n \quad (\text{B.31})$$

The temperature exponent n varies between 0.5 and 1 depending on the colliding partner. Increasing the temperature decreases the broadening, while increasing the pressure leads to a linear increase. Due to the lack of broadening coefficients for different species, generally, reference experimental values for Ar are taken. In [165] the authors reported that N₂ was a more effective broadening species and that the N₂ broadening is slightly depending on the rotational number (up to $J'' < 5.5$). Higher rotational number dependencies were reported for CO₂ in [166] and absolute higher broadening by the H₂O molecule. Unfortunately, the literature lacks complete values for the broadening coefficients and the temperature exponent. Davidson et al. [41] recommended $2\gamma_i = 0.140 \text{ cm}^{-1}/\text{bar}$ and $n = 0.75$ for a wide range of temperature and pressure based on experiments in Ar. The final equation is then expressed as:

$$\Delta\nu_C = 0.14 \left(\frac{p}{10325} \right) \left(\frac{296}{T} \right)^{0.75} [\text{cm}^{-1}] \quad (\text{B.32})$$

where p is chosen in Pa and T in K. The rotational dependency and additional species are neglected due to the lack of data. Additional information regarding pressure broadening can be found in [73, 104, 109, 180].

B.5.3 Doppler broadening

The dominating line broadening at high temperature is the thermal Doppler broadening. The frequency of a moving and emitting molecule is shifted relative to a detector at rest due to the Doppler effect. An approaching molecule has a higher frequency, while a molecule moving away has a lower frequency than its average frequency. The broadening depends on the velocity distribution and therefore on the temperature. The Maxwell-Boltzmann relation describes the velocity distribution for a given temperature. To calculate the FWHM $\Delta\nu_D$ of a broadened line, the Doppler shift is determined for each velocity component and averaged over the distribution of velocities.

$$\Delta\nu_D = \frac{2\nu_0}{c} \sqrt{\frac{2\ln(2)kT}{m}} \quad (\text{B.33})$$

where c is the speed of light, ν_0 is the center frequency and m is the molecular mass. Then, the Doppler line shape is defined by the Gaussian form as:

$$g_D(\nu) = \frac{c}{\nu_0} \sqrt{\frac{m}{2\pi kT}} \exp \left[-4\ln 2 \frac{(\nu - \nu_0)^2}{\Delta\nu_D^2} \right] \quad (\text{B.34})$$

$\Delta\nu_D$ at 2000 K is calculated as 0.27461 cm^{-1} , which is more than six times higher than the pressure broadening (0.04095 cm^{-1}) at atmospheric pressure. Hence, the latter is typically neglected at atmospheric pressure, high temperature investigations.

B.5.4 Voigt profile

Generally, Doppler and collision broadening mechanisms occur simultaneously and are overlapped. The result is a so-called Voigt profile, which is mathematically described by a convolution assuming decoupled Doppler and collision effects. The Voigt profile $V(a,x)$ is defined as:

$$g(\nu) = 2\sqrt{\frac{\ln 2}{\pi}} \frac{V(a,x)}{\Delta\nu_D} \quad (\text{B.35})$$

and

$$V(a,x) = \frac{a}{\pi} \int_{-\infty}^{\infty} \frac{\exp(-y^2)}{a^2 + (x - y)^2} dy \quad (\text{B.36})$$

where a and x are defined by:

$$a = \sqrt{\ln 2} \frac{\Delta\nu_c}{\Delta\nu_D} \quad (\text{B.37})$$

$$x = 2\sqrt{\ln 2} \frac{(\nu - \nu_0)}{\Delta\nu_D} \quad (\text{B.38})$$

An approximation for the Voigt FWHM is given as [44]:

$$\Delta\nu_V = 0.535\Delta\nu_C + \sqrt{0.2166\Delta\nu_C^2 + \Delta\nu_D^2} \quad (\text{B.39})$$

Fig. B.4 shows the three profiles for OH, simulated for atmospheric pressure and 2000 K. The Lorentzian effect is insignificant. The overlap of a Gaussian and a Lorentzian profile leads to broader flanks and smaller FWMH.

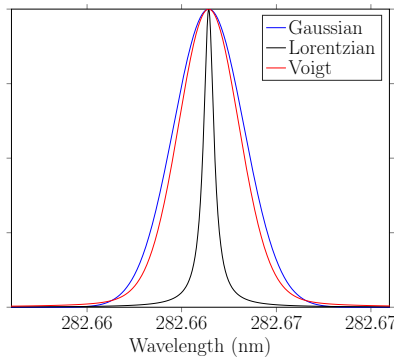


Figure B.4: Simulated spectral profiles for $T = 2000 \text{ K}$, $p = 1 \text{ atm}$ for OH.

Appendix C

Test Bench Details

Fig. C.1 shows some images of the real test bench and the test section. A drawing of the mechanism to fix the TC is provided in Fig. C.2.

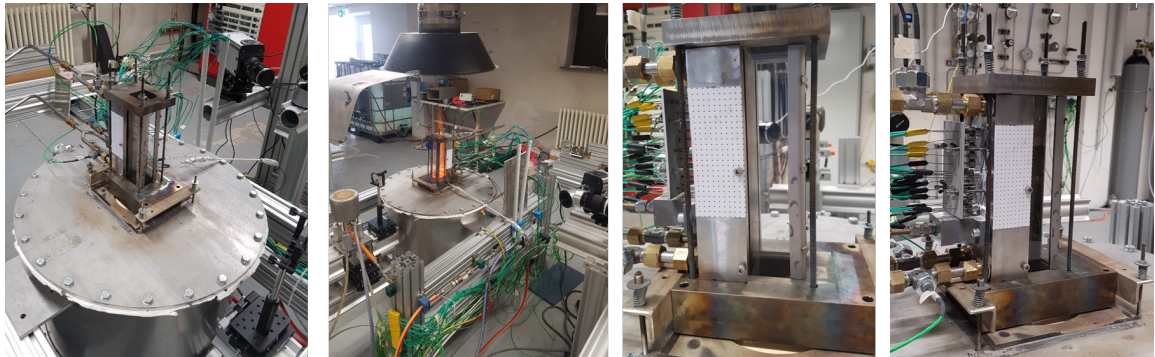


Figure C.1: Actual test bench and test section photographed from different angles.

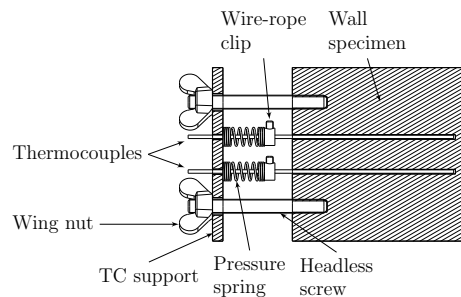


Figure C.2: TC mounting mechanism drawing.

Appendix D

CFD Simulation

D.1 Governing equations

The conservation law of physics provide the basic principle to describe the properties of an isolated fluid element. Therefore, a set of partial differential equations are formulated. The most prominent formulations are the so-called Navier-Stokes (NS) equations, which describe the conservation of mass and momentum. For non-isothermal and for reactive flows, the energy balance equation and the conservation of species mass fraction are required additionally. As turbulent flows consist of time-dependent fluid motions on different scales, fine meshes would be necessary to resolve the fine turbulent structures and the numerical solution of the NS equations becomes impractical in terms of calculation time and computational power. However, in most industrial and scientific problems, the focus is on the mean flow properties and the effect of the turbulence, rather than the detailed resolution of each turbulent fluctuation. Hence, the partial differential equations are simplified using the Reynolds decomposition, leading to the Reynolds-averaged Navier-Stokes (RANS) equations. In the current case, the density is subject to variations due combustion, hence the Favre-averaging is rather used, which is a mass-weighted averaging method. Based on the decomposition principle, a flow variable ϕ is split into a mean $\tilde{\phi}$ and a fluctuating component ϕ'' :

$$\phi = \tilde{\phi} + \phi'' \quad (\text{D.1})$$

and the Favre-averaging is defined as:

$$\tilde{\phi} = \frac{\overline{\rho\phi}}{\bar{\rho}} \quad (\text{D.2})$$

The idea is then to substitute each flow variable with its decomposed expression and perform a Favre-averaging, considering that the averaged fluctuating values are $\widetilde{\phi''} = 0$, but $\widetilde{\phi''_i \phi''_j} \neq 0$. Without further details, the final transport equations in tensor notation for turbulent combustion modeling are [118, 159, 196]:

- **Continuity:**

$$\frac{\partial \tilde{\rho}}{\partial t} + \frac{\partial}{\partial x_i} \bar{\rho} \tilde{u}_i = 0 \quad (\text{D.3})$$

where x_i denotes the i-th component Cartesian coordinate, while u_i is the i-th component of the corresponding velocity vector.

- **Momentum:**

$$\frac{\partial \bar{\rho} \tilde{u}_i}{\partial t} + \frac{\partial}{\partial x_j} (\bar{\rho} \tilde{u}_i \tilde{u}_j) = - \frac{\partial \bar{p}}{\partial x_i} + \frac{\partial}{\partial x_j} \left(\tilde{\tau}_{ij} - \bar{\rho} \widetilde{u''_i u''_j} \right) \quad (\text{D.4})$$

where $\tilde{\tau}_{ij}$ is the shear stress or viscous tensor:

$$\tilde{\tau}_{ij} = \mu \left(\frac{\partial \tilde{u}_i}{\partial x_j} + \frac{\partial \tilde{u}_j}{\partial x_i} - \frac{2}{3} \delta_{ij} \frac{\partial \tilde{u}_k}{\partial x_k} \right) \quad (\text{D.5})$$

with δ_{ij} as the Kronecker symbol (1 for $i = j$, else 0) and molecular dynamic viscosity μ .

- **Species:**

$$\frac{\partial \bar{\rho} \tilde{Y}_k}{\partial t} + \frac{\partial}{\partial x_i} (\bar{\rho} \tilde{u}_i \tilde{Y}_k) = - \frac{\partial}{\partial x_i} \left(-\bar{\rho} \bar{D}_k \frac{\partial \tilde{Y}_k}{\partial x_i} + \bar{\rho} \widetilde{u''_i Y''_k} \right) + \bar{\omega}_k \quad (\text{D.6})$$

where $\bar{\omega}_k$ is the species reaction rate of the species k , also referred to as species source term due to combustion.

- **Sensible enthalpy:**

$$\frac{\partial \bar{\rho} \tilde{h}_s}{\partial t} + \frac{\partial}{\partial x_j} (\bar{\rho} \tilde{u}_j \tilde{h}_s) = \frac{\partial}{\partial x_j} \left(\bar{k} \frac{\partial \tilde{T}}{\partial x_j} - \bar{\rho} \widetilde{u''_j h''_s} + \tilde{u}_i \tilde{\tau}_{ij} \right) + \bar{\omega}_T \quad (\text{D.7})$$

where $\bar{\omega}_T$ is the energy source term due to chemical reaction and obtained from the reaction rates and the mass formation enthalpy $\Delta h_{f,k}^0$ by $\bar{\omega}_T = - \sum_{k=1}^N \Delta h_{f,k}^0 \bar{\omega}_k$.

In the current study, only time-averaged numerical simulations are performed. Consequently, the time derivative terms are $\frac{\partial}{\partial t} = 0$.

The decomposition and Favre-averaging of the conservation equations produce additional, non-linear terms related to fluctuations, leading to a larger number of unknowns than equations. Thus, the system of equations cannot be closed and the task to handle those non-resolved terms is called *closure problem*. Here, it is attempted to approximate the turbulent variables by the corresponding mean variables. To address the momentum equation, turbulence models are used, which are generally applied to close the NS equations in the field of non-reactive flows. According to the Boussinesq concept, the Reynolds stresses are related to the turbulent viscosity μ_t and approximated by an expression similar to the stress tensor of a Newtonian fluid:

$$\bar{\rho} \widetilde{u''_i u''_j} = -\mu_t \left(\frac{\partial \tilde{u}_i}{\partial x_j} + \frac{\partial \tilde{u}_j}{\partial x_i} - \frac{2}{3} \delta_{ij} \frac{\partial \tilde{u}_k}{\partial x_k} \right) + \frac{2}{3} \bar{\rho} k \quad (\text{D.8})$$

where k is the turbulent kinetic energy $k = \frac{1}{2} \sum_{k=1}^3 \widetilde{u''_k u''_k}$. A considerable number of models are presented in the literature to model the turbulent viscosity μ_t . For applications containing near-wall flows, recirculation zones and free-stream interaction, the two-equation Menter SST $k-\omega$ -model proved to be successful and is recommended. Hence, it is selected in this case without modification of the model constants. The model basically introduces two additional transport equations for k and ω , which are solved along side Eq. (D.3) - Eq. (D.7). For a detailed description the reader is referred to [196].

The remaining scalar turbulent species and enthalpy fluxes are modeled on the basis of the gradient assumption:

$$\bar{\rho} \widetilde{u''_j Y''_k} = - \frac{\mu_t}{Sc_{kt}} \frac{\partial \widetilde{Y}_k}{\partial x_j} \quad (\text{D.9})$$

$$\bar{\rho} \widetilde{u''_j h''_s} = - \frac{\mu_t}{Pr_t} \frac{\partial \widetilde{h}_s}{\partial x_j} \quad (\text{D.10})$$

where Sc and Pr are the Schmidt and Prandtl numbers, respectively, and the subscript t highlights turbulent properties.

D.2 Combustion modeling

Finally, the reaction rate is subject to the closure problem. Reactive, fine structure properties are labeled by $*$, while the remaining flow properties are marked by 0. The characteristic length γ of the fine structure and its residence time or EDC mixing time τ^* are related to the turbulence properties by:

$$\gamma = C_\gamma \left(\frac{\nu \varepsilon}{k^2} \right)^{0.25} = 2.1377 \left(\frac{\nu \varepsilon}{k^2} \right)^{0.25} = 2.1377 (Re_t)^{-0.25} \quad (\text{D.11})$$

$$\tau^* = C_\tau Re_t^{-0.5} \frac{k}{\varepsilon} = 0.4082 Re_t^{-0.5} \frac{k}{\varepsilon} \quad (\text{D.12})$$

where Re_t is the turbulent Reynolds number and ε is the dissipation rate of turbulent kinetic energy. The mean reaction rate as a source term for the species conservation equation Eq. (D.6) based on the properties in Eq. (D.11) is expressed as:

$$\bar{\omega}_k = \frac{\rho \gamma^2}{\tau^*(1-\gamma)} (Y_k^* - \bar{Y}_k) \quad (\text{D.13})$$

For a detailed derivation, it is recommended to consider the cited literature. The average mass fraction of the mentioned fluid volume is obtained from:

$$\bar{Y}_k = \gamma^3 Y_k^* + (1 - \gamma^3) Y_i^0 \quad (\text{D.14})$$

And fine scale reactions take place within a perfectly stirred reactor assuming constant pressure, adiabatic conditions:

$$\frac{dY_k^*}{dt} = \frac{\dot{\omega}_k}{\rho^*} + \frac{1}{\tau^*} (Y_i^0 - Y_k^*) \quad (\text{D.15})$$

where Eq. (D.15) is then integrated for the reactive period from 0 to τ^* . However, this leads to a stiff, non-linear system of ordinary differential equations, which may cause convergence issues. Thus, a plug flow reactor (a steady state reactor) is often used considering that the reactor is self-contained and the composition is not altered during the mixing time, which simplifies Eq. (D.15) to [123]:

$$\frac{dY_k^*}{dt} = \frac{\dot{\omega}_k}{\rho^*} \quad (\text{D.16})$$

This formulation reduces computational time significantly compared to Eq. (D.15). That is the implementation in Ansys Fluent.

The benefit of the EDC model is, that it allows the inclusion of detailed mechanisms and it takes into account the finite-rate chemistry by introducing the species production rate $\dot{\omega}_k$ into the fine scale reaction volume. The individual reaction rates are determined from Eq. (2.34).

D.3 Mesh sensitivity

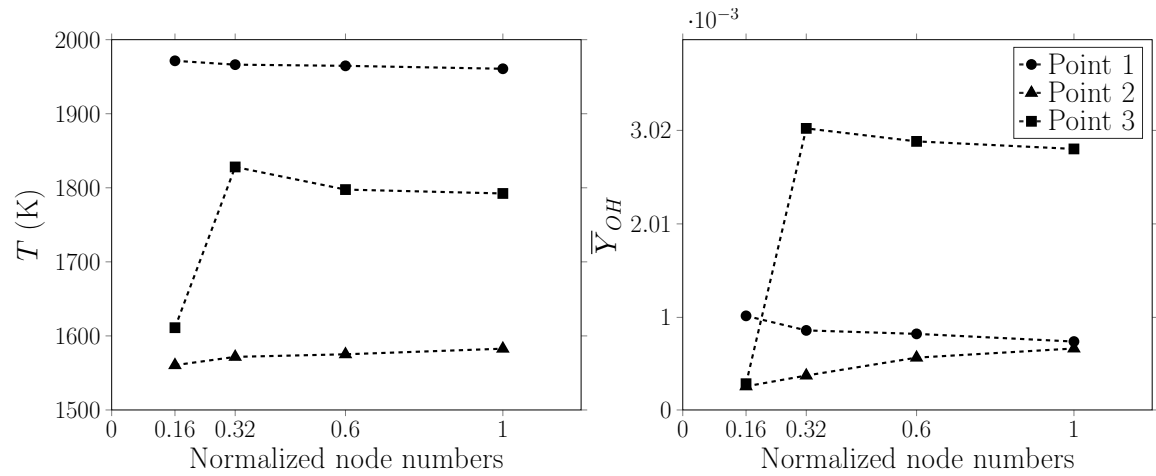


Figure D.1: CFD mesh sensitivity analysis.

Appendix E

Inverse Heat Transfer

Table E.1: Positions of TC with respect to the local coordinate system. Part 1.

ID TC	5	8	11	12	13	16	19	20	21	22	23
-x (mm)	3.38	3.76	4.09	4.90	3.95	3.26	3.85	2.76	3.28	2.89	3.34
y (mm)	0	0	0	0	0	0	0	0	0	0	0
z (mm)	-35.5	19.5	29.5	39.5	49.5	59.5	69.5	79.5	89.5	99.5	109.5

Table E.2: Positions of TC with respect to the local coordinate system. Part 2.

ID TC	1	9	17	24	2	10	18	25
-x (mm)	4.26	3.47	3.12	2.99	3.81	4.65	3.52	3.69
y (mm)	15	15	15	15	-15	-15	-15	-15
z (mm)	-35.5	19.5	59.5	109.5	-35.5	19.5	59.5	109.5

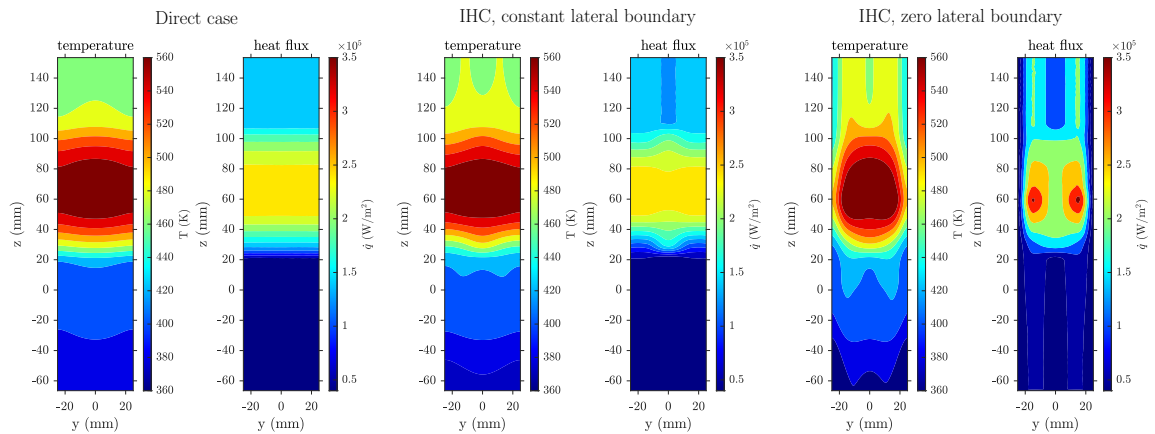


Figure E.1: IHC Validation. Temperature and heat flux distribution. Left: direct case with 1D heat boundary. Center: IHC with constant heat flux lateral boundary. Right: IHC with zero heat flux lateral boundary.

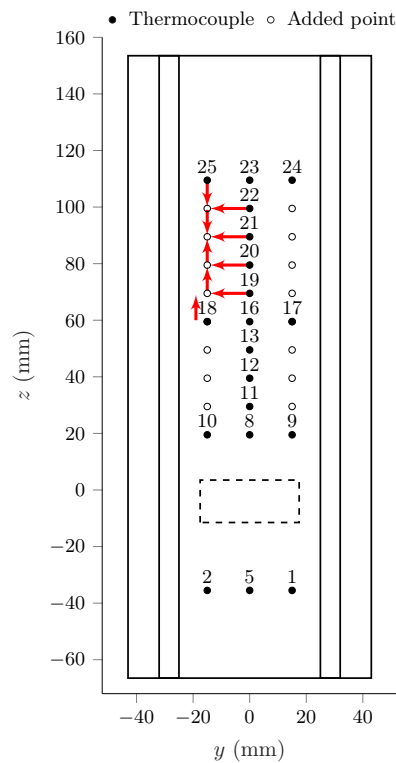


Figure E.2: IHC heat flux profile construction. Numbered markers represent sensors projected onto the surface. Unfilled circles highlight added locations for the interpolation. Red arrows show the interpolation direction.

Appendix F

Complementary Results

F.1 Tracer PLIF boundary conditions

The injection and main flow conditions of the tracer PLIF experiments are presented in this section. The temperature data are obtained from TC measurements. Velocities and Reynolds numbers are calculated from the supplied mass flow rates and the geometry. As the MFC provide information about the actual volume flow at normal conditions, the temperature values are used to account for the actual flow temperature.

Table F.1: Tracer PLIF. Boundary conditions of normal injection.

Case	1N	2N	3N	4N	5N	6N	7N	8N	9N	10N
T_c (K)		284					285			
u_c (m/s)	6	14	20	8	11.38	18	25.48	31	36.4	51
$Re_{D,c}$	229	507	714	290	409	649	916	1123	1308	1826
T_∞ (K)		284					288 - 284			
\bar{u}_∞ (m/s)		4.38					8.09 - 7.8			
Re_d		15600					28400			
Re_z		60300					110000			
I	2	10	19.6	0.96	1.93	4.88	9.74	14.68	20	39

Table F.2: Tracer PLIF. Boundary conditions of angled injection. Part 1.

Case	1A	2A	3A	4A	5A	6A	7A	8A
T_c (K)		285				285		
\bar{u}_c (m/s)	14	20	39	14	20	29	40	78
$Re_{D,c}$	375	525	1019	375	524	749	1049	2031
T_∞ (K)		290				289		
\bar{u}_∞ (m/s)		2.2				4.43		
Re_d		7700				15400		
Re_z		30000				60000		
I	40	80	303	10	20	41	81	301

Table F.3: Tracer PLIF. Boundary conditions of angled injection. Part 2.

Case	9A	10A	11A	12A	13A	14A	15A	16A
T_c (K)	285							
\bar{u}_c (m/s)	11	18	26	31	36	51	72	140
$Re_{D,c}$	300	472	667	817	952	1334	1889	3657
T_∞ (K)	287 - 283							
\bar{u}_∞ (m/s)	8.06 - 7.97							
Re_d	28500							
Re_z	110000							
I	1.96	4.88	9.76	14.6	20	39	79	296

F.2 Reactive PLIF boundary conditions

The injection conditions of the reactive experiments are presented in this section. Velocities and Reynolds numbers are calculated from the supplied mass flow rates and the geometry. As the MFCs provide information about the actual volume flow at normal conditions, measured temperature values from TC are used to account for the actual flow temperature.

Table F.4: Boundary conditions of the reactive normal experiments.

Fuel	H ₂					CH ₄					C ₃ H ₈				
$Re_{D,c}$	162	228	367	534	761	364	517	833	1192	1698	1032	1470	2375	3399	4848
\bar{u} (m/s)	45	62	96	135	187	16	22	34	48	66	11	16	24	34	48
I	0.9	1.8	4.3	8.6	16.8	0.9	1.8	4.4	8.7	16.9	1.3	2.6	6.5	13	25.4
\dot{m} (g/min)	0.22	0.3	0.48	0.68	0.96	0.61	0.86	1.37	1.94	2.73	1.27	1.79	2.83	4.02	5.67
															7.24

Table F.5: Boundary conditions of the reactive angled experiments.

Fuel	H ₂					CH ₄					C ₃ H ₈				
$Re_{D,c}$	122	166	267	385	540	27	374	601	851	1215	598	842	1344	1930	2748
\bar{u} (m/s)	50	68	107	153	210	16	23	37	52	73	9	13	21	29	40
I	1.1	2	5	10.2	19.6	1	1.9	4.9	9.7	19.3	0.9	1.8	4.4	8.7	17.2
\dot{m} (g/min)	0.12	0.16	0.26	0.38	0.53	0.33	0.47	0.75	1.05	1.5	0.54	0.76	1.21	1.71	2.41

F.3 Non-reactive PLIF results

F.3.1 Angled injection

As the orifice diameter was 0.4 mm and smaller than that of the normal injection, the resolution had a higher impact. Nevertheless, a quantitative description can still be given. The low and high momentum cases in the first and second graphs, respectively, show a concentration decrease to $\xi = 0.5$ at around $z/D = 20$, which is twice the distance as for normal jets. And between $z/D = 30$ to 40, the PMF peak approaches values of $\xi = 0.2$ - 0.3. Similarly to normal jets, there was no mainstream Re-number effects worth mentioning, as

seen on the last graph in Fig.F.1. As the mixed composition state is around $z/D = 40$, chemical reaction and auto-ignition might be expected in that downstream location and thus further downstream compared to the normal jet injections.

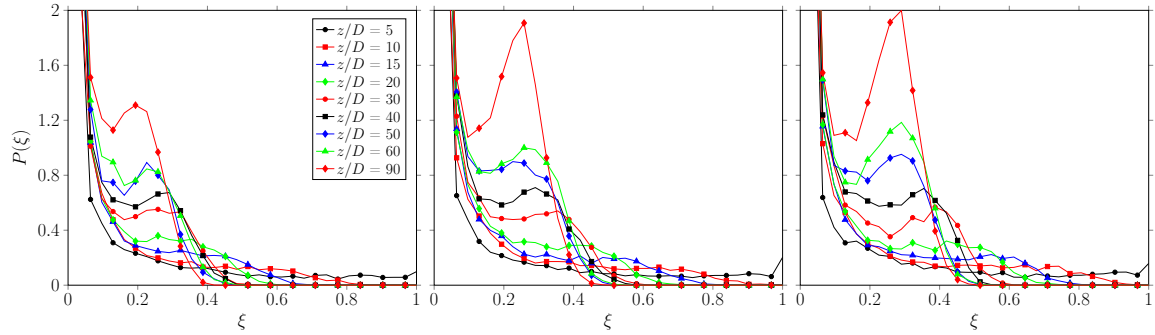


Figure F.1: Calculated PMF of angled injection for $I = 5$ (left) and 20 (center) at $Re_d = 28500$ and $I = 20$ (right) at $Re_d = 15400$. Data was divided into 32 bins.

F.4 CFD simulation

F.4.1 Normal injection

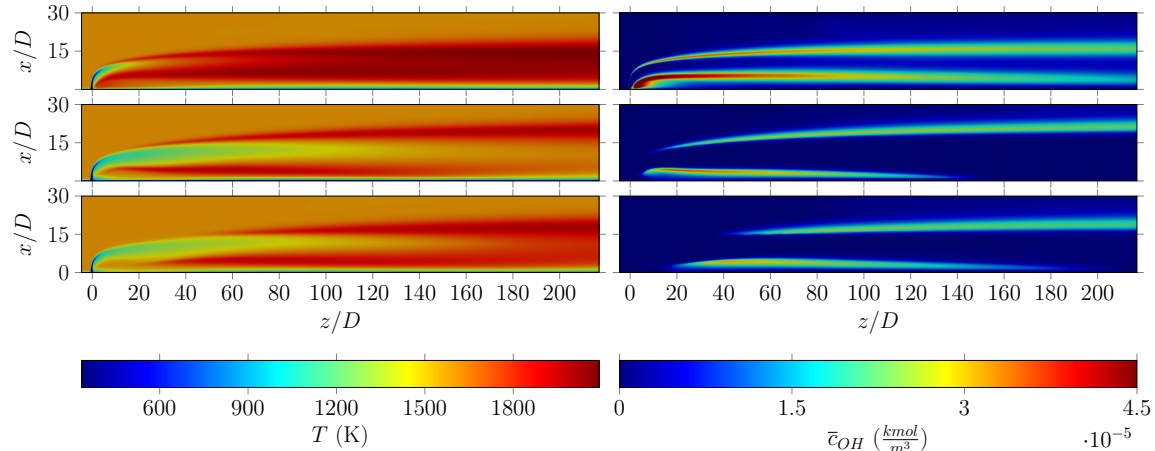


Figure F.2: CFD simulation results. Left: temperature. Right: OH molar concentration. Top row: H_2 . Center row: C_3H_8 . Bottom row: CH_4 . Main flow temperature 1570 K.

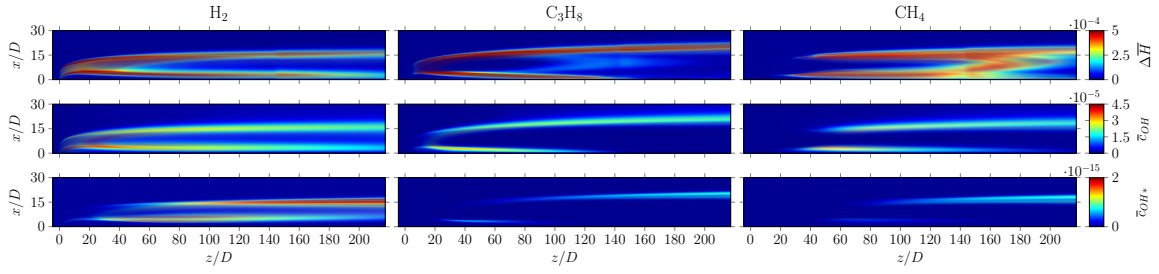


Figure F.3: Line-of-sight averaged CFD results. Top row: heat of reaction (W). Center row: OH molar concentration (kmol/m^3). Bottom row: OH^* molar concentration (kmol/m^3). Main flow temperature 1570 K.

F.4.2 Angled injection

Table F.6: CFD boundary conditions of angled injection cases.

Fuel	H ₂	CH ₄	C ₃ H ₈
T_c	374	365	345
\dot{m} (g/min)	0.24	0.66	1.02
I	10.2	9.7	8.7

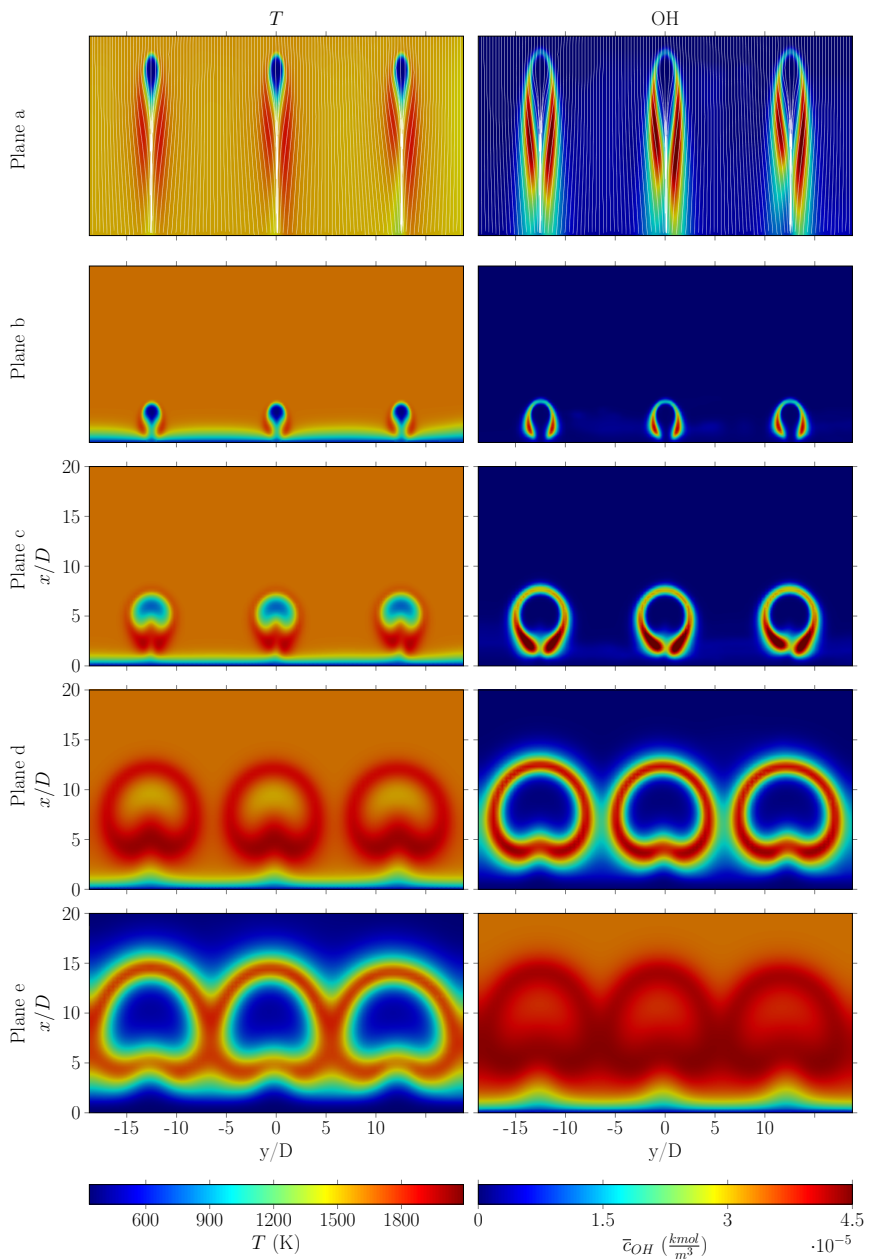


Figure F.4: H₂ simulation results of angled injection. Left: temperature. Right: OH molar concentration. Plane a contains velocity streamlines. Main flow temperature 1620 K.

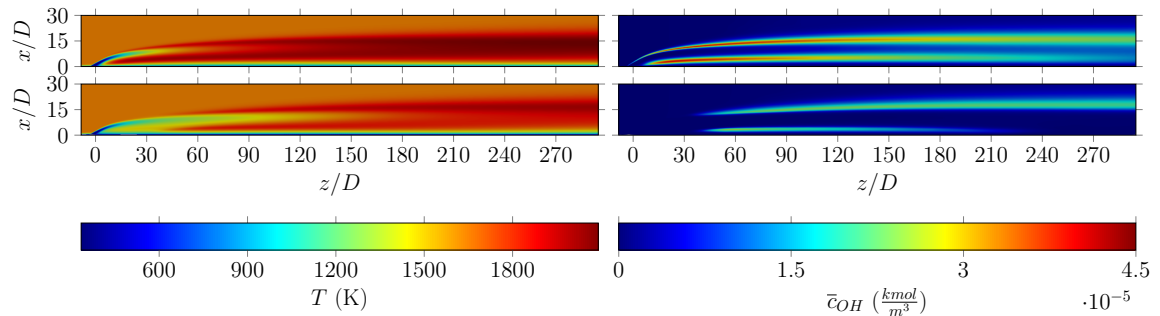


Figure F.5: CFD simulation results of angled injection. CFD simulation results. Left: temperature. Right: OH molar concentration. Top row: H_2 . Bottom row: CH_4 . Main flow temperature 1620 K.

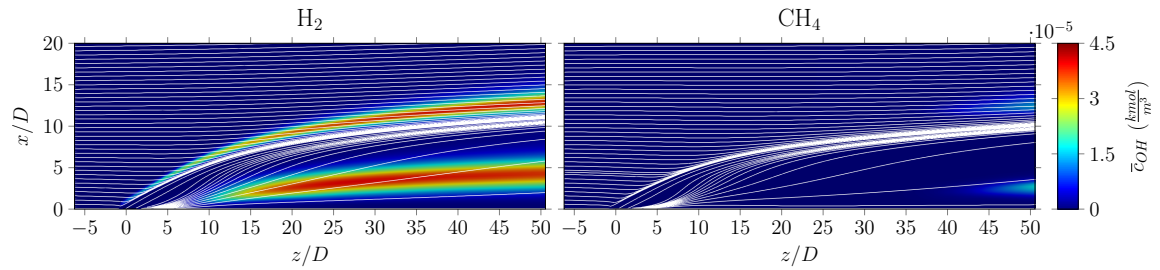


Figure F.6: Magnified views with added streamlines. Left: H_2 injection. Right: CH_4 injection.

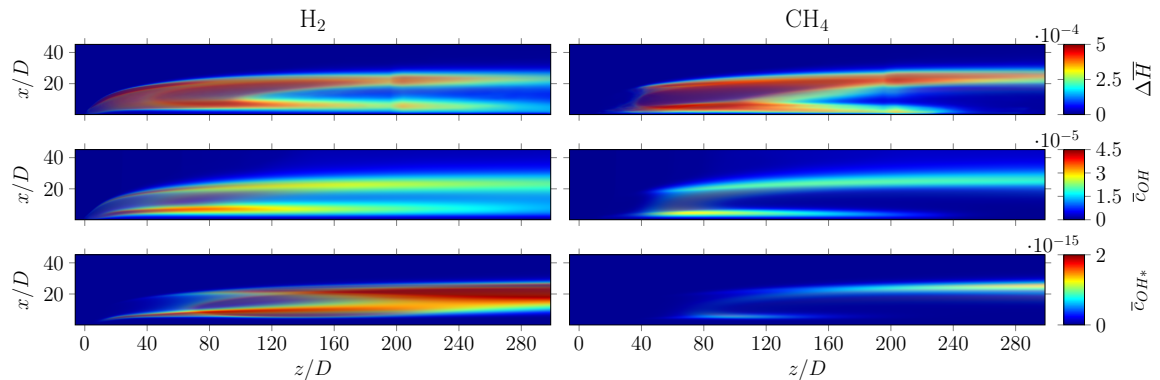


Figure F.7: Line-of-sight averaged CFD results of angled injection. Top row: heat of reaction (W). Center row: OH molar concentration (kmol/m^3). Bottom row: OH^* molar concentration (kmol/m^3). Main flow temperature 1620 K.

Appendix G

Additional Subjects

G.1 Radiation convection correction

The application of TC as an intrusive measurement technique in hot flows is subject to energy exchange with its environment. Considering (quasi-) steady-state flows, the thermal condition of the sensor is described by the equilibrium between heat convection from the flow to the sensor's surface and heat radiation and heat conduction from the sensor to the environment. Heat conduction is often neglected due to the small wire diameter relative to the sensor bead. However, the neglect here is justified as a sufficient length of the sensor is located within the hot environment and the heat loss of the sensor bead due to conduction is reduced. The energy balance equation is defined as follows:

$$h(T_h - T_{TC}) = \sigma \varepsilon (T_{TC}^4 - T_\infty^4) \quad (\text{G.1})$$

where subscripts h , TC and ∞ highlight hot flow, TC and solid environment properties, respectively. σ is the Stefan-Boltzmann constant and ε is the emissivity of the TC. ε depends on parameters such as surface characteristics, roughness and oxidation, material and to some extent on the temperature. Thus, suitable values are difficult to find in literature. As the wires of a type B TC consist largely of Platinum (70 % and 94 %), a temperature dependent emission coefficient for Platinum reported by Sato et al. [171] was used:

$$\varepsilon(T_{TC}) = 9.6 \cdot 10^{-5} T_{TC} + 0.056 \quad (\text{G.2})$$

The heat transfer coefficient h was determined from the relation:

$$h = Nu \frac{k}{D} \quad (\text{G.3})$$

where k is the thermal conductivity of the surrounding fluid and D is the sensor diameter. Various Nusselt correlations are reported in literature for different geometrical shapes (cylindrical, spherical, ...) and flow conditions (laminar, turbulent) [19, 53, 195]. For Re-numbers up to 10^6 the Gnielinski correlation based on the laminar and turbulent parts is proposed for spheres in literature [53, 195]:

$$Nu = 2 + \sqrt{Nu_{lam}^2 + Nu_t^2}; \quad Nu_{lam} = 0.644 Re_D^{1/2} Pr^{1/3}; \quad Nu_t = \frac{0.037 Re_D^{0.8} Pr}{1 + 2.443 Re_D^{-0.1} (Pr^{2/3} - 1)} \quad (\text{G.4})$$

where the flow properties are evaluated at the so-called film temperature T_f , calculated from the arithmetic average of the TC surface temperature and the flow temperature. As

the flow properties are a function of the unknown temperature, the radiation correction is solved iteratively.

The TC in this study were welded from two wires, each of the diameter 0.5 mm. The corresponding bead diameters were usually in the range of 1 - 1.5 mm. This means, that the ratio of bead diameter to wire diameter was in the range of 2 - 3. However, as the two wires were aligned from the same direction, the ratio reduced and the TC was rather of cylindrical than of spherical type. Especially at low Re-numbers, the deviations in the Nusselt number might be large. Hence, the Kramers Nusselt correlation for cylindrical geometries was used for these regimes [179]

$$Nu = 0.42Pr^{0.2} + 0.57Pr^{1/3}Re_D^{1/2} \quad (G.5)$$

which is valid for $0.01 < Re_D < 10^4$. Assuming $Pr = 0.72$, the Gnielinski and the Kramers correlation are plotted in Fig. G.1. As the $Re \rightarrow 0$, the Gnielinski correlation approaches 2, while the Kramers correlation approaches $0.42Pr^{0.2} = 0.393$ and is significantly lower. The higher the Re-number, the lower is the relative difference.

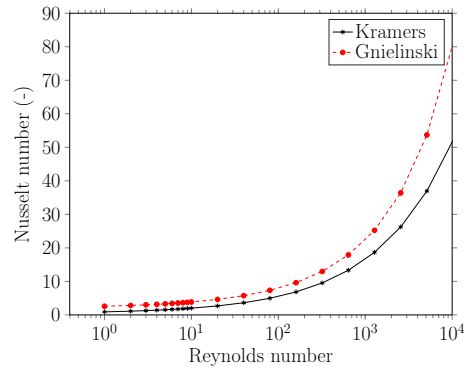


Figure G.1: Comparison of Nusselt correlations. $Pr = 0.72$.

The Reynolds number Re_D for the flow around the TC was around 100 - 200 for the reacting jet experiments and the calibration flame experiments.

G.2 Random error evaluation

To show the dependency of the random error on the number of averaged data, an intensity pair leading to a specific temperature corresponding to the calibration curve of $I_{ratio} = R_{22}(13)/P_{11}(22)$ was generated and each intensity line was superimposed with a zero-mean stochastic noise of 1000 K. Then, recalculating the temperature from n data points and calculating the standard deviation led to the curve in Fig. G.2, which matches to a $1/\sqrt{n}$ curve.

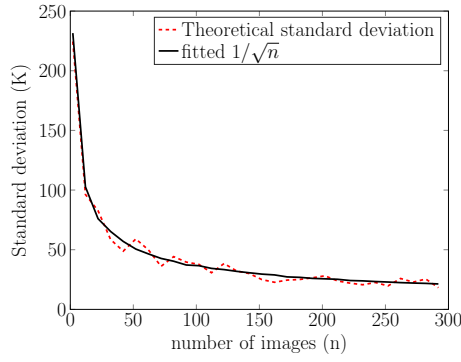


Figure G.2: Standard deviation depending on number of averaged data.

G.3 Light sheets

Fig. G.3 shows recorded and normalized laser light sheet profiles for the considered rotational lines. A profile describes the vertical laser intensity distribution which excites OH radical. As the lines $P_{11}(2)$, $R_{22}(13)$ and $Q_{11}(5)$ are spectrally close to each other, their profiles are almost equal. Whereas $Q_{11}(14)$ is located spectrally distanced from the other lines and its intensity distribution differs. This is attributed to mechanical properties of the dye laser.

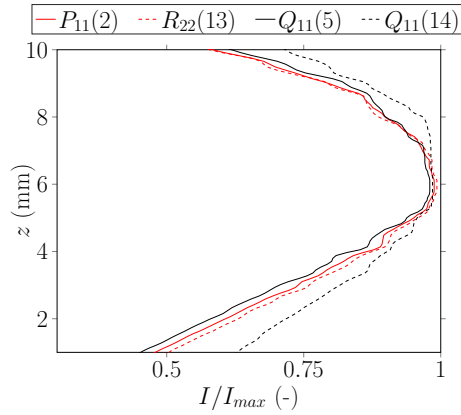


Figure G.3: Spatial light sheet distribution of different transitions.

Bibliography

- [1] Acetone. <https://webbook.nist.gov/cgi/cbook.cgi?ID=C67641&Mask=4&Type=ANTOINE&Plot=on>. Accessed: 2021-11-09.
- [2] Cantera. <https://cantera.org/>. Accessed: 2021-08-10.
- [3] CHEMKIN-PRO 15112, Reaction Design: San Diego, 2011.
- [4] EL-FLOW. <https://www.bronkhorst.com/de-de/produkte/gas-durchfluss/el-flow-select/>. Accessed: 2021-09-03.
- [5] Flat Flame Burners. <https://www.flatflame.com/>. Accessed: 2021-08-09.
- [6] Hastelloy[®] C-22[®] alloy. [www.haynesintl.com/alloys/alloy-portfolio/_Corrosion-resistant-Alloys/HASTELLOY-C-22/principal-features.aspx](http://haynesintl.com/alloys/alloy-portfolio/_Corrosion-resistant-Alloys/HASTELLOY-C-22/principal-features.aspx). Accessed: 2020-06-30.
- [7] Hastelloy[®] C-22[®] alloy. http://haynesintl.com/docs/default-source/pdfs/_new-alloy-brochures/corrosion-resistant-alloys/brochures/c-22-brochure.pdf?sfvrsn=f7929d4_24. Accessed: 2021-05-16.
- [8] Issendorff Thermoprozesstechnik e.K. <https://www.i-tpt.de/>. Accessed: 2020-11-23.
- [9] Hiroshi Akima. A New Method of Interpolation and Smooth Curve Fitting Based on Local Procedures. *J. ACM*, 17:589–602, 1970.
- [10] Dario Alviso, Miguel Mendieta, Jorge Molina, and Juan Carlos Rolón. Flame imaging reconstruction method using high resolution spectral data of OH*, CH* and C2* radicals. *International Journal of Thermal Sciences*, 121:228–236, 2017.
- [11] J. Andreopoulos and W. Rodi. Experimental investigation of jets in a crossflow. *Journal of Fluid Mechanics*, 138:93–127, 1984.
- [12] Ansys. Ansys. <https://www.ansys.com/>. Release: 2019R3, Accessed: 2021-11-15.
- [13] Ansys. Ansys Fluent, Fluid Simulation Software. www.ansys.com/de-de/products/fluids/ansys-fluent. Release: 2019R3, Accessed: 2021-11-15.
- [14] P. Atkins and J. de Paula. *Atkins' Physical Chemistry*. OUP Oxford, 2010.
- [15] P.W. Atkins, P.C.F.L.C.P. Atkins, V. Walters, and J. De Paula. *Physical Chemistry*. W. H. Freeman, 2006.

- [16] B.O. Ayoola, Ramanarayanan Balachandran, J.H. Frank, Epaminondas Mastorakos, and Clemens Kaminski. Spatially resolved heat release rate measurements in turbulent premixed flames. *Combustion and Flame*, 144:1–16, 01 2006.
- [17] S. Baldauf, M. Scheurlen, A. Schulz, and S. Wittig. Correlation of Film-Cooling Effectiveness From Thermographic Measurements at Enginelike Conditions . *Journal of Turbomachinery*, 124(4):686–698, 11 2002.
- [18] S. Baldauf, A. Schulz, and S. Wittig. High-Resolution Measurements of Local Heat Transfer Coefficients From Discrete Hole Film Cooling . *Journal of Turbomachinery*, 123(4):749–757, 02 1999.
- [19] Arindam Banerjee and Malcolm J. Andrews. A Convection Heat Transfer Correlation for a Binary Air-Helium Mixture at Low Reynolds Number. *Journal of Heat Transfer*, 129(11):1494–1505, 04 2007.
- [20] Frédérique Battin-Leclerc, John M. Simmie, and Edward Blurock, editors. *Cleaner Combustion*. Springer London, 2013.
- [21] J. H. Bechtel. Temperature measurements of the hydroxyl radical and molecular nitrogen in premixed, laminar flames by laser techniques. *Appl. Opt.*, 18(13):2100–2106, Jul 1979.
- [22] T.L. Bergman, F.P. Incropera, D.P. DeWitt, and A.S. Lavine. *Fundamentals of Heat and Mass Transfer*. Wiley, 2011.
- [23] Richard Bluemner, Myles D. Bohon, C. O. Paschereit, and E. Gutmark. Experimental Study of Reactant Mixing in Model Rotating Detonation Combustor Geometries. *Flow, Turbulence and Combustion*, 102:255–277, 2019.
- [24] David Blunck, Amy Lynch, Joseph Zelina, James Gord, Stanislav Kostka, Sukesh Roy, Marc Polanka, and Scott Stouffer. Flame Structure of Vitiated Fuel-Rich Inverse Diffusion Flames in a Cross-Flow (Postprint). In *7th US Combustion Meeting – Paper T05*, 01 2011.
- [25] D. G. Bogard and K. A. Thole. Gas Turbine Film Cooling. *Journal of Propulsion and Power*, 22(2):249–270, 2006.
- [26] Brian Bohan, David Blunck, Marc Polanka, Stanislav Kostka, Naibo Jiang, and Scott Stouffer. Impact of an Upstream Film-Cooling Row on Mitigation of Secondary Combustion in a Fuel Rich Environment. *Journal of Turbomachinery*, 136:031008, 09 2013.
- [27] Paola Breda and Michael Pfitzner. Delayed Detached Eddy Simulations with Tabulated Chemistry for Thermal Loads Predictions. *Journal of Propulsion and Power*, 37(1):29–46, 2021.
- [28] J. Broadwell and R. Breidenthal. A Simple Model of Mixing and Chemical Reaction in a Turbulent Shear Layer. *Journal of Fluid Mechanics*, 125:397 – 410, 12 1982.
- [29] J. E. Broadwell and R. E. Breidenthal. Structure and mixing of a transverse jet in incompressible flow. *Journal of Fluid Mechanics*, 148:405–412, 1984.

- [30] T. Cambonie, N. Gautier, and J.-L. Aider. Experimental study of counter-rotating vortex pair trajectories induced by a round jet in cross-flow at low velocity ratios. *Experiments in Fluids*, 54:1–13, February 2013.
- [31] Robert Cattolica. OH rotational temperature from two-line laser-excited fluorescence. *Appl. Opt.*, 20(7):1156–1166, Apr 1981.
- [32] Robert J. Cattolica. OH radical nonequilibrium in methane air flat flames. *Combustion and Flame*, 44(1):43 – 59, 1982.
- [33] N. T. Clemens and M. G. Mungal. Large-scale structure and entrainment in the supersonic mixing layer. *Journal of Fluid Mechanics*, 284:171–216, 1995.
- [34] Marcelo Colaco, Helcio Orlande, and George Dulikravich. Inverse and Optimisation Problems in Heat Transfer. *Journal of the Brazilian Society of Mechanical Sciences and Engineering*, XXVIII, 03 2006.
- [35] R. N. Compton and M. A. Duncan. *Laser Experiments for Chemistry and Physics*. Oxford University Press, 2016.
- [36] Colin Copeland, Jacob Friedman, and Metin Renksizbulut. Planar temperature imaging using thermally assisted laser induced fluorescence of OH in a methane-air flame. 2005. 2005 Combustion Institute/Canadian Section (CI/CS) Spring Technical Meeting ; Conference date: 15-05-2005 Through 18-05-2005.
- [37] The MARQUARDT CORPORATION. Thrust Chamber Cooling Techniques for Spacecraft Engines. Technical report, 1963.
- [38] J. Coxon. Optimum molecular constants and term values for the X₂Π (v ≤5) and A₂Σ (v≤3) states of OH. *Canadian Journal of Physics*, 58:933–949, 02 2011.
- [39] Rahand Dalshad, Tobias Sander, and Michael Pfitzner. Characterization of a Newly Designed Test Bench for Investigations of Flame-Wall-Interaction. volume 3A: Combustion, Fuels, and Emissions of *Turbo Expo: Power for Land, Sea, and Air*, 06 2021. V03AT04A043.
- [40] Rahand Dalshad, Tobias Sander, and Michael Pfitzner. Characterization of a Newly Designed Test Bench for Investigations of Flame–Wall Interaction . *Journal of Engineering for Gas Turbines and Power*, 144(4), 01 2022. 041006.
- [41] D.F. Davidson, M. Roehrig, E.L. Petersen, M.D. Di Rosa, and R.K. Hanson. Measurements of the OH A-X (0,0) 306 nm absorption bandhead at 60 atm and 1735 K. *Journal of Quantitative Spectroscopy and Radiative Transfer*, 55(6):755 – 762, 1996.
- [42] J. de Vries and E.L. Petersen. Autoignition of methane-based fuel blends under gas turbine conditions. *Proceedings of the Combustion Institute*, 31(2):3163 – 3171, 2007.
- [43] Michael R. DeLallo, Marc D. Polanka, and David L. Blunck. Impact of Trench and Ramp Film Cooling Designs to Reduce Heat Release Effects in a Reacting Flow. volume Volume 4: Heat Transfer, Parts A and B of *Turbo Expo: Power for Land, Sea, and Air*, pages 927–936, 06 2012.

- [44] W. Demtröder. *Laserspektroskopie 1*. SpringerLink : Bücher. Springer Berlin Heidelberg, 2011.
- [45] W. Demtröder. *Laserspektroskopie 2: Experimentelle Techniken*. SpringerLink : Bücher. Springer Berlin Heidelberg, 2013.
- [46] W. Demtröder. *Molekülphysik: Theoretische Grundlagen und experimentelle Methoden*. Oldenbourg Wissenschaftsverlag, 2013.
- [47] R. Devillers, G. Bruneaux, and C. Schulz. Development of a two-line OH-laser-induced fluorescence thermometry diagnostics strategy for gas-phase temperature measurements in engines. *Appl. Opt.*, 47(31):5871–5885, Nov 2008.
- [48] G.H. Dieke and H.M. Crosswhite. The ultraviolet bands of OH Fundamental data. *Journal of Quantitative Spectroscopy and Radiative Transfer*, 2(2):97 – 199, 1962.
- [49] Paul E. Dimotakis. The mixing transition in turbulent flows. *Journal of Fluid Mechanics*, 409:69–98, 2000.
- [50] A.C. Eckbreth. *Laser Diagnostics for Combustion Temperature and Species*. Combustion science and technology book series. Taylor & Francis, 1996.
- [51] Christoph Eichhorn. *Über die Mehr-Photonen-Spektroskopie an Xenon zur plasma-diagnostischen Untersuchung elektrischer Weltraumantriebe*. PhD thesis, Universität Stuttgart, 2014.
- [52] L. El-Gabry, Douglas R. Thurman, and Philip E. Poinsatte. Procedure for Determining Turbulence Length Scales Using Hotwire Anemometry. National Aeronautics and Space Administration, December 2014. NASA/TM—2014-218403.
- [53] N. Ellendt, A.M. Lumanglas, S. Imani Moqadam, and L. Mädler. A model for the drag and heat transfer of spheres in the laminar regime at high temperature differences. *International Journal of Thermal Sciences*, 133:98–105, 2018.
- [54] Dave Evans, Paul King, Marc Polanka, Joe Zelina, Wesly Anderson, and Scott Stouffer. Impact of Heat Release in Turbine Film Cooling. In *47th AIAA Aerospace Sciences Meeting including The New Horizons Forum and Aerospace Exposition*, 2009.
- [55] Dave S. Evans. The Impact of Heat Release in Turbine Film Cooling. Master’s thesis, Air Force Institute of Technology, June 2008. AFIT/GAE/ENY/08-J02.
- [56] G. Fast, D. Kuhn, A.G. Class, and U. Maas. Auto-ignition during instationary jet evolution of dimethyl ether (DME) in a high-pressure atmosphere. *Combustion and Flame*, 156(1):200 – 213, 2009.
- [57] Richard Fearn and Robert P. Weston. Vorticity Associated with a Jet in a Cross Flow. *AIAA Journal*, 12(12):1666–1671, 1974.
- [58] Andreas J. C. Fenner. *Two-Color/Two-Dye Planar Laser-Induced Fluorescence Thermography for Temperature Measurements at an Evaporating Meniscus*. PhD thesis, Technische Universität, Darmstadt, 2017.

- [59] Thomas Fiala. *Radiation from High Pressure Hydrogen–Oxygen Flames and its Use in Assessing Rocket Combustion Instability*. Dissertation, Technische Universität München, München, 2015.
- [60] Thomas G. S. Fiala and Thomas Sattelmayer. Heat release and UV–Vis radiation in non-premixed hydrogen–oxygen flames. *Experiments in Fluids*, 56:1–15, 2015.
- [61] Lukas Fischer, Paola Breda, Rahand Dalshad, and Michael Pfitzner. Numerical characterization of a novel test bench featuring secondary reactions of methane. *Aerospace Science and Technology*, 119:107203, 2021.
- [62] Lukas Fischer, Michael Straußwald, and Michael Pfitzner. Analysis of LES and 1D Hot-Wire Data to Determine Actively Generated Main Flow Turbulence in a Film Cooling Test Rig. volume Volume 5A: Heat Transfer — Combustors; Film Cooling of *Turbo Expo: Power for Land, Sea, and Air*, 06 2021.
- [63] Julia Fleck, Peter Griebel, Adam Steinberg, Christoph Arndt, Clemens Naumann, and Manfred Aigner. Autoignition of hydrogen/nitrogen jets in vitiated air crossflows at different pressures. *Proceedings of the Combustion Institute*, 34:3185–3192, 12 2013.
- [64] N. W. Foster and D. Lampard. The Flow and Film Cooling Effectiveness Following Injection through a Row of Holes. *Journal of Engineering for Power*, 102:584–588, 07 1980.
- [65] T. F. Fric and A. Roshko. Vortical structure in the wake of a transverse jet. *Journal of Fluid Mechanics*, 279:1–47, 1994.
- [66] Mirko Gamba and M. Godfrey Mungal. Ignition, flame structure and near-wall burning in transverse hydrogen jets in supersonic crossflow. *Journal of Fluid Mechanics*, 780:226–273, 2015.
- [67] A. Gaydon. *The Spectroscopy of Flames*. Springer Netherlands, 1974.
- [68] Josef Gerold. *Experimentelle und numerische Untersuchung von Gas-Freistrahlen*. PhD thesis, Universität der Bundeswehr München, 2015.
- [69] L. Gevorkyan, T. Shoji, D. R. Getsinger, O. I. Smith, and A. R. Karagozian. Transverse jet mixing characteristics. *Journal of Fluid Mechanics*, 790:237–274, 2016.
- [70] Tomasz Gierczak, James B. Burkholder, Stefan Bauerle, and A. R. Ravishankara. Photochemistry of acetone under tropospheric conditions. *Chemical Physics*, 231(2):229–244, June 1998.
- [71] R. Giezendanner-Thoben. *Untersuchung von Verbrennungsinstabilitäten mit phasenkorrelierten Lasermesstechniken*. PhD thesis, Universität Stuttgart, 2006.
- [72] Robert Giezendanner-Thoben, Ulrich Meier, Wolfgang Meier, Johannes Heinze, and Manfred Aigner. Phase-locked two-line OH planar laser-induced fluorescence thermometry in a pulsating gas turbine model combustor at atmospheric pressure. *Appl. Opt.*, 44(31):6565–6577, Nov 2005.

- [73] J. J. Girard, S. Clees, and R. K. Hanson. Collisional broadening and shift of five OH $A^2\Sigma^+ \leftarrow X^2\Pi$ (0-0) transitions in the Q₁-branch, by H₂O, O₂, CO₂, N₂ and Ar, at 1220 K. *Journal of Quantitative Spectroscopy and Radiative Transfer*, 240:106681, January 2020.
- [74] S. G. Goebel, N. Abuaf, J. A. Lovett, and C.-P. Lee. Measurements of Combustor Velocity and Turbulence Profiles. volume Volume 3A: General of *Turbo Expo: Power for Land, Sea, and Air*, 05 1993.
- [75] R. J. Goldstein, K. Y. Lau, and C. C. Leung. Velocity and turbulence measurements in combustion systems. *Experiments in Fluids*, 1:93–99, June 1983.
- [76] Richard J. Goldstein. Film Cooling. volume 7 of *Advances in Heat Transfer*, pages 321–379. Elsevier, 1971.
- [77] Michael Gritsch, Will Colban, Heinz Schär, and Klaus Döbbeling. Effect of Hole Geometry on the Thermal Performance of Fan-Shaped Film Cooling Holes. *Journal of Turbomachinery*, 127:718–725, 04 2005.
- [78] Joanna Grzelak and Zygmunt Wiercinski. Length scale of free stream turbulence and its impact on bypass transition in a boundary layer. 10:713–724, 01 2017.
- [79] Jonas Gustavsson and Corin Segal. Characterization of a perfluorinated ketone for LIF applications. In *46th AIAA Aerospace Sciences Meeting and Exhibit*, page 259, 2008.
- [80] Jonas P.R. Gustavsson and Corin Segal. Fluorescence Spectrum of 2-Trifluoromethyl-1,1,1,2,4,4,5,5,5-nonafluoro-3-pentanone. *Appl. Spectrosc.*, 61(8):903–907, Aug 2007.
- [81] Effie Gutmark, Irene Ibrahim, and Shanmugam Murugappan. Circular and noncircular subsonic jets in cross flow. *Physics of Fluids*, 20, 07 2008.
- [82] H. Haken and H.C. Wolf. *Molekülphysik und Quantenchemie: Einführung in die experimentellen und theoretischen Grundlagen*. Springer-Lehrbuch. Springer Berlin Heidelberg, 2006.
- [83] HAMAMATSU. HIGH-SPEED GATED IMAGE INTENSIFIER UNIT. https://www.hamamatsu.com/resources/pdf/etd/GateII_TII0006E.pdf. accessed: 06.10.2021.
- [84] Stephen Hammack, Campbell Carter, Clemens Wuensche, and Tonghun Lee. Continuous hydroxyl radical planar laser imaging at 50 kHz repetition rate. *Appl. Opt.*, 53(23):5246–5251, Aug 2014.
- [85] R.K. Hanson, R.M. Spearrin, and C.S. Goldenstein. *Spectroscopy and Optical Diagnostics for Gases*. Springer International Publishing, 2015.
- [86] M. Hari. *Free Radical OH: A Molecule of Astrophysical and Aeronomics Interest*. NASA SP. Scientific and Technical Information Office, National Aeronautics and Space Administration, 1975.
- [87] E. F. Hasselbrink and M. G. Mungal. Transverse jets and jet flames. Part 2. Velocity and OH field imaging. *Journal of Fluid Mechanics*, 443:27–68, 2001.

- [88] Ernest F. Hasselbrink and M. G. Mungal. Transverse jets and jet flames. Part 1. Scaling laws for strong transverse jets. *Journal of Fluid Mechanics*, 443:1–25, 2001.
- [89] Lei He, Qinghua Guo, Yan Gong, Fuchen Wang, and Guang suo Yu. Investigation of OH* chemiluminescence and heat release in laminar methane–oxygen co-flow diffusion flames. *Combustion and Flame*, 201:12–22, 2019.
- [90] Johannes Heinze, Ulrich Meier, Thomas Behrendt, Chris Willert, Klaus-Peter Geigle, Oliver Lammel, and Rainer Lückerath. PLIF Thermometry Based on Measurements of Absolute Concentrations of the OH Radical. *Zeitschrift für Physikalische Chemie*, 225(11-12):1315 – 1341, 01 Dec. 2011.
- [91] Jens Hermann. *Laseroptische Untersuchung der Flamme-Kühlluft-Interaktion in einer effusionsgekühlten Brennkammer*. PhD thesis, Technische Universität, Darmstadt, 2017.
- [92] I.V. Hertel and C.P. Schulz. *Atome, Moleküle Und Optische Physik 2 Moleküle Und Photonen - Spektroskopie Und Streuphysik*. Atome, Moleküle und optische Physik. Springer Berlin Heidelberg, 2010.
- [93] I.V. Hertel and C.P. Schulz. *Atome, Moleküle und optische Physik 1: Atomphysik und Grundlagen der Spektroskopie*. Springer-Lehrbuch. Springer Berlin Heidelberg, 2015.
- [94] H. M Hertz and Marcus Aldén. Calibration of Imaging Laser-induced Fluorescence Measurements In Highly Absorbing Flames. *Applied Physics B: Photophysics and Laser Chemistry*, 42(2):97–102, 1987.
- [95] G. Herzberg. *The Spectra and Structures of Simple Free Radicals: An Introduction to Molecular Spectroscopy*. Dover Books on Chemistry Series. Dover Publications, 1988.
- [96] G. Herzberg. *Molecular Spectra and Molecular Structure Vol 1*. Number Bd. 1. Read Books, 2008.
- [97] G. Herzberg, J.W.T. Spinks, and K.P. Huber. *Molecular Spectra and Molecular Structure: Electronic spectra and electronic structure of polyatomic molecules*. Electronic Spectra & Electronic Structure of Polyatomic Mole. Van Nostrand, 1950.
- [98] M. M. Holton, P. Gokulakrishnan, M. S. Klassen, R. J. Roby, and G. S. Jackson. Autoignition Delay Time Measurements of Methane, Ethane, and Propane Pure Fuels and Methane-Based Fuel Blends. *Journal of Engineering for Gas Turbines and Power*, 132(9), 06 2010. 091502.
- [99] Marcus Hultmark and Alexander J Smits. Temperature corrections for constant temperature and constant current hot-wire anemometers. *Measurement Science and Technology*, 21(10):105404, aug 2010.
- [100] F. Joos. *Technische Verbrennung: Verbrennungstechnik, Verbrennungsmodellierung, Emissionen*. Springer Berlin Heidelberg, 2006.
- [101] Yasuhiro Kamotani and Isaac Greber. Experiments on a Turbulent Jet in a Cross Flow. *AIAA Journal*, 10(11):1425–1429, 1972.

- [102] Ann R. Karagozian. Transverse jets and their control. *Progress in Energy and Combustion Science*, 36(5):531–553, 2010.
- [103] P. S. Karasso and M. G. Mungal. Scalar mixing and reaction in plane liquid shear layers. *Journal of Fluid Mechanics*, 323:23–63, 1996.
- [104] V. Kasyutich. Pressure broadening parameters of the hydroxyl radical $A2\Sigma$ ($v' = 0$) $\leftarrow X 2\Pi\ 3/2$ (v'') transitions at ca. 308 nm. *Eur. Phys. J. D*, 33:29–33, 04 2005.
- [105] Viswanath Katta, David Blunck, Naibo Jiang, Amy Lynch, James Gord, and Sukesh Roy. On flames established with air jet in cross flow of fuel-rich combustion products. *Fuel*, 150, 06 2015.
- [106] W.M. Kays and M.E. Crawford. *Convective Heat and Mass Transfer*. McGraw-Hill series in mechanical engineering. McGraw-Hill, 1993.
- [107] Robert J Kee, Michael E Coltrin, Peter Glarborg, and Huayang Zhu. *Chemically Reacting Flow*. Wiley, 09 2017.
- [108] R. M. Kelso, T. T. Lim, and A. E. Perry. An experimental study of round jets in cross-flow. *Journal of Fluid Mechanics*, 306:111–144, 1996.
- [109] W.J. Kessler, M.G. Allen, and S.J. Davis. Rotational level-dependent collisional broadening and line shift of the $A2\Sigma$ $X2\Pi$ (1, 0) band of OH in hydrogen-air combustion gases. *Journal of Quantitative Spectroscopy and Radiative Transfer*, 49(2):107 – 117, 1993.
- [110] D. R. Kirk, G. R. Guenette, S. P. Lukachko, and I. A. Waitz. Gas Turbine Engine Durability Impacts of High Fuel-Air Ratio Combustors—Part II: Near-Wall Reaction Effects on Film-Cooled Heat Transfer. *Journal of Engineering for Gas Turbines and Power*, 125(3):751–759, 08 2003.
- [111] Marco Kirschner. *Laserinduzierte Fluoreszenzspektroskopie von Molekülen in einem Hochenthalpie-Freistrahl zur Bestimmung der Rotationstemperatur*. PhD thesis, Universität der Bundeswehr München, 2017.
- [112] Andreas Koch. *Experimentelle Untersuchung und Analyse zum Einfluss der Brennstoffzusammensetzung auf das Zündverhalten von gasturbinen-typischen Vormischbrennern*. PhD thesis, Universität Stuttgart, 2009.
- [113] M. Koochesfahani and P. Dimotakis. Mixing and chemical reactions in a turbulent liquid mixing layer. *Journal of Fluid Mechanics*, 170:83–112, 1986.
- [114] Stanislav Kostka, David Blunck, Naibo Jiang, Amy Lynch, M. Polanka, S. Stouffer, J.R. Gord, and S. Roy. Temperature of inverse diffusion flames in a vitiated cross-flow using two-color PLIF thermometry. In *Fall Technical Meeting of the Eastern States Section of the Combustion Institute Hosted by the University of Connecticut, Storrs, CT Oct 9-12, 2011*, pages 637–647, 01 2011.
- [115] Stanislav Kostka, Sukesh Roy, Patrick J. Lakusta, Terrence R. Meyer, Michael W. Renfro, James R. Gord, and Richard Branam. Comparison of line-peak and line-scanning excitation in two-color laser-induced-fluorescence thermometry of OH. *Appl. Opt.*, 48(32):6332–6343, Nov 2009.

- [116] Charlie Koupper, Gicquel L.Y.M., Florent Duchaine, Tommaso Bacci, Bruno Facchini, Alessio Picchi, Lorenzo Tarchi, and Guillaume Bonneau. Experimental And Numerical Calculation Of Turbulent Timescales At The Exit Of An Engine Representative Combustor Simulator. *Journal of Engineering for Gas Turbines and Power*, 138, 02 2016.
- [117] Dietmar Kuhn. *Messung von Temperatur- und Konzentrationsprofilen mittels Laserinduzierter Fluoreszenz (LIF)*. PhD thesis, 2001. 11.02.06; LK 01; Karlsruhe 2001. (Wissenschaftliche Berichte. FZKA. 6685.) Fak. f. Maschinenbau, Diss. v. 17.7.2001.
- [118] Ryno Laubscher. *Utilization of artificial neural networks to resolve chemical kinetics in turbulent fine structures of an advanced CFD combustion model*. PhD thesis, Stellenbosch University, 2017.
- [119] M Lauer and Thomas Sattelmayer. Determination of turbulent flame temperature from vibrationally resolved OH* chemiluminescence measurements. January 2009. Technische Universität München.
- [120] M Lauer and Thomas Sattelmayer. On the utilization of OH* chemiluminescence as a measure for local heat release in turbulent flames. January 2011. Technische Universität München.
- [121] Chung K. Law. *Combustion Physics*. Cambridge University Press, 2006.
- [122] A. H. Lefebvre and D. R. Ballal. *Gas Turbine Combustion: Alternative Fuels and Emissions, Third Edition*. Taylor & Francis, 2010.
- [123] Michał T. Lewandowski and Ivar S. Ertesvåg. Analysis of the Eddy Dissipation Concept formulation for MILD combustion modelling. *Fuel*, 224:687–700, 2018.
- [124] COMSOL Multiphysics® v. 5.5. LiveLink for Matlab. COMSOL AB, Stockholm, Sweden. www.comsol.com.
- [125] Eva-Maria Loew. *Analyse von Verbrennungsvorgängen im selbstzündungsdominierten Regime mittels Mischungsstatistik*. Dissertation, Technische Universität München, München, 2016.
- [126] Antonio Lozano, Brandon Yip, and Ronald K. Hanson. Acetone: a tracer for concentration measurements in gaseous flows by planar laser-induced fluorescence. *Experiments in Fluids*, 13:369–376, 1992.
- [127] Tianfeng Lu and Chung K. Law. A directed relation graph method for mechanism reduction. *Proceedings of the Combustion Institute*, 30(1):1333–1341, 2005.
- [128] S. P. Lukachko, D. R. Kirk, and I. A. Waitz. Gas Turbine Engine Durability Impacts of High Fuel-Air Ratio Combustors-Part I: Potential for Secondary Combustion of Partially Reacted Fuel . *Journal of Engineering for Gas Turbines and Power*, 125(3):742–750, 08 2003.
- [129] J. Luque and D. Crosley. LIFbase: Database and Spectral Simulation. <https://www.sri.com/case-studies/lifbase-spectroscopy-tool/>, 1999.

- [130] Jorge Luque and David R. Crosley. Transition probabilities in the A $2\Sigma^+ \leftarrow$ X 2Π electronic system of OH. *The Journal of Chemical Physics*, 109(2):439–448, 1998.
- [131] E. Lutum and B. V. Johnson. Influence of the Hole Length-to-Diameter Ratio on Film Cooling With Cylindrical Holes. *Journal of Turbomachinery*, 121:209–216, 04 1999.
- [132] Kenji Maeda, Michael L Wall, and Lincoln D Carr. Hyperfine structure of the hydroxyl free radical (OH) in electric and magnetic fields. *New Journal of Physics*, 17(4):045014, apr 2015.
- [133] Bjørn F. Magnussen. The eddy dissipation concept a bridge between science and technology. In *ECCOMAS Thematic Conference on Computational Combustion*, Lison, Portugal, 2005.
- [134] Krishnan Mahesh. The Interaction of Jets with Crossflow. *Annual Review of Fluid Mechanics*, 45:379–407, 2013.
- [135] Quentin Malé and CERFACS. C3H8_37_129_QM skeletal mechanism. https://chemistry.cerfacs.fr/en/chemical-database/mechanisms-list/c3h8_37_129_qm-skeletal-mechanism/. accessed: 20.09.2021.
- [136] R.J. Margason, United States. National Aeronautics, Space Administration, and Langley Research Center. *The Path of a Jet Directed at Large Angles to a Subsonic Free Stream*. NASA technical note. National Aeronautics and Space Administration, 1968.
- [137] Epaminondas Mastorakos. Ignition of turbulent non-premixed flames. *Progress in Energy and Combustion Science*, 35(1):57–97, 2009.
- [138] MATLAB. *version 9.7.0 (R2019b)*. The MathWorks Inc., Natick, Massachusetts, 2019.
- [139] Daniel J. Micka and James F. Driscoll. Stratified jet flames in a heated (1390K) air cross-flow with autoignition. *Combustion and Flame*, 159:1205–1214, 2012.
- [140] D. W. Milanes, D. Kirk, K. Fidkowski, and I. Waitz. Gas Turbine Engine Durability Impacts of High-Fuel-Air Ratio Combustors: Near Wall Reaction Effects on Film-Cooled Backward-Facing Step Heat Transfer. *Journal of Engineering for Gas Turbines and Power-transactions of The ASME*, 128:318–325, 2003.
- [141] Robert S. Mulliken and Andrew Christy. Λ-Type Doubling and Electron Configurations in Diatomic Molecules. *Phys. Rev.*, 38:87–119, Jul 1931.
- [142] M. G. Mungal and P. E. Dimotakis. Mixing and combustion with low heat release in a turbulent shear layer. *Journal of Fluid Mechanics*, 148:349–382, November 1984.
- [143] Suman Muppidi and Krishnan Mahesh. Study of trajectories of jets in crossflow using direct numerical simulations. *Journal of Fluid Mechanics*, 530:81–100, 2005.
- [144] Suman Muppidi and Krishnan Mahesh. Direct numerical simulation of passive scalar transport in transverse jets. *Journal of Fluid Mechanics*, 598:335–360, January 2008.
- [145] G.F. Naterer. *Advanced Heat Transfer*. CRC Press, 2018.

- [146] T. H. New, T. T. Lim, and S. C. Luo. Effects of jet velocity profiles on a round jet in cross-flow. *Experiments in Fluids*, 40:859–875, June 2006.
- [147] Tim Nielsen. *Zitaufgelöste Laserspektroskopie*. PhD thesis, Bielefeld University, 1999.
- [148] W. Nitsche and A. Brunn. *Strömungsmesstechnik*. VDI-Buch. Springer, 2006.
- [149] Venkata Nori and Jerry Seitzman. Chemiluminescence Measurements and Modeling in Syngas, Methane and Jet-A Fueled Combustors. volume 8, 01 2007.
- [150] Venkata Narasimham Nori. *Modeling and analysis of chemiluminescence sensing for syngas, methane and jet-A combustion*. PhD thesis, Georgia Institute of Technology, August 2008.
- [151] Kei Okamoto. *Optimal numerical methods for inverse heat conduction and inverse design solidification problems*. PhD thesis, Washington State University, December 2005.
- [152] M. N. Ozisik. *Inverse Heat Transfer: Fundamentals and Applications*. Taylor & Francis, 2000.
- [153] Gregory P. Smith, David M. Golden, Michael Frenklach, Nigel W. Moriarty, Boris Eiteneer, Mikhail Goldenberg, C. Thomas Bowman, Ronald K. Hanson, Soonho Song, William Jr. C. Gardiner, Vitali V. Lissianski, and Zhiwei Qin. GRI-Mech. <http://combustion.berkeley.edu/gri-mech/>. accessed: 06.09.2021.
- [154] Yulia V. Peet. *Film cooling from inclined cylindrical holes using large eddy simulations*. PhD thesis, Stanford University, 2006.
- [155] Nikolaos Perakis and Oskar J. Haidn. Inverse heat transfer method applied to capacitively cooled rocket thrust chambers. *International Journal of Heat and Mass Transfer*, 131:150–166, 2019.
- [156] Eric L. Petersen, Danielle M. Kalitan, Stefanie Simmons, Gilles Bourque, Henry J. Curran, and John M. Simmie. Methane/propane oxidation at high pressures: Experimental and detailed chemical kinetic modeling. *Proceedings of the Combustion Institute*, 31(1):447 – 454, 2007.
- [157] Michael Pfitzner. Wärme- und Stoffübertragung. Vorlesungsfolien, Universität der Bundeswehr München, Institut für Thermodynamik, Werner-Heisenberg-Weg 39, 85577, Deutschland, September 2020.
- [158] Stephanie Pohl, Gabriele Frank, and Michael Pfitzner. Heat Transfer in Reacting Cooling Films: Influence and Validation of Combustion Modeling in Numerical Simulations. *Journal of Turbomachinery*, 137(8), 08 2015. 081003.
- [159] T. Poinsot and D. Veynante. *Theoretical and Numerical Combustion*. Edwards, 2005.
- [160] Marc D. Polanka, Joseph Zelina, Wesly S. Anderson, Balu Sekar, Dave S. Evans, Cheng-Xian Lin, and Scott D. Stouffer. Heat Release in Turbine Cooling I: Experimental and Computational Comparison of Three Geometries. *Journal of Propulsion and Power*, 27(2):257–268, 2011.

- [161] Stephen B. Pope. *Turbulent Flows*. Cambridge University Press, 2000.
- [162] James S. Porter. *Influence of Inlet Flow Configuration on the Flow Field Within and Around a Fan-Shaped Film Cooling Hole*. PhD thesis, University of Tasmania, 2010.
- [163] B. D. Pratte and W. Baines. Profiles of the Round Turbulent Jet in A Cross Flow. *Journal of Hydraulic Engineering*, 93:53–64, 1967.
- [164] William H. Press and Saul A. Teukolsky. Savitzky-Golay Smoothing Filters. *Computers in Physics*, 4(6):669–672, 1990.
- [165] E.C. Rea, A.Y. Chang, and R.K. Hanson. Shock-tube study of pressure broadening of the $A2\Sigma \leftarrow X2\Pi$ (0,0) band of OH by Ar and N₂. *Journal of Quantitative Spectroscopy and Radiative Transfer*, 37(2):117 – 127, 1987.
- [166] E.C. Rea, A.Y. Chang, and R.K. Hanson. Collisional broadening of the $A2\Sigma \leftarrow X2\Pi$ (0,0) band of OH by H₂O and CO₂ in atmospheric-pressure flames. *Journal of Quantitative Spectroscopy and Radiative Transfer*, 41(1):29 – 42, 1989.
- [167] Daniel R. Richardson, Naibo Jiang, David L. Blunck, James R. Gord, and Sukesh Roy. Characterization of inverse diffusion flames in vitiated cross flows via two-photon planar laser-induced fluorescence of CO and 2-D thermometry. *Combustion and Flame*, 168:270 – 285, 2016.
- [168] Daniel R. Richardson, Naibo Jiang, Andrew W. Caswell, Sukesh Roy, David L. Blunck, Amy Lynch, and James R. Gord. Characterization of Inverse Diffusion Flames in High Temperature Cross-flow. In *52nd Aerospace Sciences Meeting*.
- [169] P.E. Roach. The generation of nearly isotropic turbulence by means of grids. *International Journal of Heat and Fluid Flow*, 8(2):82–92, 1987.
- [170] Arnab Roy, Jonas PR Gustavsson, and Corin Segal. Spectroscopic properties of a perfluorinated ketone for PLIF applications. *Experiments in fluids*, 51(5):1455–1463, 2011.
- [171] A. Sato, K. Hashiba, M. Hasatani, S. Sugiyama, and J. Kimura. A correctional calculation method for thermocouple measurements of temperatures in flames. *Combustion and Flame*, 24:35 – 41, 1975.
- [172] H. Schlichting and J. Kestin. *Boundary-layer Theory*. McGraw-Hill classic textbook reissue series. McGraw-Hill, 1979.
- [173] Christof Schulz and Volker Sick. Tracer-LIF diagnostics: quantitative measurement of fuel concentration, temperature and fuel/air ratio in practical combustion systems. *Progress in Energy and Combustion Science*, 31(1):75–121, 2005.
- [174] Florian Seffrin. *Geschwindigkeits- und Skalarfeld-Charakterisierung turbulenter stratifizierter Vormischflammen*. tuprints, Darmstadt, Februar 2011. Druckausg.: Göttingen, Cuvillier, 2011. - ISBN 978-3-86955-649-9.
- [175] J. M. Seitzman, R. K. Hanson, P. A. DeBarber, and C. F. Hess. Application of quantitative two-line OH planar laser-induced fluorescence for temporally resolved planar thermometry in reacting flows. *Appl. Opt.*, 33(18):4000–4012, Jun 1994.

- [176] Jerry M. Seitzman and Ronald K. Hanson. Comparison of excitation techniques for quantitative fluorescence imaging of reacting flows. *AIAA Journal*, 31(3):513–519, 1993.
- [177] B. Shirinzadeh, D. M. Bakalyar, and Charles C. Wang. Measurement of collision-induced shift and broadening of the ultraviolet transitions of OH. *The Journal of Chemical Physics*, 82(7):2877–2879, 1985.
- [178] Chen Shuang, Su Tie, and Li et al . Zhong-Shan. Quantitative measurement of hydroxyl radical (OH) concentration in premixed flat flame by combining laser-induced fluorescence and direct absorption spectroscopy. *Chin. Phys. B*, 25(10), 2016.
- [179] Ajay V. Singh. *Temperature*, pages 1–12. Springer International Publishing, Cham, 2018.
- [180] G. Singla, P. Scouflaire, C. Rolon, and S. Candel. Planar laser-induced fluorescence of OH in high-pressure cryogenic LO_x/GH₂ jet flames. *Combustion and Flame*, 144(1):151 – 169, 2006.
- [181] A. K. Sinha, D. G. Bogard, and M. E. Crawford. Film-Cooling Effectiveness Downstream of a Single Row of Holes With Variable Density Ratio. *Journal of Turbomachinery*, 113(3):442–449, 07 1991.
- [182] S. H. Smith and M. G. Mungal. Mixing, structure and scaling of the jet in crossflow. *Journal of Fluid Mechanics*, 357:83–122, 1998.
- [183] Tamara Sopek. *Temperature measurements in hypervelocity flows using thermally-assisted laser-induced fluorescence*. PhD thesis, The University of Queensland, 2018.
- [184] L.J. Spadaccini and M.B. Colket. Ignition delay characteristics of methane fuels. *Progress in Energy and Combustion Science*, 20(5):431 – 460, 1994.
- [185] P. Stainback and K. Nagabushana. Review of Hot-Wire Anemometry Techniques and the Range of their Applicability for Various Flows. In *Electronic Journal of Fluids Engineering, Transaction of the ASME*, 1997.
- [186] Adam Steinberg, R Sadanandan, C Dem, Peter Kutne, and Wolfgang Meier. Structure and stabilization of hydrogen jet flames in cross-flows. *Proceedings of the Combustion Institute*, 34:1449–1507, 12 2013.
- [187] D. Surek and S. Stempin. *Technische Strömungsmechanik: Für Studium, Examen und Praxis*. Springer-Lehrbuch. Springer Fachmedien Wiesbaden, 2014.
- [188] Jan Taler and Piotr Duda. *Solving Direct and Inverse Heat Conduction Problems*. Springer Berlin Heidelberg, 2006.
- [189] Masayuki Tamura, P A Berg, J E Harrington, J Lique, J B Jeffries, G P Smith, and D R Crosley. Collisional quenching of CH(A), OH(A), and NO(A) in low pressure hydrocarbon flames. *Combustion and Flame*, 114(3-4), 8 1998.

- [190] N. Taniguchi, T. J. Wallington, M. D. Hurley, A. G. Guschin, L. T. Molina, and M. J. Molina. Atmospheric Chemistry of C₂F₅C(O)CF(CF₃)₂: Photolysis and Reaction with Cl Atoms OH Radicals and Ozone. *The Journal of Physical Chemistry A*, 107(15):2674–2679, 2003.
- [191] J.R. Taylor. *An Introduction to Error Analysis: The Study of Uncertainties in Physical Measurements*. ASMSU/Spartans.4.Spartans Textbook. University Science Books, 1997.
- [192] Inc. The MathWorks. *Symbolic Math Toolbox*. Natick, Massachusetts, United State, 2020.
- [193] Mark C. Thurber, Frédéric Grisch, Brian J. Kirby, Martin Votsmeier, and Ronald K. Hanson. Measurements and modeling of acetone laser-induced fluorescence with implications for temperature-imaging diagnostics. *Appl. Opt.*, 37(21):4963–4978, Jul 1998.
- [194] COMSOL Multiphysics® v. 5.5. COMSOL AB, Stockholm, Sweden. www.comsol.com.
- [195] Verein deutscher Ingenieure. *VDI-Wärmeatlas*. VDI-Buch. Springer, Berlin Heidelberg, 11 edition, 2013.
- [196] H.K. Versteeg and W. Malalasekera. *An Introduction to Computational Fluid Dynamics: The Finite Volume Method*. Pearson Education Limited, 2007.
- [197] Jan VORÁČ. *Plasma diagnostics based on laser induced fluorescence*. Doctoral theses, dissertations, Masaryk University, Faculty of Science, Brno, 2014 [cit. 2020-10-17].
- [198] J. Warnatz, U. Maas, and R.W. Dibble. *Combustion: Physical and Chemical Fundamentals, Modeling and Simulation, Experiments, Pollutant Formation*. Springer Berlin Heidelberg, 2010.
- [199] Li Xu, Sun Bo, You Hongde, and Wang Lei. Evolution of Rolls-royce Air-cooled Turbine Blades and Feature Analysis. *Procedia Engineering*, 99:1482–1491, 2015. 2014 Asia-Pacific International Symposium on Aerospace Technology, APISAT2014 September 24-26, 2014 Shanghai, China.
- [200] Joseph Zelina, Jeffrey Ehret, R. Hancock, Dale Shouse, W. Roquemore, and G. Sturgess. Ultra-Compact Combustion Technology Using High Swirl For Enhanced Burning Rate. In *38th AIAA/ASME/SAE/ASEE Joint Propulsion Conference and Exhibit*, 07 2002.
- [201] Joseph Zelina, Geoff Sturgess, and Dale Shouse. The Behavior of an Ultra-Compact Combustor (UCC) Based on Centrifugally-Enhanced Turbulent Burning Rates. In *40th AIAA/ASME/SAE/ASEE Joint Propulsion Conference and Exhibit*, 07 2004.